

CP 364-17

# **SANDIA REPORT**

SAND2001-8274  
Unlimited Release  
Printed June 2001

## **Kinetics of Supercritical Water Oxidation- SERDP Compliance Technical Thrust Area Project 364-DOE Final Report**

Steven F. Rice

Prepared by  
Sandia National Laboratories  
Albuquerque, New Mexico 87185 and Livermore, California 94550

Sandia is a multiprogram laboratory operated by Sandia Corporation,  
a Lockheed Martin Company, for the United States Department of  
Energy under Contract DE-AC04-94AL85000.

Approved for public release; further dissemination unlimited.



**Sandia National Laboratories**

2002-0913085

Issued by Sandia National Laboratories, operated for the United States  
Department of Energy by Sandia Corporation.

**NOTICE:** This report was prepared as an account of work sponsored by an agency of the United States Government. Neither the United States Government, nor any agency thereof, nor any of their employees, nor any of their contractors, subcontractors, or their employees, make any warranty, express or implied, or assume any legal liability or responsibility for the accuracy, completeness, or usefulness of any information, apparatus, product, or process disclosed, or represent that its use would not infringe privately owned rights. Reference herein to any specific commercial product, process, or service by trade name, trademark, manufacturer, or otherwise, does not necessarily constitute or imply its endorsement, recommendation, or favoring by the United States Government, any agency thereof, or any of their contractors or subcontractors. The views and opinions expressed herein do not necessarily state or reflect those of the United States Government, any agency thereof, or any of their contractors.

Printed in the United States of America. This report has been reproduced directly from the best available copy.

Available to DOE and DOE contractors from  
Office of Scientific and Technical Information  
P.O. Box 62  
Oak Ridge, TN 37831

Prices available from (703) 605-6000  
Web site: <http://www.ntis.gov/ordering.htm>

Available to the public from  
National Technical Information Service  
U.S. Department of Commerce  
5285 Port Royal Rd  
Springfield, VA 22161

NTIS price codes  
Printed copy: A07  
Microfiche copy: A01



**REPORT DOCUMENTATION PAGE**Form Approved  
OMB No. 074-0188

Public reporting burden for this collection of information is estimated to average 1 hour per response, including the time for reviewing instructions, searching existing data sources, gathering and maintaining the data needed, and completing and reviewing this collection of information. Send comments regarding this burden estimate or any other aspect of this collection of information, including suggestions for reducing this burden to Washington Headquarters Services, Directorate for Information Operations and Reports, 1215 Jefferson Davis Highway, Suite 1204, Arlington, VA 22202-4302, and to the Office of Management and Budget, Paperwork Reduction Project (0704-0188), Washington, DC 20503

<b>1. AGENCY USE ONLY (Leave blank)</b>		<b>2. REPORT DATE</b> June 2001	<b>3. REPORT TYPE AND DATES COVERED</b> Final Report	
<b>4. TITLE AND SUBTITLE</b> Kinetics of Supercritical Water Oxidation - SERDP Compliance Technical Thrust Area			<b>5. FUNDING NUMBERS</b> N/A	
<b>6. AUTHOR(S)</b> Steven F. Rice				
<b>7. PERFORMING ORGANIZATION NAME(S) AND ADDRESS(ES)</b> Sandia National Laboratories Albuquerque, New Mexico Livermore, California			<b>8. PERFORMING ORGANIZATION REPORT NUMBER</b> N/A	
<b>9. SPONSORING / MONITORING AGENCY NAME(S) AND ADDRESS(ES)</b> SERDP 901 North Stuart St. Suite 303 Arlington, VA 22203			<b>10. SPONSORING / MONITORING AGENCY REPORT NUMBER</b> N/A	
<b>11. SUPPLEMENTARY NOTES</b> No copyright is asserted in the United States under Title 17, U.S. code. The U.S. Government has a royalty-free license to exercise all rights under the copyright claimed herein for Government purposes. All other rights are reserved by the copyright owner.				
<b>12a. DISTRIBUTION / AVAILABILITY STATEMENT</b> Approved for public release; distribution is unlimited.				<b>12b. DISTRIBUTION CODE</b>
<b>13. ABSTRACT (Maximum 200 Words)</b> This final report has two purposes. The first is to provide a single document that contains a description of this project's goals, activities, and accomplishments over the 8 year period of performance from January, 1993 to August, 2000. The second purpose is to provide an overview of the technical results that have been obtained and to submit a roadmap that identifies the publications and reports where the details of these technical results can be found. This report is not intended to republish the complete contents of the quarterly progress reports of the several dozen reviewed publications and Sandia reports that have resulted from this project. However, sufficient detail of the experimental and modeling results is included to illustrate the most important technical conclusions. Specifically, detailed results are presented here that answer the two fundamental questions that have motivated this work. They are: 1) what are the rate-controlling processes in the oxidation of a variety of organic compounds in supercritical water; and 2) how does this oxidation chemistry compare to combustion chemistry and, if so, can the same elementary reaction modeling approaches that have met with success.				
<b>14. SUBJECT TERMS</b> SERDP, SERDP collection, super critical water oxidation (SCWO), Ramen				<b>15. NUMBER OF PAGES</b> 157
				<b>16. PRICE CODE</b> N/A
<b>17. SECURITY CLASSIFICATION OF REPORT</b> unclass	<b>18. SECURITY CLASSIFICATION OF THIS PAGE</b> unclass	<b>19. SECURITY CLASSIFICATION OF ABSTRACT</b> unclass	<b>20. LIMITATION OF ABSTRACT</b> UL	

NSN 7540-01-280-5500

Standard Form 298 (Rev. 2-89)  
Prescribed by ANSI Std. Z39-18  
298-102

20020913 085

SAND2001-8274  
Unlimited Release  
Printed June 2001

**Kinetics of Supercritical Water Oxidation-SERDP  
Compliance Technical Thrust Area  
Project 364-DOE  
Final Report**

Steven F. Rice  
Principal Investigator

Sandia National Laboratories/California

**Abstract**

This final report has two purposes. The first is to provide a single document that contains a description of this project's goals, activities, and accomplishments over the 8 year period of performance from January, 1993 to August, 2000. The second purpose is to provide an overview of the technical results that have been obtained and to submit a roadmap that identifies the publications and reports where the details of these technical results can be found. This report is not intended to republish the complete contents of the quarterly progress reports or the several dozen reviewed publications and Sandia reports that have resulted from this project. However, sufficient detail of the experimental and modeling results is included to illustrate the most important technical conclusions. Specifically, detailed results are presented here that answer the two fundamental questions that motivated this work. They are: 1) what are the rate-controlling processes in the oxidation of a variety of organic compounds in supercritical water; and 2) how does this oxidation chemistry compare to combustion chemistry and, if so, can the same elementary reaction modeling approaches that have met with success

AQMO2-12-3131



This page intentionally left blank

**Kinetics of Supercritical Water Oxidation**  
**SERDP Compliance Technical Thrust Area**  
**Project 364-DOE**  
**Final Report**

Steven F. Rice

Sandia National Laboratories  
Combustion Research Facility

Summary of work performed at Sandia, MIT, and Princeton University  
over the period 1993-2000

*Executive Summary*

**Project team**

Principal Investigator:	Steven F. Rice
Project Manager:	Donald R. Hardesty
Project Associates, Sandia:	Richard R. Steeper, William S. Winters, Thomas B. Hunter, Costanzo A. LaJeunesse, Russell G. Hanush, Jason D. Aiken
Visiting Scientists:	Eric Croiset, Åsa Rydén
University Collaborators:	Prof. Jefferson W. Tester, MIT Prof. Jack Howard, MIT Prof. Kenneth Brezinsky, U. of Illinois, Chicago Prof. Irvin Glassman, Princeton University

**E.1 Report Contents**

This final report has two purposes. The first is to provide a single document that contains a description of this project's goals, activities, and accomplishments over the 8 year period of performance from January, 1993 to August, 2000. The second purpose is

to provide an overview of the technical results that have been obtained and to submit a roadmap that identifies the publications and reports where the details of these technical results can be found. This report is not intended to republish the complete contents of the quarterly progress reports or the several dozen reviewed publications and Sandia reports that have resulted from this project. However, sufficient detail of the experimental and modeling results is included to illustrate the most important technical conclusions. Specifically, detailed results are presented here that answer the two fundamental questions that motivated this work. They are: 1) what are the rate-controlling processes in the oxidation of a variety of organic compounds in supercritical water; and 2) how does this oxidation chemistry compare to combustion chemistry and, if so, can the same elementary reaction modeling approaches that have met with success in the combustion arena be used to model supercritical water oxidation (SCWO)?

The primary motivation for the project can be summarized as follows. If elementary reaction modeling can be used quantitatively, then this project can develop a reaction kinetics tool to be used by SCWO design engineers in the future to make innovative changes to first generation SCWO pilot plants. Such innovation will lead to improved energy efficiency, greater durability, and wider applicability of SCWO that should bring capital and operation costs down. Presumably, accompanying a significant reduction in these costs, SCWO can transition from the pilot/developmental stage to commercialization with widespread use by the DoD, DOE, and their contractors for demilitarization and waste disposal.

#### Index of sections:

1. Introduction
2. Technical Approach and Methods
3. Validation of Gas Phase Assumptions. Part 1 - Experiments
4. Validation of Gas Phase Assumptions. Part 2 - Reaction Pathways
5. Role of Hydrogen Peroxide
6. Role of Water
7. Large Molecules
8. Heteroatoms
9. Computational Fluid Dynamics Modeling of Transpiration-wall SCWO Reactors

## E.2 Project Description

This basic research project consists of experiments and theoretical modeling designed to improve our understanding of the detailed chemical kinetics of supercritical water oxidation processes. The objective of the five-year project is to develop working models that accurately predict the oxidation rates and mechanisms for a variety of key organic species over the range of temperatures and pressures important for industrial applications. Our examination of reaction kinetics in supercritical water undertakes *in situ* measurements of reactants, intermediates, and products using optical spectroscopic techniques, primarily Raman spectroscopy. Our focus is to measure the main oxidation

steps that occur in the oxidation of C1 compounds such as methane and methanol as well as higher alcohols and aromatics. The project has also explored several aspects of the presence of halogens and nitrogen. We place special emphasis on identifying reaction steps that involve hydroxyl radicals, hydroperoxyl radicals, and hydrogen peroxide.

Most of the measurements were conducted in two optically accessible reactors located at Sandia's Combustion Research Facility (CRF), the supercritical flow reactor (SFR) and the supercritical constant volume reactor (SCVR), designed to operate at temperatures and pressures up to 600 °C and 30.0 MPa (SFR) and 550°C and 50 MPa (SCVR). For reference, 1 MPa = 145 psi = 10 bar. The combination of these two reactors permits reaction rate measurements ranging from 0.1 s to many hours.

In addition, experiments using flow reactors at MIT and Princeton University have significantly contributed to the results. Direct support was provided to the project by collaborators at MIT and Princeton University who contributed to model development for phenol, other aromatics, and halogenated species. These researchers employed established quench and sample methods that are well suited for identifying and quantifying complicated product distributions.

This project has produced predictive chemical reaction models to be used to aid the design and operation of large-scale SCWO equipment. These engineering design models implicitly center on an accurate description of the chemistry of the key oxidation-resistant species. The insight and understanding needed to develop these models is generated by coupling an extensive experimental program to a parallel theoretical effort producing quantitative mechanistic descriptions of the oxidation processes. In the end, this is leading to a model that integrates chemistry, fluid mechanics, and heat and mass transport in a multidimensional flow computational code for complete SCWO reactor simulation.

### **E.3 Partners and Related Activities**

This project was a direct collaboration with Princeton University and Massachusetts Institute of Technology on the chemistry of aromatic compounds, specifically phenol and benzene. Prof. K.E. Brezinsky (now at U. of Illinois, Chicago) and colleagues at Princeton, including Prof. Irvin Glassman, developed the mechanistic description of phenol and anisole oxidation under intermediate temperature conditions. This work provided us with a starting point for the development of an aromatic species mechanism. Collaboration with Prof. J.W. Tester, Prof. Jack Howard, and their co-workers at MIT focused on experiments and model development for aromatics in supercritical water concurrently with the mechanistic work at Princeton. In addition, the MIT team developed a comprehensive model for the role of hydrolysis in the overall conversion of halogenated species under oxidizing and pyrolytic conditions. Both the MIT and Princeton teams were only partially supported by this SERDP project. In addition to the SERDP funding from this project, the MIT work was supported by the

Army Research Office and Princeton was supported by the DOE Office of Basic Energy Sciences.

In addition to the direct collaboration included in this program, the team remained in contact with researchers at Stone and Webster, General Atomics, and Foster Wheeler Development Corporation, who are working with DOE and the military services in developing and implementing this technology from the standpoint of pilot reactor design, fabrication, and operation. Under the project direction of U.S. Army TACOM - ARDEC, Sandia has been closely involved in the application of SCWO for the disposal of dyes and smoke formulations at Pine Bluff Arsenal (PBA). The basic research conducted on this SERDP project has had an invaluable impact on the progress of the PBA plant.

#### **E.4 Benefit**

Supercritical water oxidation technology is presently in the pilot reactor and production prototype stage at several government laboratories and private industrial facilities. Equipment being fabricated at this stage of technology development uses only the simplest processing concepts and reaction rate information. For these prototype systems, processing and fabrication costs are small relative to development costs. The next generation of SCWO processing equipment will be beyond the pilot plant scale and will need to realize significant operational savings, relative small-scale systems, to be viable. In this project, experiments on mechanisms and rate controlling processes in this unusual environment lead to predictive models for reactor design, predictions of destruction efficiency, and methods for industrial-scale system optimization.

#### **E.5 Accomplishments**

There are two major accomplishments. The first is the body of experimental work conducted within this project that establishes a foundation for the development of both global rate expressions and detailed mechanisms. The second is the interpretation of the accuracy of straightforward elementary reaction mechanistic modeling for the application to SCWO. When combined, these two achievements produce a tool that can be used by others to explore reactor design innovation.

The body of experimental work is primarily represented by a number of publications in the reviewed engineering and scientific literature as well as by unlimited-release Sandia Reports and conference proceedings. Appendix A provides a complete list of written reports and papers. The second accomplishment is less concrete, but equally valuable. This is the establishment of a continuous research effort and unique chemical engineering expertise at Sandia which over a number of years, had the breadth of activity needed to make revolutionary advances in the design engineering of SCWO reactors. These advances will lead to successful processing of complicated and unusual wastes generated by the DoD and DOE.

## ***Section 1: Introduction***

### **1.1 Project Overview**

#### ***1.1.1 Historical background***

Supercritical water oxidation (SCWO) is a chemical processing technology under development by government laboratories, universities, and private industry primarily for the treatment of aqueous hazardous waste. It is also suited for treatment of waste materials that are best handled in water for environmental or safety reasons such as obsolete munitions, rocket motors, and chemical warfare agents. The process operates at temperatures and pressures above the critical point of water with typical conditions: 450 - 650°C and 25 MPa (3600 psi), and is applicable to waste streams containing 0 - 20 percent organics in water. The gaseous and liquid effluent from the process can be evaluated relatively easily for compliance with applicable discharge regulations before release, ensuring protection of the environment.

Early patents and reports for the process<sup>1-4</sup> include data showing 99.99% destruction of many normal and halogenated hydrocarbons including trichloroethylene, DDT, and PCBs. Since then, the number of organic solvents, inorganic chemicals, and complex mixtures treated by SCWO has grown considerably. However, the application of SCWO to most DoD and DOE waste treatment issues requires that the technology be advanced beyond the level of development that had been achieved at the onset of this project. At that time, it was generally recognized that these improvements would not be possible without better predictive models for the time, temperature, density, and concentration dependence of the oxidation process. Chemical kinetics predictive mechanisms would be implemented in a chemical engineering process model for SCWO conditions to be used to design and optimize economical plants. In turn, this understanding would be integrated into process control algorithms for safe and reliable operation.

During the oxidation process, real waste streams exhibit complications. Heteroatoms such as sulfur, nitrogen, and halogens as well as metals can contribute to the formation of solids and acid gases that can exist as transient intermediates and as final products. These materials lead to corrosion and plugging within the flow. Identification of the conditions for the formation of these effluent components is critical.

Figure 1.1 shows a simple picture of SCWO processing. A pressurized aqueous feed is preheated and delivered to a high temperature reactor where most of the conversion takes place. If necessary, subsequent liquid and gaseous effluent monitoring and neutralization is possible.

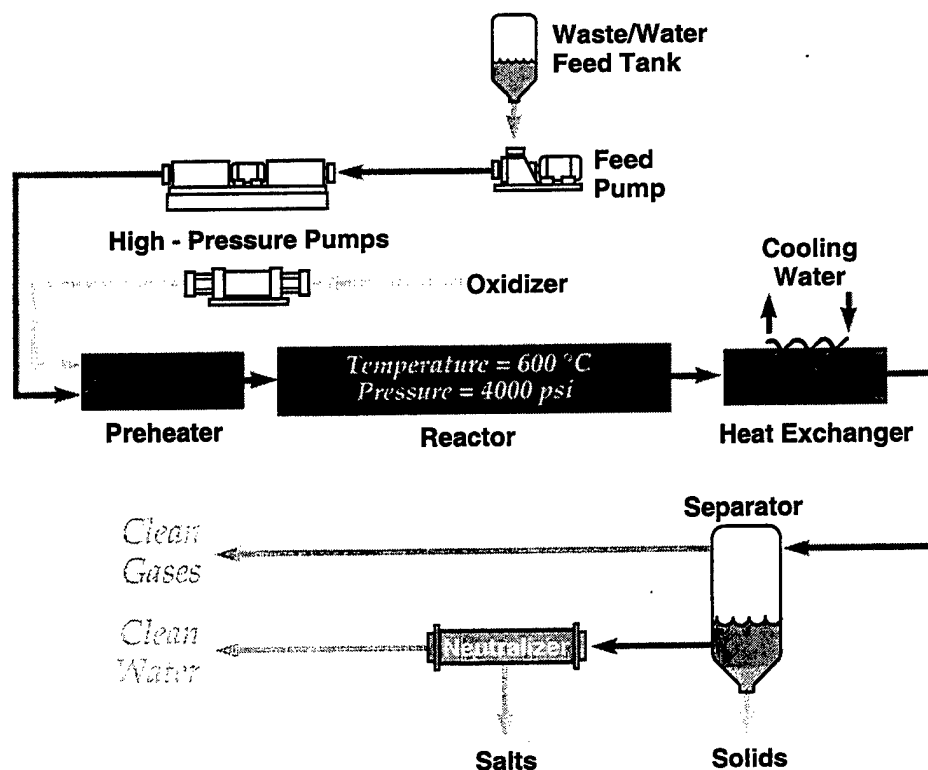


Figure 1.1 Schematic of the SCWO process.

In the early 1990's, the understanding of the rates and mechanisms of reactions in supercritical water was limited to a handful of empirical mechanisms for very simple chemicals. These mechanisms are of limited use in the formulation of a predictive model of SCWO. To be generally applicable and valuable as a design tool, models must be based on elementary reaction steps or at least a detailed quantitative mechanistic description incorporating all the key fundamental reactions. Valuable progress using this approach had been made by several research teams in the late 1980's and early 1990's, but agreement between elementary models and experiment was only qualitative in most cases. In addition, there was a wide variation in experimental results and model predictions from different research efforts as a function of feed concentration and other reaction conditions, which emphasized the need for closer collaboration among researchers.

Sandia National Laboratories had a role in some of this early progress through a number of projects designed to evaluate the viability of SCWO for the complicated waste feeds present in the DOE and DoD. These precursor projects were supported internally by Sandia in laboratory-directed research and by several other federal organizations including DARPA, the Naval Civil Engineering Laboratory at Port Hueneme, and the DOE HAZWRAP program.

### ***1.1.2 Project goals***

A thorough understanding of operative chemical kinetics at the level of basic science is required to underpin applications of supercritical water oxidation technology. In 1993, this project was first proposed as a basic research project designed to experimentally investigate the uncertain chemical kinetics of SCWO and was intended to expand our understanding of SCWO chemistry by directly measuring the time, temperature, and density dependencies of key reacting chemical species. The emphasis was to be placed, not simply on the conversion of the feed organic material, but to sort out the complicated role of the various radical chain-propagating species that participate in the elementary steps of converting organics to carbon dioxide and water. These experimental measurements were to provide the backbone needed to improve the theoretical basis of reaction mechanistic models. Once these key steps are established, the project extended the scope of the mechanistic models beyond the oxidation of simple single carbon organic systems to larger aromatic species and organic molecules containing nitrogen or chlorine.

The final goal of this project is to produce predictive chemical reaction models to be used to aid the design and operation of large-scale SCWO equipment. These engineering design models implicitly center on an accurate description of the chemistry of the key oxidation-resistant species. Such a design tool must rely on state-of-the-art computational methods to properly represent chemical kinetics, fluid dynamics, and heat and mass transport in complicated flow geometries. The insight and understanding needed to develop these models is generated by coupling an extensive experimental program to a parallel theoretical effort producing quantitative mechanistic descriptions of the oxidation processes. These quantitative mechanisms can then be formalized into predictive comprehensive computer models. The final goal of the project is to formulate such a model for an actual pilot scale SCWO reactor.

### ***1.1.3 Technical approach overview***

Actual wastes generated at DoD and DOE facilities are complicated formulations of large organic molecules and inorganic compounds such as paints, dyes, bonded explosives, solvents, and oils. However, work at Sandia and elsewhere has indicated that even at mild SCWO operating conditions, feeds of these complicated materials very rapidly convert to mixtures of simple chemicals. These intermediate species are oxidation-resistant molecules such as methane and methanol, simple amines and nitrates, or phenol and other small aromatic ring species. Chlorinated systems represent an exceptionally important waste treatment problem for SCWO where hydrolysis and oxidation reactions are closely coupled. The oxidation rates of these intermediate species are the limiting processes for the complete destruction of complex feed materials.

The experimental portion of the research entails determining the concentration of reactants, stable intermediates, and products associated with the oxidation of model chemical species in supercritical water. The time-temperature-concentration profiles that are measured provide the foundation for the mechanistic description of the many steps that even simple organic molecules pass through to complete oxidation.



Measurements of species concentration profiles of key intermediates are critical to developing chemical mechanisms. The experimental profiles of reactants and products provide test and verification of the quantitative capabilities of the predictive models.

Early work at Sandia, prior to the initiation of this project, proved spontaneous Raman spectroscopy to be a very useful method for measuring concentrations of a variety of chemical species in supercritical water. We had recorded strong signals from CH<sub>4</sub>, CH<sub>3</sub>OH, CO<sub>2</sub>, CO, H<sub>2</sub>, O<sub>2</sub>, and N<sub>2</sub> at concentrations below 0.01 mole/liter. At that time, data collected during 1993 on the oxidation of methane had already contributed to the understanding of the temperature and concentration dependence of methane oxidation under SCWO conditions. This early work demonstrated the power of *in situ* spectroscopic methods for collecting the detailed experimental data necessary to completely describe chemical reactivity over a wide range of pressure, temperature, and reactant feed concentrations. Much of the experimental data collected in this project used these Raman methods that were established through several small projects at Sandia in the 1988-1993 timeframe.

The quantitative mechanism and model development proceeded in parallel with the experiments. Initially, predictions from combustion-based elementary reaction mechanisms for low-density, high temperature processes were compared to results from SCWO experiments. These comparisons guided the design of new experiments and suggested modifications to the model. Subsequently, the results of the experiments were used to improve the predictive performance of the models.

We emphasize that the goal of this project has been to produce predictive models for the oxidation of key species in supercritical water and not simply to illustrate the effectiveness of SCWO.

## 1.2 Benefit

### 1.2.1 Connection to other SCWO technology development efforts

The initiation of this project did not occur in a vacuum and the research path was not independent of other technological developments in SCWO that occurred from 1994-2000. Progress in technology development activities not directly related to this project at Sandia and elsewhere has steered the research and placed demands on its relevancy. Over the past six years, several dozen organizations in the U.S. (and many more worldwide), large and small, have contributed to SCWO development. These other participants in the field range from academic researchers to venture capital commercialization interests. There have been numerous research sponsors within the federal agencies that have recognized the potential of SCWO to solve waste disposal problems affiliated with a particular agency. The unusual nature of many of the types of wastes owned by the DoD and DOE has placed these agencies in the forefront of technology development support. Actual public expenditure alone is probably near \$100M. Total investment in the private sector worldwide is also in the tens of millions

of dollars. Therefore, it is important to recognize that this work is only a small part of the progress SCWO has made in the 1990s.

This project has made a conscious effort to make its results public at the earliest opportunity to aid these other efforts. This was done through regular detailed technical quarterly reports with a wide distribution that sped the release of new technical discovery by nearly a year over a journal publication route. These reports have enabled many results to become available that would not be suitable for the academic chemical kinetics literature.

There are now at least six pilot scale plants worldwide (defined as costing between \$5-\$15 million) in operation or nearing operation. These systems vary in design principle only slightly, but vary in design detail greatly. Many of the details of these systems are held as proprietary. However, the principal challenges to the implementation of the technology beyond the present point are the same for all of the systems.

### ***1.2.2 SCWO performance challenges***

As mentioned above, the implementation of the SCWO concept into actual hazardous waste treatment systems presents a number of practical engineering challenges. These are:

1. The destruction of the waste feed must be sufficiently complete to meet the goals of the application.
2. The corrosive nature of the SCWO process must be mitigated to provide adequate equipment lifetime and operating safety.
3. The buildup of insoluble material within a continuously flowing system must be prevented to ensure operating stability.
4. The fabrication and operating costs must be kept to a level that makes the application of SCWO in a particular instance affordable and preferable to other approaches to waste disposal.
5. The heat release must be managed to ensure safe operation.

The results and conclusions of this basic research project address all of these issues directly or indirectly. The project addresses (1) directly by providing as a deliverable a collection of submechanisms that can be combined together, depending on the specific composition of the material to be treated, to calculate destruction rates. However, the results from this project are more far-reaching and have important indirect implications regarding the other four technological development challenges.

A successful overall system design must meet (2-5) as well and will require a clear understanding of how reactions are initiated in SCWO and how rapidly heat is released as the oxidation process proceeds. This project provides a predictive structure that can

describe accurately not only longer time destruction efficiency to determine reaction times required for high conversion, but also provides predictive capability for reaction initiation. By knowing the characteristics of how heat is released in the early stages of oxidation, novel approaches can be explored for feeding the reactants. In fact, it will be these innovations in reactant feed and reaction initiation methods that will permit the implementation of clever corrosion and scaling prevention strategies.

### *1.2.3 Pine Bluff Arsenal SCWO reactor design*

The past two years (1999-2000) have witnessed several significant developments in the progress of supercritical water oxidation (SCWO) from a laboratory scale endeavor to implementation on a larger scale for the actual disposal of some difficult DoD waste remediation problems. Among the more important of these developments is the construction of two small-footprint units designed for shipboard excess hazardous material removal and a larger facility at Pine Bluff Arsenal (PBA).<sup>5,6</sup> The PBA production prototype system is unique in that it is designed for the disposal of a variety of unusual munition materials that, for a number of reasons, are incompatible with more traditional disposal methods. It displays several innovative design concepts. The PBA unit and the above-mentioned Office of Naval Research systems have improved on the earlier pilot-scale systems by integrating novel corrosion mitigation methods with better strategies for preventing scaling and fouling due to solids accumulation. In doing so, these systems represent several different approaches to solving these key issues that have, until now, presented significant impediments to the commercialization and acceptance of SCWO as a generally-applicable waste treatment technology.

Sandia National Laboratories has collaborated with Foster Wheeler Development Corp. (FWDC) and Aerojet GenCorp to use Aerojet's sophisticated platelet transpiration-wall technology as a foundation for simultaneously eliminating both the corrosion and scaling problems.<sup>7,8</sup> This design strategy as well as alternative methods used by General Atomics, who have also recently claimed significant advances in corrosion mitigation, have highlighted (5) in the list above as a very important aspect of the practical use of SCWO. This is the issue of heat management in such a high-pressure, high-temperature exothermic process.

The FWDC/Aerojet/Sandia transpiration-wall reactor design, pictured in Figure 1.2, is intended to take advantage of an injector to minimize preheat while simultaneously maintaining a turbulent plug flow to assure high conversion and greater simplicity for effluent management. By combining this feed method with a transpiration-lined vessel, low corrosion and minimal scaling can be achieved in a simple plug flow system with well-defined residence time. Sandia's Engineering Evaluation Reactor (EER) demonstrated the successful operation of this design, on a 1.1-inch scale, in 1995-1996. The success of the reactor originates from two major design ideas. First, the use of the transpiration boundary layer to prevent the contact of sticky solids and corrosive gases with the liner wall, and second, the development of an injector for the feed streams that significantly reduces the need for external preheating, while permitting the reactants to be transported through the reactor in plug flow.

The effectiveness in preventing the adherence of deposits on the wall of the reactor as well as the utility of the multiport injector have been documented in published Sandia reports. These tests established the foundation for the PBA system design. However, budgetary and schedule considerations prevented the exploration of this small-scale system to gain a full working knowledge of the range of useful operating conditions and their relationship to waste conversion. Moreover, exploration of the operation of the injector and the various reaction initiation approaches, which might afford the simplest and most reliable start-up procedures, could not be pursued.

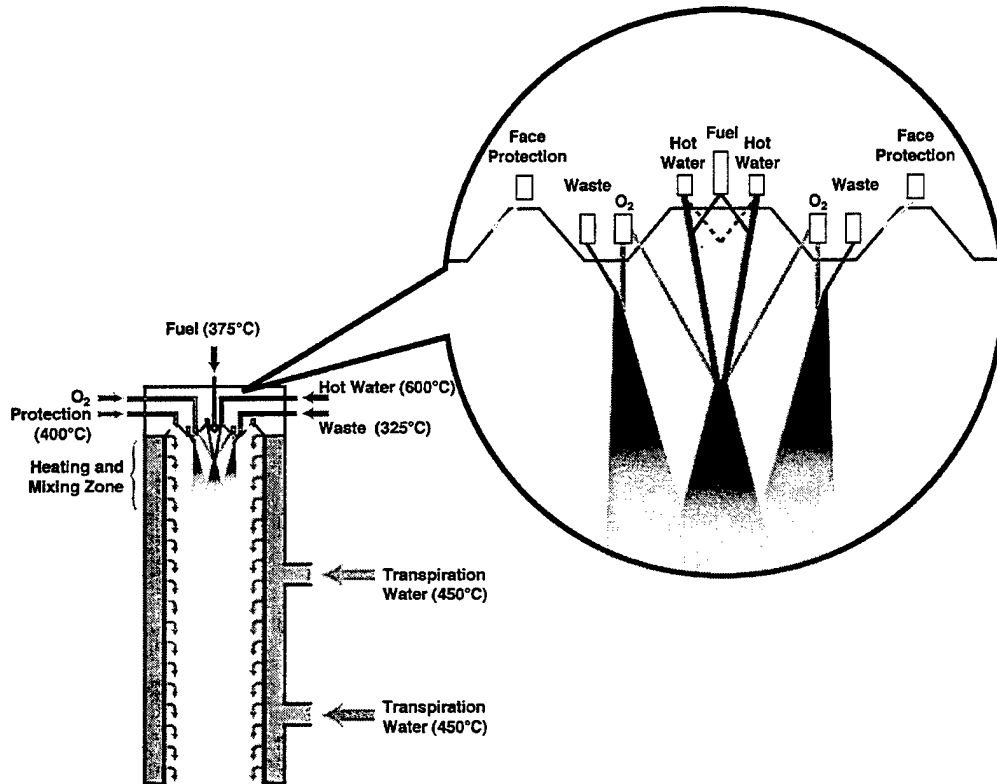


Figure 1.2 Schematic diagram of the transpiration-wall strategy combined with a two-stage fuel and waste feed injector. The transpiration protection water is nearly axisymmetric, whereas the injector has fourfold symmetry.

As the PBA plant commences the DoD Environmental Security Test and Certification Program (ESTCP) test regimen, discussion within the start-up team has focused on the need to move quickly from conservative operation with limited feed rates to full flow operation and effectively survey the range of feed parameters that provide the best and most stable long term operating conditions. The plant possesses a high degree of flexibility over operating parameters such as feed flow rates, preheat temperatures etc. and monitors numerous input and output variables, but lacks internal diagnostics in the reactor vessel itself. Because of this, the development of relationships between feed parameters and performance within a prescribed safe operating envelope will rely on phenomenological observation. Process improvement will be slow and characterized

by small incremental adjustments. A computationally efficient, quantitative model of the reacting flow within the high temperature part of the reactor, including the transpiration boundary layer and its interaction with the bulk flow, could prove invaluable.

The development of such a model and its application to the specifics of the PBA plant provides three benefits. The first is short-term and will have a direct impact on the efficiency of that plant, as it is transitioned from a demonstration/validation unit to part of the Army's demil capability for unusual materials. The second benefit is longer term and applies not only to the development of SCWO within the transpiration-wall strategy, but to any feed system that relies on autothermal (i.e. minimal or no preheating) initiation of the reactants.

The work initiated in the last year of this SERDP project can contribute to the improvement and safety of injector configurations for SCWO reactors that use other methods to mitigate corrosion and scaling (i.e. methods that employ liners of special materials and high flow velocities). The third benefit will be the guidance that can be gained from modeling regarding scaling issues. The PBA SCWO, and other reactors of similar throughput, do not significantly take advantage of the reduced cost per process pound that can be realized by either scaling to a larger vessel or by multiplexing reactor units operating from a single feed supply and effluent management system. The reactor systems that have been constructed to date generally have inefficient quenching and effluent post-treatment methods which can be significantly improved when combined with a more detailed understanding of feed preheating requirements.

### 1.3 References

1. M. Modell, G.G. Gaudet, M. Simson, G.T. Hong, K. Biemann "Supercritical Water. Testing Reveals New Process Holds Promise" *Solids Waste Management* 25, 26, 1982.
2. M. Modell "Processing Methods for the Oxidation of Organics in Supercritical Water" U.S. Patent No 4,338,199, 1982.
3. M. Modell "Processing Methods for the Oxidation of Organics in Supercritical Water" U.S. Patent No 4,543,190, 1985.
4. M. Modell "Section 8.11, Supercritical-Water Oxidation" in *Standard Handbook of Hazardous Waste Treatment and Disposal*; Freeman, H. M., Ed.; McGraw-Hill: New York, pp. 8.153-8.167, 1989.
5. C.A. LaJeunesse, J.P. Chan, T.N. Raber, D.C. Macmillan, S.F. Rice, K.L. Tschritter "Supercritical Water Oxidation of Colored Smoke, Dye, and Pyrotechnic Compositions. Final Report: Pilot Plant Conceptual Design" Sandia Report SAND94-8202, 1993.

6. S.F. Rice, B.C. Wu, W.S. Winters, C.D. Robinson "Engineering Modeling of the Pine Bluff Arsenal Supercritical Water Oxidation Reactor" *Proceedings of The Fifth International Symposium on Supercritical Fluids* Atlanta, GA April 8-12, 2000.
7. M.F. Young, M.C. Stoddard, B.L. Haroldsen, K.S. Ahluwalia, C.D. Robinson "The Transpiring Wall Platelet Reactor for Supercritical Water Oxidation of Materials with High Inorganic Loading"; *Proceedings of The Fourth International Symposium on Supercritical Fluids*, Sendai, Japan May 11-14, p. 167. 1997.
8. C.A. LaJeunesse, B.L. Haroldsen, S.F. Rice, B.G. Brown "Hydrothermal Oxidation of Navy Shipboard Excess Hazardous Materials" Sandia Report SAND97-8212, 1997.

This page intentionally left blank

## *Section 2: Technical Approach and Methods*

### **2.1 Overview**

#### *2.1.1 Mechanism development strategy*

The successful development of an elementary reaction model that can predict oxidation kinetics in supercritical water rests on verifying whether several key assumptions intrinsic to this kind of combustion-based mechanistic approach can be applied in supercritical water. If these assumptions hold for SCWO, it should be relatively straightforward to correct key reaction rate parameters to the high density and lower temperature conditions that pertain to a SCWO environment. Therefore the first issue to be addressed is to determine whether the oxidation of the simplest organic molecules that have well-established gas phase combustion mechanisms can be predicted. The sequence of activities are:

- 1) Determine the oxidation rates of some simple organic compounds and measure the formation of intermediate and final products. The key test species are  $H_2$ ,  $CO$ ,  $CH_4$ , and  $CH_3OH$ .
- 2) Use these data to test the accuracy of existing elementary reaction mechanisms to confirm the applicability of the gas phase approach for these high-density environments.
- 3) Determine if changes need to be made to these models to accurately represent the data, such as including non-idealities in the mixture thermodynamics or if the presence of water, in great excess, invalidates assumptions related to the gas phase nature of the model.
- 4) Conduct measurements to improve the accuracy of the kinetic parameters of specific key reactions, if necessary.
- 5) Extend the simple single carbon mechanism to high molecular weight species and develop rules for determining the oxidation pathways of large hydrocarbons.
- 6) Extend the backbone C/H/O mechanism to include specific functional groups that are especially relevant to DoD and DOE typical SCWO waste feed materials.

It was clear from the outset of this project that there was a need to detect intermediates as they are produced and consumed during the course of the oxidation reaction. Because of the high-temperature nature of supercritical water, it appeared likely that kinetics experiments that rely on taking samples of the reacting flow, followed by off-line chromatographic analysis, would limit the types of intermediates that could be



detected. As a result, we developed an *in situ* analytical method based on Raman spectroscopy and combined it with two high-temperature, high-pressure reactors that are capable of a wide range of reaction conditions and time scales. Figure 2.1 illustrates this approach.

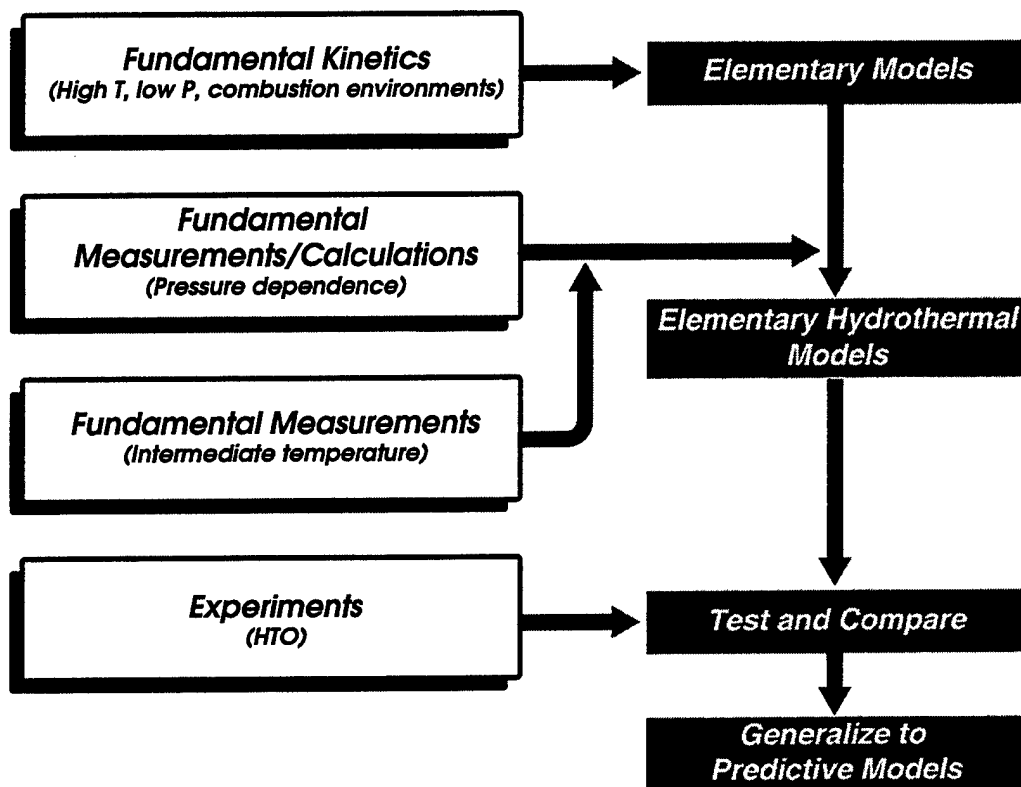


Figure 2.1 Schematic of the approach to developing and verifying predictive mechanisms for the oxidation of organic molecules in supercritical water and hydrothermal oxidation (HTO) conditions. HTO refers to both super and near(sub)- critical conditions (e.g.  $T < 374^{\circ}\text{C}$ ).

### 2.1.2 Publications and reports on SCWO reactors

R.R. Steeper, S.F. Rice, M.S. Brown, S.C. Johnston "Methane and Methanol Diffusion Flames in Supercritical Water" *J. Supercritical Fluids* 5, 262, 1992.

R.R. Steeper, S.F. Rice, M.S. Brown, S.C. Johnston, "Methane and Methanol Diffusion Flames in Supercritical Water" Sandia Report SAND92-8474, 1992.

C.A. LaJeunesse, S.F. Rice, J.J. Bartel, M. Kelley, C.A. Seibel, L.G. Hoffa, T.F. Eklund, B.C. Odegard, "A Supercritical Water Oxidation Reactor: The Materials Evaluation Reactor (MER)" Sandia Report SAND91-8623, 1992.

R.R. Steeper, S.F. Rice "Optical Monitoring of the Oxidation of Methane in Supercritical Water"; in *Physical Chemistry of Aqueous Systems*, (H.J. White, J.V. Sengers, D.B. Neumann, J.C. Bellows Eds.) Begell House, New York, p. 652 1995.

R.G. Hanush, S.F. Rice, T.B. Hunter, and J.D. Aiken, "Operation and Performance of the Supercritical Fluids Reactor (SFR)" Sandia National Laboratories Report SAND96-8203, Livermore, CA, 1996.

S.F. Rice, R.R. Steeper, C.A. LaJeunesse, R.G. Hanush, J.D. Aiken. "Design Strategies for High-Temperature, High-Pressure Optical Cells" Sandia Report SAND99-8260, 1999.

## 2.2 Supercritical Flow Reactor (SFR)

### 2.2.1 Hardware

The Supercritical Fluids Reactor (SFR) at Sandia National Laboratories, CA has been developed to examine and solve engineering, process, and fundamental chemistry problems associated with the development of supercritical water oxidation (SCWO). The apparatus consists of pressurization, feed, preheat, reactor, cool down, and separation subsystems with ancillary control and data acquisition hardware and software. Its operating range is from 375 - 650 °C at 3250 - 6300 psi with residence times from 0.09 to 250 seconds.

A schematic of the reactor is shown in Figure 2.2. In the pump and preheating subsystem, fuel and oxidant are handled in separate lines. Each line consists of a gravity-feed tank, a peristaltic pump, a high-pressure feed pump, and a group of heaters. Each peristaltic pump supplies a constant pressure to its respective high-pressure pump in a recirculation loop. The high-pressure pumps are pneumatically actuated, single stage, piston pumps, allowing the total flow from both lines to be varied from approximately 0.5 to 1.6 ml/s. Each reactant is pumped into its preheater section consisting of a length of high-pressure tubing contained in four 875 W radiant tube furnaces and a section wrapped with two 375 W cable heaters. All of the preheater high-pressure tubing is Inconel 625, 0.48 cm (3/16") inner-diameter (ID) and 1.43 cm (9/16") outer-diameter (OD). The total length of the preheater is 310 cm. The sections are joined with Inconel 625 high-pressure unions. A 1/16 inch, Inconel sheathed, Type K thermocouple is installed in each union to measure the fluid temperature and provide feedback to the appropriate heater controller. Thermocouples are also installed on all tubing surfaces to monitor for overheating. All exposed heated sections and unions are wrapped with alumina insulation to minimize heat loss.

The preheated fuel and oxidant streams are introduced into the upstream end of the flow reactor and mixed under turbulent conditions by combining the flows at a 180° angle of incidence. The combined flow exits the mixing tee orthogonally to the original flows. Reynolds numbers of the combined flow in the reactor range from 4800 to 14700, ensuring turbulent flow throughout, over the entire range of operating conditions.

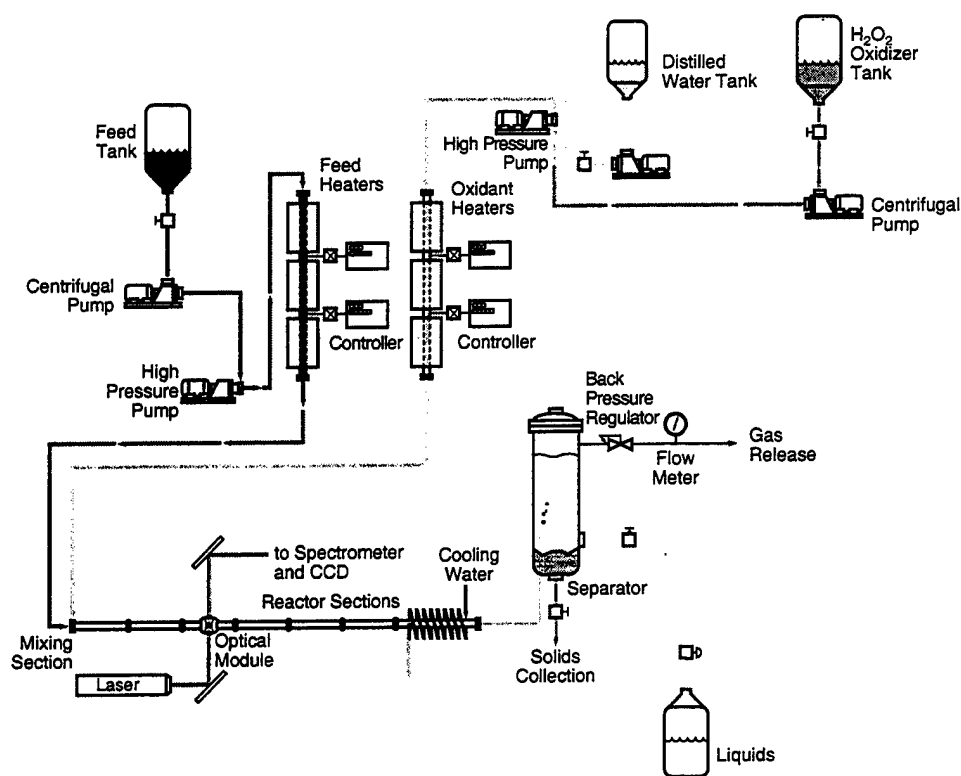


Figure 2.2 Schematic of Sandia's Supercritical Fluid Reactor ( SFR) using two preheat lines.

An alternative feed method is shown in Figure 2.3. In this configuration, only the oxidizer, consisting of water and O<sub>2</sub> is preheated. A much smaller volume of a pure reactant or a concentrated solution is injected rapidly into the oxidizing flow at the mixing head at the inlet to the reactor. This feed is supplied by a low-flow HPLC pump. This configuration is useful for preventing hydrolysis or pyrolysis of reactive feeds in the long reactant preheating section.

The combined flows then pass into the reactor subsystem. The reactor consists of six 61-cm sections of Inconel 625 tubing (0.48 cm ID and 1.43 cm OD) joined by Inconel tee fittings with Type K thermocouples inserted into the centerline of the flow. These thermocouples measure the fluid temperatures and provide feedback for the reactor temperature controllers. The optical module, used for Raman measurements, can be installed at any point along the entire 380 cm length of the reactor, allowing for a wide range of residence times. Each of the reactor sections is wrapped with a 375-W cable heater and is insulated to minimize heat loss and provide isothermal operation of the flow reactor. In addition, each length of tubing can be wrapped with air cooling coils for the removal of heat from the reaction, if needed to assist the stability of the control loop.

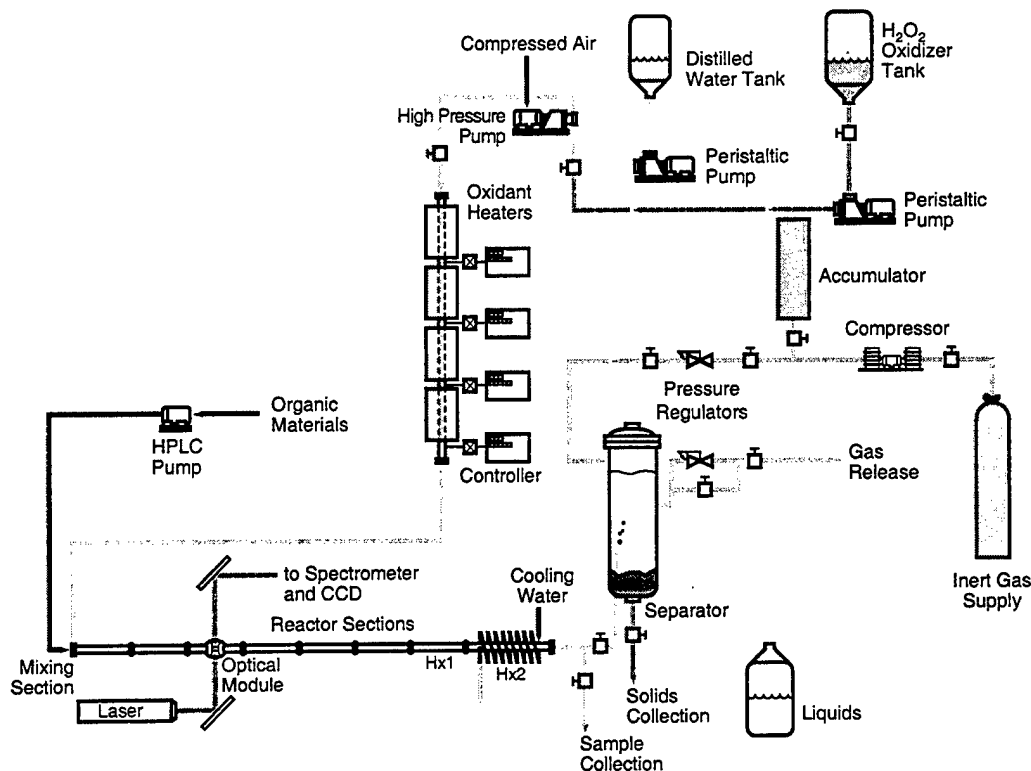


Figure 2.3 Schematic of the reactor layout using a single preheat line.

The cooling and separation subsystem, to handle the effluent from the process, consists of a convective heat exchanger, a water-cooled, counter-flow heat exchanger, and a gravity separator. The reacting flow is first cooled in the convective heat exchanger and then brought to ambient temperature in the counterflow heat exchanger. The cooled products then pass into the separator where the gaseous and liquid effluents are removed for collection and/or analysis. The gaseous effluent, which is primarily CO<sub>2</sub> and O<sub>2</sub>, is exhausted to the atmosphere. The liquid effluent is collected in an external vessel. There is a liquid effluent sampling valve that permits sampling prior to the separator for compositional analysis and species identification via chromatographic or other analytical methods.

### 2.2.2 H<sub>2</sub>O<sub>2</sub> reactant

The oxidizer is fed to the system in the form of a solution of H<sub>2</sub>O<sub>2</sub> in water which is subsequently thermally decomposed in the preheating section of the reactor into a high-pressure mixture of O<sub>2</sub> in supercritical water. It is critical that the H<sub>2</sub>O<sub>2</sub> be completely converted O<sub>2</sub>, prior to the onset of reaction with the fuel, to assure the reliability of the experimental results. Early in the project, we had estimated the decomposition rate based on data in subcritical pressurized water. This estimate found that the decomposition of H<sub>2</sub>O<sub>2</sub> in liquid-density water for temperatures up to 280 °C has an Arrhenius behavior with a first-order rate constant of 0.24 s<sup>-1</sup> at 280 °C. Extrapolating this experimental temperature dependence to 450 °C, yields a rate constant of 9.4 s<sup>-1</sup>. Using the maximum oxidizer flow rate for our experiments, about 0.8 g/s, the residence

time in the preheating subsystem is approximately 7 seconds at 450°C. This combination of operating conditions results in over sixty lifetimes of the disproportionation reaction before the oxidizer and fuel are mixed. Effluent samples from the oxidizer line show no residual  $\text{H}_2\text{O}_2$  in solution above our detection limit (iodometric titration) of  $5 \times 10^{-5}$  mol/L. To verify this, we conducted tests to confirm this extrapolation. Hydrogen peroxide was injected into water at 390 °C at the mixing tee, and permitted to react for 1.7 s before rapid quenching. This short reaction time results in a measurable amount of residual  $\text{H}_2\text{O}_2$  in the quenched solution that reduces to a first order rate constant of  $3.1 \text{ s}^{-1}$ , agreeing very well with the extrapolated value at 390 °C of  $3.2 \text{ s}^{-1}$ . Later in the project, we conducted an in-depth examination of  $\text{H}_2\text{O}_2$  thermolysis and confirmed in detail these earlier proof-of-principle tests.

### 2.2.3 Raman spectroscopic diagnostic

The optical module is constructed from a single piece of Inconel 625. It has three high-pressure window ports, radially opposed at 90° intervals. This allows a laser beam to pass through the reacting flow with the Raman-scattered signal collected orthogonally to the pump beam. The windows are made of synthetic sapphire and have an aperture of  $0.32 \text{ cm}^2$ . The windows are held in conical seats using a spring washer and nut assembly. The design is based on that originally suggested for cryogenic systems by Abdullah and Sherman.<sup>1</sup> Figure 2.4 illustrates this design.

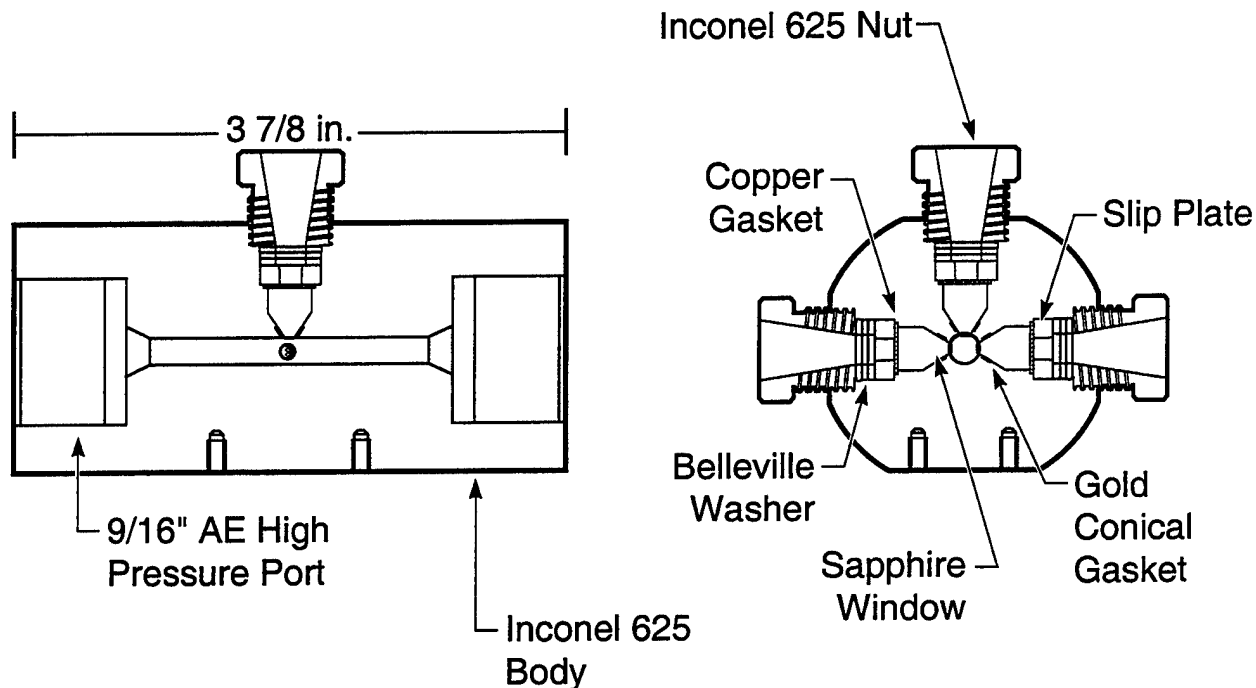


Figure 2.4 High-pressure Raman cell for the Supercritical Flow Reactor.

Figure 2.5 displays the simple Raman set-up. To generate the Raman scattering signal, the probe volume is excited with the 514 nm line of an argon ion laser operating at a nominal power of 1 to 5 W. The beam is focused into the optical module with a 500-mm focal length lens producing a beam diameter of approximately 0.06 mm. The scattered light is collected with an  $f/3$  aperture and imaged through a lens and mirror system onto the entrance slit of a 0.5-m single spectrometer, equipped with a 2400 rule/mm grating. To aid in rejection of the scattered laser light, a colored glass filter (RG 570 or RG 540) is employed in front of the spectrometer. The relevant portion of the Raman spectrum is imaged onto a 384 x 576 pixel CCD array. The resulting Raman signal is collected, processed, and stored using a Labview data acquisition program.

The power of the Raman signal,  $P_r$ , can be expressed as

$$P_r = P_i n \left( \frac{\partial \sigma}{\partial \Omega} \right) \Omega \ell \epsilon \quad (2.1)$$

where  $P_i$  is the pump laser power,  $n$  is the species number density,  $d\sigma/d\Omega$  is the differential Raman cross section,  $\Omega$  is the collection solid angle,  $\ell$  is the sampling length, and  $\epsilon$  is the collection efficiency. It is evident that the Raman signal power is directly proportional to the species number density. Therefore, by integrating the observed intensity of a Raman band over wavelength, a value which is proportional to the species concentration can be obtained. The absolute concentration of a species can be calculated following calibration of the system.

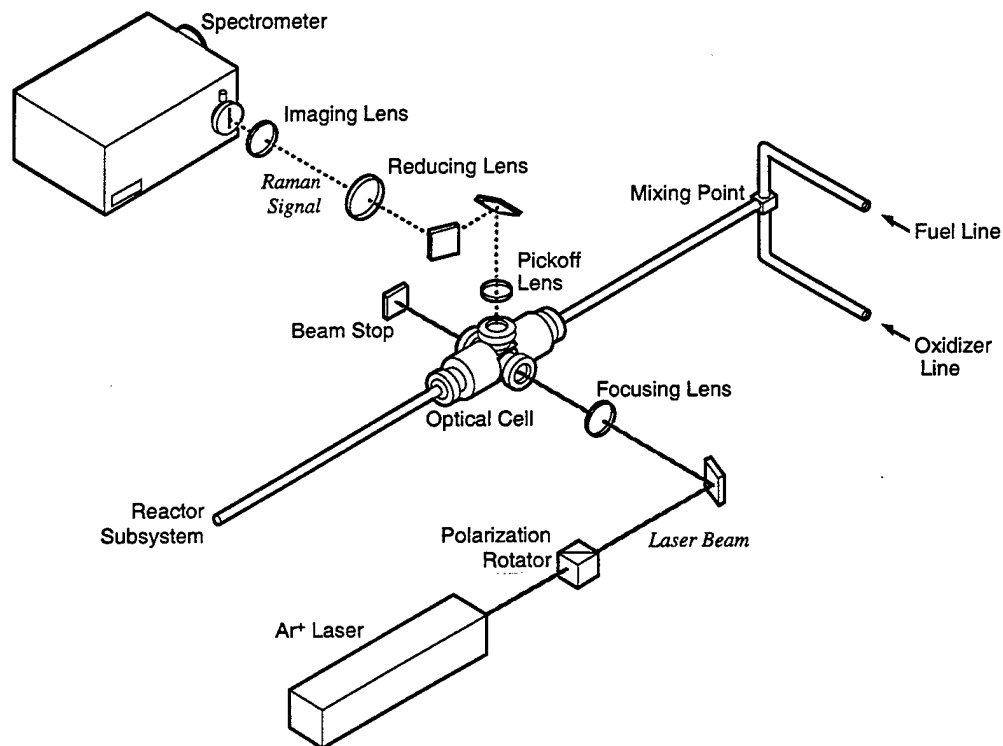


Figure 2.5 Optical layout for Raman spectroscopic diagnostic.

The optical system was calibrated by flowing a known concentration of the species of interest without oxidizer, through the optical module, and recording the resulting Raman signal. To account for changes in the parameters of Eq. 2.1 which could affect the absolute magnitude of the signal over time, each species signal was referenced to the O-H stretch from water, centered at a Raman shift of  $\sim 3628\text{ cm}^{-1}$ . By normalizing the species signal to the water signal, any drift in the system parameters in Eq. 2.1 (notably,  $P_i$  and the alignment of the collection geometry expressed by  $\Omega$ ) are accounted for, with the exception of the temperature dependence of the differential cross section. We examined the calibration response of the key species over a range of temperatures. Typically, we found little variation in cross section at temperatures over the critical temperature of water.

#### **2.2.4 Residence time calculation**

Residence times were calculated by combining the frequency of the high-pressure pumps with the known displacement, to produce the volumetric flow rate into the system at ambient temperature and elevated pressure. By calculating the density of each stream, the mass flow rate of fuel and oxidizer into the system can be determined. The accuracy of the calculation was verified by measuring total feed mass over time. Feed stream densities were calculated based on ideal solutions of feed organic compounds in water and  $\text{H}_2\text{O}_2$  in water at ambient temperature and pressure. However, to calculate the residence time, the volumetric flow rate, at the experimental temperature and pressure, must be determined. This requires knowledge of the density and composition of the final mixed stream and an assumption regarding the mixing of species. The composition of the fuel stream is known (assuming no pyrolysis has occurred). As stated previously, the  $\text{H}_2\text{O}_2$  in the oxidizer stream rapidly and completely undergoes decomposition to form  $\text{O}_2$  and  $\text{H}_2\text{O}$  when heated to the reaction temperature; therefore, the composition of the oxidizer stream is also determined.

Lastly, an accurate equation of state is needed for the mixture of water, fuel, oxygen and products. If it is assumed that the species mix to form an ideal solution, the density of each pure component is all that is necessary to complete the calculation. The density of water at reaction conditions is calculated using NBS Steam Tables. The density of fuel, which accounts for less than a few percent of the final mixture, was assumed equal to that of water. Finally, the density of  $\text{O}_2$  was calculated at experimental conditions using a generalized compressibility factor correction to the ideal gas law ( $\text{O}_2$  accounts for approximately 1.5 mol% of the final mixture, for most experiments). With the density and the mass flow rate, the residence time (from the mixing point) can be calculated by making a plug flow approximation. Plug flow conditions are met because the flow is always turbulent and typically  $\text{Re} > 4000$ . Although the reaction products change this composition, the density is assumed to remain constant throughout.

Within these approximations, the calculation of residence time is directly proportional to density at all flow rates. The possible deviation in actual density at these low concentrations of fuel and oxidizer streams, relative to this theoretical calculation using

the empirical equation of state of water and ideal mixing, will be on the order of several percent and not grossly affect the validity of the results.

## 2.3 Stirred Constant Volume Reactor (SCVR)

### 2.3.1 Hardware

The Stirred Constant Volume Reactor (SCVR) is a batch-type reactor capable of similar operating conditions as the SFR, but providing a larger internal volume and larger windows. As its name implies, it can be equipped with a mechanical stirring device. A schematic is presented in Figure 2.6. It is based on a design by Schilling and Franck.<sup>2</sup>

Machined out of a single piece of Inconel 718, it has an internal volume of about 18 ml and is fitted with three sapphire windows for optical access. Five high-pressure ports provide an inlet and outlet for fluids at pressures to 55.0 MPa, as well as access for pressure and temperature transducers. Band heaters are mounted on each of the three legs to heat the reactor uniformly to internal temperatures up to 550 °C. The reactor is wrapped in insulation and mounted on translation stages. During operation, it is enclosed within a steel barricade that provides secondary containment in case of window or tubing failure.

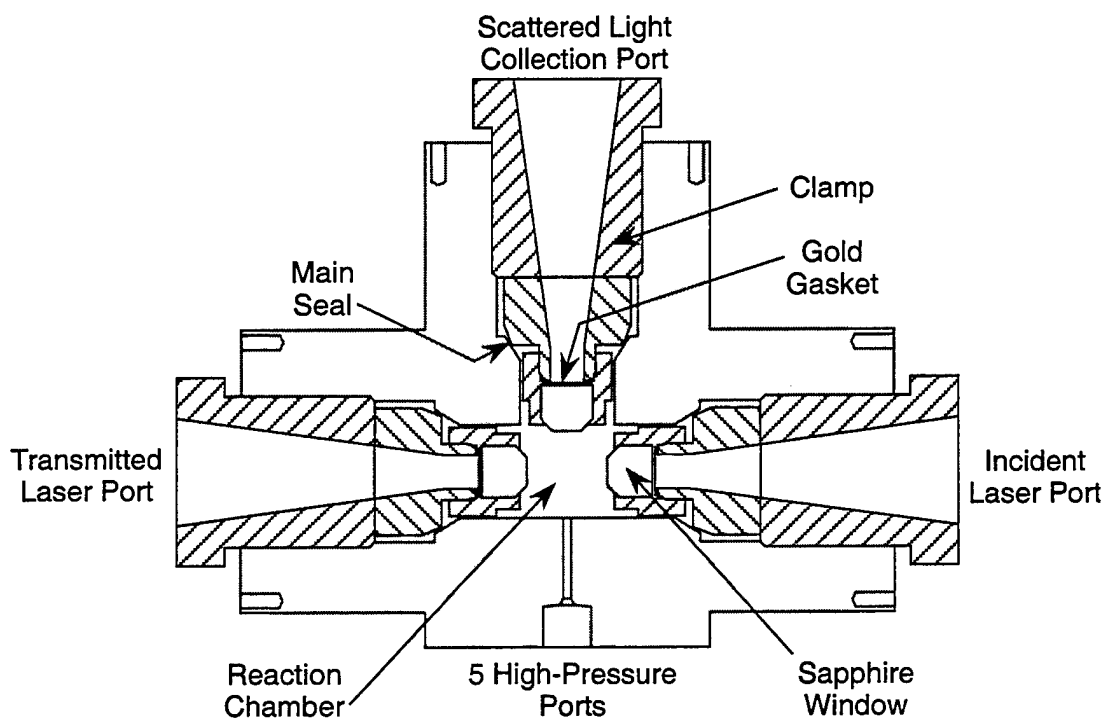


Figure 2.6 High-pressure Raman cell for the Stirred Constant Volume Reactor without the stirring system installed.



The batch reactor is typically used for reaction kinetics experiments in which a reactant is rapidly injected into a high-density mixture of supercritical water and other reactants so that its reactivity can be measured by Raman spectroscopy. Following injection, we have found that unaided mixing occurs on a time scale of several minutes. This is adequate for kinetics experiments with time scales of tens of minutes to hours. But for faster reactions, we require mechanical mixing.

Figure 2.7 is a schematic of the stirring system. Similar to other mechanically-actuated high-pressure feedthroughs,<sup>3</sup> it is based on a packed valve stem with dimensions similar to Autoclave Engineers, Inc. high-pressure valves. The shaft is driven by a variable speed electric motor and is operated at approximately 200 rpm for 5 seconds during injection in a typical experiment—sufficient time to thoroughly mix the reactor contents. The horseshoe-shaped paddle is designed so that when positioned vertically, it does not interfere with the input laser beam or the scattered light collection.

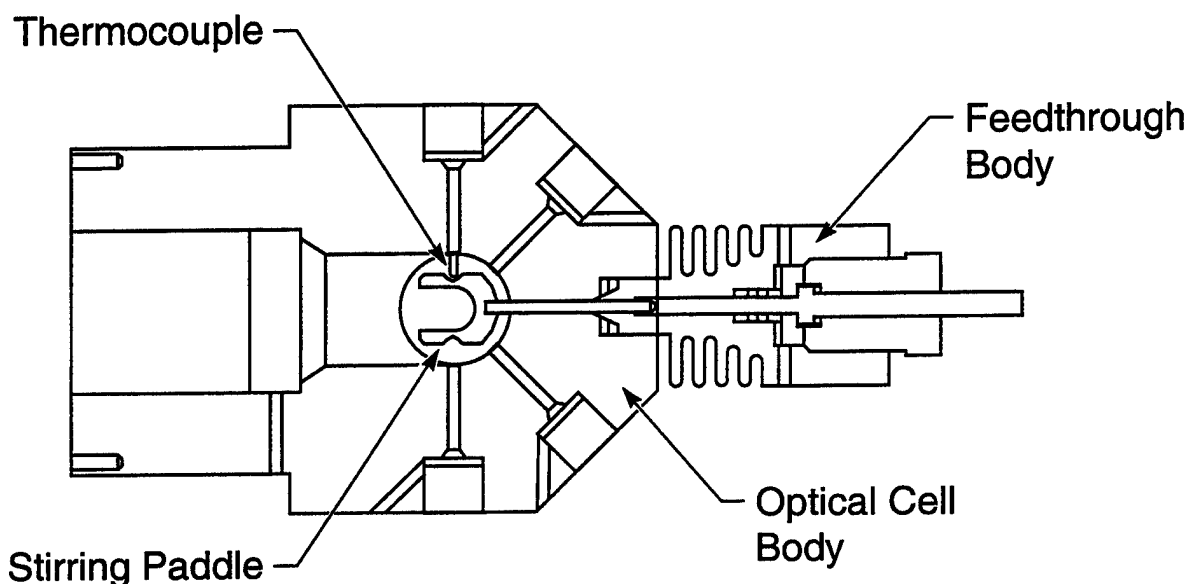


Figure 2.7 High-pressure Raman cell for the SCVR with stirrer installed. This is a side view of the same cell shown in Figure 2.6 looking down the axis of the laser ports. The stirrer is inserted through the center port of the five high-pressure ports.

### 2.3.2 Operation and procedures

Water is loaded into the reactor using a high-pressure liquid chromatography pump. Gases are pressurized to experimental conditions using a cylinder fitted with a floating piston. The gases are loaded on one side of a supply piston and are compressed by pressurizing the other side with water from the pump. Experimental conditions are monitored with a pressure transducer and a 1.6-mm diameter, Inconel-sheathed thermocouple inserted into the reactor. A computer continually records the pressure

and temperature data and controls the heating of the reactor. The sapphire windows enable the use of a variety of optical diagnostics. Typically, an argon ion laser provides a 5-W, 514.5-nm probe beam for spontaneous Raman spectroscopic measurements that are made with a 0.85-m double monochromator and a diode array detector. PCs control the detector, record the Raman spectra, and integrate spectral peaks to extract the desired species concentrations.

The first step of a typical experiment is calibration of the Raman spectroscopic system. The gas to be calibrated (e.g. methane, oxygen-nitrogen mixture, carbon dioxide, carbon monoxide) is loaded into the preheated reactor and the Raman signal is recorded at pressures from 5–50 bar. Thus, our calibrations provide the functional relationship between integrated Raman signals collected during our experiments and the corresponding time-resolved concentrations of reactant or product gas.

Following calibration, the preheated reactor is charged with water and allowed to come to the target experimental temperature. An estimated amount of reactant is added to create a nominal mixture near the desired concentration in water. The reactant concentration is measured spectroscopically at this point to establish initial conditions. In oxidation experiments, predetermined amount of oxidizer, chosen to produce the desired initial equivalence ratio, is then quickly injected into the reactor (within 20–40 s) as the experimental clock is started. The remainder of the experiment consists of serially recording Raman spectra of the species of interest along with time, temperature, and pressure values.

## **Section 2.4 - Model Methodology**

### **2.4.1 General**

Elementary reaction modeling has been under development for combustion applications for many years. Initially, focus was on predicting properties of premixed methane/air flames. Over time, however, this type of modeling approach has met with success in a wide variety of combustion related topics, including NO<sub>x</sub> reduction, internal combustion engine preignition, turbulent flame dynamics, chemical vapor deposition, explosive initiation, and soot formation. There are a number of computer code packages available, both custom and generic, that are designed to perform the numerical work that combines a set of first order differential equations that describe reaction chemical kinetics with an application environment.

Sandia National Laboratories has developed a system of programs called CHEMKIN III that is easy to use and computationally efficient. All of the model development for this project has been done within the CHEMKIN suite of programs. However, the value of the mechanism validation work that has been a large part of this project is not limited to this platform and can be adapted to other codes. CHEMKIN III is available through Reaction Design Inc.

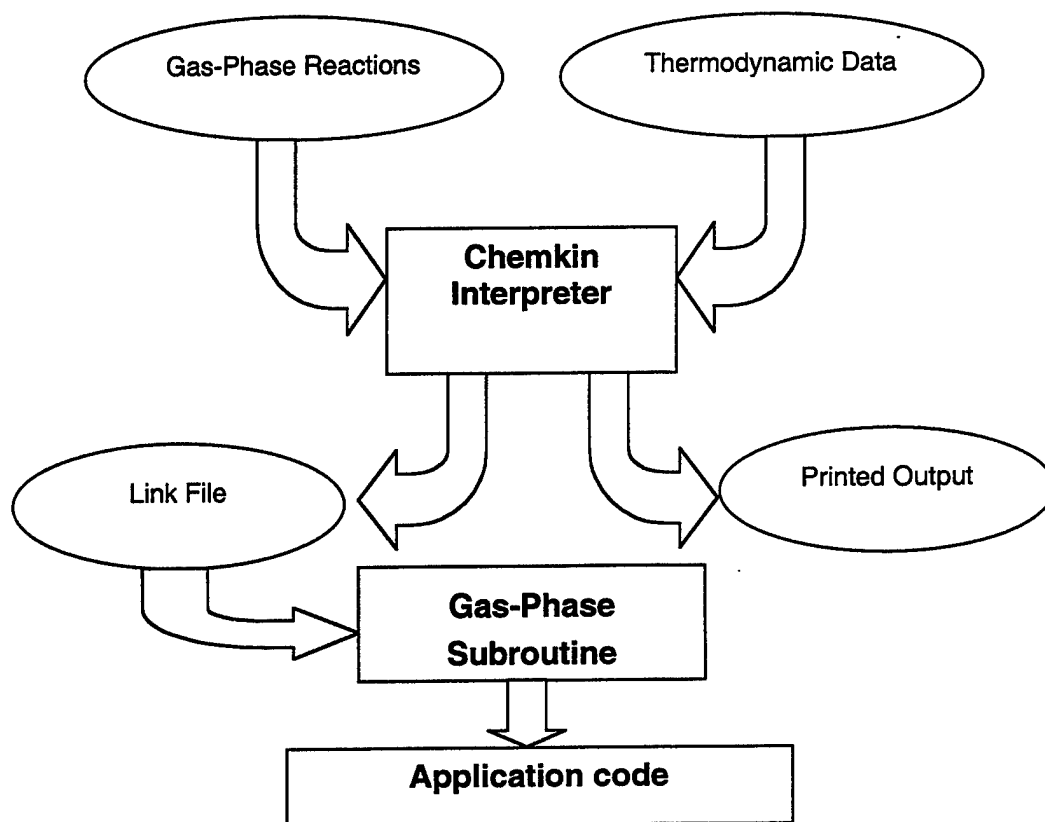


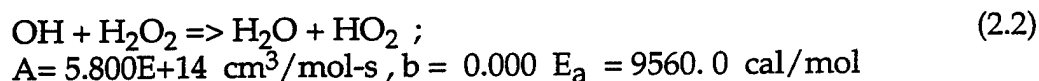
Figure 2.8 Overview of the Chemkin computational environment.

#### 2.4.2 CHEMKIN structure

Elementary reaction modeling using CHEMKIN is organized by placing the specifics of the system to be studied into several input files. It has a *mechanism*, a *thermodynamic database*, and an *input file*. The CHEMKIN suite of subprograms is manipulated by a main driver program that describes the *application*. The structure is illustrated in Figure 2.8.

The *mechanism* is a set of elementary or global gas phase reactions. Each reaction is given a set of parameters that permits the calculation of a rate constant for the reaction as a function of temperature. These are usually expressed as  $R1+R2 \Rightarrow P1+P2$ , with parameters  $A$ ,  $b$ , and  $E_a$ , such that  $-d[R1]/dt = A (1/T)^b \exp(-E_a/RT) [R1][R2]$ .

An ordinary differential equation can be written for  $R2$  as well. Here,  $[R1]$  and  $[R2]$  are the molar concentrations of species  $R1$  and  $R2$ . This is the typical Arrhenius expression that is generally used to describe reaction kinetics. As a specific example,



CHEMKIN can seamlessly handle pseudo-first order reactions as well, such as



where M is any collision partner. High-pressure limitations to this type of reaction, which is critically important for SCWO applications, are also accommodated.

The Chemkin III package can also handle a combination of elementary reactions and global expressions such as



The *thermodynamic database* contains parameters that permit the calculation of enthalpy- and entropy-of-formation data for each species as a function of temperature. This information is needed to calculate temperature rises and to calculate reverse reaction rates based on microscopic reversibility, when rate data for the reverse direction of a reaction are unavailable.

The *input file* contains the specifics of the reaction conditions, such as initial temperature, pressure, species mole fractions, and other characteristics of the calculation, such as whether conditions should be isothermal or adiabatic. The input file also contains a number of other pieces of information specific to the output of the calculation.

The other key component needed to use the CHEMKIN suite of subprograms is an *application* code. This is the main or driver program that calls the CHEMKIN subprograms. SENKIN is an ideal application for investigating the use of this type of modeling for SCWO flow reactor and SCVR experiments and is the application that has been used in this project. SENKIN calculates the species evolution of a perfectly mixed system as a function of time.

It is important to point out that the detailed chemical mechanism used is independent of the application. As it describes only reaction rates, these mechanisms can be used in more complicated flow geometries. A Sandia two-dimensional computation fluid dynamics code, CURRENT, can be used to apply the information gained from a plug flow geometry to feed injectors and systems that have axial diffusion or a variety of more complicated flow structures.

During the course of this project, we made extensive use of the Chemkin framework and specifically the SENKIN application as a mechanism evaluation environment for developing SCWO kinetic models. This environment is used to successfully explicitly model methanol, methane, ethanol, and benzene oxidation.

## 2.5 References

- 1 A.H Abdullah, W.F. Sherman "Variable Temperature High-Pressure Raman Cell" *Journal of Physics E: Scientific Instruments* **13**, 1155-1159, 1980.
- 2 W. Schilling, E. U. Franck "Combustion and Diffusion Flames at High Pressures to 2000 bar" *Ber. Bunsenges. Phys. Chem.* **92**, 631-636, 1988.
- 3 M. Costantino "A High Pressure-High Temperature Valve Packing" *Rev. Sci. Instrum.*, **62**, 1668-1669, 1991.

## ***Section 3: Validation of Gas Phase Assumptions. Part 1-Experiments***

### **3.1 - Methane and Methanol Overview**

#### **3.1.1 Introduction**

This section reports the key experimental results that reflect this project's development of the small molecule mechanisms for SCWO. Most of these experiments were directed at answering a number of specific questions regarding the quantitative accuracy of combustion based models. These methane and methanol conversion measurements served as an initial data set by which the combustion-based modeling could be examined from a conversion and intermediates formation standpoint.

This section, "Validation of Gas Phase Assumptions. Part 1: Experiments" focuses solely on the experimental results on two of the best-studied combustion systems, methane and methanol. The next section, "Validation of Gas Phase Assumptions. Part 2: Reaction Pathways" interprets these results in the context of elementary reaction schemes and illustrates some of the similarities and differences between spatially distributed and lower temperature SCWO and high temperature localized flame combustion.

In the methane subsection, Raman spectroscopic measurements of methane oxidation kinetics in supercritical water are reported. Our experimental facility enables measurements at concentrations typical of the SCWO process, and the results complement previous low-concentration methane oxidation measurements made using a sample-and-analyze (off-line) technique. The objectives of the work are to: (1) determine global reaction rates for supercritical water oxidation of methane at high fuel concentrations; (2) assess the ability of current elementary reaction mechanisms to predict these rates; and (3) compare our results with those presented by Webley and Tester<sup>1</sup> on this system.

In our work on methanol oxidation, the experimental goals moved from establishing an improved data set for global kinetics to collecting data on potential key intermediates for subsequent evaluation of elementary reaction models. The experiments successfully identified the formation and consumption of formaldehyde. Subsequent mechanistic modeling of the data led to the first comprehensive description of C1 chemistry in SCW, appearing in this project's Quarterly report for July-September, 1995.

#### **3.1.2 Papers and reports**

R.R. Steeper, S.F. Rice "Optical Monitoring of the Oxidation of Methane in Supercritical Water"; in *Physical Chemistry of Aqueous Systems*, (H.J. White, J.V. Sengers, D.B. Neumann, J.C. Bellows Eds.) Begell House, New York, 1995, p. 652.

R.R. Steeper, S.F. Rice "Kinetics Measurements of Methane in Supercritical Water" *Journal of Physical Chemistry* **100**, 184-189, 1996.

S.F. Rice, T.B. Hunter, Å.C. Rydén, R.G. Hanush; "Raman Spectroscopic Measurement of Oxidation in Supercritical Water I. Conversion of Methanol to Formaldehyde" *Industrial and Engineering Chemistry Research*.35, 2161-2171, 1996.

### 3.2 Methane

#### 3.2.1 Experimental results

All methane experiments were conducted in the SCVR using the methods described in Section 2.3. Figure 3.1 presents typical results from a fuel-lean experiment conducted at 413 °C and 26.5 MPa. Included on the graph are carbon and oxygen balances. The carbon balance is the sum of CH<sub>4</sub>, CO<sub>2</sub>, and CO concentrations and is compared to its theoretical value, the initial methane concentration. The oxygen balance is calculated as:

$$\begin{aligned} [\text{O}_2]_{\text{total}} &= [\text{O}_2] + [\text{CO}_2] + 0.5 [\text{CO}] + 0.5 [\text{H}_2\text{O}] \\ &= [\text{O}_2] + 2 [\text{CO}_2] + 1.5 [\text{CO}] \end{aligned} \quad (3.1)$$

This balance can be compared to 49/51 times the N<sub>2</sub> concentration (the mixture ratio on the O<sub>2</sub> feed). The non-reacting nitrogen was include to monitor the data collection stability. Both balances are within 6% of the theoretical value throughout the experiment.

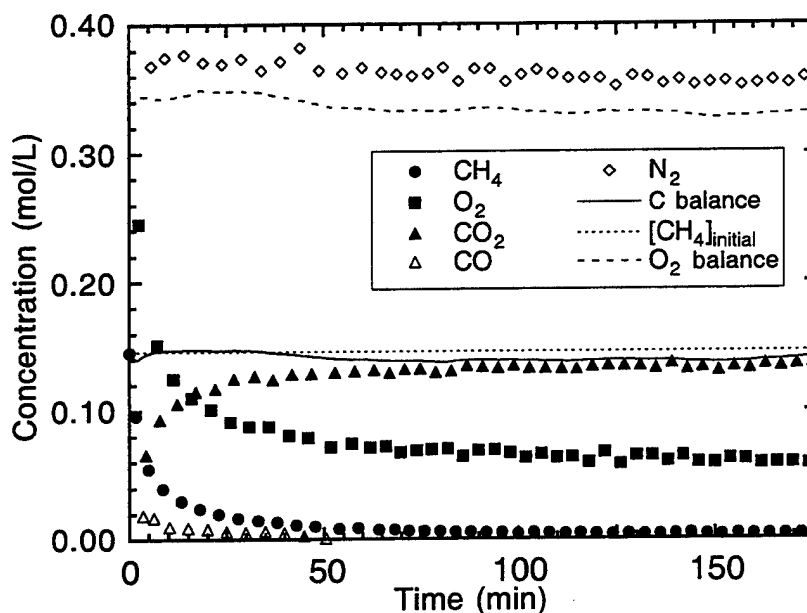


Figure 3.1 Concentration profiles recorded during the oxidation of methane in supercritical water in the SCVR at 413 °C and 26.5 MPa. Lines represent carbon and oxygen balances.

Many experiments of this nature were conducted, mapping out the CH<sub>4</sub>, CO, and CO<sub>2</sub> concentrations as a function of stoichiometry, temperature and pressure. The experiments comprised three series: (1) a series of experiments at a nominal pressure of 27.0 MPa and variable temperature and stoichiometry; (2) a series at half that pressure, 13.5 MPa, and variable temperature and stoichiometry; and (3) a series at a constant nominal temperature of 412 °C and variable pressure.

### 3.2.2 Global reaction rate expressions.

The fifteen 27.0-MPa and twelve 13.5-MPa experiments sampled a range of temperatures, initial methane concentrations, and fuel equivalence ratios. The data comprise over 800 individual methane measurements, each of which can be considered a separate rate measurement. The abridged data from the 27.0-MPa and 13.5-MPa series were fitted separately to a global reaction rate expression:

$$d[\text{CH}_4]/dt = -k [\text{CH}_4]^a [\text{O}_2]^b \quad (3.2)$$

where  $k = A \exp (-E_a/RT)$ , and  $[\text{O}_2]$  is related to  $[\text{CH}_4]$  by assuming that each reacting mole of CH<sub>4</sub> consumes 2 moles of O<sub>2</sub>. We have not explicitly included water concentration in Eq. 3.2 — the non-monotonic effect of water concentration on reaction rates is discussed in the next section.

We compared our work to the results of Webley and Tester<sup>1</sup> with the full knowledge that differences in the experimental design of that study dictated a higher temperature range and significantly lower initial methane concentrations than in our experiments. Comparison of our 27.0-MPa fit with the Webley fit in Table 3.1 indicates sizable differences in the derived global rate expression parameters. Our preexponential factor and activation energy parameters are higher than those of Webley, although it should be noted that each of the three fits shows a high correlation coefficient between this pair of parameters. The result is that a higher activation energy, for example, can be compensated by a higher preexponential factor to yield a comparable fit. The differences in reaction orders,  $a$  and  $b$ , are more significant. Webley determined a value near unity for the reaction order with respect to methane, and similar values have been reported for other simple organics. In contrast, Table 3.1 shows that our methane reaction order is close to two. The reaction order with respect to oxygen is effectively zero in the current fit and is about two-thirds in the Webley fit. Zeroth-order oxygen dependence has been previously determined for methanol and carbon monoxide oxidation in supercritical water. Finally, the average errors, if normalized using appropriate initial fuel concentrations, indicate relative errors of approximately 7% for our experiments, and about 2% for those of Webley.

The fitted global reaction rate expressions can be used to calculate effective rate constants, providing the means to compare rates at our experimental conditions with those of Webley. In Figure 3.2, the effective rate constant is defined as the inverse of the time required to reduce methane concentration to 1/e of its initial concentration. At the



upper left are data and global rate expression predictions from the Webley experiments. At the lower right are two lines representing rate predictions for the Sandia experiments at two different initial methane concentrations. The lower, solid, line estimates rates at an initial concentration that matches the Webley experiments. Comparing this line with the Webley dashed line suggests that the two data sets are not incompatible: a single curve could connect the two given a modest temperature dependence of the slope (i. e., activation energy).

**Table 3.1. Fitted global rate expression parameters.**

(units of kcal, mol, L, s)	Sandia data 270 bar	Sandia data 135 bar	Webley Fit 246 bar
Preexponential Factor, $\log_{10} A$	17.1 ( $\pm 0.49$ )	35. ( $\pm 3.6$ )	11.4 ( $\pm 1.1$ )
Activation Energy, $E_a$	60. ( $\pm 1.4$ )	115 ( $\pm 11.6$ )	42.8 ( $\pm 4.3$ )
Reaction Order w.r.t. Methane, $a$	1.84 ( $\pm 0.084$ )	1.8 ( $\pm 0.14$ )	0.99 ( $\pm 0.08$ )
Reaction Order w.r.t. Oxygen, $b$	-0.06 ( $\pm 0.065$ )	0.15 ( $\pm 0.075$ )	0.66 ( $\pm 0.14$ )
Average Error (mol/L)	$7 \times 10^{-3}$	$5 \times 10^{-3}$	$4 \times 10^{-5}$

For our 270-bar experiments,  $T = 391\text{--}442^\circ\text{C}$ ,  $P = 265\text{--}276$  bar,  $[\text{CH}_4]_{\text{init}} = 0.11\text{--}0.19$  mol/L, initial fuel equivalence ratio = 0.5–1.1. For our 135-bar experiments,  $T = 391\text{--}419^\circ\text{C}$ ,  $P = 134\text{--}144$  bar,  $[\text{CH}_4]_{\text{init}} = 0.02\text{--}0.16$  mol/L, initial fuel equivalence ratio = 0.1–1.4. For the Webley experiments,  $T = 560\text{--}630^\circ\text{C}$ ,  $P = 246$  bar,  $[\text{CH}_4]_{\text{init}} = 0.0011\text{--}0.0043$  mol/L, fuel equivalence ratio = 0.6–3.2,  $P = 246$  bar.

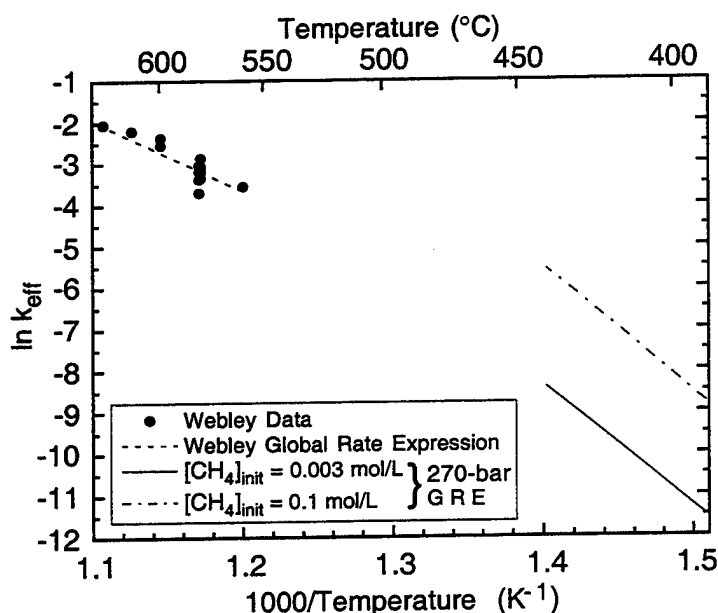


**Figure 3.2** Effective rate constants,  $k_{\text{eff}}$ , for the current experiments compared with those of Webley. Effective rate constants for the Sandia data are estimated at two different initial methane concentrations using the 27.0 MPa global rate expression.

An important distinction between the two data sets is highlighted by the chain-dashed line in Figure 3.2. Because our data are characterized by a methane reaction order greater than unity (see Table 3.1), the effective rate constants are higher at higher methane concentrations, i. e., the line for  $[\text{CH}_4]_{\text{initial}} = 0.1$  is situated well above the line for  $[\text{CH}_4]_{\text{initial}} = 0.003$  mol/L. In contrast, the reaction order equal to unity found by Webley (over a low concentration range) means that effective rate constants are independent of methane concentration at those conditions. Extrapolating those results to higher methane concentrations would leave the effective rate constant calculations unchanged, resulting in overly low rate predictions.

Global reaction rate expressions are used in engineering models of the SCWO process for predictions of destruction efficiencies, residence times, and heat release rates. Because our experiments were conducted at fuel concentrations representative of commercial processes, the 27.0 MPa global rate expression should provide improved estimates of methane reaction rates in that environment. Our results indicate that rate predictions based on extrapolations from low-concentration experimental data risk underpredicting overall methane destruction rates at typical commercial process conditions.

### 3.2.3 Water concentration dependence.

There are several ways that water concentration can affect oxidation rates in supercritical water. First, water is an explicit reactant in many elementary reactions, so that rates of these reactions are directly dependent on water concentration. Second, water is the most important collision partner for unimolecular reactions in the SCWO environment. Unimolecular reaction rates become insensitive to collision partner concentrations at the familiar high-pressure limit, so water's role in these reactions is pressure-dependent. A final way that water influences reactions derives from its interaction with transition state complexes: the presence of water can change both the energetics (i.e., which reactions are thermodynamically favored) and the activation volumes (i.e., how reaction rates change as a function of pressure) of these complexes. In this section, results from experiments performed over a range of water concentrations are used to examine the water-concentration dependence of methane oxidation.

Figure 3.3 compares observed methane concentration histories from a 27.0-MPa and a 13.5-MPa experiment. The two experiments were conducted at approximately the same temperature and initial reactant concentrations. To improve the comparison, time was shifted for both so that a common concentration (well beyond the settling period) was set at time zero. Surprisingly, the data indicate that consumption of methane is faster at the *lower* pressure. The same conclusion is obtained from every pair of 13.5- and 27.0-MPa experiments that is close enough in initial conditions to be compared. Comparisons can also be made using predictions from the two global rate expressions derived above. With this method, identical initial conditions can be specified, and the results are representative of the entire set of data points. Predictions of the global rate

expressions are included in Figure 3.3: the predictions reinforce the conclusion that rates are significantly faster at 13.5 MPa than at 27.0 MPa.

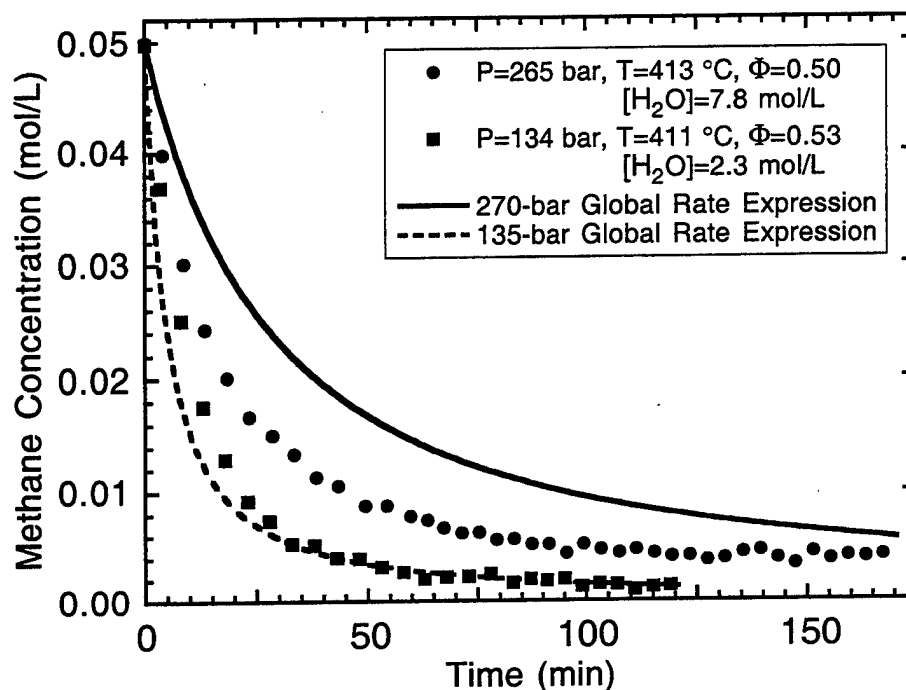


Figure 3.3 Comparison of methane consumption at 27.0 and 13.5 MPa. The curves are predictions of the global reaction rate expressions. Note that neither curve is a direct fit to the data; each is calculated using the appropriate set of four constant parameters that represents the data from dozens of experiments. ( $\Phi$  is the initial fuel equivalence ratio.)

The observed decrease in methane reaction rate with increasing pressure is unexpected. Because of the increase in collision partners with pressure, the primary effect of a pressure increase should be to raise reaction rates. The rate of oxidation of phenol in supercritical water has been observed to increase with water density over a range from 6 to 29 mol/L. A similar effect was observed for hydrogen and carbon monoxide over a range of water densities from 1.8 to 4.6 mol/L. To examine further the observed water concentration dependence, we performed a series of seven experiments. These experiments were conducted at constant initial methane concentration and temperature, while water concentration was varied from 0 to 8 mol/L. The corresponding experimental pressures ranged from 3.5 to 27.0 MPa. To compare these experimental results, effective rate constants were calculated as described above: they are plotted in Figure 3.4 as a function of water concentration. The circles in Figure 3.4 indicate an initial steady increase in rate constant as water content is increased. However, at a water concentration above 5 mol/L, there is an abrupt downturn in rate. The rate at water concentrations near 8 mol/L has fallen by more than a factor of two from the rate

at half that concentration. Included as well in Figure 3.4 are predictions from the two global rate expressions evaluated at appropriate initial conditions. These two points indicate that the ensemble of 13.5-MPa and 27.0-MPa data supports the observation that rates depend inversely on water content at high water concentrations. Possible explanation for this behavior is discussed in the next section within the context of the elementary reaction steps and their explicit sensitivity to water concentration.

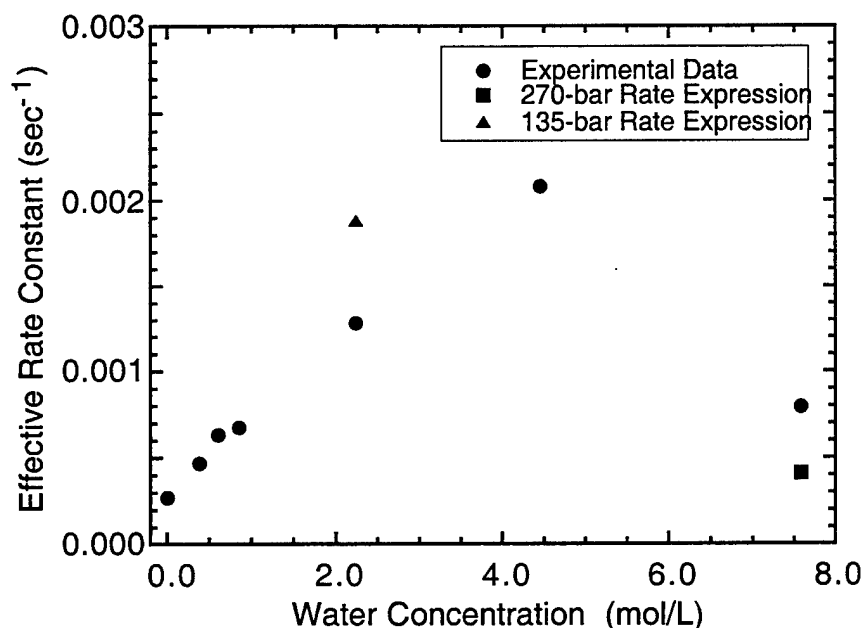


Figure 3.4 Methane reaction rate constants as a function of water concentration at constant temperature: experimental data and predictions of global reaction rate expressions. For the experimental data,  $T = 410\text{--}413\text{ }^{\circ}\text{C}$ ,  $[\text{CH}_4]_{\text{initial}} = 0.1\text{--}0.15\text{ mol/L}$ , initial fuel equivalence ratio = 0.8–1.0.

### 3.3 Methanol

#### 3.3.1 Gas Chromatographic (GC) results

The work on methanol was approached by initially making a series of conversion vs. temperature measurements to get an idea of its reaction rate at higher concentration than had been previously reported. These experiments were carried out in the SFR, as were all the methanol oxidation measurements reported in this section. An Arrhenius plot for the GC results is shown in Figure 3.5. In the figure, the observed normalized methanol concentration,  $[\text{CH}_3\text{OH}]/[\text{CH}_3\text{OH}]_0$ , is related to an effective first-order rate constant,  $k_{\text{eff}}$ , defined by

$$k_{\text{eff}} = -\ln ([\text{CH}_3\text{OH}]/[\text{CH}_3\text{OH}]_0) t^{-1} \quad (3.3)$$

where  $[\text{CH}_3\text{OH}]_0$  is the initial methanol concentration,  $[\text{CH}_3\text{OH}]$  is the measured effluent concentration, and  $t$  is the residence time.

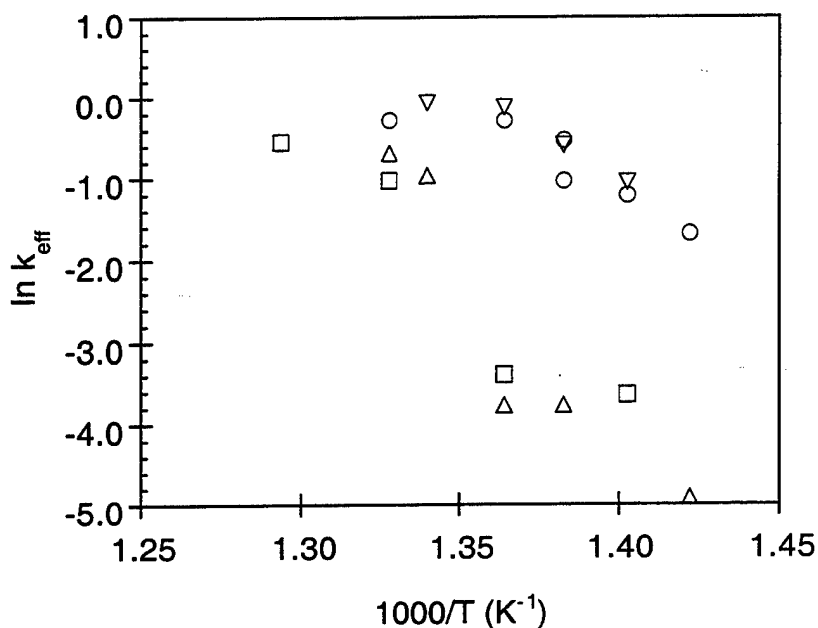


Figure 3.5 Arrhenius plot of the effective first-order rate constant,  $k_{\text{eff}}$ , versus  $1000/T$  for various initial  $\text{CH}_3\text{OH}$  feed concentrations, 0.011 wt%  $\Delta$ , 0.056 wt%  $\square$ , 0.39 wt%  $\circ$ , 1.2 wt%  $\nabla$ . All results are from the sample-and-quench technique and subsequent analysis by gas chromatography for experiments with the SFR.

It is evident that the effective first-order rate constant varies significantly with initial feed concentration. Higher initial feed concentrations exhibit greater effective reaction rate constants than low feed concentrations. In addition, the conversion rate for the low feed concentrations appears to increase more steeply with temperature. Other than the empirical utility of the conversion-versus-residence-time data, there is an important observation to be drawn from this experiment. Since all of the data points do not fall on the same line, the results show that a first-order representation of the data is not a good description of the rate behavior over a wide range of feed concentration. This implies, given a high initial feed concentration, that the same effective rate that describes the oxidation rate for the first 90% of conversion of an industrial feed may not accurately describe the conversion from 99.9% to 99.99%. The data also show that the same effective activation energy for the reaction, represented by the slope of the plot for a given feed concentration as a function of temperature, varies with the initial feed. At high fuel concentration, the activation energy is distinctly less than at low fuel feeds.

This suggests that the rate limiting step or steps consuming the bulk of the initial methanol at high concentration are not the same when the fuel concentration is low.

### 3.3.2 Raman spectroscopic measurements

Figure 3.6 shows SFR results of oxidation for selected temperatures at an equivalence ratio of 0.85. The form of the data suggests a period of time, analogous to an ignition delay for a combustible mixture, before the bulk of the methanol reacts that also varies with temperature. In relating the analysis of the data to an elementary model, these two characteristic stages of the methanol consumption profile can be examined for their temperature dependence and then compared to Arrhenius factors of key steps in the mechanism identified by a sensitivity analysis. At 500 °C, the reaction is sufficiently fast that the 0.17 s minimum experimental time is not fast enough to measure the induction period with certainty. However, extrapolation of the 440–490 °C curves shows an induction time of approximately 0.6 to 0.2 s, corresponding to approximately the first 10% of conversion. During this period, the slope of the fuel disappearance curve is much less than during the final 90% of conversion.

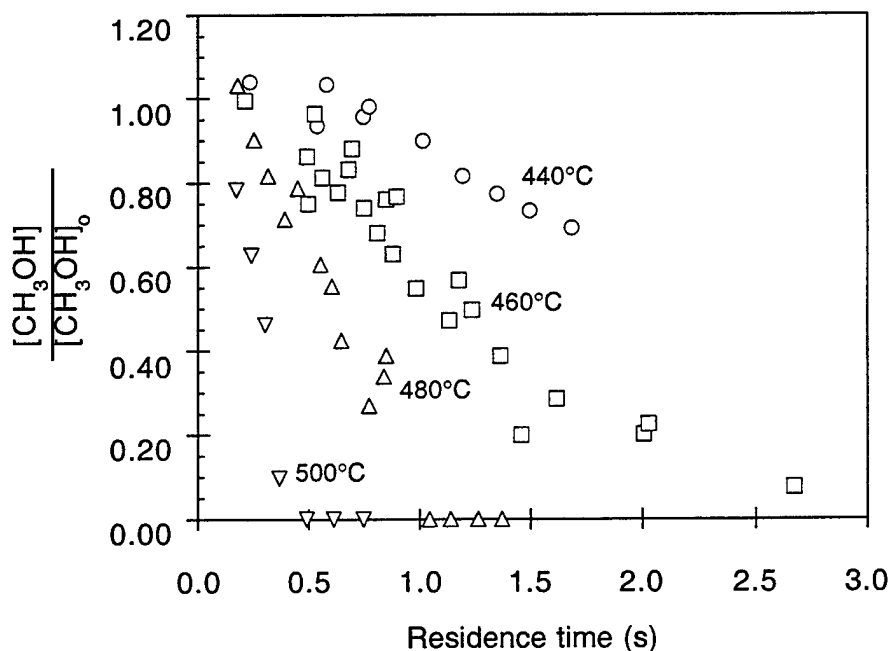


Figure 3.6 Normalized methanol concentration, measured in the SFR, plotted versus residence-time for an initial equivalence ratio of 0.85. Here, normalized refers to simply dividing the measured concentration of methanol by the known concentration in the feed. Results are shown for four of the seven isothermal conditions tested 440°C ○, 460°C □, 480°C △, and 500°C ▽.

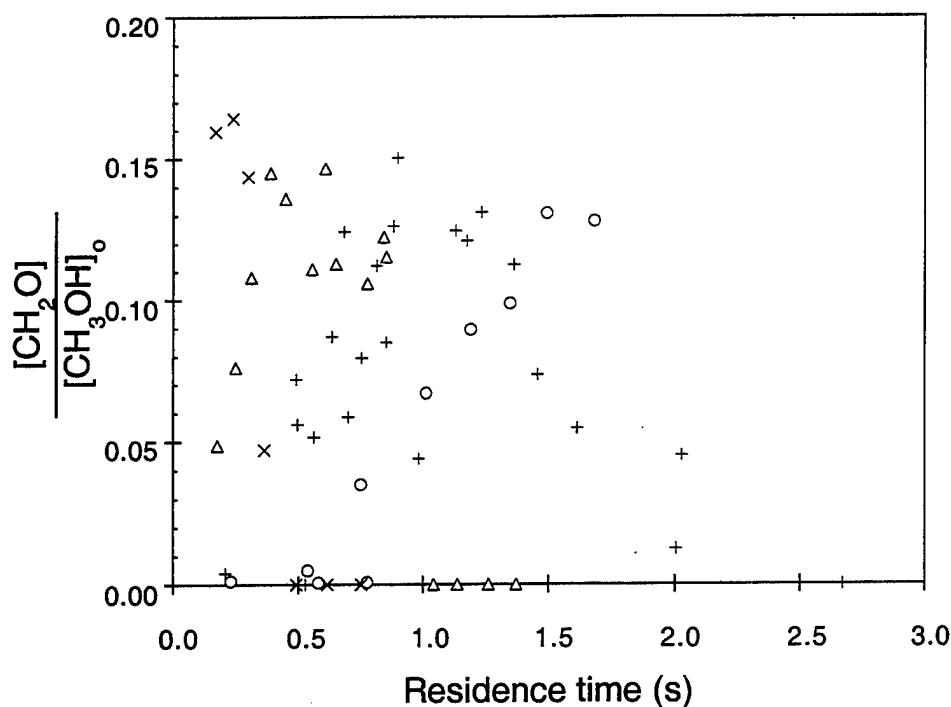


Figure 3.7 Measured normalized formaldehyde concentration plotted versus residence time for an initial equivalence ratio of 0.85. Results are shown for four of the seven isothermal conditions tested, 440°C ○, 460°C +, 480°C Δ, and 500°C ×.

Formaldehyde is formed as a stable intermediate during the oxidation of methanol in supercritical water and can be easily measured in the SFR. A subset of the data collected during lean methanol oxidation is reported in Figure 3.7. Note that formaldehyde concentrations approach 17% of the initial methanol feed. After the accumulation of formaldehyde, it appears to be oxidized at a rate comparable to that of methanol. At 500 °C, only the decay of the formaldehyde is observed. For 490–450 °C both the accumulation and subsequent loss is observed. At 440 °C measurements were not performed at sufficiently long residence times to observe the consumption of formaldehyde. Examining the production and destruction of formaldehyde provides important additional information to help determine the validity of detailed kinetic models, as discussed in the next section.

### 3.4 C1 Experimental Summary

Concentration histories of reactants, intermediates, and products were spectroscopically determined in the SFR during the oxidation of methane in supercritical water. For methane, the derived preexponential factor, activation energy, and methane reaction order at 27.0 MPa were all significantly higher than values previously obtained for a similar pressure but lower initial fuel concentrations. Reaction orders with respect to

methane and oxygen were close to two and zero, respectively, under these conditions. Experiments conducted at constant reactant concentrations and temperature revealed a reversal in the dependence of methane consumption rate on water concentration. Data recorded on methanol reveals it to be much more reactive than methane. In addition, formaldehyde is shown to be an important and detectable intermediate. These data, when combined with work by the MIT group on CO and H<sub>2</sub> provide the first critical test of the applicability of gas phase modeling to SCWO. The interpretation of these data is presented in the next section as we compare these observations with the results from explicit computational models.

### 3.5 References

1. P. A Webley; J.W. Tester; "Fundamental Kinetics of Methane Oxidation in Supercritical Water" *Energy & Fuels*, 5, 411-419, 1991.



This page intentionally left blank

## **Section 4: Validation of gas phase assumptions.**

### **Part 2-Reaction pathways**

#### **4.1 Introduction**

##### **4.1.1 Background**

The first attempt to use an elementary reaction model to describe the kinetics of oxidation of simple organics in supercritical water was reported by Webley and Tester in the late 1980's.<sup>1,2</sup> Their approach was to modify a successful mechanistic scheme designed for high-temperature gas-phase oxidation for high-density effects on unimolecular reaction rates. This mechanism successfully reproduced the existing methanol oxidation data, but failed to even approximate the experimental results that had been obtained for methane. More recently, a number of updated elementary reaction models for the oxidation of methane and methanol in supercritical water have been developed.<sup>3-6</sup> These newer models are significantly more extensive than the original attempt by Webley and Tester and have explicit treatment of high-pressure behavior for several key reactions. However, other than in the work of Brock and Savage, methane and methanol were not both tested with the same model. In the initial work by Brock and Savage, where both fuels were considered, agreement with experimental results was approximate, however that mechanism was subsequently updated in 2000 to reproduce the bulk of the data that had been published at low concentrations.<sup>7</sup>

The goal of this project in the 1995-1997 timeframe was to make the connection between the results from the experiments, described above in Section 3 of this report, to the current "best effort" from the combustion community at representing oxidation of methane and to explore the applicability of this mechanism to methanol oxidation. It was important to establish this relationship with the smallest amount of customization as possible, with all of the parameters for both the mechanism and species thermodynamics originating from a single well-documented source and the computation conducted in a well-established code.

##### **4.1.2 Papers and reports**

S.F. Rice "Application of the GRI 1.2 Methane Oxidation Model to Methane and Methanol Oxidation in Supercritical Water" *Proceedings of The Fourth International Symposium on Supercritical Fluids*, Sendai, Japan May 11-14, p. 571, 1997.

R.R. Steeper and S.F. Rice "Kinetics Measurements of Methane in Supercritical Water" *Journal of Physical Chemistry* **100**, 184-189, 1996.

R.R. Steeper, "Methane and Methanol Oxidation in Supercritical Water: Chemical Kinetics and Hydrothermal Flame Studies" Sandia Report SAND96-8208, 1996.

S.F. Rice, T.B. Hunter, Å.C. Rydén, R.G. Hanush "Raman Spectroscopic Measurement of Oxidation in Supercritical Water I. Conversion of Methanol to Formaldehyde" *Industrial and Engineering Chemistry Research* 35, 2161-2171, 1996.

## 4.2 Methane Mechanistic Modeling

### 4.2.1 Examination of global parameters

A global fit to the data on methane oxidation in Section 3.2 produces the relationship

$$-d[\text{CH}_4]/dt = k_g [\text{CH}_4]^{1.84} [\text{O}_2]^{-0.06} \quad (4.1)$$

where the concentrations are in mol/l,  $k_g = 10^{17.1} \exp(-30100/T)$ , and the units of the preexponential factor are chosen so the rate is in mol/l-s. Note that these low-temperature experiments covered both lean and rich conditions, but essentially no oxygen concentration dependence was observed. A global fit to the high temperature data from Webley gives an expression for the fuel consumption to be

$$-d[\text{CH}_4]/dt = k_g [\text{CH}_4]^{0.99} [\text{O}_2]^{0.66} \quad (4.2)$$

where  $k_g = 10^{11.1} \exp(-21500/T)$ . However, Webley and Tester<sup>2</sup> also provide a calculation for an effective first-order rate constant,  $k_{\text{eff}}$ , from those same data, assuming no  $\text{O}_2$  concentration dependence expressed as

$$-d[\text{CH}_4]/dt = k_{\text{eff}} [\text{CH}_4] \quad (4.3)$$

To compare the high concentration results in in Section 3.2 to those Webley measured at a fuel concentration in the range of  $10^{-3}$  mol/l, an effective first-order rate constant is calculated from the parameters in Eq. 4.1. This is done assuming the dependence on  $\text{CH}_4$  concentration is unity and the exponent characterizing dependence on oxygen is zero at an initial fuel concentration of 0.003 mol/l.

Figure 3.2 displays these results and, as discussed in section 3.2, the data at high temperature (Webley) and at low temperature (this work) connect well and appear to be in good agreement. Unfortunately, if we look deeper into the results, the picture is more complicated. The high-concentration data that we collected in this project reveal that the global representation assuming first order kinetics removes the higher order fuel concentration dependence that is characteristic of a radical chain propagation mechanism. In addition, that interpretation masks the apparent change in oxygen order from low to high temperature. That is, the high temperature data show a significant oxygen dependence and the low temperature data indicate the rate is largely independent of whether there are rich or lean conditions.

### 4.2.2 GRI 1.2 model and pathways

To evaluate the applicability of elementary reaction modeling from a combustion-based mechanism, the GRI 1.2 methane oxidation mechanism was used to directly predict the

conversion of methane at both low (this report, Section 3.2) and at high temperatures in supercritical water (Webley). The agreement of the Chemkin calculation using the unmodified GRI mechanism with the experimental data is excellent. The GRI 1.2 mechanism can reproduce accurately the available fuel consumption effective rate constants for the oxidation of methane at high temperature and connects smoothly to the low temperature results. It does not appear that special considerations of the nonideality of the density of water are necessary to provide agreement with the data.

Fig. 4.1 shows a qualitative view of the pathway of methane conversion to  $\text{CO}_2$  in the model. Only a very small fraction of  $\text{CH}_3\text{O}$  is converted to methanol by reaction with water, so this path does not appear in the figure. Later in this report, in the discussion of ethanol oxidation in Section 6, we will return to this particular reaction. It suffices to say here that, even if methanol were formed, it would be converted quickly and not accumulate in the system as a stable intermediate because methanol is significantly more reactive than methane. In fact, no large amount of transient non-radical species are accumulated, other than  $\text{CO}$  and  $\text{CO}_2$ . However, a very small amount of formaldehyde could be detected at  $400^\circ\text{C}$  experimentally. This is in contrast to the results for methanol oxidation where formaldehyde and hydrogen peroxide are produced in significant quantities.

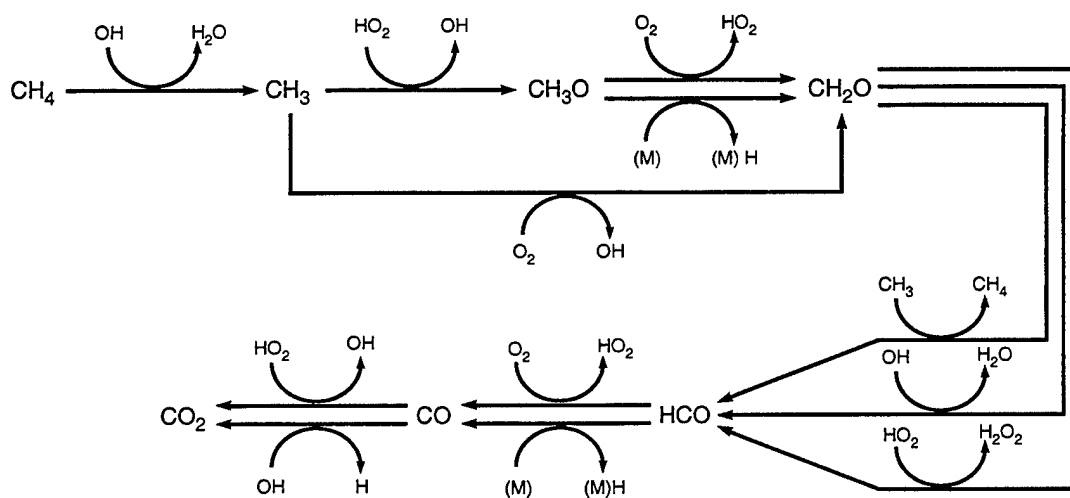


Figure 4.1. Flux diagram of the major carbon species in the oxidation of  $\text{CH}_4$  at  $500^\circ\text{C}$  and  $25.0\text{ MPa}$  in supercritical water predicted by the GRI 1.2 mechanism.

The performance of the GRI mechanism at these conditions can be evaluated on aspects other than fuel consumption rates. The global fit expressed in Eq. 4.2 suggests that there is an oxygen concentration dependence of order 0.66. Table 4.1 shows GRI mechanism predictions for varying the equivalence ratios at constant fuel mole fraction of 0.0005 (0.0017 mol/l) at  $600^\circ\text{C}$ . The calculation reveals an oxygen concentration exponent of 0.734, in acceptable agreement with the data. However, in this calculation this  $[\text{O}_2]$  dependence is preserved at lower temperature in contrast to Eq. 4.1.

Table 4.1. Effect of Oxygen Concentration on Rate of Methane Oxidation <sup>a</sup>

O <sub>2</sub> mole fraction	Equivalence ratio	k <sub>eff</sub> (s <sup>-1</sup> ) <sup>b</sup>	Fitted k <sub>eff</sub> (s <sup>-1</sup> ) <sup>c</sup>
0.0133	0.075	0.256	0.294
0.00665	0.15	0.182	0.176
0.00400	0.25	0.132	0.121
0.00266	0.375	0.102	0.090
0.00133	0.75	0.0571	0.0542
0.00100	1.0	0.0438	0.0439
0.00067	1.5	0.0284	0.0327

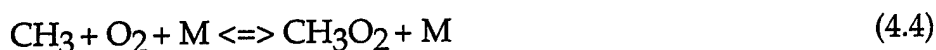
<sup>a</sup>Initial methane mole fraction =  $5.0 \times 10^{-4}$ , T=600 °C, P=250 bar.

<sup>b</sup>Defined as  $k_{\text{eff}} = 1/t$ , with reaction time, t, at  $[\text{CH}_4]/[\text{CH}_4]_0 = 1/e$ .

<sup>c</sup>Prediction from fit to  $k_{\text{eff}} = a(\text{O}_2 \text{ mole fraction})^b$ , which yields  $a = 7.02$  and  $b = 0.734$

#### 4.2.3 The role of methyl peroxy radical (CH<sub>3</sub>O<sub>2</sub>)

Closer inspection of the experimental results on the O<sub>2</sub> concentration dependence at high and low temperature illustrates where the GRI model begins to break down. Fig. 4.2 shows a more complete flux diagram for the oxidation of methane using the mechanism developed by Schmitt et al.<sup>8</sup> and Alkam et al.<sup>5</sup> that includes the formation of CH<sub>3</sub>O<sub>2</sub> by the reaction:



The route by which methane is oxidized is very different if this key reaction, and the subsequent reactions of CH<sub>3</sub>O<sub>2</sub> as an oxidizer with fuel species, especially itself, are included. These reactions are not included in the GRI mechanism.

An examination of the O<sub>2</sub> concentration dependence analogous to Table 4.1 using the scheme in Fig. 4.2 shows the [O<sub>2</sub>] exponent to be zero. The inclusion of the rapid equilibrium with O<sub>2</sub> serves to remove any oxygen dependence from the predicted rate. This suggests that the GRI mechanism, when compared with the low temperature data, is not fully representing the additional pathways associated with temperatures below 450°C. In this more complicated scheme, CH<sub>3</sub>O<sub>2</sub> is both the oxidizer and the fuel. This may which may also explain the observed global order near two for CH<sub>4</sub> in the lower temperature data.

The GRI combustion mechanism is appropriate at higher temperature and represents the data well, but it appears that the CH<sub>3</sub>O<sub>2</sub> chemistry must be included to model the kinetics at lower temperature. This may be the origin of the slightly higher rates

•



—

—

—



—



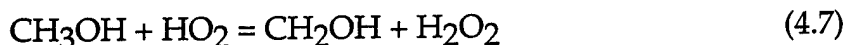
Increasing the rate of Reaction 4.6 in the direction written slows the overall consumption of methane. Note that water concentration affects the rate of both of these reactions since water is an explicit reactant in Reaction 4.6, and is the predominant collision partner (represented by M) in Reaction 4.5.

At low pressures, increasing water concentration increases rates of both elementary reactions linearly. As a result, the difference in rates between Reaction 4.5 and Reaction 4.6 grows, and the overall methane consumption rate increases. At a pressure near 200 bar, however, Reaction 2 reaches its high-pressure limit and at this point it becomes insensitive to the concentration of water. As a result, further increases in water concentration have no effect on Reaction 4.5. The rate of Reaction 4.6 continues to increase however, causing the rate of overall methane consumption to fall with increasing water concentration. In support of this simplified hypothesis, we found that increasing the rate of Reaction 4.6 moved model predictions in the direction of the observed data: overall rates dropped and the location at which rates begin to fall moved to lower water concentrations.

### 4.3 Methanol mechanistic modeling

#### 4.3.1 GRI 1.2 Mechanism - methanol conversion

Fig. 4.3 shows a comparison of the rate of methanol disappearance predicted from the GRI mechanism and some of the experimental data. The agreement between the GRI mechanism and the measurements is poor. In fact, when left unmodified, the GRI mechanism fails to produce any reaction at 450 °C. This is primarily because the mechanism lacks two key reactions:



and



The role of Reaction 4.8 is not particularly significant at SCWO conditions since there is a small equilibrium concentration of  $\text{HO}_2$  in oxygen/water mixtures at these temperatures, but without Reaction 4.7, an unreasonably long induction period is calculated. Fig. 4.3 shows the results from a calculation when these steps, and reverse reactions, are added to the scheme with the following parameters used for Reaction 4.7:  $A_f = 3.98 \times 10^{13}$ ,  $E_{a_f} = 19.4$  kcal/mol,  $b_f = 0.00$ ,  $A_r = 3.13 \times 10^{15}$ ,  $E_{a_r} = 10.75$  kcal/mole,  $b_r = -0.90$ ; where f and r refer to the forward and reverse reactions, and  $k = A \exp T^b (E_a/RT)$ . Clearly, agreement with the data is greatly improved.

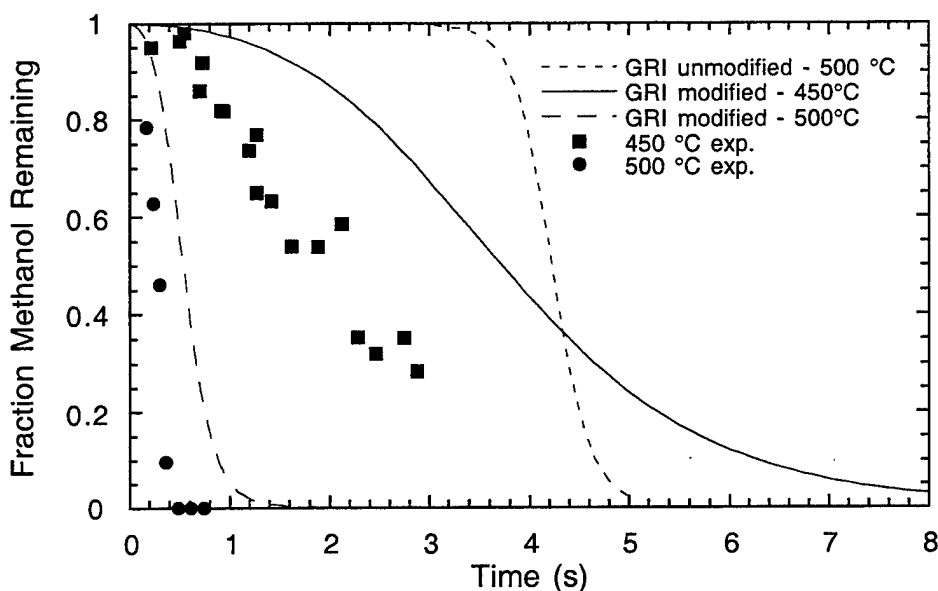
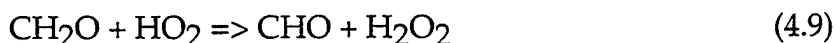


Figure 4.3 Comparison of experimental results from methanol oxidation at 450 °C and 500 °C at 27 MPa with the predictions from the GRI 1.2 mechanism, with (denoted "modified") and without the addition of Reactions 4.7 and 4.8. The unmodified calculation shows essentially no reaction at 450 °C.

#### 4.3.2 Formaldehyde formation

The GRI mechanism, with Reactions 4.7 and 4.8, still does not predict the accumulation of formaldehyde that is observed in this system with peak concentrations appearing about a factor of five below the observed values. This is because the parameters chosen for the reaction



( $A = 1.0 \times 10^{12} \text{ cm}^3\text{-mol/s}$  and  $E_a = 8.0 \text{ kcal/mol}$ ) cause it to be too fast and thus the intermediate  $\text{CH}_2\text{O}$  is consumed very rapidly. Surprisingly, the parameters chosen, especially for  $E_a$ , are significantly different than those recommended by Baulch et al. ( $A = 3.01 \times 10^{12} \text{ cm}^3\text{-mol/s}$  and  $E_a = 13076 \text{ kcal/mol}$ ). The two parameters sets do produce similar rate constants at 2000 K, but extrapolate to lower temperature very differently. Significantly better agreement with the experimental results for transient formaldehyde formation is achieved using the Bauch kinetic parameters<sup>9</sup>, producing the  $\text{CH}_2\text{O}$  intermediate at concentrations up to 18% of the initial methanol mole fraction. Since these observations, a new set of rate parameters has been put forth by Eiteneer (from the Frenklach group - one of the GRI MECH authors), that are consistent with the slower reaction.<sup>10</sup>



### 4.3.3 Feed concentration dependence

Figure 4.4 illustrates an important characteristic of the predictions from the elementary reaction model showing a pronounced variation in effective rate constant as a function of the initial feed concentration of methanol in the SFR. At high feed concentration ( $10^{-2}$  mole fraction), there is first a relatively short induction period that is followed by a second stage converting a little over two orders of magnitude of the feed. This second stage can be accurately represented as being first order in methanol concentration. These two characteristic reaction stages are illustrated by a straight line on the plot and its extrapolation to an induction time,  $t$ , of approximately 0.4 s. At lower feed concentrations, but the same reaction temperature and pressure, the induction time increases and approaches 1.5 s prior to the period where the kinetics are dominated by a first-order reaction.

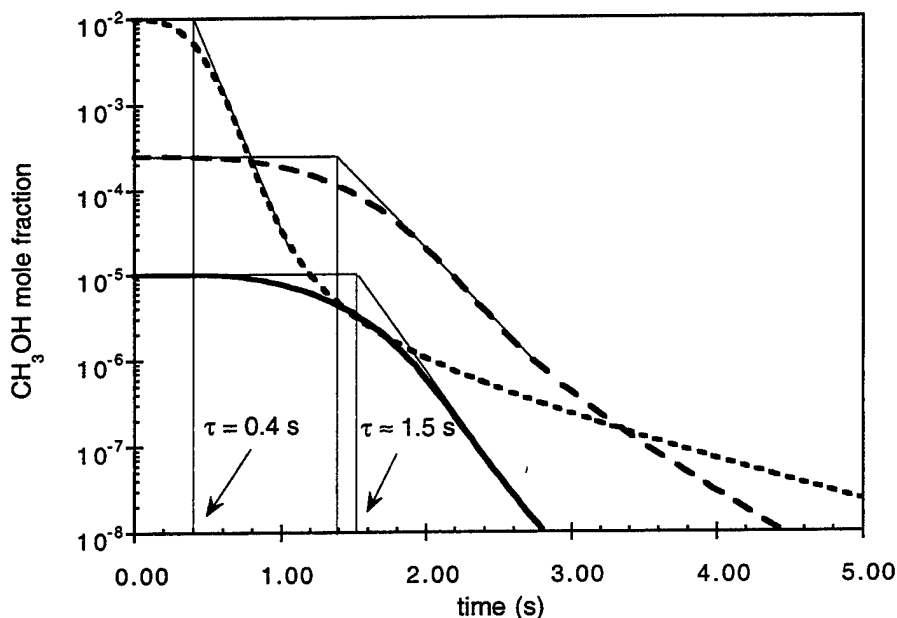


Figure 4.4. Predicted mole fraction of methanol as a function of time for different initial feed conditions at 500 °C and 25 MPa predicted using the modified GRI mechanism described above. Initial mole fractions are  $1.0 \times 10^{-2}$  (dotted line),  $2.5 \times 10^{-4}$  (dashed line), and  $1.0 \times 10^{-5}$  (solid line).

Fig.4.4 reveals that a first-order analysis of the concentration of methanol in samples taken from a reacting flow, described by

$$-\ln (C/C_0)/t = k_{\text{eff}} \quad (4.10)$$

where  $C$  and  $C_0$  are the measured and initial concentrations respectively,  $t$  is the reaction time, and  $k_{\text{eff}}$  is the effective first-order rate constant; will produce very different values for  $k_{\text{eff}}$  when evaluated for different feed concentrations and net conversions. For example, feeds at  $10^{-2}$  mole fraction and  $C/C_0 = 0.5$ , yields  $k_{\text{eff}} = 1.73 \text{ s}^{-1}$ , but at  $C/C_0 = 0.1$   $k_{\text{eff}} = 3.68 \text{ s}^{-1}$  and for  $C/C_0 = 0.01$ , (99% conversion)  $k_{\text{eff}} = 5.38 \text{ s}^{-1}$ . However, in the case of a more dilute feed (e.g. a mole fraction of  $2.5 \times 10^{-4}$ ), these same three conversions result in rate constants of  $0.52 \text{ s}^{-1}$ ,  $1.16 \text{ s}^{-1}$ , and  $1.84 \text{ s}^{-1}$  for the same fractional conversions. Thus, a difference in effective rate constant of over an order of magnitude can be observed for the same temperature and pressure. This discrepancy becomes more severe as temperature is lowered to  $450^\circ\text{C}$  and below.

This initial concentration dependence can be interpreted as follows. The induction time originates from the slower reaction rate associated with  $\text{HO}_2 + \text{CH}_3\text{OH} \Rightarrow (\text{CH}_2\text{OH or CH}_3\text{O}) + \text{H}_2\text{O}_2$  which dominates the fuel consumption at early time. The "first order" part of the reaction is dominated by  $\text{OH} + \text{CH}_3\text{OH}$ , but is rate controlled by the dissociation of  $\text{H}_2\text{O}_2$  to supply  $\text{OH}$ . The  $\text{H}_2\text{O}_2$  is accumulated during the chain branching induction period. The rate of the chain branching process depends on the concentration of  $\text{CH}_3\text{OH}$  and therefore, at constant equivalence ratio, is a function of fuel mole fraction.

## 4.4 C1 Modeling Summary

### 4.4.1 Methane

The GRI 1.2 methane oxidation mechanism is applied to the oxidation of methane by oxygen in water at 27 MPa and temperatures ranging from  $400 - 630^\circ\text{C}$ . The low temperature end of the SCWO conditions ( $380 - 450^\circ\text{C}$ ) deviate substantially from the much higher temperature and lower pressure conditions at which it was designed and optimized ( $1800^\circ\text{C}$ ). However, the results for the oxidation of methane with no modification of the mechanism agree very well with the available experimental results at SCWO temperatures near  $600^\circ\text{C}$ .

At lower temperature some flaws in the simple GRI mechanism appear and are more easily seen in the disappearance of the oxygen concentration dependence. We conclude that the shifting of the mechanistic pathway from the "flame chemistry" of Fig. 4.1 to the peroxide chemistry or Fig. 4.2 is the most probable explanation. Thus, there is evidence that the mechanism may be incomplete when applied to the  $<450^\circ\text{C}$  range; perhaps because the GRI mechanism does not contain  $\text{CH}_3\text{O}_2$  chemistry.

### 4.4.2 Methanol

In the case of methanol, to represent properly the oxidation kinetics and the formation of formaldehyde, the simple addition of one reaction (Eq 4.7) to the mechanism was essential. With this modification, good agreement was achieved in the temperature range of  $440 - 500^\circ\text{C}$ . Much of the methanol oxidation pathway is imbedded in the methane mechanism in Fig. 4.2 with the exception of the hydrogen abstraction reaction by  $\text{HO}_2$  that serves to initiate the radical chain process. Work by Savage and co-

workers<sup>4</sup> has pointed to a somewhat different chemistry for the conversion of CO to CO<sub>2</sub> involving the formation of HOCO and the subsequent reaction with O<sub>2</sub> to form HO<sub>2</sub> and CO<sub>2</sub>. However, there has been no direct measurement that can distinguish between these two pathways. Obviously, from a waste treatment perspective, the rate of full conversion to CO is very important from an emissions standpoint. In the future, this simple yet very important mechanistic detail warrants additional attention.

Further examination of the predictions from the model illustrates that care must be taken when comparing experimental results from different sources and that, in particular, the experimental fuel concentration range and overall conversion must be given special attention. Even after over a decade of careful study, the subtleties of methanol conversion kinetics and how to choose appropriate rates to use in an engineering sense, for both low conversion and high conversion considerations, have not been fully resolved.

#### 4.5 References

1. P.A. Webley, J.W. Tester "Chapter 17, Fundamental Kinetics of Methanol Oxidation in Supercritical Water." in *Supercritical Fluid Science and Technology*; Johnston, K. P., Penninger, J. M. L., Eds.; American Chemical Society: Washington, DC; Vol. 406; pp 259-275. 1989.
2. P. A. Webley; J.W. Tester "Fundamental Kinetics of Methane Oxidation in Supercritical Water" *Energy & Fuels*, 5, 411-419, 1991.
3. E.E. Brock; P.E. Savage "Detailed Chemical Kinetics Model for Supercritical Water Oxidation of C<sub>1</sub> Compounds and H<sub>2</sub>" *AIChE Journal* 41, 1874-1888. 1995.
4. E.E. Brock, Y. Oshima, P.E. Savage, J.R. Barker "Kinetics and Mechanism of Methanol Oxidation in Supercritical Water" *J. Phys. Chem.* 100, 15834-15842, 1996.
5. M.K. Alkam, V.M. Pai, P.B. Butler, W.J. Pitz "Methanol and Hydrogen Oxidation Kinetics in Water at Supercritical States" *Combust. Flame* 106, 110-130, 1996.
6. P. Dagaut, M. Cathonnet, J-C. Boettner "Chemical Kinetic Modeling of the Supercritical-Water Oxidation of Methanol" *J. Supercrit. Fluids*, 98, 33-42, 1996.
7. P.E. Savage, J. Rovira, N. Stylski, C.J. Martino "Oxidation Kinetics for Methane/Methanol Mixtures in Supercritical Water" *J. Supercrit. Fluids*, 17, 155-170, 2000.
8. R.G. Schmitt, P.B. Butler, N.E. Bergan, W.J. Pitz, C.K. Westbrook, "Destruction of Hazardous Waste in Supercritical Water. Part II: A Study of High-Pressure Methanol Oxidation Kinetics"; 1991 Fall Meeting of the Western States Section/The Combustion Institute, 1991, University of California at Los Angeles, CA.

9. D.L. Baulch, C.J. Cobos, R.A. Cox, P. Frank, G. Hayman, T. Just, J.A. Kerr, T. Murrells, M.J. Pilling, J. Troe, R.W. Walker, J. Warnatz "Evaluated Kinetic Data for Combustion Modelling - Supplement I" *J. Phys. Chem. Ref. Data* **23**, 847-1033, 1994.
- 10.B. Eiteneer, C.L. Yu, M. Goldenberg, M. Frenklach "Determination of Rate Coefficients for Reactions of Formaldehyde Pyrolysis and Oxidation in the Gas-Phase." *J. Phys. Chem. A*, **102**, 5196-5205, 1998.

This page intentionally left blank

## Section 5: Role of Hydrogen Peroxide

### 5.1 Overview

#### 5.1.1 Introduction

Kinetics modeling in several of the papers referenced in Section 4, as well as our own work, points out the high sensitivity of organic oxidation to hydrogen peroxide decomposition:



where the collision partner, M, is water. Unfortunately, experimental data available for this reaction are either in the gas phase at high temperatures (shock tube) or in the aqueous phase for temperatures below 280 °C. At the onset of this project, no direct measurements of the reaction rate of hydrogen peroxide decomposition at supercritical water conditions were available in the literature for use in the mechanistic schemes.

For purposes of elementary modeling for high-pressure hydrothermal oxidation, Holgate and Tester estimated the reaction rate by means of RRKM calculations, which provided an assessment of the high-pressure limit. Using this calculated rate constant, elementary models succeeded fairly well in reproducing experimental data in supercritical water conditions in the case of hydrogen oxidation at 550 and 570 °C. Yet, the predicted conversion of methanol for temperatures below 490 °C appears to be slower than the conversion given by the experimental data, with the discrepancies increasing at lower temperatures. Because the dissociation of hydrogen peroxide was found to be rate controlling in the elementary reaction model during most of the methanol oxidation reaction, the principal cause of discrepancy between experimental results and model prediction may likely originate from the rate of  $\text{H}_2\text{O}_2$  decomposition.

In this section, two main activities are described. The first is the direct measurement of  $\text{H}_2\text{O}_2$  decomposition in the SFR obtained by direct sampling of the effluent. The second is the use of Raman spectroscopy to observe the formation of this key intermediate during the oxidation of several alcohols in the SFR.

#### 5.1.2 Papers and Reports

E. Croiset, S.F. Rice, R.G. Hanush "Hydrogen Peroxide Decomposition in Supercritical Water" *AIChE Journal* **43**, 2343-2352, 1997.

E. Croiset, S.F. Rice "Direct Observation of  $\text{H}_2\text{O}_2$  During Alcohol Oxidation by  $\text{O}_2$  in Supercritical Water" *Ind. Eng. Chem. Res.* **37**, 1755-1760, 1998.

## 5.2 Hydrogen Peroxide Decomposition in Supercritical Water

### 5.2.1 Experimental measurements

In this project, we determined the rate constant of hydrogen peroxide decomposition by direct measurements in the SFR, for pressures ranging from 5.0 to 34.0 MPa, and for temperatures up to 450 °C.

In the work described in this section, global kinetics of hydrogen peroxide decomposition are assumed to follow first-order reaction kinetics:

$$-\frac{d[H_2O_2]}{dt} = k_g [H_2O_2] \quad (5.2)$$

where  $[H_2O_2]$  is the hydrogen peroxide molar concentration, and  $k_g$  is the global  $H_2O_2$  decomposition rate constant, in  $s^{-1}$ . The rate constant is defined in terms of the experimental measurements by integrating Eq. 5.2 to yield:

$$\ln\left(\frac{[H_2O_2]_f}{[H_2O_2]_i}\right) = -k_g t \quad (5.3)$$

where the indice "i" represents the initial concentration and the indice "f" represents the measured final concentration after some reaction time,  $t$ .

The first set of measurements were aimed at determining the global hydrogen peroxide decomposition rate constant. During the course of the experiments, we found that this global rate includes homogeneous decomposition and decomposition due to catalysis by the reactor surface. By conducting specific experiments that vary the system surface-to-volume ratio, the wall-catalyzed decomposition rate can be separated from the homogeneous process.

Experiments were performed in the SFR at 24.5 and 34.0 MPa, for temperatures ranging from 150 °C to 450 °C. Figures 5.1 and 5.2 show the plots of  $\ln([H_2O_2]_f / [H_2O_2]_i)$  versus residence time at 24.5 MPa, for temperatures below, and above, the critical temperature of water  $T_c$  (374 °C). The curves obtained are straight lines, which confirms that the decomposition of hydrogen peroxide follows first order global kinetics. However, comparison between these two figures shows important differences between experiments conducted above and below the critical temperature of water. For experiments well below  $T_c$ , the straight lines pass through the origin indicating no significant  $H_2O_2$  decomposition inside the injector, whereas near and above  $T_c$ , the straight lines do not pass through the origin implying considerable  $H_2O_2$  decomposition before the mixing point. However,  $H_2O_2$  decomposition inside the injector does not prevent the interpretation of the results, because only the slope of the curve is necessary to determine the rate constant.

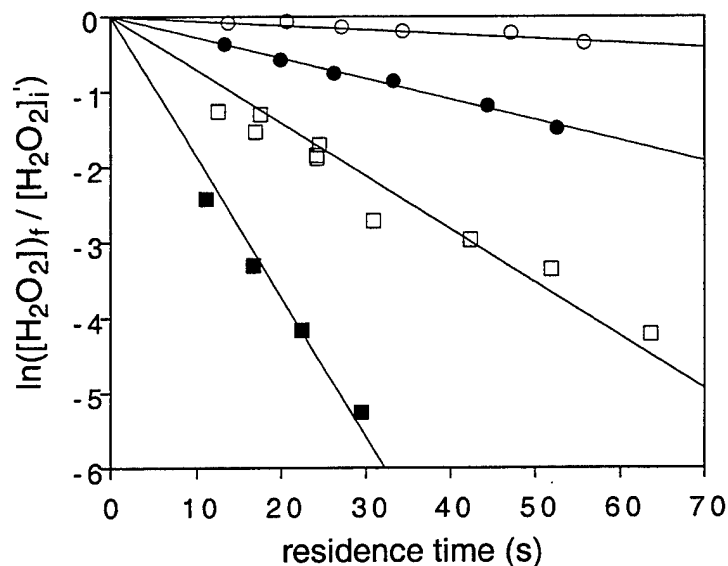


Figure 5.1 Variation of  $\ln([H_2O_2]_f / [H_2O_2]_i)$  versus residence time. Pressure = 24.5 MPa. Results are shown for temperatures *below the critical temperature* of water: 150 °C ○, 200 °C ●, 250 °C □, 300 °C ■.

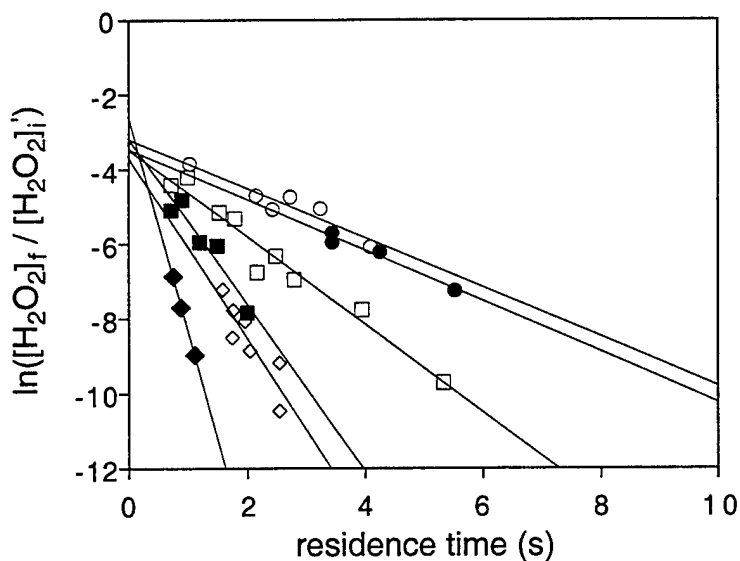


Figure 5.2. Variation of  $\ln([H_2O_2]_f / [H_2O_2]_i)$  versus residence time. Pressure = 24.5 MPa. Results are shown for temperatures *above the critical temperature* of water: 380 °C ●, 390 °C ○, 400 °C □, 420 °C ■, 425 °C ◇, and 440 °C ◆.

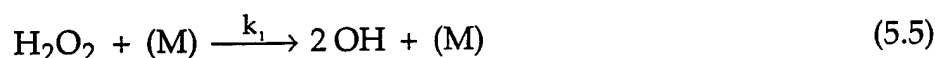


### 5.2.2 Global rate constant

The experimental data were used to determine the rate constant of the elementary reaction of  $\text{H}_2\text{O}_2$  dissociation, which, as it will be seen, can be derived from the measured homogeneous rate constant. Above, hydrogen peroxide decomposition is described by the decomposition reaction



where  $k_g$  is the global rate constant determined from the slopes of the curves in Fig. 5.1 and Fig. 5.2. It has been suggested by others that this reaction proceeds by a pathway with the rate limiting step being



A detailed analysis has shown that a steady-state assumption for  $[\text{OH}]$  and  $[\text{HO}_2]$  can be used to obtain:

$$\frac{d[\text{H}_2\text{O}_2]}{dt} = -2 k_1 [\text{H}_2\text{O}_2] \quad (5.6)$$

which indicates that the rate measured experimentally is twice the elementary first order rate constant for Reaction 5.4. From our data, in the supercritical region the rate constant  $k_1$  becomes

$$k_1 = 10^{13.4 \pm 1.2} \exp[(-180 \pm 16 \text{ kJ/mol})/RT] \quad (5.7)$$

Likewise, in the aqueous phase, the rate constant  $k_1$  is

$$k_1 = 10^{3.3 \pm 0.3} \exp[(-49 \pm 3 \text{ kJ/mol})/RT] \quad (5.8)$$

Considering the state of water in the supercritical region as dense gas, it is meaningful to compare our rate constants in the supercritical region with the high-pressure-limit rate constants in the vapor phase determined by others. The commonly accepted expression for the gas-phase rate constant is the one recommended by Baulch *et al.*<sup>2</sup> The rate constant of Holgate<sup>1</sup> at 24.6 MPa was determined from RRKM calculations and was found to be very close to the high-pressure limit. The expression derived by Holgate and Tester is in fact very close to the expression of Baulch *et al.*<sup>2</sup> and represents an extrapolation of Baulch values to the temperature range 400 - 600 °C. Our direct measurement of the rate constant at supercritical conditions is approximately a factor of five greater than these extrapolated values at 400 °C. Our results point to a slightly lower activation energy for this reaction and the expression in Eq. 5.7, when extrapolated to high temperature, very accurately predicts the low-pressure shock tube data.

### 5.2.3 $\text{H}_2\text{O}_2$ decomposition and methanol oxidation in SCWO

The observation that hydrogen peroxide decomposition plays a key role during the oxidation of methanol in supercritical water has been expressed by many authors. In Section 4 above, it was found that the model of Schmitt *et al.*<sup>3</sup> reproduces our experimental data fairly well, but predicts rates that are measurably slower for temperatures below 490 °C. We have repeated this calculation with the former expression for the rate of  $\text{H}_2\text{O}_2$  decomposition replaced by the new expression found in the Section 5.2.2. The new prediction of methanol oxidation behavior was then compared with the former prediction and with the experimental data. The new values of the  $\text{H}_2\text{O}_2$  decomposition rate parameters, obtained in our own work, improve the prediction of the model considerably at 440 and 450 °C, that is, in the temperature range of the present work. Extrapolations to temperatures above 450 °C provide good agreement with the experimental data, although at 470 and 490 °C the rate of methanol disappearance is predicted to be slightly too fast. Nonetheless there is a significant overall improvement when compared with the data.

### 5.2.4 Summary

The decomposition rate of hydrogen peroxide was determined in SFR experiments at pressures ranging from 5.0 to 34.0 MPa and temperatures up to 450 °C. It is found that  $\text{H}_2\text{O}_2$  decomposition in water follows first order kinetics in the aqueous, vapor, and supercritical phases. The homogeneous dissociation rate of hydrogen peroxide is found to be independent of the dissociation on surfaces of the reactor. The important factor determining the homogeneous rate of hydrogen peroxide thermal decomposition in water is the water density. The catalytic decomposition of  $\text{H}_2\text{O}_2$  at a surface was also determined and is found to vary with water density; its importance decreases when the density increases. In the liquid phase, where the density is the highest, the influence of surface reactions is small, whereas in the gas phase surface reactions can dominate, especially at low temperatures. Due to higher fluid densities, surface reactions have a smaller effect under supercritical conditions than in the subcritical high pressure steam phase.

By considering the surface effect, the true homogeneous rate of  $\text{H}_2\text{O}_2$  decomposition is determined and found to be equal to  $10^{13.4 \pm 1.2} \exp[(-180 \pm 16 \text{ kJ/mol})/RT]$  in the supercritical region at 24.5 and 34.0 MPa. In the temperature range considered here (380 - 450 °C), this rate leads to values higher than those found from RRKM calculations. In addition, results for experiments conducted in the gas phase at 5.0 and 10.0 MPa reflect essentially the hydrogen peroxide decomposition on the reactor's surface, which allows us to determine the corresponding reaction rate based on a simple theoretical expression derived from kinetic theory of gases. However, this theoretical expression fails in describing the surface effect in the supercritical region and an empirical Arrhenius form expression was found to be more relevant. Finally, at supercritical water conditions, and for temperatures below 470 °C, the reaction rate for hydrogen peroxide thermal decomposition determined in the present work improves significantly the accuracy of the methanol oxidation model.

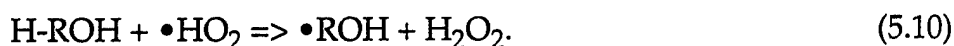
### 5.3 Direct Observation of H<sub>2</sub>O<sub>2</sub> during Alcohol Oxidation by O<sub>2</sub> in Supercritical Water

#### 5.3.1 Introduction

Our initial modeling showed that hydrogen peroxide plays an important role during the oxidation of methanol by oxygen in supercritical water and by analogy it is likely that it is also formed during the oxidation of other simple alcohols. It is formed during the early stages of oxidation through the hydrogen abstraction reactions



and



Sensitivity analysis of elementary reaction mechanisms shows that it is the most important species determining the overall rate of conversion. H<sub>2</sub>O<sub>2</sub> functions as a relatively unreactive reservoir of oxidizer and controls the rate of conversion through its thermal decomposition by metering the supply of OH radicals to the system. Above, the rate constant of H<sub>2</sub>O<sub>2</sub> thermal decomposition in supercritical water was measured experimentally and the new value was shown to improve the agreement between model and experiment. However, no data have been reported concerning direct measurement of hydrogen peroxide during oxidation experiments in supercritical water. This sub-section presents the quantitative direct observation of H<sub>2</sub>O<sub>2</sub> by Raman spectroscopy during ethanol, methanol, and n-propanol oxidation by oxygen in supercritical water. Experimentally observed transient H<sub>2</sub>O<sub>2</sub> concentration during methanol oxidation is compared to that predicted by two similar elementary reaction mechanisms.

#### 5.3.2 Hydrogen peroxide calibration and measurement.

The Raman spectrum of hydrogen peroxide is known to have a very strong resonance at 863.5 cm<sup>-1</sup> in the gas phase and at  $\approx$  880 cm<sup>-1</sup> in the liquid phase, corresponding to the O-O symmetric stretching vibration. The H<sub>2</sub>O<sub>2</sub> peak is detected at 884 cm<sup>-1</sup> in the liquid phase at ambient conditions and at 874 cm<sup>-1</sup> in the supercritical phase as shown in Figure 5.3 and is used to identify the presence of H<sub>2</sub>O<sub>2</sub> as a transient intermediate.

Previous experiments in the SFR in which we monitored the reactivity of methanol and i-propanol established the utility of Raman scattering intensity to measure stable species concentration with a detection limit of less than 0.001 mol/L, depending on the specific species. Figure 5.3a shows the Raman spectrum of the  $\approx$  870 cm<sup>-1</sup> band of hydrogen peroxide at various temperatures in liquid water used for calibration purposes. Figure 5.3b includes spectra collected in the supercritical phase at 390, 410, and 430 °C. The Raman resonance is best represented by a sum of two Gaussians that vary in relative intensity as a function of temperature. This is clear in Figure 5.3b, but a shoulder can be seen at temperatures even as low as 300 °C.

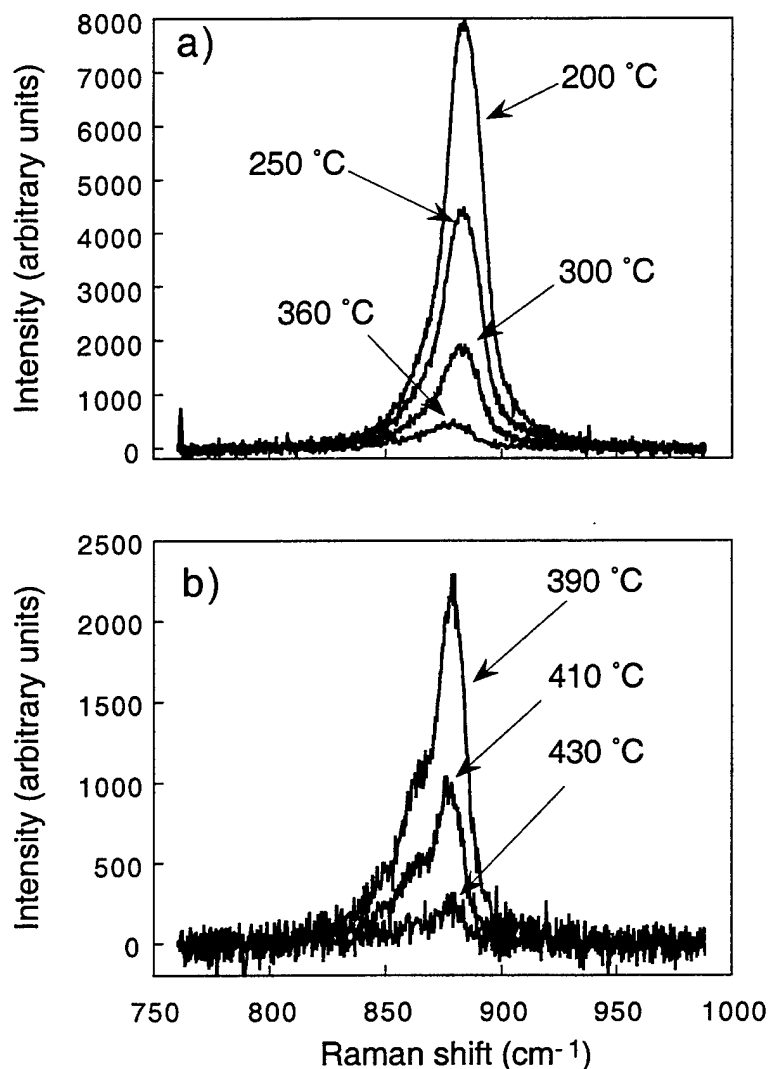


Figure 5.3. Raman spectra of hydrogen peroxide obtained in the SFR at 24.5 MPa. a) Aqueous liquid phase at 200, 250, 300, and 360 °C. For each temperature, the initial H<sub>2</sub>O<sub>2</sub> mole fraction at the mixing point was 0.53 wt %. b) Raman spectra of H<sub>2</sub>O<sub>2</sub> in the supercritical phase at 390, 410, and 430 °C obtained with higher feed concentrations than were used in a).

We devoted considerable effort to accurately calibrating the Raman signal that we measured from H<sub>2</sub>O<sub>2</sub>. This required using the decomposition data reported in the previous subsection, as well as careful analysis of the spectral bandshape as a function of temperature.

### 5.3.3 Detection during ethanol oxidation

An accurate Raman spectrum waveform of  $\text{H}_2\text{O}_2$  at 410 °C in supercritical water and a reliable method to extrapolate the scattering cross section permit a quantitative analysis of the formation of hydrogen peroxide during SCWO of ethanol and methanol in the SFR. Similar measurements for n-propanol oxidation are also presented below, but were not analyzed in depth. All the experiments were carried out at 24.5 MPa.

Figure 5.4 illustrates the determination of ethanol and hydrogen peroxide contributions to the Raman spectrum in the 750-1000  $\text{cm}^{-1}$  region at 430 °C and at different residence times. This figure shows the disappearance of ethanol and the formation of hydrogen peroxide during ethanol oxidation in supercritical water.

Some difficulties arise in the quantitative analysis due to the overlap of  $\text{H}_2\text{O}_2$  and ethanol peaks in the region of 870  $\text{cm}^{-1}$ . The sum spectrum is assumed to be a linear combination of the pure species spectra. The pure hydrogen peroxide spectrum is fitted by a sum of two Gaussian peaks of different widths centered at 874  $\text{cm}^{-1}$  and 863  $\text{cm}^{-1}$ . This shape was obtained from the spectrum at 430 °C in Figure 5.3b. The ethanol spectrum is fitted by a double Gaussian with both peaks centered at 890  $\text{cm}^{-1}$  obtained from a fit to the spectrum in the absence of an oxidizer. Thus, the relative amounts of  $\text{H}_2\text{O}_2$  and ethanol could be determined by fitting the spectrum obtained during oxidation by adjusting only the relative magnitude of these two waveforms. Without the independent determination of the pure species bandshapes, reliable concentrations could not be determined from the overlapping features.

### 5.3.4 $\text{H}_2\text{O}_2$ concentration during methanol oxidation

Methanol oxidation was examined at 480 °C and 24.5 MPa with an initial methanol concentration of 0.028 mol/L. These measurements show much lower concentrations of hydrogen peroxide than predicted by the models. The greatest amount detected corresponds to an  $\text{H}_2\text{O}_2$  concentration of only about 8% of the initial methanol concentration. As shown in Figure 5.5, the model predicts relatively well the behavior of methanol and formaldehyde that we have observed using this technique, but overestimates the formation of hydrogen peroxide. Also included on the plot are data from the elementary reaction modeling, which show good agreement for methanol conversion at 480 °C. Despite the improved agreement with methanol conversion, these data illustrate that further investigation and model development is warranted to fully explain the evolution of all of the key species during methanol oxidation in supercritical water despite the present good agreement with conversion rates.

In fact, Alkam and co-workers and independently Brock et al.<sup>5</sup> have suggested that the presently accepted rate of reaction for the abstraction of hydrogen from methanol by  $\text{HO}_2$  may be incorrectly too high for models of supercritical water oxidation since the rate used in these models is an extrapolation of a theoretical estimate, and not from direct measurement. We have shown that  $\text{H}_2\text{O}_2$  thermal decomposition is faster than the extrapolation from high-temperature low-pressure data suggests in the 400 - 440 °C region. The combination of these two adjustments to the elementary reaction models may result in preserving reasonable agreement with overall methanol conversion rates

at 480 °C, and also significantly reducing predicted peak concentrations of transient  $\text{H}_2\text{O}_2$ , thus permitting better agreement with these data presented here.

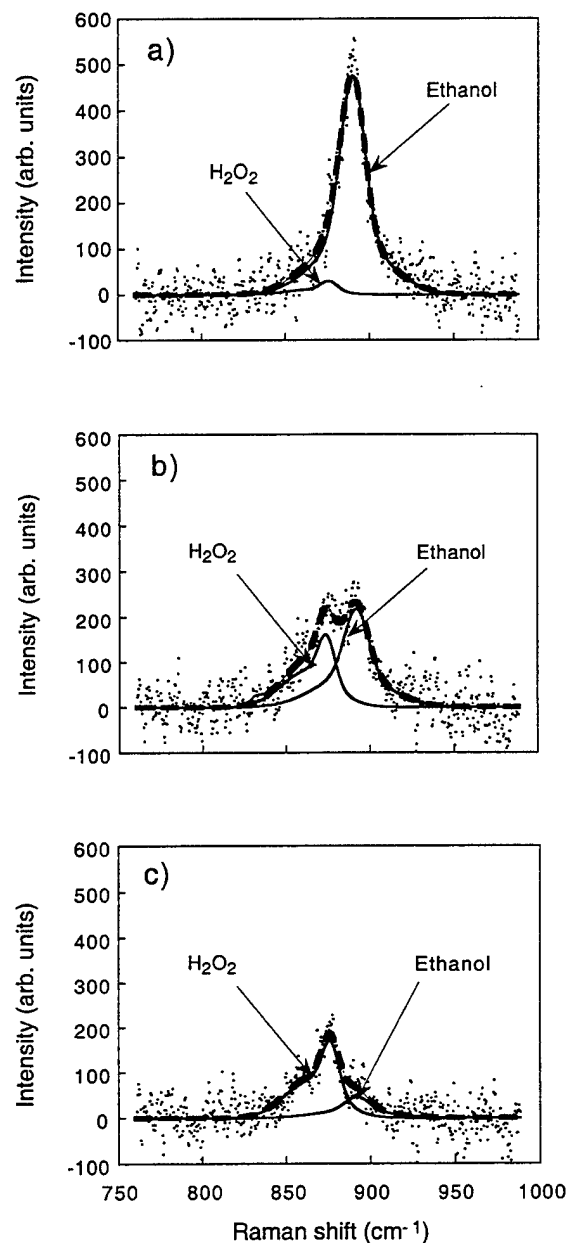


Figure 5.4. Variation of ethanol and  $\text{H}_2\text{O}_2$  spectra during ethanol oxidation at 430 °C and at different residence times: a) 0.6 s, b) 1.2 s, c) 1.7 s. The dotted line represents a fit to a sum of the spectra of the two species.

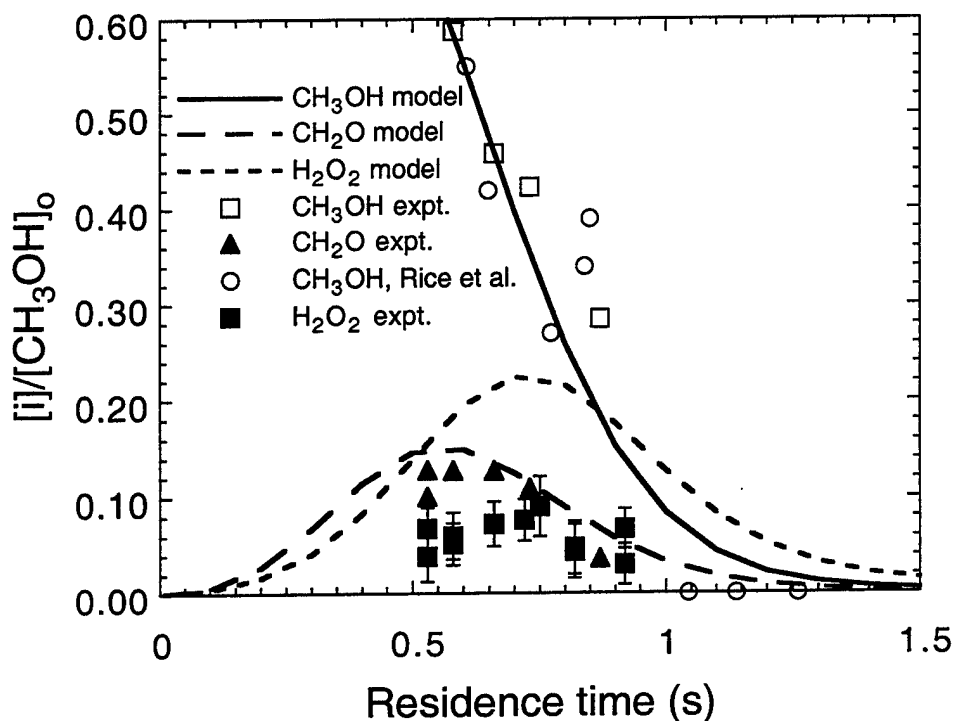


Figure 5.5. Normalized concentration of methanol, formaldehyde, and hydrogen peroxide as a function of time as determined by the mechanism developed by Schmitt<sup>3</sup> and experimental data from this work. Normalized concentration,  $[i]/[\text{CH}_3\text{OH}]_0$  represents the concentration of species  $i$ , in the legend, divided by the initial methanol concentration. Error bars on the  $\text{H}_2\text{O}_2$  concentration are  $\pm 2\sigma$ .

### 5.3.5 *N*-propanol oxidation

*N*-propanol oxidation was examined in a small set of experiments to observe the presence of  $\text{H}_2\text{O}_2$  since *n*-propanol has an oxidative reactivity comparable to ethanol. Figure 5.6 illustrates a typical spectrum collected during *n*-propanol oxidation, and shows clear evidence of the presence of hydrogen peroxide. The concentration of  $\text{H}_2\text{O}_2$  in Figure 5.6 is  $5.0 \times 10^{-3}$  mol/L, corresponding to 21% of the initial *n*-propanol concentration when 46% of the initial *n*-propanol is remaining. The amount of hydrogen peroxide formed during *n*-propanol oxidation appears to be comparable to the ethanol results and is much higher than during methanol oxidation.

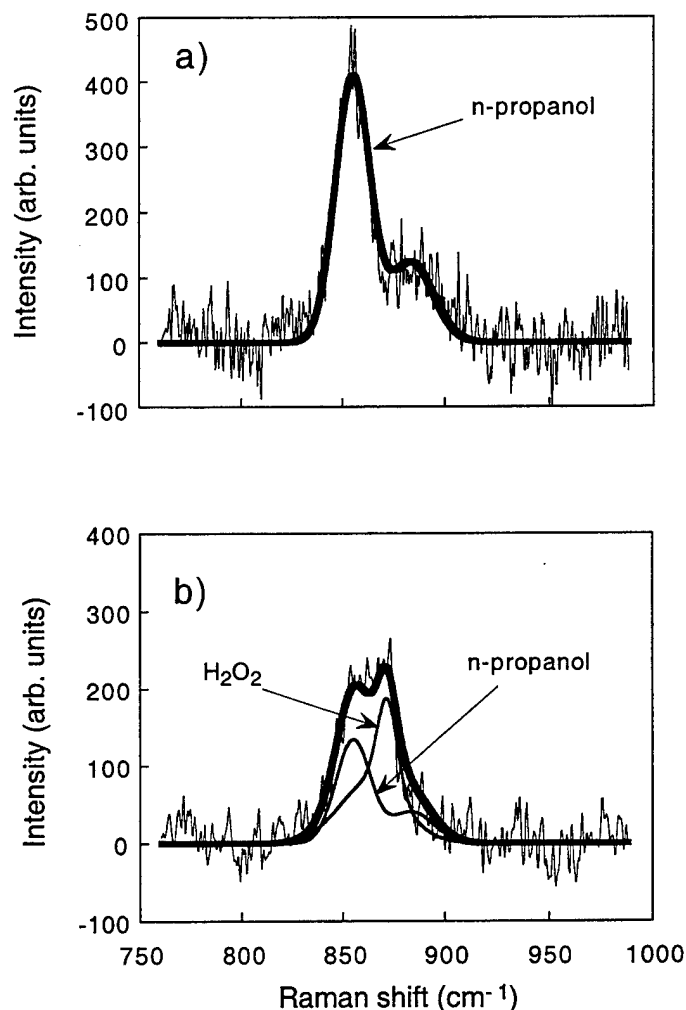


Figure 5.6 Comparison between a spectrum of a) pure n-propanol and b) a spectrum collected during n-propanol oxidation in the SFR under SCWO conditions. Both spectra were recorded at 410 °C and 25 MPa. The solid lines are individual species contributions that are adjusted in relative magnitude to fit the complete spectrum. b) shows evidence of hydrogen peroxide formation during n-propanol oxidation at a residence time of 1.71 s.

### 5.3.6 Summary

This sub-section shows that hydrogen peroxide can be detected and quantified during oxidation reactions in supercritical water using Raman spectroscopy. The hydrogen peroxide peak is located at about 874 cm⁻¹ and has a characteristic shape that can be fitted by the sum of two Gaussian waveforms. Hydrogen peroxide calibration is possible with the assumption that its Raman scattering cross section is similar in both the high-temperature liquid phase and in the supercritical regime. Results indicate formation of high concentrations of H₂O₂ in the case of ethanol and n-propanol



oxidation, but lower concentrations during methanol oxidation. In the case of methanol, two similar elementary reaction kinetic models over-estimate the amount of hydrogen peroxide formed, indicating that more work is needed to complete the understanding of the role of hydrogen peroxide in oxidation kinetics at supercritical water conditions. Considering the importance of hydrogen peroxide during alcohol oxidation in supercritical water, direct  $\text{H}_2\text{O}_2$  measurement will be valuable in determining reaction pathways and to validating kinetic models.

#### 5.4 References

- 1 H. R. Holgate, J. W. Tester "Oxidation of Hydrogen and Carbon Monoxide in Sub- and Supercritical Water: Reaction Kinetics, Pathways, and Water-Density Effects. 2. Elementary Reaction Modeling" *Journal of Physical Chemistry* **98**, 810-822, 1994.
- 2 D. L. Baulch, C. J. Cobos, R. A. Cox, P. Frank, G. Hayman, T. Just, J. A. Kerr, T. Murrells, M. J. Pilling, J. Troe, R. W. Walker, J. Warnatz "Evaluated Kinetic Data for Combustion Modelling - Supplement I" *J. Phys. Chem. Ref. Data* **23**, 847-1033, 1994.
- 3 R. G. Schmitt, P. B. Butler, N. E. Bergan, W. J. Pitz, C. K. Westbrook. "Destruction of Hazardous Waste in Supercritical Water. Part II: A Study of High-Pressure Methanol Oxidation Kinetics", 1991 Fall Meeting of the Western States Section/The Combustion Institute, University of California at Los Angeles, CA., 1991.
- 4 M. K. Alkam, V. M. Pai, P. B. Butler, W. J. Pitz "Methanol and Hydrogen Oxidation Kinetics in Water at Supercritical States" *Combustion and Flame* **106**, 110-130, 1996.
- 5 E. E. Brock, Y. Oshima, P. E. Savage, J. R. Barker "Kinetics and Mechanism of Methanol Oxidation in Supercritical Water" *J. Phys. Chem.* **100**, 15834-15842, 1996.

## Section 6: Role of water

### 6.1.Introduction

#### 6.1.1 Background

The early development of supercritical water oxidation in the 1980's was simultaneously accompanied by other supercritical fluid research that recognized the unique solvent properties of supercritical carbon dioxide. In addition, SCWO was in some ways a logical follow-on to the attempts to use supercritical and near critical (300-350°C) high-pressure water as a medium for coal liquefaction. This has been both a compliment and a detriment to the formation of a complete and accurate picture of the salient physical processes associate with organic oxidation chemistry by oxygen in water at 400-650 °C and 25-30 MPa.

Prior to the first SCWO patents by Modell,<sup>1-3</sup> work in supercritical water had been dominated by the interest in better equations of state for nuclear power plants. Only the unique work by Franck<sup>4-6</sup> and coworkers over a dozen years focuses on supercritical water as a solvent, but still this work was primarily devoted to mixture EOS and phase behavior. The idea of SCWO appeared as it was recognized that the rate and extent of organic conversion could be increased several orders of magnitude relative to established Wet-Air Oxidation by going to higher temperatures to increase reaction rate and higher pressures to maintain a single phase of oxidizer and fuel. Thus, the idea of SCWO was the result of the liquefaction work that established the high solubility of organics in supercritical water and the EOS work that established the miscibility of gases. These two principles lead to the utility of waste oxidation in a single phase.

Nowhere in either of these two principles is there really any highlight about being above or below the critical point of water itself and nowhere is there special properties attributed to the unusual fluid physics associated with fluid structure properties very near a critical point. Rapidly (e.g. by the early 1990's) the application-oriented technology development efforts were focusing on typical operating conditions of >600°C and approximately 25 MPa, which result in reduced densities ( $\rho/\rho_c$ ,  $\rho_c$ =density of water at its critical point) of 0.3 or less. Water under these conditions is a dense, but nearly ideal, relatively unreactive, gas. There are no unusual properties associated with the compressibility or heat capacity at these conditions. It would be unlikely that there is anything unusual about reactions in water as a buffer or solvent at these conditions that could not be predicted by the chemistry of the reactants themselves.

Unfortunately, these concepts went overlooked by many. The lore of SCWO was caught up in poorly defined ideas and sales pitches such as "molecular charisma" and the like designed to suggest that SCWO was somehow a greater discovery than it was in its own right. Much of this came from coupling to the supercritical carbon dioxide community, where typical experimental conditions were indeed very near mixture

critical points and many of the special properties of near critical phenomena did play an important role in a number of applications.

It became important within the context of understanding reaction kinetics to determine more specifically the actual conditions under which water begins to affect otherwise gas-kinetic reactivity. This project focused initially on a particular suggestion by a Sandia coworker (C. Melius) that illustrated perhaps where the line could be drawn between unusual near-critical or special reaction properties of water in supercritical water chemistry and the application of 600 °C, 25 MPa water as a reaction buffer environment for waste disposal. Melius had noted the water-gas shift equilibrium,  $\text{CO} + \text{H}_2\text{O} = \text{CO}_2 + \text{H}_2$ , might be unusually sensitive to water density. This analysis pointed out a special range of conditions under which water would facilitate rapid conversion of CO to  $\text{CO}_2$  and why. Section 6.2 explores this proposition experimentally and reveals that water can play an unusual role but, as stated above, truly near-critical densities are needed.

Another set of experiments that illustrates the simple dense gas nature of supercritical water is reported in section 6.3. These Raman measurements serve to reinforce the suitability of the binary collision approximation at supercritical water densities typical for waste oxidation applications.

#### **6.1.2 Papers and Reports**

S.F. Rice, R.R. Steeper, J.D. Aiken "Water Density Effects on Homogeneous Water-Gas Shift Reaction Kinetics" *J. Phys. Chem. A* **102**, 2673-2678, 1998.

R.R. Steeper, S.F. Rice, J.D. Aiken "Water-Gas Shift Reaction Kinetics in Supercritical Water" *Proceedings of The Fourth International Symposium on Supercritical Fluids*, Sendai, Japan May 11-14, p. 575, 1997.

S.F. Rice J. J. Wickham "Hydrogen Raman Linewidths in Supercritical Water and Carbon Dioxide" *J. Raman Spectroscop.* **31**, 619-624, 2000.

### **6.2 Water-Gas Shift Chemistry In Supercritical Water**

#### **6.2.1 The Melius model**

It has been suggested that an important aspect of modeling elementary reactions in supercritical water is determining whether neighboring water molecules in the dense fluid participate in the reaction chemistry. It could be possible that the presence of high-density water enables individual elementary reactions to proceed at rates that are significantly different from rates predicted by extrapolating from gas phase expressions to higher pressure. In fact, there are a number of ways that water can affect the rate of a reaction under these conditions. In the case of the water-gas shift reaction, we are interested in whether the presence of water at high density can modify the energetics of a transition state complex. Thus, for example, additional water molecules can be incorporated into the transition state structure directly, or act in concert to stabilize that

complex through solvent-like electrostatic forces. The formation of higher density clusters surrounding a solute in a supercritical mixture has received considerable attention over the past fifteen years by both experimentalists and theorists. This work provides the framework for interpreting the pressure dependence of the water-gas shift reaction in supercritical water.

Several years ago, Melius and coworkers conducted a theoretical investigation of the homogenous, gas-phase water-gas shift mechanism.<sup>7</sup> They suggested that, at sufficiently high water densities, the activation energies for CO conversion to formic acid and the subsequent decomposition of formic acid to CO<sub>2</sub> and H<sub>2</sub> are significantly reduced by the participation of additional water molecules in the transition state complex.

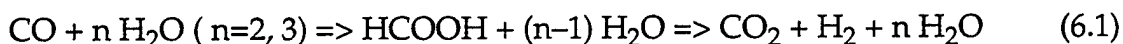


Fig. 6.1 (top) shows the transition state structure for the formation of formic acid from CO and two water molecules. Since the two hydrogen atoms in the product formic acid originate from different water molecules, the transition state structure is less strained and has a reduced heat of formation relative to the transition state that uses only one molecule. When the extra water molecule is not present, the structure is much more strained and requires more energy to form. There is another structure suggested, involving three water molecules, that provides even more stabilization. The calculated activation energies for the one-, two-, and three-molecule activated complexes are 61.7, 35.6, and 19.3 kcal/mole, respectively.

There are also water-assisted transition states for the decomposition of formic acid to CO<sub>2</sub> and H<sub>2</sub>. The activation energies of these structures are significantly lower than the calculated 64 kcal/mole for the unassisted unimolecular decomposition. A complex including a single additional water molecule is shown in Fig. 6.1 (bottom). Note that in this case, analogous to the formation of formic acid, the two hydrogen atoms that form the product hydrogen molecule do not both come from formic acid but one of the hydrogen atoms originates from the additional water molecule.

The proposed detailed structure of the transition state provides the means to calculate the thermodynamics of the reactants, transition state, and products in the supercritical fluid over a range of temperature and pressure conditions, leading to qualitative predictions of the variation in reaction rate with these state variables. The calculations implicitly explored the effect of neighboring water molecules on the overall system's thermodynamics using a Peng-Robinson equation of state (EOS) for dilute mixtures,

$$P = RT/(v-b) - a/(v^2 - 2bv - b^2). \quad (6.2)$$

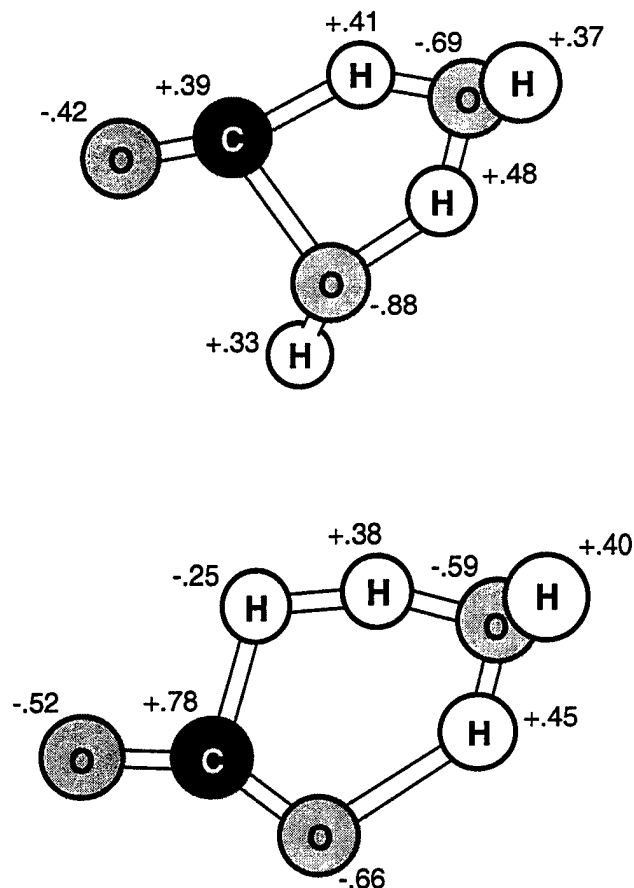


Figure 6.1. Transition state geometries and charge distributions for  $\text{CO} + 2\text{H}_2\text{O}$  (top), and  $\text{HCOOH} + \text{H}_2\text{O}$  (bottom) from Melius and coworkers.

Individual species' critical properties  $T_c$ ,  $V_c$ , and acentric factors for the transition state complexes were estimated using some simple rules and analogy to similar-sized species with similar dipole moments and atomic charge distributions. These were combined using the corresponding states mixing rules to yield the  $a$  and  $b$  parameters in Eq. 6.2. This equation of state for water, with a dilute concentration of solute, provided the partial molar departure functions,  $\mu_i^D$ , that represent the change in the molar Gibbs energy due to non-ideal dense gas effects. These were then used to calculate the partial molar volume of activation,  $\Delta v^\ddagger$ , for the formation of the transition states described above,  $[\text{CO}+n\text{H}_2\text{O}]^*$ , through the relationship

$$\Delta v^\ddagger = RT(\partial \Delta G^\ddagger / \partial P). \quad (6.3)$$

In the thermodynamic formulation of transition state theory, the rate constant,  $k$ , is expressed as

$$k = (k_b T / h) v^{\Delta v} \exp(-\Delta G^\ddagger / RT) \quad (6.4)$$

where  $v$  is the molar volume;  $\Delta G^\ddagger$  is the difference in the Gibbs free energy between the reactants and the transition state complex;  $\Delta v$  is the change in the molecularity to form the activated complex; and  $k_b$ ,  $h$ , and  $R$  are Boltzmann's, Planck's, and gas constants. This leads to an approximate expression for the pressure dependence of a reaction (omitting possible diffusional pressure effects and the linear temperature term in the preexponential factor) as

$$\partial(\ln k)/\partial P \approx -\Delta v^\ddagger/RT, \quad (6.5)$$

where  $\Delta v^\ddagger$  is the volume of activation. For our analysis, the rate constant,  $k$ , is psuedo first-order in CO conversion with units  $s^{-1}$ .

By examining the magnitude of the pressure dependence of a reaction, Eq. 6.5 yields information about transition state structure. Melius and coworkers found large negative volumes of activation ( $\approx -1100 \text{ cm}^3/\text{mol}$ ) associated with the polar nature of the structures in Figure 6.1 at densities near the critical density of water. They calculated that at gas-like densities ( $< 5.0 \text{ mol/l}$ ) and again at liquid densities ( $\sim 50 \text{ mol/l}$ ) the magnitudes of  $\Delta v^\ddagger$  and therefore  $\partial(\ln k)/\partial P$  to be much smaller.

### 6.2.2 Experimental Results

Fig. 6.2 shows the results of kinetics experiments conducted for a range of total pressures at  $450^\circ\text{C}$ . The measurements were conducted in the SCVR and consisted of monitoring the concentration of CO in an initial mixture of CO and supercritical water using Raman spectroscopy. Attempts to fit the higher pressure data to a first-order expression were generally successful. However, the data, especially at lower pressure ( $< 35 \text{ MPa}$ ), show initially a faster reaction rate, consuming about 10-20% of the CO, followed by a rate that is slower by as much as a factor of two.

The initial rapid disappearance of CO at lower pressures indicates that the reaction mechanism is more complicated than a simple first-order process. In fact, the model presented by Melius suggests that the two steps, formation and decomposition of formic acid, may have comparable rate constants. At higher pressures, the carbon balances are generally good (within the approximately  $\pm 5\%$  measurement accuracy), while at lower pressures there is a deficit of carbon (as much as 20%) for early times as measured by the sum of the CO and  $\text{CO}_2$  concentrations. However, no intermediates have been spectroscopically identified. We attempted to measure directly the decomposition of formic acid in supercritical water in this temperature and pressure range and found that complete conversion to  $\text{CO}_2$  occurred within 10 s; the same timescale associated with reactant injection into the SCVR. Since no intermediates could be observed and carbon balances were generally good, especially at the higher pressures most relevant to this work, the evidence suggests that the rate-limiting step in this two-step model is the formation of formic acid and not the subsequent decomposition to  $\text{H}_2$  and  $\text{CO}_2$ .

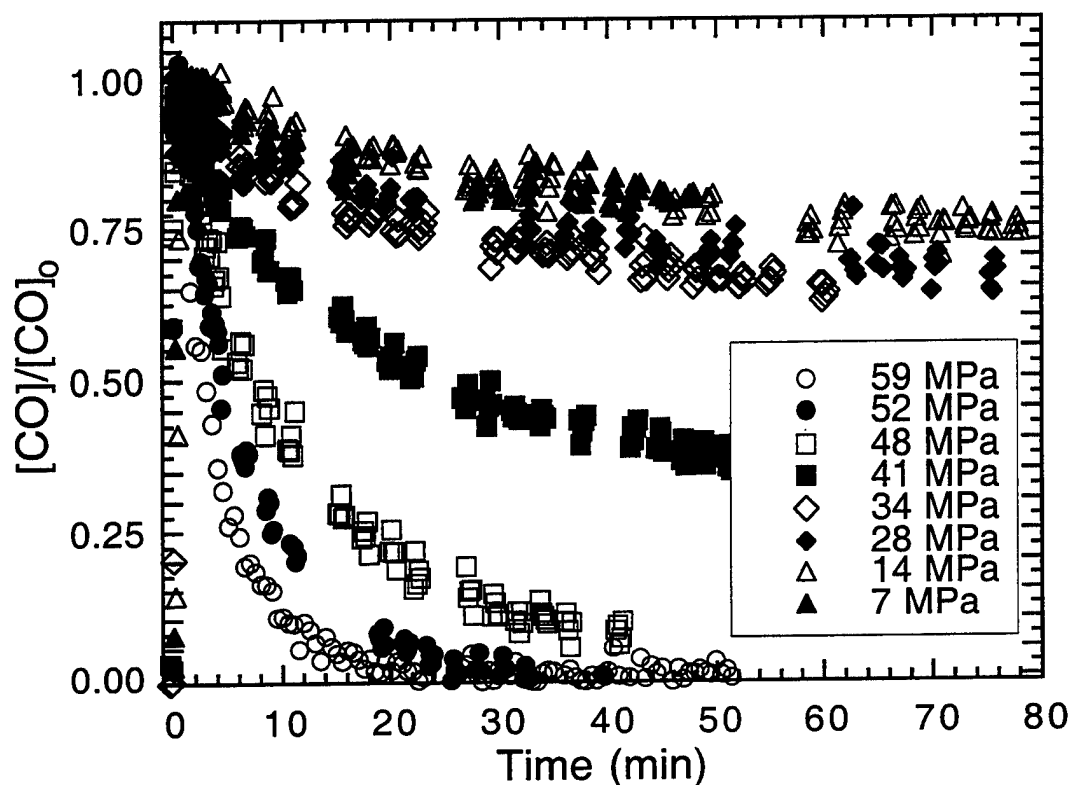


Figure 6.2. Observed concentration of CO reacting in supercritical water in the SCVR at 450 °C for a range of pressures. All the data were recorded with an initial CO concentration of approximately 0.15 mol/l in H<sub>2</sub>O.

For analysis purposes, we have chosen to discard the early data points in the lower-pressure measurements and fit a first-order reaction rate to the subsequent later-time data. However, this is the primary source of error in the subsequent development. All of the experiments produced at least some variation in the fitted rate constant depending on the length of time discarded at beginning of the reaction or the duration of the individual data run. Although the statistical error in the fits was typically less than 3%, the lack of precise first order kinetics produces considerable scatter in the data.

Fig. 6.3 shows a plot of our complete set of measurements evaluated using first-order rate constants,  $k_{\text{eff}}$ , expressed as

$$d[\text{CO}]/dt = -k_{\text{eff}}[\text{CO}] \quad (6.6)$$

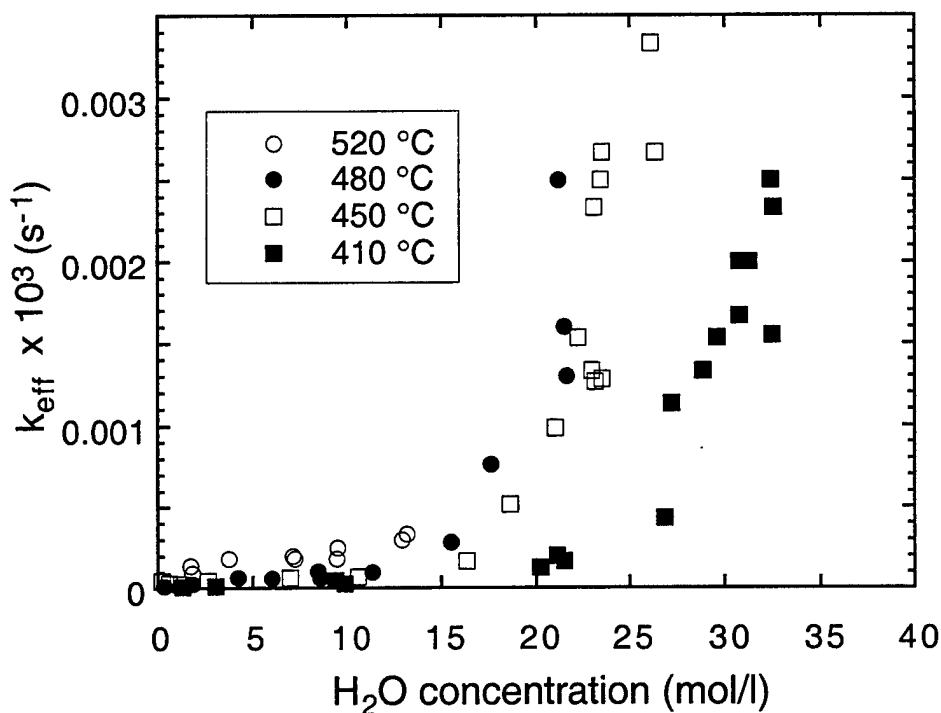


Figure 6.3 CO conversion rate constants vs. water concentration at four experimental temperatures in the SCVR.

Evaluating the Arrhenius expression for  $k_{\text{eff}}$ ,

$$k_{\text{eff}} = A \exp(-E_a/RT) \quad (6.7)$$

at a water concentration of 20 mol/l, for instance, produces  $A = 10^{7.22 \pm 2.6} \text{ s}^{-1}$  and  $E_a = 34.7 \pm 8.6 \text{ kcal/mol}$ . This effective activation energy agrees well with the water-assisted activation energy for the transition state shown in Figure 6.1 and obtained in the calculation. However, as is pointed out by Melius, there are competing effects in this system as temperature is raised. In addition to water's direct role in the activated complexes in Figure 6.1, significant stabilization can originate from the structure of surrounding water molecules.

The model presented by Melius predicts that the  $\Delta v^\ddagger$  of this reaction varies greatly with the density of the supercritical fluid. At conditions near the critical density (29.5 MPa, 427 °C,  $\rho=0.19 \text{ g/cm}^3$ , for example), the  $\Delta v^\ddagger$  is calculated to be  $-1178 \text{ cm}^3/\text{mol}$  for the transition state in Figure 6.1 (top). This is much greater than typical liquid-like values for known pressure-dependent reactions (no greater than  $-50 \text{ cm}^3/\text{mol}$ ). At low density, where an ideal-gas equation of state is adequate, only a small  $\Delta v^\ddagger$  is predicted.



Likewise, at higher pressure and near liquid conditions, (98.6 MPa, 427 °C  $\rho=0.65 \text{ g/cm}^3$ ) a modest value of  $-119 \text{ cm}^3/\text{mol}$  is predicted.

Figure 6.4 shows the data in Figure 6.3 plotted vs. pressure. The widest density range belongs to the set at 410 °C, which extends to  $0.6 \text{ g/cm}^3$ . The slope of the curve goes through a maximum at about 36 MPa. Fitting the 20 - 50 MPa range to a line, we obtain  $\partial(\ln k)/\partial P = 0.2 \pm 0.02 \text{ MPa}^{-1}$ . Inserting this into Eq. 6.5 results in a value of  $\Delta v^\ddagger = -1135 \text{ cm}^3/\text{mol}$ . Note that at higher density the slope decreases. This is in excellent agreement with the model's prediction. The higher temperature curves at 450 °C and at 480 °C begin to show an increase in the rate with pressure at higher total pressures, with all three curves exhibiting this behavior near the critical density.

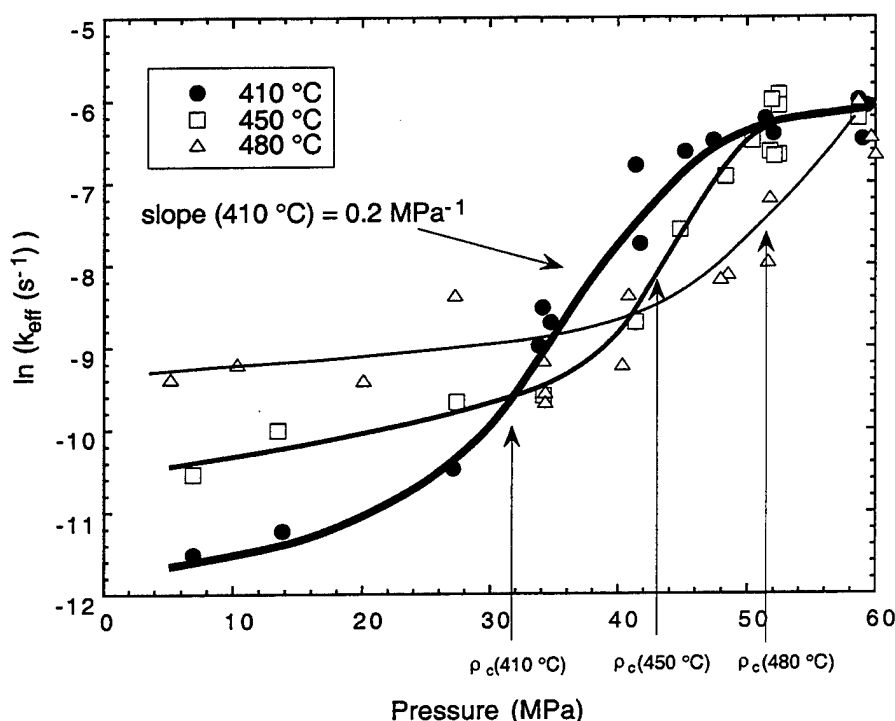


Figure 6.4 Pressure dependence of the rate constant at 410 °C, 450 °C, and 480 °C. The fit to the steepest part of the data at 410 °C is centered at approximately 36 MPa,  $\rho = 0.42 \text{ g/cm}^3$ .

### 6.2.3 Interpretation

Debenedetti and co-workers<sup>8,9</sup> created a classification scheme for solutes in supercritical fluids describing them as repulsive, weakly attractive, or attractive, based on the strength of the solute-solvent interaction. The relationship

$$v_2^\infty \rho = \rho RT\beta - \xi_c \quad (6.8)$$

was developed and provides an explicit form to connect the infinite dilution solute partial molar volumes to Eckert's clustering concept. Here,  $v_2^\infty$  is the partial molar volume of the solute at infinite dilution and  $\beta$  is the solvent isothermal compressibility,  $-(1/v)(\partial v/\partial P)_T$ . In this expression,  $\xi_c$  is a cluster number, defined as the excess number of solvent molecules (relative to the bulk density) surrounding an infinitely dilute solute molecule.

Since the infinite dilution partial molar volume of activation,  $\Delta v^\ddagger$ , is the difference of the partial molar volumes of the transition state and the reactants, Eq. 6.8 becomes

$$\Delta v^\ddagger \rho = \rho (v_{ts}^\infty - v_{co}^\infty) = \xi_{co} - \xi_{ts} \quad (6.9)$$

for the reaction considered here where  $\xi_{co} - \xi_{ts}$  is the change in cluster number from separated reactants and that of the transition state.

Extending these data to a measurement of the local density surrounding the transition state requires the application of Eq. 6.9, which in turn relies on obtaining an estimate of  $\xi_{co}$ . At this stage, since there is no PVT data available for CO in supercritical water, we are forced to use nitrogen data to obtain an estimate of CO partial molar volumes in supercritical water. This is done with some reservation since CO does have a small dipole moment and is not likely to be as repulsive as  $N_2$ . For instance, in the EOS used by Melius at 300 atm and 700 K  $v_{co}^\infty = +585 \text{ mol/cm}^3$  and the results from Gallagher and coworkers<sup>10</sup> for nitrogen is  $+673 \text{ mol/cm}^3$  at 30 MPa and 700 K. Inserting the experimental  $\Delta v^\ddagger$  above at 36 MPa and 410 °C into Eq. 6.9 yields,  $\xi_{ts} = 15.5$ . This was obtained using a rough estimate of  $\xi_{co} = -9.2$  derived from  $v_{co}^\infty(680 \text{ K}, 36 \text{ MPa}) = 500 \text{ mol/cm}^3$ . At 480 °C, the maximum slope in Figure 6.4 is approximately  $0.15 \text{ MPa}^{-1}$  at 50 MPa and  $\Delta v^\ddagger = -935 \text{ cm}^3/\text{mol}$ . With  $v_{co}^\infty(750 \text{ K}, 50 \text{ MPa}) \leq 360 \text{ mol/cm}^3$  (from NIST Tables for nitrogen<sup>10</sup>) we obtain  $\xi_{co} \geq -4.4$ , such that  $\xi_{ts} \leq 11.1$ . Expressing this as an upper limit results from the estimate of  $v_{co}^\infty \leq 360 \text{ mol/cm}^3$  as an upper limit for CO. Thus, the clustering is beginning to break down away from  $T_c$  but still remains persistent at  $T_r=1.15$ .

The large negative volume of activation near water's critical density shows the profound effect that the clustering of a supercritical fluid can have on reaction rates, where there is the possibility of activated complexes with electronic structure characteristics very different from the reactants. The data are consistent with a mechanism having a very polar transition state with many water molecules collapsing to solvate it. At higher densities, above the critical density, the fluid approaches liquid density, where there is less of a volume change associated with the transition state.

In the thermodynamic interpretation of activated complex theory, the empirical activation energy,  $E_a$ , determined above to be  $34.7 \text{ kcal/mol}$ , can be interpreted as  $\Delta H^\ddagger$  from

$$k_f = k_b T / h \exp(-\Delta G^\ddagger / RT) \quad (6.10)$$

and

$$\Delta G^\ddagger = \Delta H^\ddagger - T\Delta S^\ddagger = \Delta E^\ddagger + P\Delta V^\ddagger - T\Delta S^\ddagger \quad (6.11)$$

where  $\Delta G^\ddagger$ ,  $\Delta H^\ddagger$ ,  $\Delta S^\ddagger$ ,  $\Delta E^\ddagger$ , and  $\Delta V^\ddagger$  are the thermodynamic quantities of activation for free energy, enthalpy, entropy, internal energy, and volume. The observed  $E_a$  of 34.7 kcal/mol is composed of the  $P\Delta V^\ddagger$  term and the gas phase term from the *ab initio* calculations where  $P\Delta V^\ddagger$  equals approximately - 10 kcal/mol at 40 MPa and  $\Delta V^\ddagger = - 1 \times 10^3 \text{ cm}^3/\text{mol}$ . This results in an energy of activation,  $\Delta E^\ddagger$ , of about 25 kcal/mol, which is in the neighborhood of the *ab initio* values calculated by Melius for one and two additional water molecules in the activated complex for the formation of formic acid.

#### 6.2.4 Summary

The results from the experimental work presented in this section on the water-gas shift reaction in supercritical water show that a modest increase in operating temperature and an increase in system pressure to 60 MPa produces conversion rates that are significantly accelerated from the low pressure homogeneous rate. The analysis of these data within the context of the Melius model suggests that densities approaching the critical density of water afford a change in the energetics of the homogenous water-gas shift mechanism that results in greatly increased conversion rates in a catalyst-free environment. The experimental parameters describing this change in energetics are in good agreement with the model. The interpretation of these data within the context of an increase in the local density of the supercritical solvent is in good agreement with the view that significant clustering can occur at temperatures significantly higher than  $T_c$ . The data support the theoretical prediction of the existence of a polar transition state complex that is characterized by an unusually large negative volume of activation that results from a dramatic change in the local density of the supercritical fluid.

However, significant effects of water on the transition state do not appear until the density of the mixture approaches the critical density of water ( $\sim 0.3 \text{ g/cm}^3$ ). This density is a factor of three or four higher than has been typically proposed for SCWO systems. Thus, these data suggest that SCWO kinetics at the elementary reaction level at processing conditions found in actual waste treatment systems will not be affected dramatically by the presence of water.

### 6.3 Validity of the Binary Collision Approximation in Supercritical Water

#### 6.3.1 Background

Over the past 20 years, there has been considerable interest in  $\text{H}_2$ ,  $\text{D}_2$ , and HD as probes of intermolecular interactions with a focus on the changes in Raman linewidths as a function of fluid density in foreign gases. The motivation for such an investigation in this project originated from the need to address a fundamental question regarding the basic physics of solvent-solute intermolecular interactions. This section explores the J dependence of the Raman linewidths of  $\text{H}_2$  in supercritical water within the context of

an exponential gap law (EGL) that describes the rate of J-changing collisions. Combining this analysis with several assumptions regarding the vibrational-level dependence of the various line broadening mechanisms, significant differences in the nature of the collisional processes are revealed for CO<sub>2</sub> and H<sub>2</sub>O with a simple solute, molecular hydrogen, at comparable concentrations. The data obtained in supercritical water reveal qualitative information in the form of a deviation from linear density dependence at high fluid concentrations that indicate the onset of conditions characteristic of a collisional environment that is not well represented by a binary collision approximation.

The identification of this regime points to where simple elementary reaction kinetics derived from gas phase data may be no longer appropriate. Clearly, at fluid densities when collisional conditions are such that individual molecular interactions are no longer simply binary in nature and the reaction dynamics are affected by the presence of additional solvent molecules, we would expect that the direct extrapolation of low density kinetic parameters would be erroneous.

A Lorentzian lineshape is expected for Raman lines under binary collision conditions. This should be the case in this work at the lower densities examined typical of ambient pressure gas phase reactions, but may not be appropriate at the higher densities presented here. The Lorentzian linewidth, expressed as a Full Width at Half Maximum (FWHM), is expected to be proportional to density within the binary collision approximation (BCA):

$$\Gamma \text{ (FWHM)} = 2\rho\gamma, \quad (6.12)$$

where  $\gamma$  is the linear broadening coefficient. The BCA is typically valid when  $(N/V)d^3 \ll 1$ , where  $N/V$  is the number density and  $d$  is approximately the collisional diameter of the molecules. For these molecules and experimental conditions, this should hold up to about 5 mol/L, or about 1/10 the density of liquid water. If water has any special clustering properties at lower densities which are characteristic of SCWO conditions, deviations from linearity as a function of density would be expected.

### 6.3.2 Results – Q-branch and S-branch in water

Figure 6.5 shows the changes in the Raman  $\Delta v=1$  Q-branch of H<sub>2</sub> as a function of pressure in gaseous high-pressure steam and supercritical water at 450 °C. There is clearly measurable broadening at pressures as low as 5 MPa. At higher pressures of water, the spectrum loses the structure of individual lines and appears as a single band, typical of a gas dissolved in a liquid. Note too, that the individual Raman lines shift in position as the water density is increased.

Figure 6.6 shows the evolution of the linewidths of the Q(1) - Q(5) lines. On the abscissa, density is the total molar density for the mixture of hydrogen and water. Note that the broadening does not vary uniformly as a function of J. We have also examined the line broadening of the "pure rotational"  $\Delta v=0$  S-branch. Figure 6.7 shows the linewidths for all of the S-branch lines that were measured. Again, the low-J lines

broaden with pressure at a greater rate than the high-J lines. However, there is no alternation in the J-dependence as is seen in the Q-branch. That is, the decrease in the broadening coefficient is monotonic in J.

At lower densities, the density dependence is linear with that of the buffer gas. However, as the total density approaches approximately one third of water's critical density ( $\rho_c = 17.4$  mole/L) the broadening begins to be less sensitive to the buffer density. The effect is more pronounced at low J and appears in both the S-branch and the Q-branch. Although this does not provide definitive evidence of a breakdown in the binary collision approximation, it does illustrate that there is a change in the origin of the line broadening.

For the most part, the differences in slope for the various rotational lines as a function of pressure is reduced for both the S- and Q-branches. However, there is a notable exception. It appears that the broadening increases for Q(4) and S(2). Both of these transitions have J=4 as the upper state. The energy differences between J=4 and its neighboring levels, J=6 and 8 are  $1244\text{ cm}^{-1}$  and  $2878\text{ cm}^{-1}$ . These have no close resonance with a mode of the water molecule itself, since the bending frequency of water is  $1592\text{ cm}^{-1}$  and the symmetric and antisymmetric stretches are  $3651\text{ cm}^{-1}$  and  $3151\text{ cm}^{-1}$  respectively. However, it may be near a somewhat lowered bending or stretching frequency of a hydrogen-bonded water structure that is formed surrounding the hydrogen molecule. A resonance could provide for a rotation-to-vibration transfer and contribute to significant broadening.

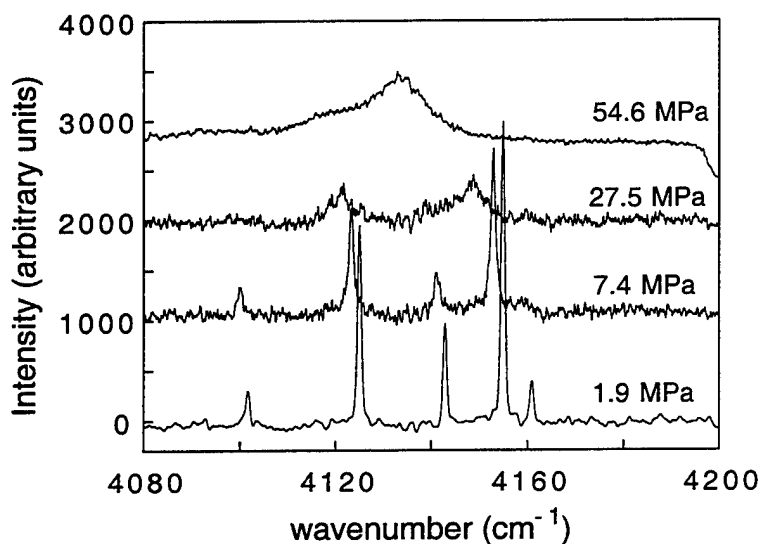


Figure 6.5 Raman spectrum of the  $\Delta v=1$  Q-branch of hydrogen as a function of system pressure generated by the addition of water vapor in the supercritical constant volume reactor. The individual spectra recorded at different pressure are arbitrarily offset for clarity.

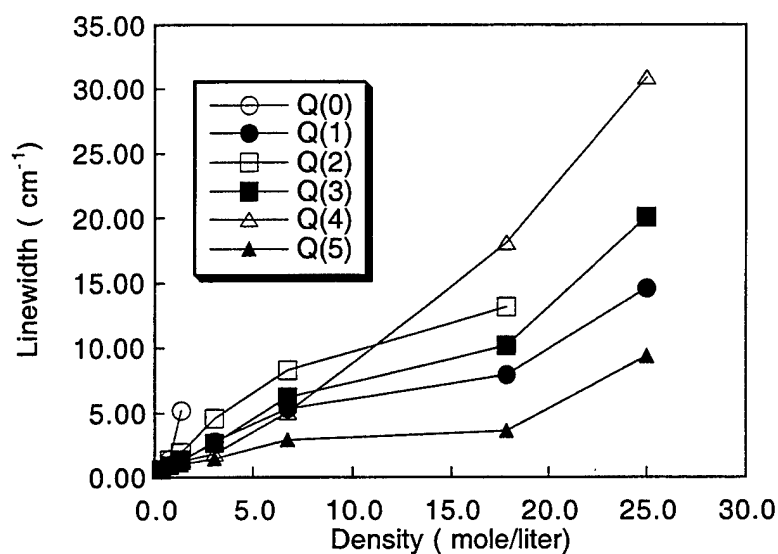


Figure 6.6 Experimental linewidths of the  $\Delta v=1$  Q-branch of hydrogen as a function of water density at 450 °C in supercritical water and high-pressure steam. Pressure ranges from 0.2-60 MPa.

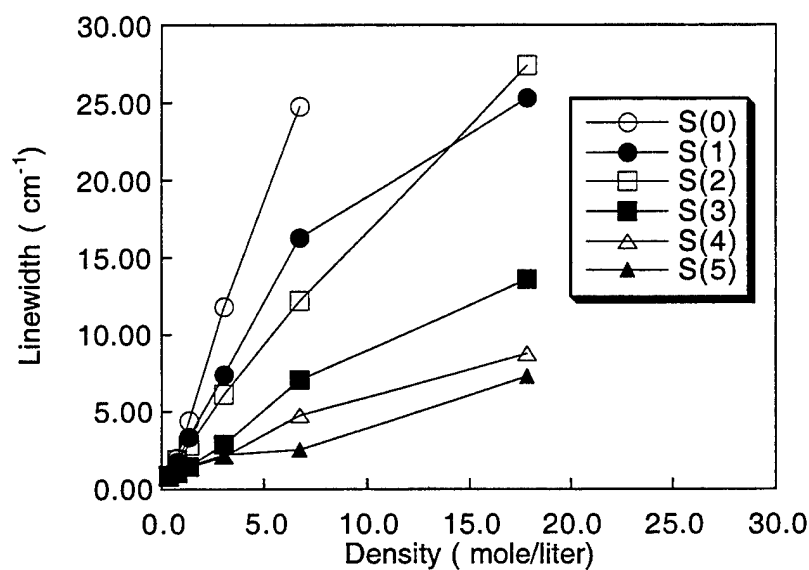


Figure 6.7 Density dependence of the pure rotational S-branch of molecular hydrogen in supercritical water.

### 6.3.3 Summary

We have experimentally measured changes in the Q-branch Raman lines of H<sub>2</sub> over a wide range of density in both supercritical water and supercritical CO<sub>2</sub> (not reported here). Our data illustrate several significant differences in the origin of the H<sub>2</sub> pure rotational S-branch and the  $\Delta v=1$  Q-branch broadening in high-pressure supercritical water and carbon dioxide. An analysis of the broadening trends as a function of density and rotational quanta show that these two media affect the rotational energy transfer differently. Aside from these specifics, we have found qualitative information in the deviation from linear density dependence that suggests the onset of a collisional environment that is not well represented by a single independent collision approximation. However, the pressure dependence of the H<sub>2</sub> linewidth indicates that at the density of SCW that is important to waste processing applications (<5 mole/liter) the nature of collisions is consistent with a gas phase single independent collision picture.

The results of the measurements on the H<sub>2</sub> linewidths support the findings from the water-gas shift reaction measurements. That is, the collisional and energy transfer environment in supercritical water at densities near or below 0.1 g/cc is that of a simple dense gas. Water has no apparent role in creating any unusual solvent sphere that would serve to affect oxidation reactions either by accelerating them or slowing them.

### 6.4 References

1. M. Modell, R.C. Reid, S.I. Amin "Gasification process" U.S. Patent No. 4113446, 1978.
2. M. Modell "Processing Methods for the Oxidation of Organics in Supercritical Water" U.S. Patent No 4338199, 1982.
3. M. Modell "Processing Methods for the Oxidation of Organics in Supercritical Water" U.S. Patent No 4543190, 1985.
4. E.U. Franck "Supercritical Water" *Endeavor*, **27**, 55-60, 1968.
5. E.U. Franck "Water and Aqueous Solutions at High Pressures and Temperatures" *Pure Appl. Chem.* **24**, 13-30, 1970.
6. E.U. Franck "Physiochemical Properties of Supercritical Solvents" *Ber. Bunsenges. Phys. Chem.* **88**, 820-825, 1984.
7. C. F. Melius, N. E. Bergan, J. E. Shepherd "Effects of Water on Combustion Kinetics at High Pressure", *Proceeding of the Twenty-Third Symposium (International) on Combustion*, Orleans, France, pp. 217-223, 1990.
8. P.G. Debenedetti "Clustering in Dilute, Binary Supercritical Mixtures : A Fluctuation Analysis" *Chemical Engineering Science* **42**, 2203-2212, 1987.

9. P.G. Debenedetti, R.S. Mohamed "Attractive, Weakly Attractive, and Repulsive Near-Critical Systems" *J. Chem. Phys.* **90**, 4528-4536, 1989.
10. Gallagher, J. S., Levelt Sengers, J. M. H., Abdulagatov, I. M., Watson, J. T. R., Fenghour, A. "Thermodynamic Properties of Homogeneous Mixtures of Nitrogen and Water from 440 to 1000 K, up to 100 MPa and 0.8 mole fraction N<sub>2</sub>" NIST Report #1404, 1993.



This page intentionally left blank

## Section 7: Large molecules

### 7.1 Overview

#### 7.1.1 Introduction

The success of the small molecule work described in Sections 3-6 is the core of the work in this project. These results lead to the key conclusion that combustion-like chemical mechanisms are appropriate to describe SCWO kinetics. Given this insight, scaled-back experimental probes of larger systems, which are prohibitively complex to model explicitly, can lead to a sufficiently general understanding of conversion rates and intermediates to complete an engineering model for novel reactor development. The key component of generalizing the small molecule picture is to have a semi-quantitative view of how aliphatic chains are reduced in length and converted to  $\text{CO}_2$  and how aromatic ring-opening occurs at SCWO conditions. Therefore, much of what is needed to describe large systems can be obtained by understanding ethanol and the simplest aromatics, benzene and phenol.

The details of ethanol reaction kinetics in supercritical water oxidation systems are important for several reasons. First, an understanding of ethanol kinetics can provide a link between the now well-established methanol reaction pathways and empirical models of higher alcohols, alkanes, and aromatics for which some quantitative data are now available. A second reason is that because ethanol is among the more reactive species to have been examined to date, it is well suited as an initiating fuel for autothermal reactor designs. In addition, low-grade ethanol is inexpensive and therefore can result in significant operational savings as a feed supplement for SCWO applications for wastes that have low heating values. Lastly, simple alcohols present a good test system for examining the effect of a small amount of a reactive compound on the overall conversion rate of kinetically robust species such as halogenated aromatics and nerve agent components such as alkyl phosphonates. Ethanol may prove to be an important additive to the waste feed in treatment systems designed for these applications.

In addition, we have conducted a number of experiments on n-propanol and isopropanol to extend the large molecule picture past ethanol. By building from C1 up to C3 systems, this work on alcohol oxidation has resulted in a fairly clear picture of how aliphatic chains are broken down into C1 species such as methanol and formaldehyde. In essence, we have developed a small set of generic reactions that represent the typical oxidation path for carbon chains.

The supercritical water work conducted on the aromatics was done at MIT and the gas phase work exploring the reactivity of the phenoxy radical,  $\text{C}_6\text{H}_5\text{O}$ , was conducted at Princeton University. The gas phase project was motivated by the supposition that benzene, and by analogy other aromatic species, would oxidize by way of  $\text{C}_6\text{H}_5\text{O}$  (phenoxy radical) and the rate determining reactions and subsequent production of product gases would be controlled by its chemistry. At the conclusion of this project

there is still debate surrounding the overall aromatic oxidation path and whether the gas phase results from the work in this project contains the answer to the unusual prompt formation of CO<sub>2</sub> during benzene oxidation. In essence, the project has produced two competing views of oxidation and ring opening of single rings aromatics in the 500–700 °C range.

As was first observed in the kinetics work by J. Tester's group at MIT, and as we have maintained from the onset of this project, the key to understanding the reaction rates of a wide variety of typical feed wastes for processing by SCWO lies in being able to predict the behavior of the "oxidizer side" of the chemistry. Reaction rates are controlled largely by the reactivity of the feed materials, not with molecular O<sub>2</sub>, but with HO<sub>2</sub>, RO<sub>2</sub>, and OH combined with the non-equilibrium concentrations of these species that are achieved during the overall reaction process. Because the oxidation kinetics of the mixture is largely controlled by the concentration of the oxidizer radicals, our models predict that kinetically robust species should be consumed at a much more rapid rate in the presence of a more reactive compounds than they would be otherwise at typically "low" temperatures. This assertion has important implications regarding the overall conversion rates of stable compounds such as aromatics. Furthermore, the ability to co-oxidize relatively unreactive feeds directly affects ideas being developed for more easily operated injection systems for SCWO applications.

#### 7.1.2 Papers and Reports

T.B. Hunter, S.F. Rice, R.G. Hanush "Raman Spectroscopic Measurement of Oxidation in Supercritical Water II. Conversion of Isopropanol to Acetone" *Ind. Eng. Chem. Res.* **35**, 3984-3990, 1996.

S.F. Rice, E. Croiset "Oxidation of Simple Alcohols in Supercritical Water III. Formation of Intermediates from Ethanol" *Ind. Eng. Chem. Res.* **40**, 86-93, 2001.

M. Pecullan, K. Brezinsky K, I. Glassman " Pyrolysis and Oxidation of Anisole near 1000 K" *J. Phys Chem. A* **101** 3305-3316, 1997.

M. Pecullan, K. Brezinsky, I. Glassman. "Pyrolysis and Oxidation of Phenol" *J. Phys Chem A* **102**, 8614-8619, 1998.

J.L. DiNaro, J.B. Howard, W.H. Green, J.W. Tester, J.W. Bozzelli, "Elementary Reaction Mechanism for Benzene Oxidation in Supercritical Water" *J. Phys Chem. A*, **104**, 10576-10586, 2000.

J.L DiNaro, J.W. Tester, J.B. Howard, K.C. Swallow "Experimental Measurements of Benzene Oxidation in Supercritical Water" *AIChE J.* **46**, 2274-2284, 2000.

## 7.2 Ethanol

### 7.2.1 Experimental measurements

Figure 7.1 shows the measured time dependence of the concentration of ethanol at four different reaction temperatures during oxidation by dissolved oxygen in supercritical water based on the intensity of a Raman band. Figure 7.1 also includes the results from the elementary reaction mechanism discussed later in this section. The data are plotted as normalized concentrations defined as the measured concentration of ethanol divided by the concentration in the initial feed. The conversion rate of ethanol is comparable to that of n-propanol, slower than that of methanol and isopropanol and much slower than methane at the same conditions. As a point of reference, n-propanol is 50% converted at 430 °C in 1.1 s, as is shown in the next sub-section, and ethanol appears to be 50% converted at 430 °C in 1.25 s. Isopropanol requires 1.6 s to be 50% converted at 430 °C and methanol requires more than 3.0 s for 50% conversion. Methane oxidation by oxygen requires approximately 6 minutes for comparable conversion at this concentration, temperature, pressure, and equivalence ratio in supercritical water.

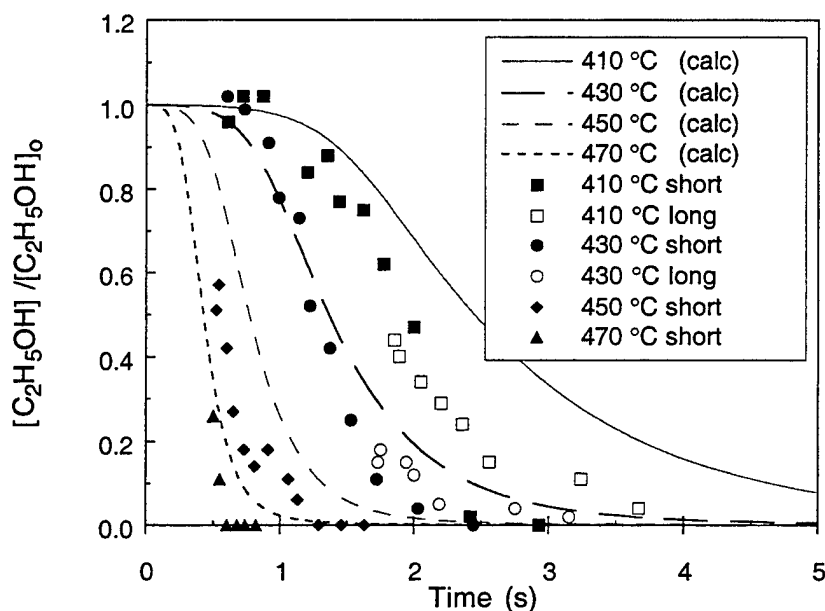


Figure 7.1 Experimental concentration of ethanol as a function of time and temperature with the results of the SENKIN calculation at the four experimental temperatures. The notations "long " and "short" refer to two positions (83.8 cm and 27.3 cm) of the Raman spectroscopic cell in the SFR. Note that there is good agreement between points recorded at similar reaction times at both high and low flow rates corresponding to the long and short detection positions.

Our earlier work had shown that formaldehyde is the only organic intermediate that is formed in appreciable concentration during methanol oxidation and only a small amount of hydrogen peroxide is accumulated. Our early work on the oxidation of isopropanol revealed that large amounts of acetone is the initial and dominant carbon-containing intermediate formed by the abstraction of the secondary hydrogen and subsequent loss of the hydroxyl hydrogen. This earlier work did not explore the presence of other intermediates; however, carbon balances determined in subsequent experiments reveal that only CO and CO<sub>2</sub> appreciably accumulate in the isopropanol system in addition to acetone. These data on isopropanol and results supporting the statements above on n-propanol oxidation rates are discussed in the next subsection. Here, the goal was to follow the concentration of all of the major carbon-containing species over the entire oxidation process to form a more complete picture for ethanol as a prototypical system.

Figure 7.2 shows the evolution of formaldehyde and methanol as a function of time and temperature in supercritical water in the SFR at the same conditions as shown in Figure 7.1. It is clear that a significant amount of formaldehyde is formed prior to methanol in this system, suggesting that there is a mechanistic route to formaldehyde in ethanol oxidation that does not include a step that first forms methanol. This indicates that although there are similarities in the fuel consumption profile for the higher alcohols relative to methanol, most notably an induction period followed by more rapid reaction, the reaction pathways are more complicated. Specifically, there are important C-C bond cleavage steps that can occur on the same timescale as H-atom abstraction. The C-C cleavage reactions effectively consume the organic chain fast enough that abstraction reactions cannot dominate all of the chemistry. The observation that solid carbon such as soot is not formed in SCWO can therefore be rationalized in terms of our mechanistic description.

### **7.2.2 Reaction mechanism**

In 1992, Norton and Dryer<sup>1</sup> developed an elementary reaction model for the oxidation of ethanol and compared the predictions of the model to experimental results in a flow reactor at approximately 820°C and atmospheric pressure. In that work, they establish the basis of a detailed mechanism and recognize that variation in the product spectrum depends on the site of initial hydrogen atom abstraction. Recently, Marinov<sup>2</sup> reported results using an elementary reaction mechanism to describe the oxidation of ethanol at high-temperature combustion conditions, including a careful quantitative assessment of the initial hydrogen abstraction rates by various reactive radicals including H, OH, HO<sub>2</sub>, and CH<sub>3</sub>. Both of these papers indicate that abstraction of the hydroxyl hydrogen atom results primarily in the production of formaldehyde and methyl radical as intermediates. Abstraction of one of the two secondary H atoms produces acetaldehyde and H atoms and abstraction of one of the three primary H atoms produces ethylene and OH radicals. In all cases, these reactions produce intermediates, having distinct structural differences from ethanol, that are easy to identify in the Raman spectra. The measurements presented here in supercritical water reflect the relative importance of these different pathways under SCWO conditions. By starting with the Marinov

mechanism, appropriately augmenting it to be suitable for SCWO conditions, and comparing with the data set, these details can be evaluated.

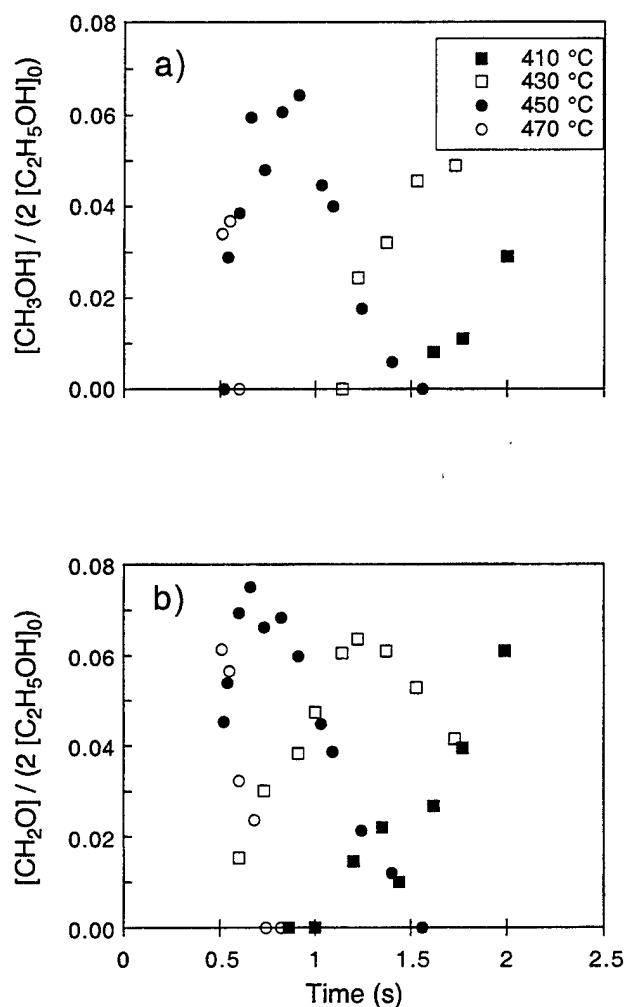


Figure 7.2. a) Evolution of methanol concentration as a function of time and temperature during the oxidation of ethanol at the same conditions as Figure 7.1. b) Evolution of formaldehyde concentration as a function of time and temperature during the oxidation of ethanol.

As a starting point, the predictions of the Marinov mechanism, left entirely unmodified, are compared with the experimental conversion of ethanol at 430 °C and 24.5 MPa. The calculation predicts a conversion rate of about a factor of three slower than observed. In addition, it shows the primary products of the reaction on this timescale to be CO and methane, which is contradictory to our experimental observations showing the primary intermediates are methanol, formaldehyde, and CO, with considerable amounts of CO<sub>2</sub> produced at later times. No methane is observed experimentally.

Note that Marinov's mechanism is designed to accommodate much higher temperature chemistry. Key reactions involving hydrogen peroxide and methylperoxyl radical are not incorporated, because reactions involving these species play no role at higher temperatures. Therefore, we have made six additions or modifications to the mechanism, including: 1) The  $\text{H}_2\text{O}_2$  decomposition rate is determined by experimental measurements at supercritical water conditions using a high-pressure limit with  $A = 2.28 \times 10^{13} \text{ s}^{-1}$ ,  $b = 0.00$ , and  $E_a = 43019 \text{ cal/mole}$  from Croiset et al.<sup>3</sup> 2) The  $\text{CH}_3\text{O}_2$  chemistry used by several authors for methane and methanol oxidation in supercritical water is included. 3) The direct reaction of  $\text{CH}_3$  with  $\text{H}_2\text{O}$  to form methanol and  $\text{H}$  is included from Brock and Savage.<sup>4</sup> 4) All the reactions identified as key reactions from the intermediate-temperature acetaldehyde oxidation reaction mechanism of Kaiser et al. are included that are not already considered by Marinov or in the  $\text{CH}_3\text{O}_2$  reactions in 2) above. 5) The  $\text{H}$ -abstraction reactions involving formic acid that are condensed in the original mechanism, are expanded to include  $\text{HOCO}$  as a distinct intermediate. The conversion reactions of  $\text{HOCO}$  to  $\text{CO}$  and  $\text{CO}_2$  are taken from Brock and coworkers.<sup>5</sup> 6) The kinetic parameters for the removal of hydrogen from formaldehyde to form  $\text{HCO}$  are updated to those recommended by Eiteneer et al.<sup>6</sup>

Included in Figure 7.1 are the results of the new mechanism comparing the conversion rate of ethanol over the temperature range examined. The agreement for conversion between the calculation and the experimental data is significantly improved by the changes in the mechanism relative to the results of the original mechanism. The ethanol conversion rate is near the observed rate and there is no significant production of methane. In addition, the final version of the mechanism represents well the observed rates of formation of both methanol and formaldehyde.

The primary reaction pathways of the major carbon containing species, as predicted by the elementary reaction mechanism at  $450^\circ\text{C}$ , are shown in Figure 7.3. The reactions noted by numbers on Figure 7.3 are listed in Table 7.1, where the relative carbon atom fluxes at the maximum ethanol conversion rate at  $t = 1.13 \text{ s}$  are listed. In Table 7.1, the total carbon flux is normalized to 1.0.

Most of the ethanol is converted by forming acetaldehyde from abstraction of the secondary hydrogen by  $\text{OH}$  and  $\text{HO}_2$  followed by removal of the hydroxyl hydrogen by oxygen to form  $\text{HO}_2$ . Some additional acetaldehyde is formed from the ethoxy radical that results from initial abstraction of the hydroxyl hydrogen. Acetaldehyde loses the aldehydic hydrogen to  $\text{HO}_2$  forming  $\text{H}_2\text{O}_2$  and  $\text{CH}_3\text{CO}$ , which decomposes to  $\text{CO}$  and  $\text{CH}_3$ . A secondary pathway originates with the abstraction of the hydroxyl hydrogen by  $\text{OH}$  to form ethoxy radical, which decomposes to form  $\text{CH}_3$  and formaldehyde. A minor pathway results from the abstraction of a primary hydrogen by  $\text{OH}$ , capture by  $\text{O}_2$  to form  $\text{HOC}_2\text{H}_4\text{O}_2$  which can undergo decomposition to form two formaldehyde molecules and  $\text{OH}$ . At this temperature, the formation of ethylene does not compete with capture by  $\text{O}_2$ . Thus, nearly all of the carbon is converted to  $\text{CO}$ ,  $\text{CH}_3$ , and  $\text{CH}_2\text{O}$ .

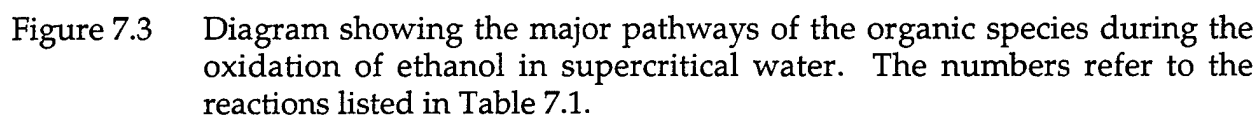




**Table 7.1. Key reactions and mole flux**

Reaction	Flux (mole fraction C)
1. $C_2H_5OH + HO_2 \Rightarrow CH_3CHOH + H_2O_2$	0.28
2. $C_2H_5OH + OH \Rightarrow CH_3CHOH + HO_2$	0.24
3. $C_2H_5OH + OH \Rightarrow CH_3CH_2O + HO_2$	0.33
4. $C_2H_5OH + OH \Rightarrow C_2H_4OH + HO_2$	0.13
5. $CH_3CHOH + O_2 \Rightarrow CH_3CHO + HO_2$	0.52
6. $CH_3CH_2O + M \Rightarrow CH_3CHO + H + M$	0.09
7. $CH_3CH_2O + M \Rightarrow CH_3 + CH_2O$	0.13
8. $C_2H_4OH + O_2 \Rightarrow HOC_2H_4O_2$	0.13
9. $HOC_2H_4O_2 \Rightarrow 2CH_2O + OH$	0.13
10. $CH_3CHO + HO_2 \Rightarrow CH_3CO + H_2O_2$	0.37
11. $CH_3CHO + HO_2 \Rightarrow HCOOH + CH_3$	0.09
12. $CH_3CO (+M) \Rightarrow CH_3 + CO$	0.36
13. $CH_3 + O_2 (+M) \Rightarrow CH_3O_2 (+M)$	0.33
14. $CH_3O_2 + H_2O_2 \Rightarrow CH_3O_2H + HO_2$	0.20
15. $CH_3O_2 + HO_2 \Rightarrow CH_3O + OH + O_2$	0.11
16. $CH_3O_2H \Rightarrow CH_3O + OH$	0.20
17. $CH_3O (+M) \Rightarrow CH_2O + H (+M)$	0.26
18. $CH_2O + OH \Rightarrow HCO + H_2O$	0.26
19. $CH_2O + HO_2 \Rightarrow HCO + H_2O_2$	0.21
20. $HCO + O_2 \Rightarrow CO + HO_2$	0.47
21. $HOCO + O_2 \Rightarrow CO_2 + HO_2$	0.02
22. $CH_3CO_2 (+M) \Rightarrow CO_2 + HO_2$	0.03

$CH_3$  is not identified in the system experimentally since the  $CH_3$  oxidation pathway in this temperature range proceeds through rapid formation of  $CH_3O_2$  and  $CH_3O_2H$  by association with  $O_2$  and subsequent hydrogen atom exchange with  $H_2O_2$ . Both of these species form  $CH_3O$ , which is mostly converted to  $CH_2O$ . Formaldehyde is converted to  $CO$  and  $CO_2$  as has been discussed in the methanol SCWO mechanism literature by a number of authors. Some of the  $CH_3O$  reacts with water,  $CH_3O_2H$ , acetaldehyde, or formaldehyde to form methanol, which accumulates in the system at early times until the supply of  $CH_3O$  begins to fall.

We conclude that the present model captures most of the important chemistry that we observe in our SCWO experiments. The greatest difference between the model and our

data is that the model predicts that methanol and formaldehyde are formed earlier in the reaction and slightly more methanol and slightly less formaldehyde is observed experimentally. This may be due to a greater reactivity of water in this unusual SCWO environment (e.g. via the reverse of the reaction  $\text{CH}_3\text{OH} + \text{OH} = \text{CH}_3\text{O} + \text{H}_2\text{O}$ ) than is provided in the mechanism. This is one of the main routes to the production of  $\text{CH}_3\text{OH}$  and would simultaneously slow the production of  $\text{CH}_2\text{O}$ , however, at this time we can only speculate that this may be the reason for this minor difference between the observations and the model.

The fact that the observed production rate of acetaldehyde is well matched by the model predictions suggests that the branching ratios for the hydrogen abstraction reactions in the original Marinov mechanism are appropriate for these conditions. Because of this good agreement, this work provides support for the quantitative accuracy of the Marinov rates of hydrogen abstraction by OH and  $\text{HO}_2$  at the hydroxyl, secondary, and primary sites during the oxidation of organics in supercritical water. In future SCWO-mechanism development, these rate parameters can be extended within the more complex schemes that have been proposed over the past decade to produce quantitative mechanisms for the oxidation of larger organic molecules.

It is widely held by many that an important and stable intermediate in SCWO is acetic acid. If this were the case, the oxidation of ethanol should probably form it. Acetic acid has strong Raman bands at  $892\text{ cm}^{-1}$  and  $2944\text{ cm}^{-1}$ . Unfortunately, the  $2944\text{ cm}^{-1}$  band is obscured by the second methanol band at the same position and the  $892\text{ cm}^{-1}$  band is indistinguishable from the ethanol  $890\text{ cm}^{-1}$  band. However, there is no persistent band at either position, at times when most of the ethanol has been consumed, but while there is still a large amount of organic carbon in the system, as evidenced by the presence of formaldehyde, methanol, and peroxide. In addition, the carbon balances are near unity. Thus, the data indicate that acetic acid is not formed during SCWO of ethanol in the temperature range that has been explored, but rather the radical chain mechanism as described above represents the oxidation path. This mechanism does not provide a path to acetic acid. These observations lead us to suggest that in SCWO of large organics, conversion proceeds through aldehydes and alkyl peroxides. Carbon chains are broken stepwise by reactions analogous to Reaction 13 in Table 7.1 and not by the formation of carboxylic acids.

### 7.2.3 Conclusions

*In situ* Raman spectroscopic measurements are used to identify all of the major carbon-containing species present during the oxidation of ethanol by oxygen in supercritical water. Overall conversion rates of ethanol to products are predicted by a detailed elementary reaction mechanism, which also predicts many of the quantitative measurements of the formation and consumption of intermediates. The model predictions show that the primary carbon-carbon bond cleavage route involves the formation of acetaldehyde that subsequently forms CO and  $\text{CH}_3$  following abstraction of the aldehydic hydrogen and decomposition of  $\text{CH}_3\text{CO}$ . It is possible that a generalization of these pathways can describe the oxidation of much more complicated species.

### 7.3 Isopropanol and n-propanol oxidation

#### 7.3.1 Experimental results

We have examined the kinetics of SCWO of isopropanol and n-propanol in a more cursory fashion than the analysis of ethanol oxidation. The main purpose was to identify the formation of acetone from isopropanol as the dominant first step and to determine that n-propanol oxidizes more similarly to ethanol. A secondary motivation was to explore the global reactivity of these inexpensive, yet reactive, solvents to be considered as potential fuels in pilot plant design options.

Figure 7.4a shows the loss of isopropanol as a function of temperature and time and Figure 7.4b shows the corresponding data for n-propanol. The figures show that the loss of n-propanol is slightly faster at a given temperature than the loss of isopropanol, such that comparable reactivity for n-propanol occurs about 20 °C lower than for isopropanol. This is only part of the picture, however.

Figure 7.5a and 7.5b show the fraction of the carbon in the system that exists as CO as a function of time and temperature during the oxidation of isopropanol and n-propanol and Figure 7.6a and 7.6b show corresponding fractions of CO<sub>2</sub>. In the case of n-propanol, much more of the initial reactant is converted to CO and CO<sub>2</sub> early in the reaction than is the case for isopropanol. For example, in the case of n-propanol at 430 °C and 1.0 seconds, 20% of the carbon exists as CO<sub>2</sub>, 40% exists as CO<sub>2</sub>, and the remaining 40% as n-propanol. At 2.0 seconds these values are 35%, 55%, and 10% respectively. For isopropanol these values are 0% CO<sub>2</sub> and CO and 80% isopropanol at 1.0 second and 10 % CO<sub>2</sub>, 15% CO, and 30% isopropanol, at 2.0 seconds. Much of the carbon during the oxidation of isopropanol exists as some other species, whereas in the case of n-propanol the route to CO and CO<sub>2</sub> is faster, with no apparent carbon-containing intermediate being accumulated.

Figure 7.7 shows the fraction of carbon existing as acetone in the oxidation of isopropanol at 430 °C is 20% at 1 s and 40 % at 2 seconds. The data show that in the case of isopropanol the formation of a stable ketone, acetone, will significantly slow the rate of conversion of organic to CO and CO<sub>2</sub>. The same trends are true over the entire temperature range that has been examined.

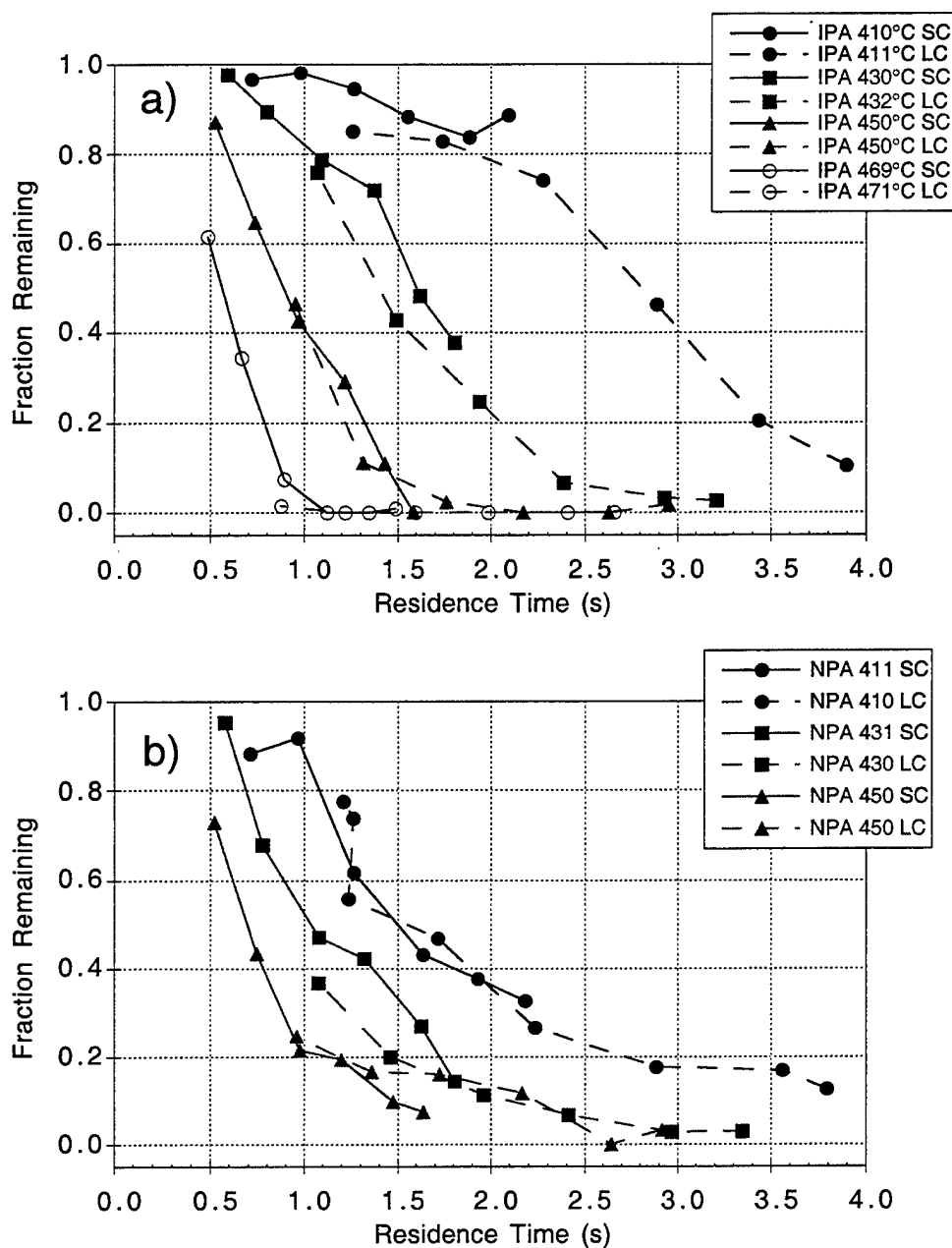


Figure 7.4 a) Oxidation of isopropanol by oxygen in supercritical water at four different temperatures at 25.0 MPa. The label on the ordinate, Fraction Remaining, refers to the fraction of feed isopropanol remaining at each measurement point (time) as detected by Raman spectroscopy. The "long" and "short" positions of the cell in the flow reactor are 44.5 cm (SC) and 81.3 cm (LC). The different residence times for fixed cell positions are obtained by varying the total flow rate. b) Oxidation of n-propanol by oxygen in supercritical water at three different temperatures at 25.0 MPa. The experimental methods were the same as used for isopropanol described above.

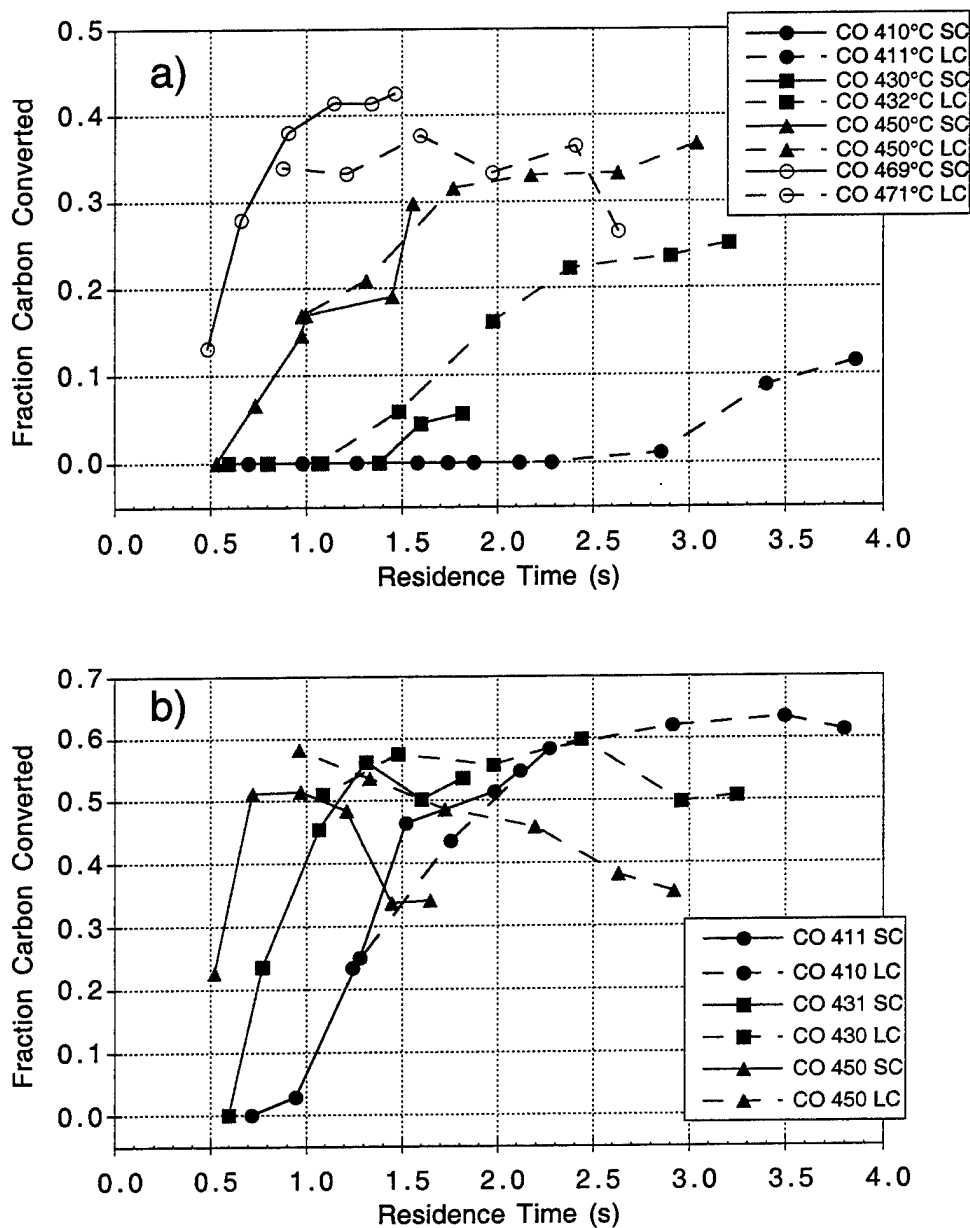


Figure 7.5. a) Production of CO during the oxidation of isopropanol in supercritical water at four different temperatures by oxygen at 25.0 MPa. Fraction Carbon converted refers to the molar fraction of initial feed alcohol that exists as CO. b) Production of CO during the oxidation of n-propanol in supercritical water at three different temperatures by oxygen at 25.0 MPa. The experimental methods were the same as for isopropanol described above.

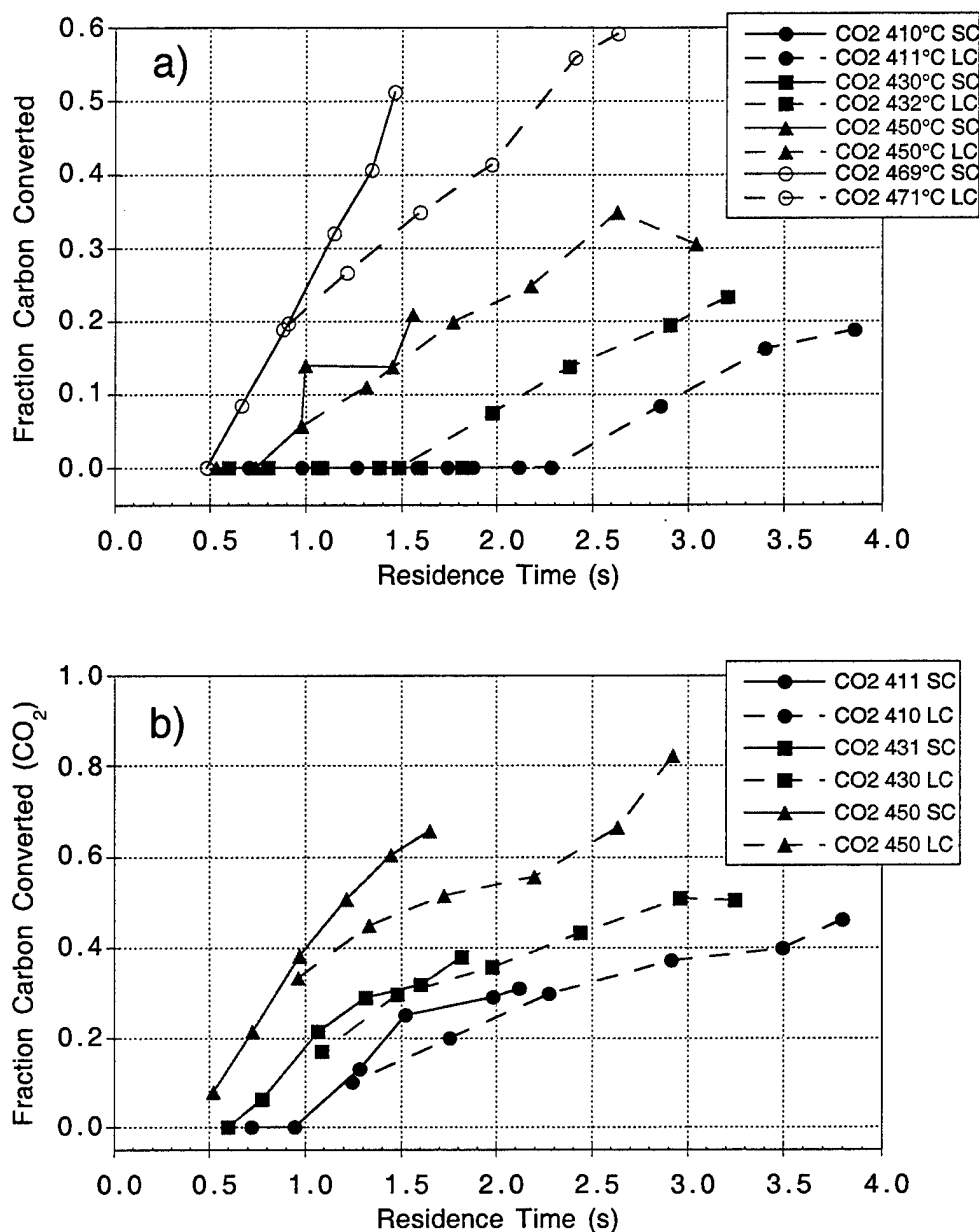


Figure 7.6. a) Production of  $\text{CO}_2$  during the oxidation of isopropanol in supercritical water at four different temperatures by oxygen at 25.0 MPa. Fraction Carbon converted refers to the molar fraction of initial feed alcohol that exists as  $\text{CO}_2$ . These data were recorded sequentially with the results in Figure 7.4 and 7.5. b) Production of  $\text{CO}_2$  during the oxidation of n-propanol in supercritical water at three different temperatures by oxygen at 25.0 MPa. The experimental methods were the same as for isopropanol described above.

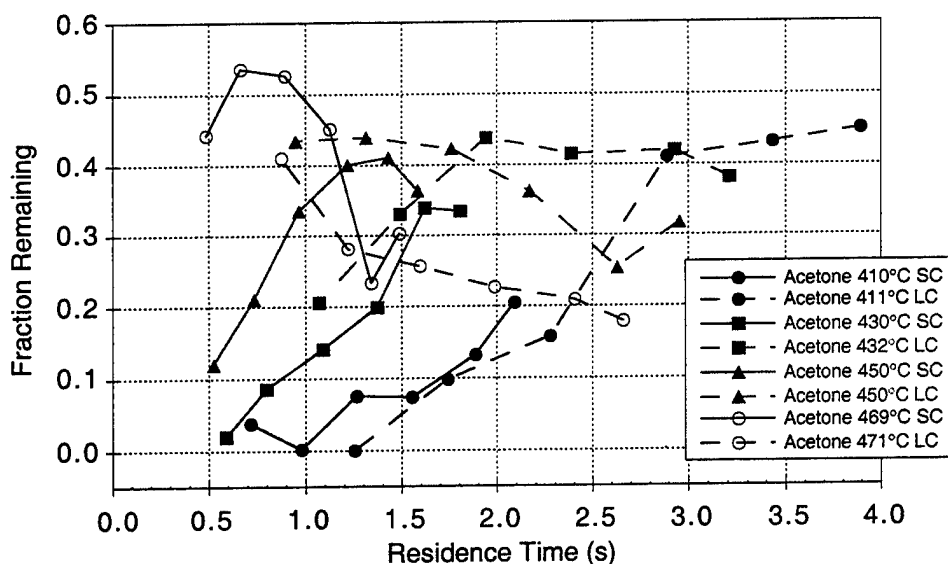
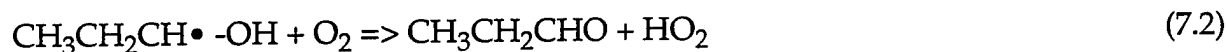


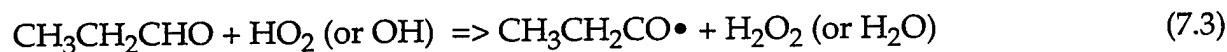
Figure 7.7. Production of acetone during the oxidation of isopropanol in supercritical water at four different temperatures by oxygen at 25.0 MPa. Fraction remaining refers to the molar fraction of initial feed isopropanol that exists as acetone. These data were recorded sequentially with the results in Figure 7.4a, 7.5a, and 7.6a.

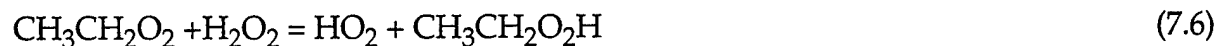
### 7.3.2 Summary of isopropanol and n-propanol oxidation

Although a great deal of data were collected on isopropanol and n-propanol the same level of mechanistic analysis was not done on these species as was completed on ethanol. It is likely that at least n-propanol oxidizes similarly to ethanol. The mechanism is dominated by the abstraction of the primary aliphatic hydrogen by  $\text{HO}_2$  and OH. Subsequent removal of the hydroxyl hydrogen produces the aldehyde.



The next step is the removal of the aldehydic hydrogen by the oxidizing radicals again and the formation of the ketyl radical that decomposes into CO and ethyl radical that is captured by  $\text{O}_2$ .





The ethyl peroxy radical then follows the type of chemistry that has been identified for methyl peroxy radical in the methane oxidation chemistry described in Section 4 and this section above (Section 7.2).  $\text{CH}_3\text{CH}_2\text{O}_2$  will lead to acetaldehyde and the carbon removal cycle in Eq. 7.4 is repeated.

The behavior of secondary alcohols is only a little different. Like isopropanol, this class of compounds will form ketones after an initial abstraction of the secondary H atom and in general be somewhat less reactive than primary alcohols that form aldehydes. However, the alpha hydrogen of the ketone has a lower bond strength than most C-H bonds and will be removed effectively by OH in the system. This radical is captured by  $\text{O}_2$  and is followed by reactions similar to 7.6, 7.7, and 7.8 which occur rapidly to form the unstable dicarbonyl which will cleave to form two ketyls. This scheme then joins the description above at reaction 7.4. The reaction sequence in Reactions 7.9 illustrates the path.



Alkane chemistry is also included in this scheme, by an initiating step of hydrogen abstraction and then joining in at reaction 7.5.

These results indicate that the path that we took to understand simple alcohols and methane has led to a generalized description that covers alcohols, ketones, aldehydes, and alkanes.

## 7.4 Aromatic systems - Phenol/Benzene

### 7.4.1 Background of aromatics in SCWO

A significant amount of the experimental effort in examining global reaction kinetics in SCWO worldwide has been focused on aromatic species. The systems that have been studied include chlorinated aromatics and substituted aromatics such as chlorobenzenes, a variety of phenols and cresols, nitro-substituted explosives and their precursors and even azo dyes. The main result of this extensive literature points to aromatics being among the most difficult of organics to oxidize in supercritical water. Most likely this is due to the necessity to initiate the radical chain branching required for rapid conversion, the reacting mixture needs to form the key oxidizing species such as  $\text{HO}_2$ ,  $\text{RO}_2$ , and OH. These species cannot be formed in adequate concentration until the aromatic ring opens to form a linear diene.



This was anticipated during the initial planning of this project and therefore an effort was conducted to contribute to the development of oxidation and pyrolysis models phenol and anisole (methoxyphenol) at intermediate temperatures. This work was conducted by the project collaborators at Princeton University. Simultaneously, a project was initiated at MIT to measure benzene oxidation in supercritical water and ultimately relate the SCWO kinetics to a well-understood gas-phase mechanism. This part of the project has been largely successful and follow-on work at MIT to produce a complete and extensive elementary reaction mechanism for benzene in supercritical water has been completed.

#### **7.4.2 Phenoxy radical reactivity from anisole**

This work is designed to develop a detailed model for the oxidation and pyrolysis chemistry of simple aromatics, phenol and anisole, as precursors to the phenoxy radical, at temperatures just below combustion conditions. It was conducted entirely at Princeton University. Unlike the case of methane and methanol, where acceptable elementary reaction schemes existed at combustion conditions, there were not reliable combustion mechanisms available to begin to modify for SCWO conditions at the beginning of this project.

Initially, species mole-fraction-versus-time profiles for intermediates formed during the high temperature, atmospheric pressure, gas phase pyrolysis and oxidation of anisole were obtained at Princeton.<sup>7</sup> This data set, spanning a range of stoichiometries (from  $\phi = 0.59$  to 1.62) at two temperatures (730 °C and 910 °C) served as the benchmark for investigation of the water-perturbed gas phase system. The reliability of the experimental data is evidenced by carbon balances within several percent and repeatability. Furthermore, the identities and relative quantities of observed reaction intermediates are consistent with the findings of other investigators.

These experimental measurements were conducted in a high-temperature, ambient-pressure flow reactor, specially configured to accommodate liquid and molten organic sample feeds. Analysis of the products is achieved by sample-and-quench methods followed by detailed gas chromatography and mass spectrometry.

Experiments at 730 °C revealed the stoichiometry independence of the initial fuel decomposition. Even in the presence of oxygen, the disappearance of anisole is dominated by its unimolecular decomposition to phenoxy and methyl radicals. Phenol, cresols, ethane, and methane, recombination products of the methyl and/or phenoxy radicals, are major reaction intermediates and their yields are virtually independent of stoichiometry as well. Other stoichiometry-independent products include benzene, toluene, and cyclopentadiene. Yields of the two remaining major species, carbon monoxide and methylcyclopentadiene, exhibit a distinct dependence upon stoichiometry suggesting a preferential oxidation of the latter. As expected, for the oxidation experiments, some C<sub>3</sub>-C<sub>5</sub> oxidation products were detected. However given the apparent insignificance of oxygen in this system, it is not surprising that these are

merely trace species. Therefore these lower temperature data, which capture the growth (and in many cases the maximum concentration) of the major species described above, demonstrate the dominance of pyrolytic chemistry in the production of early reaction intermediates in the anisole-oxygen system. Results obtained from the complementary higher temperature (910 °C) experiments capture the destruction of these species in which oxygen, as expected, plays an important role.

Following this work, reaction intermediate mole fraction versus time profiles for the atmospheric pressure, gas phase, water-perturbed pyrolysis and oxidation of anisole were obtained. The addition of a large amount of water vapor to the system explored whether any special consideration in the mechanism might be required when extended to SCWO conditions. This data set was collected for comparison with data acquired from the unperturbed anisole/oxygen system at the same nominal temperature (727 °C) and stoichiometries (pyrolysis and lean oxidizing with  $\phi=0.6$ ). Observed shifts in species profiles due to the addition of water were expected to aid in the identification of chemical pathways involving water and thereby provide a starting point for the development of a detailed kinetic model for the supercritical water oxidation of anisole. At high excess water loadings, the anisole pyrolysis and oxidation chemistry appears to be unaffected. Figure 7.8 shows that species profiles from the water-perturbed experiments are, within experimental error, indistinguishable from those obtained from the unperturbed system, pointing to the general applicability of these gas phase results to SCWO conditions.

At the experimental conditions employed ( $T=727$  °C,  $\phi=0.62-1.71$ ), the destruction of anisole was found to proceed exclusively via homolysis of the  $\phi\text{O-CH}_3$  bond ( $\phi$  = phenyl). It is inferred that, even in the presence of oxygen, the chemistry is primarily pyrolytic. The first step in anisole conversion under all conditions, involves the formation of the key phenoxy radical. Thus, accurate characterization of the pyrolysis chemistry is essential to the development of a model for the oxidation of anisole. More importantly, phenoxy oxidation chemistry will appear as a subset of anisole oxidation chemistry.

A pyrolysis model was developed that consists of 66 reversible reactions involving 31 species. Elementary reaction rate parameters for much of the dominant chemistry were obtained from thermodynamic estimations, QRRK analysis, and semi-empirical molecular orbital calculations. Model predictions of anisole decay and CO production, descriptors of overall reaction progress, agree well with experiment. Excellent agreement is also obtained between experimental data and model predictions of methylcyclopentadiene (Figure 7.9).

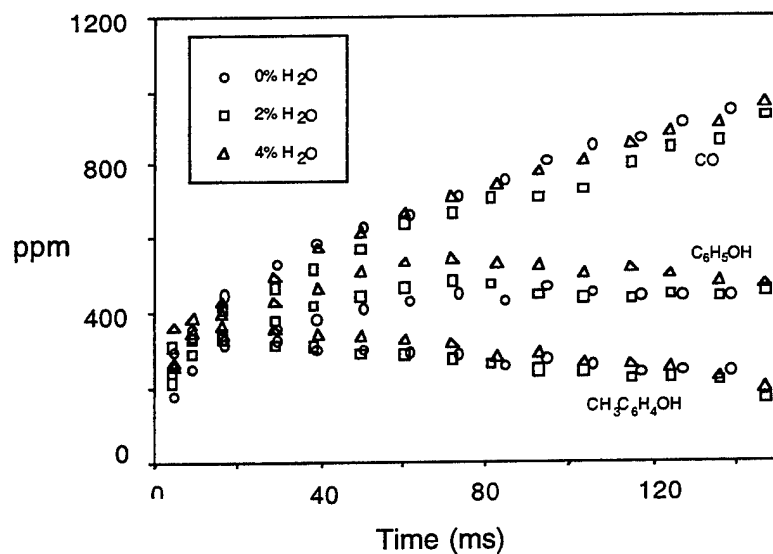


Figure 7.8 Carbon Monoxide, Phenol, and Cresol profiles, obtained in the Princeton atmospheric pressure flow reactor, for lean oxidation of anisole with and without water at 727 °C and  $\Phi=0.6$ .

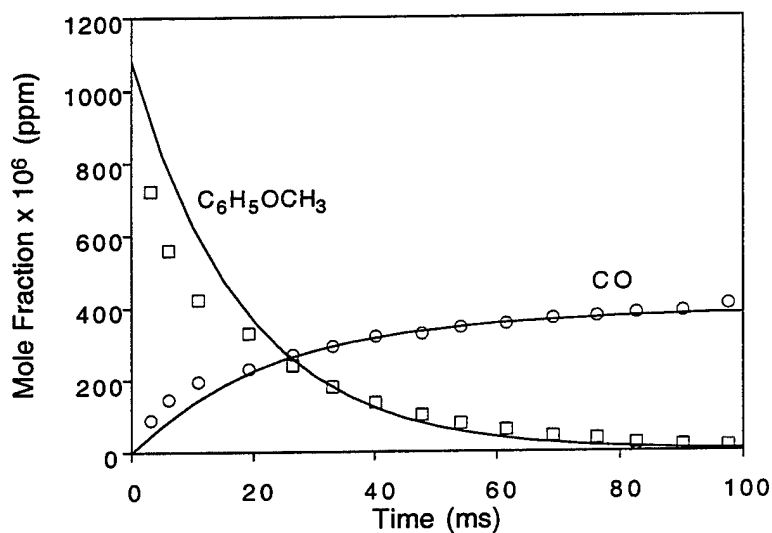


Figure 7.9 Comparison of experimental data and model predictions of anisole and carbon monoxide. Solid lines indicate model results.

As stated above, the central concern of this work is not pyrolysis chemistry of anisole, it is the oxidation of phenoxy radical. The data in figure 7.9 highlight that anisole forms phenoxy radical and then the phenoxy radical undergoes a unimolecular decomposition to form cyclopentadienyl radical and CO. It is possible that this is this source of the prompt CO and subsequent CO<sub>2</sub> that is seen in the oxidation of benzene in supercritical water. In the case of the anisole system, the phenoxy that is formed by dissociation with CH<sub>3</sub> can undergo an exchange of a ring H atom with a CH<sub>3</sub> radical to form (CH<sub>3</sub>)-C<sub>5</sub>H<sub>4</sub>O, methylphenoxy radical. In this case, all subsequent chemistry is with methylcyclopentadienyl. However, the oxidation chemistry that follows is the same for the either the substituted or the unsubstituted species.

As mentioned above, reaction intermediate data from the oxidation of anisole over a range of equivalence ratios ( $\phi = 0.62 - 1.71$ ) was found not to differ substantially from anisole pyrolysis data. More specifically, yields of anisole, cresols, phenol, benzene, cyclopentadiene, methane, and ethane were independent of  $\phi$ . Oxidation was found to occur preferentially through methylcyclopentadiene, accompanied by the production of CO and C<sub>2</sub>-C<sub>4</sub> hydrocarbons including acetylene, ethene, allene, propene, methylacetylene, and 1,3-butadiene. These results suggest that: 1) a model for the oxidation of anisole will rely heavily on the pyrolytic chemistry already developed and 2) extension of the pyrolysis model will involve primarily the addition of reaction steps describing the oxidation of methylcyclopentadiene.

Only two isomers of methylcyclopentadiene are observed experimentally, but all three are present in the reacting system. 5-CH<sub>3</sub>C<sub>5</sub>H<sub>5</sub> is formed initially and is rapidly converted to 1-CH<sub>3</sub>C<sub>5</sub>H<sub>5</sub> which in turn is converted to 2-CH<sub>3</sub>C<sub>5</sub>H<sub>5</sub>. Abstraction of an allylic H, from any one of the three forms, yields the same resonantly stabilized methylcyclopentadienyl radical. Addition of O or HO<sub>2</sub> to CH<sub>3</sub>C<sub>5</sub>H<sub>4</sub>· yields an energized adduct, which can decompose to lower energy, non-cyclic products by  $\beta$ -scission reactions. These radical recombination routes are depicted in Figure 7.10.

Recombination of HO<sub>2</sub> with CH<sub>3</sub>C<sub>5</sub>H<sub>4</sub>· yields a methylcyclopentadienyl hydroperoxide that will rapidly dissociate either back to reactants or to a methylcyclopentadienyl-oxy radical and OH. This is likely one of the most important chain branching reactions; the OH product is more reactive than HO<sub>2</sub> and thus will accelerate the overall reaction via abstractions. These reactions are analogous to the chain reduction reaction described for alcohols and alkanes above.

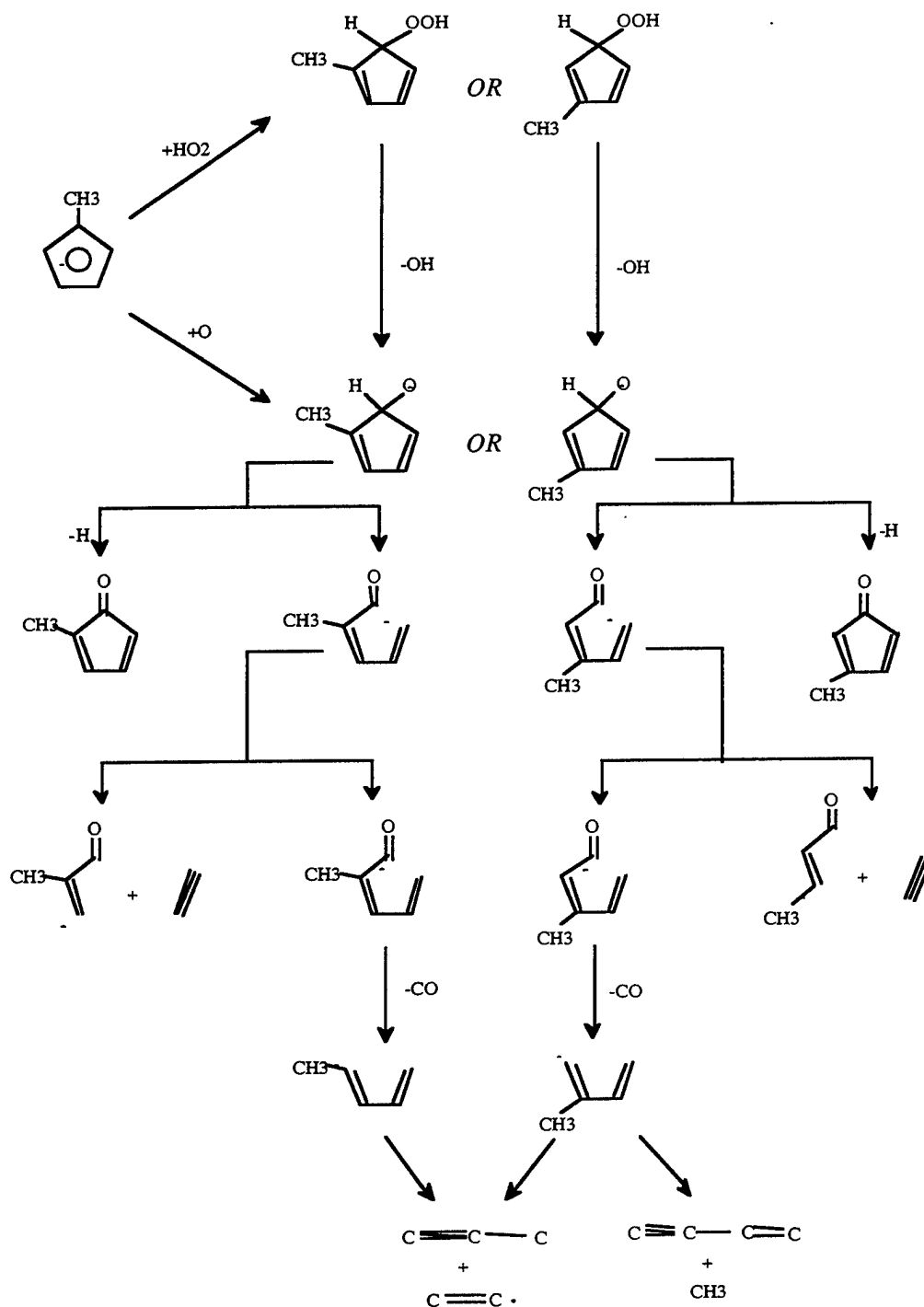


Figure 7.10 Methylcyclopentadiene oxidation mechanism showing the pathway to smaller hydrocarbons as is observed during the pyrolysis of anisole.

The methylcyclopentadienyl-oxy radical may also be formed directly by recombination of O atom with  $\text{CH}_3\text{C}_5\text{H}_4\cdot$ . This is a "combustion route" that probably does not occur in low temperature SCW but may be important above 600 °C. The radical will undergo rapid unimolecular dissociation near 700 °C via two low energy channels. One of these yields a methylcyclopentadienyl ketone and H atom. The second is a ring opening reaction to form a methylpentadienyl aldehyde radical. This radical may decompose to acetylene and a  $\text{C}_4$  aldehyde radical, but is more likely to undergo rapid internal abstraction of the aldehydic hydrogen to form a more thermodynamically stable carbonyl radical. The carbonyl radical will decompose to CO and a  $\text{C}_5$  hydrocarbon radical. The structure of this hydrocarbon radical is determined by the site at which the initial recombination (i.e. of O or  $\text{HO}_2$  with  $\text{CH}_3\text{C}_5\text{H}_4\cdot$ ) took place; either the straight-chain 1,3-pentadien-4-yl radical or the branched 2-methyl-1,3-butadien-1-yl radical is formed. Subsequent reactions of these radicals yield  $\text{C}_2$ - $\text{C}_4$  species. The straight-chain pentadienyl radical undergoes  $\beta$ -scission to form methylacetylene + vinyl. 2-methyl-1,3-butadien-1-yl, a radical of isoprene, may decompose via two distinct  $\beta$ -scission channels to yield either methylacetylene + vinyl or vinylacetylene + methyl.

Allene may be formed via isomerization of methylacetylene. Recombination of vinyl with H, methyl, or vinyl yields ethene, propene, and 1,3-butadiene, respectively. Alternatively, vinyl may unimolecularly decompose to acetylene + H.

The scheme described above accounts qualitatively for  $\text{C}_2$ - $\text{C}_4$  methylcyclopentadiene oxidation products observed in the anisole experiments. Further development of this model would involve consideration of radical addition to unsaturated bonds of the parent species. As yet, measured rates and thermodynamic data for the relevant reactions and species do not exist, and development of a model for quantitative prediction must rely heavily on estimations. Recent advances at Princeton in the modeling of the unsubstituted species cyclopentadiene are expected to aid in the present modeling effort.

#### ***7.4.3 Kinetics of benzene oxidation in supercritical water***

A bench-scale flow reactor was used to measure the rates and extents of benzene and phenol disappearance as functions of temperature, pressure (or density), and the inlet oxygen and aromatic concentrations. All of this work on pure benzene oxidation in supercritical water was conducted at MIT. The initial intent is to represent these data using global kinetic rate expressions that correlate the reaction rates of benzene and phenol in supercritical water to the feed concentrations and temperature. Analysis of benzene and its partial and final oxidation products was conducted using gas chromatography (GC) with both flame-ionization (FID) and thermal conductivity (TCD) detectors.<sup>8</sup>

Benzene oxidation rates were measured over the temperature range of 475 to 580°C with a 6.2 second residence time, an initial benzene concentration of 0.6 mM, a fuel equivalence ratio of 1.1, and a pressure of 24.6 MPa. The initial benzene concentration results from using a saturated benzene/water solution as the reactor feed. Figure 7.11 presents the resulting conversion versus temperature profile. Conversion is linear with

temperature from 520 to 570°C and asymptotically approaches 100% for temperatures above 575°C. Replotting the data from Fig. 7.11 as the assumed first order rate constant,  $\ln k$  versus the reciprocal of temperature yields a straight line with an apparent activation energy of 221.5 kJ/mol obtained from a linear least squares fit to the data. The major partial and final oxidation products are carbon monoxide and carbon dioxide, with trace phenol and methane. Carbon balances calculated using only these species range from 88 to 100%, improving with temperature as the amount of oxidized carbon appearing in form of carbon monoxide and carbon dioxide increases. Carbon monoxide concentrations increase with temperature at a 6.2 second residence time until about 550°C, after which the carbon monoxide is fully oxidized to carbon dioxide. Phenol is observed as an intermediate only in the range of 520 to 560°C, presumably being formed and oxidized rapidly for temperatures above 560°C. Methane is the most refractory of the partial oxidation products; its concentration does not decrease even at the highest temperature studied.

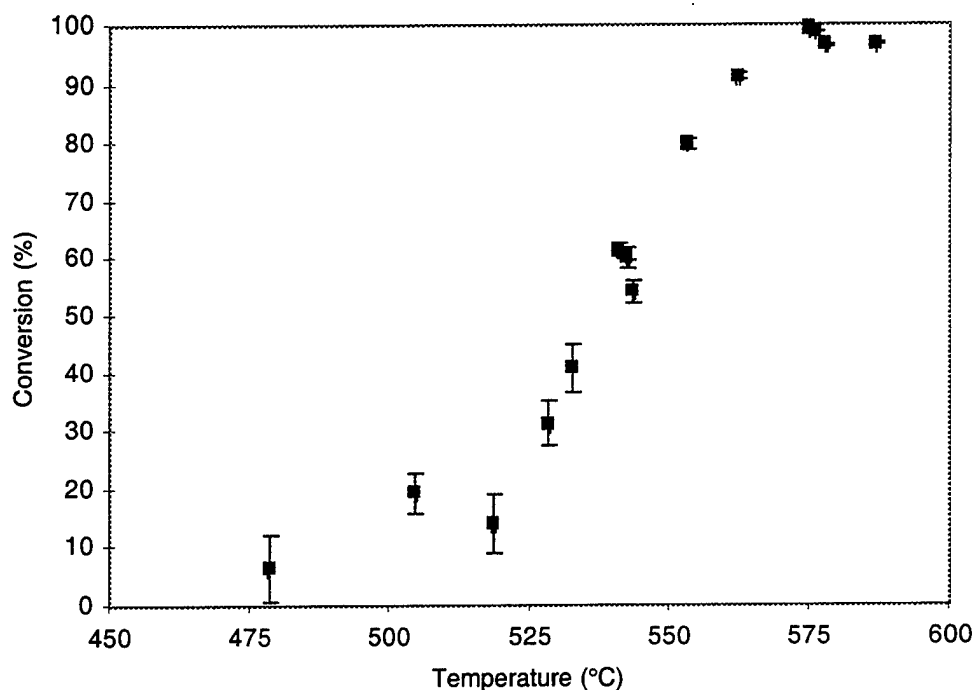


Figure 7.11 Benzene conversion measured as a function of temperature in the MIT bench-scale SCWO flow reactor. ( $[\text{C}_6\text{H}_6]_0 = 0.60 \pm 0.05$  mM,  $t = 6.2 \pm 0.2$  s,  $P = 246 \pm 2$  bar,  $\phi = 1.1 \pm 0.1$ ).

The next set of oxidation experiments included experiments where the fuel equivalence ratio was varied from 0.48 to 2.5 at 540°C. These experiments were designed to study the influence of the fuel equivalence ratio ( $\Phi$ ), initial benzene concentration, density and residence time on conversion. Conversion was measured as  $\Phi$  was varied from 0.48 to 2.4 at  $P = 24.6$  MPa and  $[\text{C}_6\text{H}_6]_0 = 0.6$  mM at residence times ranging from 3 to 7 seconds. Further, we examined the dependence of conversion on the initial benzene concentration by generating residence time profiles at 540 and 550°C while varying the

initial benzene concentration from 0.4 to 1.2 mM and maintaining a fixed pressure of 24.6 MPa and a stoichiometric level of oxygen ( $\Phi=1.0$ ). Finally, the pressure (density) dependence of benzene conversion was investigated by conducting experiments where the pressure ranged from 13.9 to 27.8 MPa ( $\rho=0.04$ -0.09 g/mL) at 540°C over a residence time range of 3 to 6 seconds with  $[C_6H_6]_0=0.6$  mM and  $\Phi=1.0$ . A global rate expression was regressed from the experimental data.

Figure 7.12 displays the dependence of benzene conversion on fuel equivalence ratio,  $\Phi$ , at 550°C. Benzene conversion increases with the initial oxygen concentration, while keeping  $[C_6H_6]_0$  fixed (a decrease in  $\Phi$  corresponds to an increase in  $[O_2]_0/[C_6H_6]_0$ ). Therefore, oxygen is obviously a participant in one or more of the rate limiting steps in benzene oxidation.

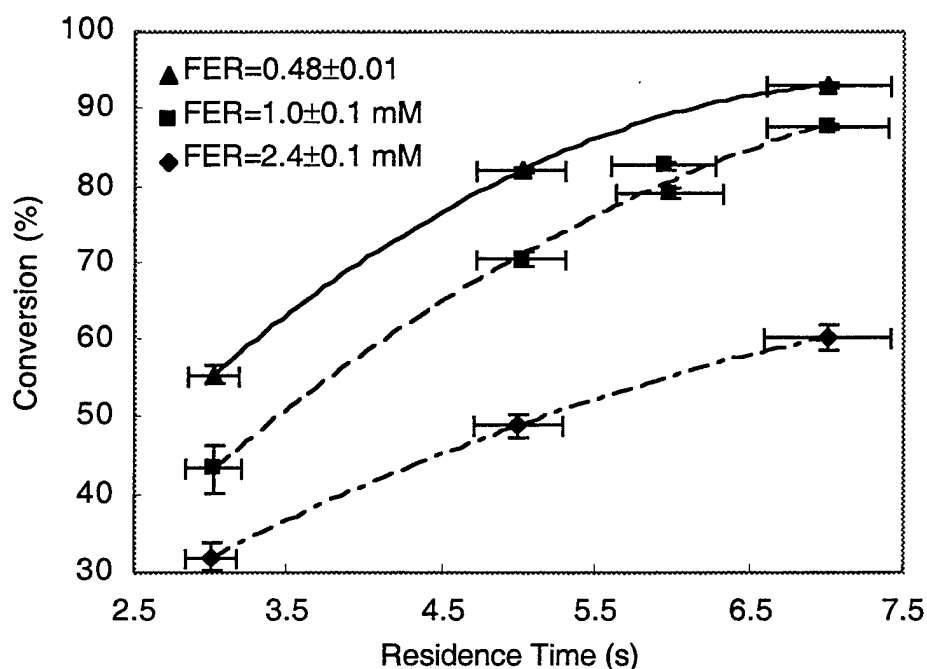


Figure 7.12. Effect of the Fuel Equivalence Ratio (FER or  $\Phi$ ) on benzene conversion ( $[C_6H_6]_0=0.59\pm0.01$  mM,  $T=550^\circ\text{C}$ ,  $P=24.6\pm0.2$  MPa).

An interesting feature of benzene SCWO is the nonlinear dependence of benzene conversion on the initial benzene concentration. This concentration dependence was studied at 530, 540 and 550°C with  $\Phi=1.0$  and  $P=24.6$  MPa. Residence time profiles from 3 to 7 seconds were obtained for initial benzene concentrations of 0.4, 0.6 and 1.2 mM.. The results showed that benzene conversion decreases as  $[C_6H_6]_0$  increases at the three temperatures studied. These data are shown in Figure 7.13.

The final set of experiments was designed to determine the effect of system pressure, or fluid density, on benzene conversion. Experiments were performed at 540°C with an initial benzene concentration of 0.6 mM and a stoichiometric amount of oxidant.



Conversions were measured at 13.9, 16.5, 19.6, 22.8, 24.6, and 27.8 MPa, corresponding to densities of 0.04, 0.05, 0.06, 0.07, 0.08, and 0.09 g/mL, respectively. At each pressure, several residence times were studied. The results, presented in Figure 7.14, show that benzene conversion is independent of pressure for subcritical pressures ( $P_c=22.1$  MPa), but clearly increases with pressure for supercritical pressures.

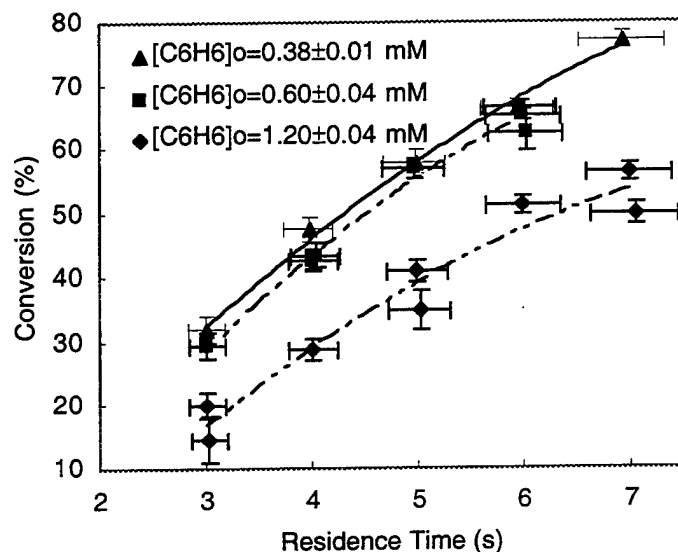


Figure 7.13. Effect of initial benzene concentration on conversion ( $T=540\pm 2^\circ\text{C}$ ,  $P=24.6\pm 0.2$  MPa,  $\phi=0.9\pm 0.1$ ).

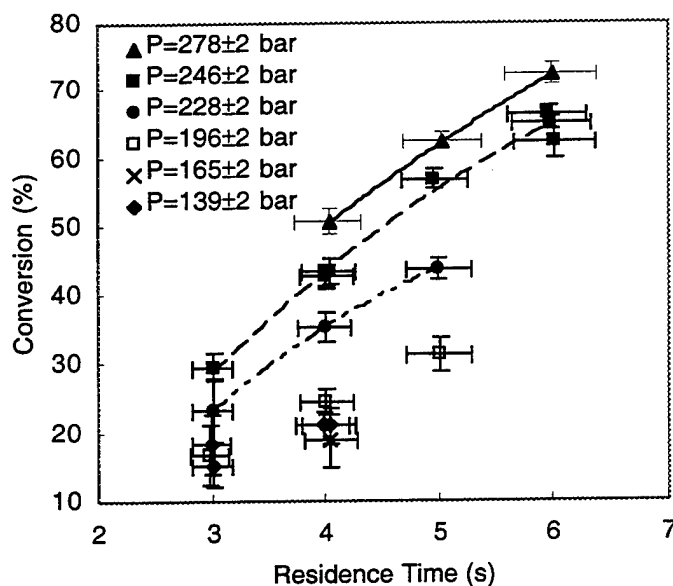


Figure 7.14. Effect of pressure on benzene conversion ( $\phi=0.9\pm 0.1$ ,  $T=540^\circ\text{C}$ ,  $[C_6H_6]_0=0.60\pm 0.03$  mM).

The conversion data from all of the benzene experiments in supercritical water with the exception of the pressure variation experiments, were fit to a global rate expression using a non-linear regression algorithm. The regression gave the following rate expression:

$$-\frac{d[C_6H_6]}{dt} = 10^{13.1 \pm 0.9} \exp(-2.4 \pm 0.1 \times 10^5 (J)/RT) [C_6H_6]^{0.40 \pm 0.06} [O_2]^{0.18 \pm 0.05} \quad (7.10)$$

The estimated errors are 95% confidence intervals on the regressed parameters.

Predicted conversions from the regressed rate law are compared to experimentally observed conversions in Figure 7.15. Perfect prediction of the experimental data by the global rate expression would result in all the points falling on the 45° line (the solid line). The global rate expression does an excellent job of representing the data at the conditions studied. Higher conversion data ( $X > 40\%$ ) are better predicted, as evidenced by the decreased degree of scatter of the points around the 45° line for  $X > 40\%$ .

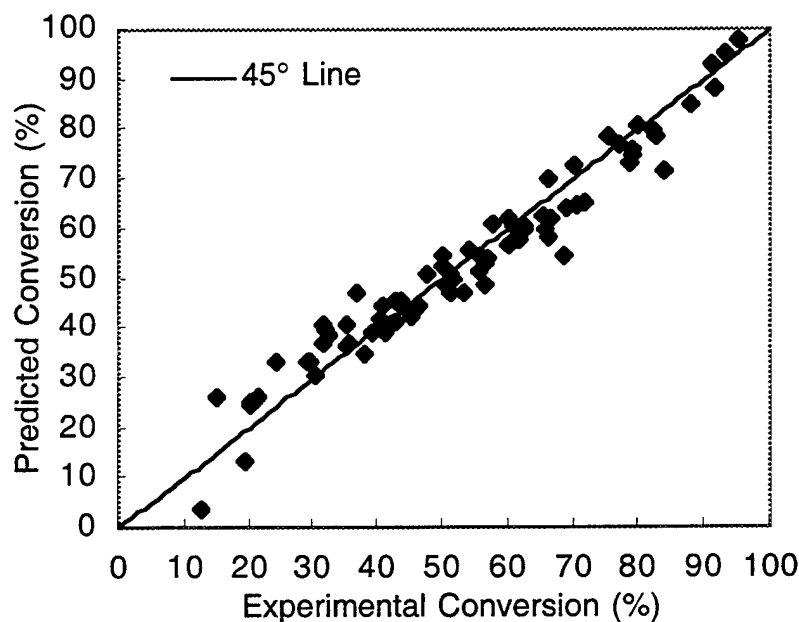


Figure 7.15. Comparison of measured benzene conversion with conversion predicted by the regressed global rate expression ( $T=475-590^{\circ}C$ ,  $[C_6H_6]_0=0.4-1.2$  mM,  $\Phi=0.5-2.5$ ,  $t=3-7$  s,  $P=24.6$  MPa)

The partial oxidation products formed during benzene oxidation in SCW appear in Figures 7.16. Carbon balances (moles of carbon recovered in products/moles of carbon in feed) calculated using only the species appearing in Figure 7.16 range from 90-105%,

indicating that these products account for the majority of the reacted carbon. Of these products, most of the reacted carbon is in the form of carbon monoxide, carbon dioxide, with very small amounts of phenol and methane, as mentioned above. Ethylene and acetylene each account for less than 1% of the reacted carbon. The early appearance of a significant quantity of carbon dioxide relative to the amount of carbon monoxide is in agreement with the observations by Savage and co-workers at the University of Michigan.<sup>9</sup> They report that the carbon dioxide yield always exceeds that of carbon monoxide in the SCWO of phenol, *o*-cresol and *p*-chlorophenol. In fact, many experiments at the different conditions presented above showed CO<sub>2</sub> yields greater than the CO yields at all times.

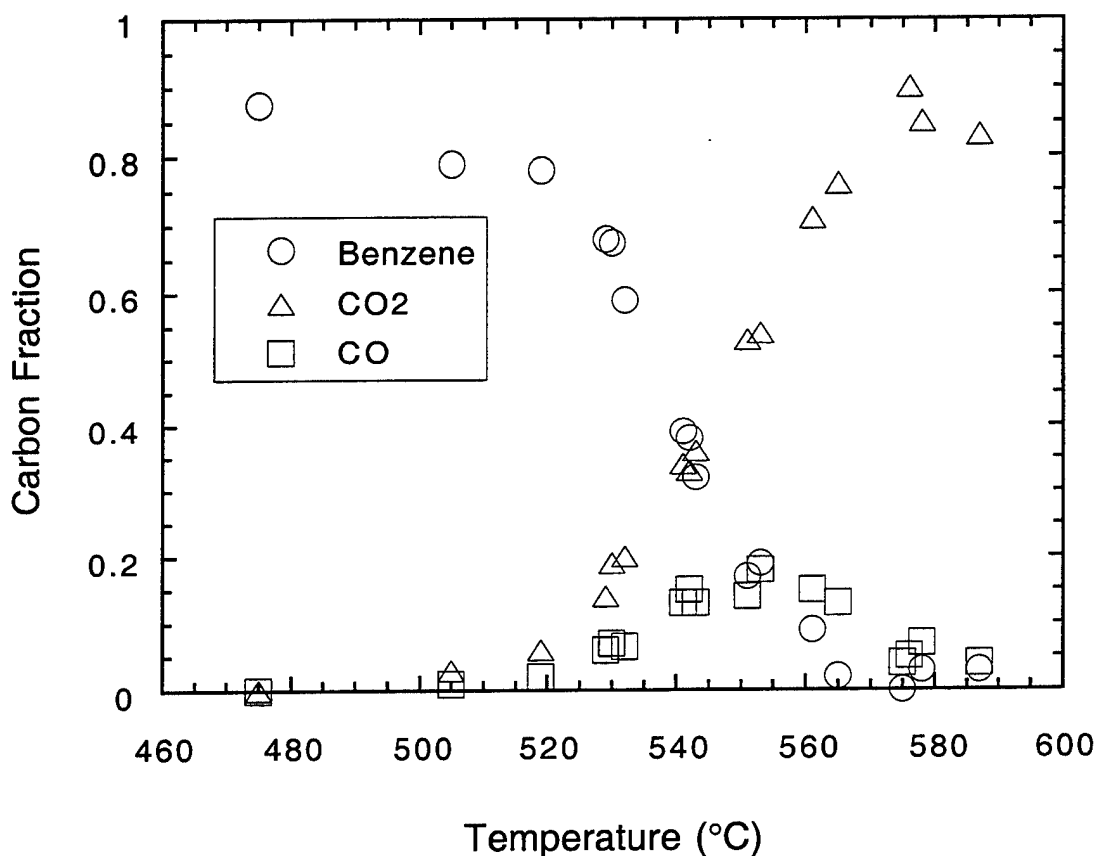


Figure 7.16 Carbon fractions of CO<sub>2</sub>, CO, and unreacted benzene as a function of temperature. Time = 6.2 s, P=24.6 MPa,  $\phi = 1.1$  [C<sub>6</sub>H<sub>6</sub>] = 0.06 mM. From Ref. 8.

Figure 7.17 shows that a minor intermediate in the oxidation of benzene is phenol as is methane. The small amount of phenol was a surprising result and has raised some doubt as to whether the benzene oxidation pathway proceeds through phenol or, more importantly even phenoxy radical.

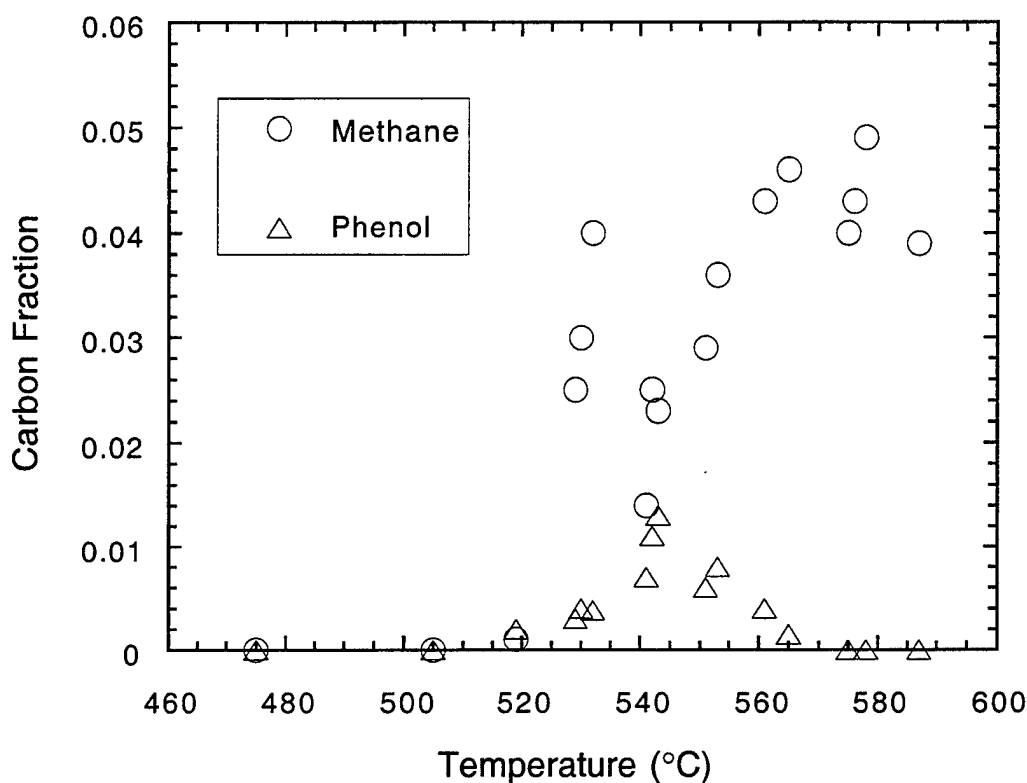


Figure 7.17 Carbon Fractions of methane and phenol as a function of temperature. Time = 6.2 s, P=24.6 MPa,  $\phi = 1.1$   $[C_6H_6] = 0.06$  mM. From Ref. 8

#### 7.4.4 Benzene oxidation mechanism

Our original hypothesis was that the probable mechanism involves hydrogen abstraction to form the  $C_6H_5$  benzyl radical which is subsequently captured by  $O_2$  to form  $C_6H_5O_2$ ,



Benzoperoxide  $C_6H_5O_2H$  is in favorable equilibrium with  $H_2O_2$  and other alkyl hydroperoxides. It undergoes unimolecular dissociation to form phenoxy and OH.



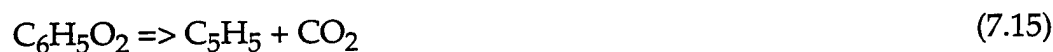
Phenoxy radical is suspected to be stable and is probably the species that is present in abundance at high temperature. Quenching the reaction with phenoxy present in the

high temperature supercritical fluid results in the formation of phenol and the stable species at low temperature. Therefore, benzene oxidation occurs in two main steps: phenoxy radical formation is the first step and subsequent oxidation of the stable phenoxy radical follows. Thus, understanding the pyrolysis and oxidation chemistry of phenoxy is pivotal as we followed up with the phenol and anisole chemistry described in the sections above. That is, phenoxy radical ejects CO and forms cyclopentadienyl radical which undergoes pyrolytic decomposition and alkyl oxidation following our scheme for simple ethanol and higher alcohols.

The lack of phenol in the effluent in the MIT experiments is somewhat inconsistent with this picture and has led the MIT group to suggest a reaction pathway that does not produce much phenoxy radical. In addition, there must be a way to produce CO<sub>2</sub> faster than CO. This scheme is described in the elementary reaction analysis presented in detail by DiNaro et al.<sup>10</sup> In that work they suggest that the phenylperoxyl radical, C<sub>6</sub>H<sub>5</sub>O<sub>2</sub>, can undergo a self-bridging rearrangement to form p-benzoquinone,



and undergoes a minor reaction to produce CO<sub>2</sub>.



The stable p-benzoquinone species is then the dominant intermediate. The net effect of its formation is to slow down radical chain branching reactions and to produce better agreement between the observed benzene conversion rates and the quantitative model predictions.

However, this model does not contain one of the key steps mentioned in the first scheme. That is the transfer of an H atom from H<sub>2</sub>O<sub>2</sub> to C<sub>6</sub>H<sub>5</sub>O<sub>2</sub> to form C<sub>6</sub>H<sub>5</sub>O<sub>2</sub>H which will also serve to reduce the rate of OH formation and slow the overall conversion rate, without having to invoke the formation of p-benzoquinone. In future work on this system it will be important to develop an experimental approach that will discriminate between these two routes.

## 7.5 Methanol/Benzene co-oxidation

### 7.5.1 Experimental Results

At Sandia, we conducted a series of SCWO experiments in the SFR exploring the rate of oxidation of benzene at relatively low temperatures in the presence of a much more reactive species, methanol. The experiments needed two preliminary pieces of information. First, we needed to measure the oxidation rate of methanol at our specific test conditions. This served two purposes: 1) to obtain high-precision data at several reaction times at 450 °C for methanol oxidation; and 2) to verify that we could reproduce our published methanol oxidation work from prior experiments. The second piece of information required was to establish that, under SCWO conditions, benzene

does not react at 450 °C on a timescale of less than 10 s with oxygen to corroborate the data from the MIT group.

Figure 7.18 shows the 992  $\text{cm}^{-1}$  Raman resonance of benzene in supercritical water at 450 °C. The integrated intensity of this feature was unaffected by the presence oxygen at an equivalence ratio of 1.00 (corresponding to exactly the stoichiometric amount of oxygen for full oxidation to  $\text{CO}_2$  and water) and a reaction time of 2.5 s. This result is entirely consistent with the data presented above on benzene oxidation in Figure 7.11. Those data, generated by the MIT group, show 5% conversion after 6 seconds at 475°C; extrapolation to 450 °C shows practically no reaction. Figure 7.19 shows the same spectral feature with the same amount of benzene in the feed, but with an equivalent amount of methanol added. The integrated intensity, which is proportional to concentration, has dropped by about 20%. This conclusively shows an accelerated removal of benzene at lower temperatures, due to the presence of methanol.

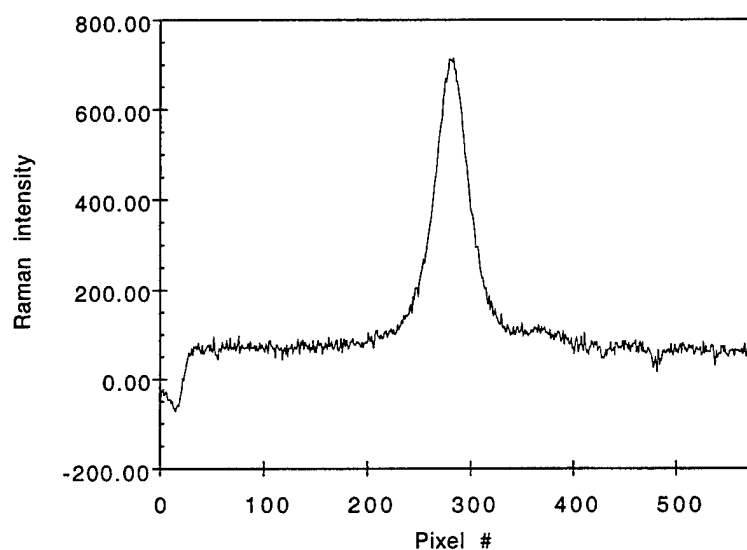


Figure 7.18 Raman spectrum of the 992  $\text{cm}^{-1}$  resonance in benzene in supercritical water and a stoichiometric amount of oxygen at 450 °C, obtained in Sandia's SFR.

Note that along with the partial conversion of the benzene, there is a distinct change in the level of background fluorescence. This additional fluorescence is not unexpected since an aromatic species such as benzene is likely to produce partial oxidation products that absorb weakly in the visible region and can be excited by the 5145 Å laser.

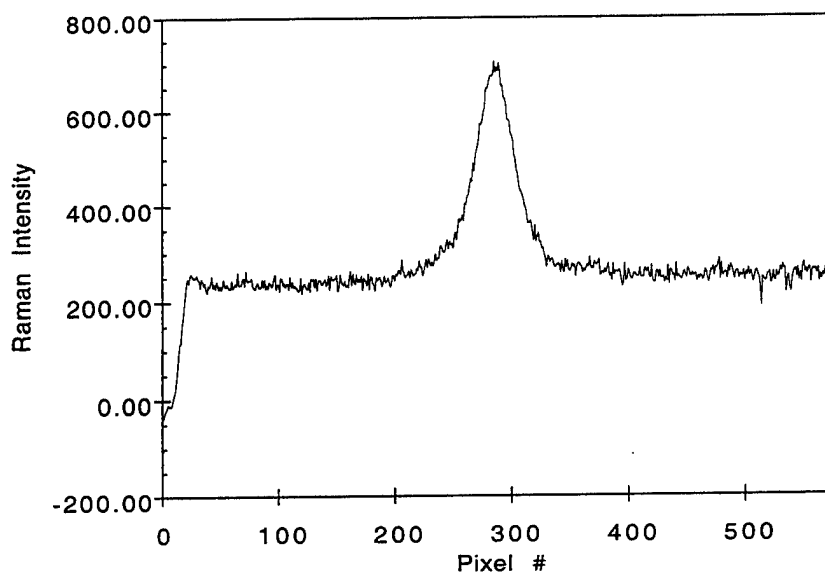


Figure 7.19. Raman spectrum of the same resonance in Figure 7.18 with methanol added to the mixture in the SFR.

Figure 7.20 summarizes the experimental results that we have obtained for the co-oxidation of benzene and methanol under SCWO conditions. First, the data show excellent agreement with the methanol oxidation in our earlier results from 1996.<sup>11</sup> The 1996 data were obtained using the original SFR configuration with the methanol preheated in a dilute solution with water and then mixed at a tee at the head of the reactor with an equal volume of oxygen and water. The later configuration used an injector, where the fuel is added as a pure material and is very rapidly preheated only milliseconds prior to introduction into a solution of supercritical water and oxygen. This agreement shows that there is no difference in the methanol conversion rate for two reactor configurations.

The data recorded for methanol on the mixtures are identified by the filled squares. The reference methanol-only data are represented by the open squares. The symbols marked as  $C_6H_6$  C-C represent the relative concentration of benzene present in the reacting flow determined from the integrated intensity of the  $992\text{ cm}^{-1}$  band shown in Figures 7.18 and 7.19. The symbols marked  $C_6H_6$  C-H are from the measured intensity of the benzene Raman feature at  $3061\text{ cm}^{-1}$  that corresponds to the symmetric carbon-hydrogen stretching frequency. Both bands are proportional to the concentration of benzene and are in fairly good agreement.

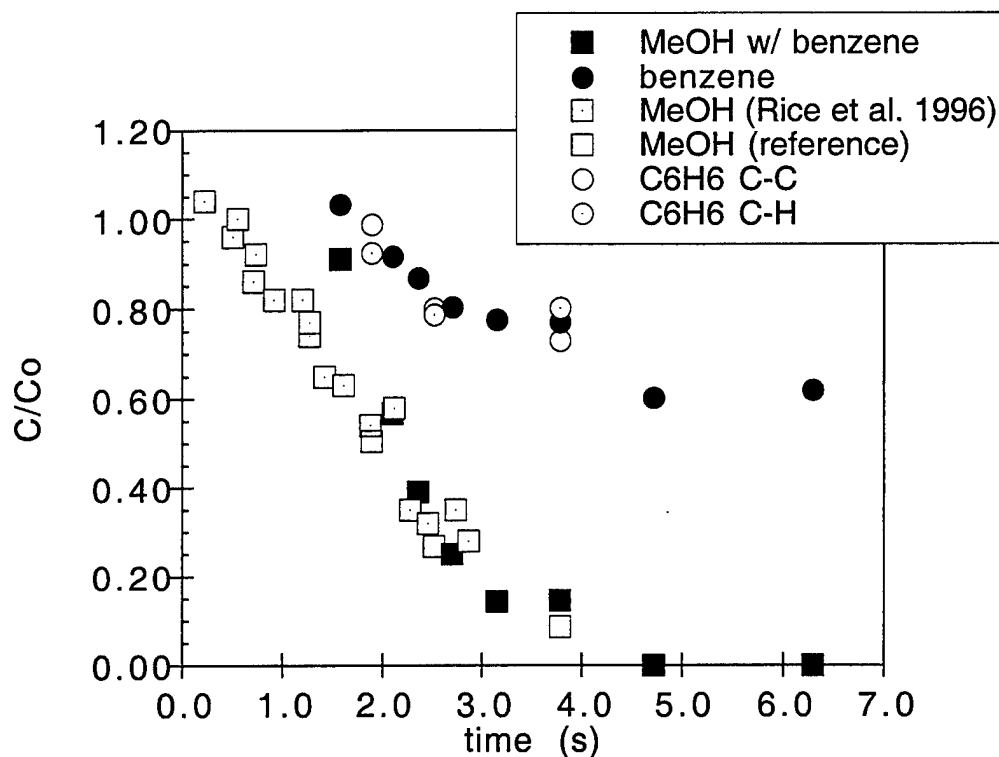


Figure 7.20. SCWO experimental results obtained in Sandia's SFR, for the concentration of methanol and benzene during co-oxidation. Included in the figure are results for methanol concentration as a function of time during oxidation by  $O_2$  in supercritical water with no benzene present. The three sets of benzene data are for experiments when only the C-H or C-C Raman bands were examined (open circles, open/dot circles) and for other experiments when these were averaged (solid circles).

### 7.5.2 OH production model

The data on benzene conversion show that very little benzene is consumed during the first 50 % of methanol oxidation. This delay is followed by a drop in the benzene concentration between 1.5 and 4.0 seconds and a subsequent slowing of the reaction rate past 5.0 seconds. Results from our methanol oxidation model, which include the updated catalytic and homogeneous  $H_2O_2$  kinetics studied reported in Section 5, are presented in Figure 7.21 and are in excellent agreement with our data regarding methanol conversion. The model shows that the peak concentration of OH occurs in the 1.5 - 4.0 s timeframe at these conditions, lagging slightly behind the maximum in the rate of methanol loss. This is when the benzene consumption is at its highest rate. As the transient OH concentration declines with completion of methanol conversion, the benzene conversion stops despite the presence of a sufficient concentration of  $O_2$ .



These tests are the final step in assuring that the C/H/O oxidation model can accurately predict the behavior of mixtures of both kinetically stable and kinetically labile organic compounds in the same feed.

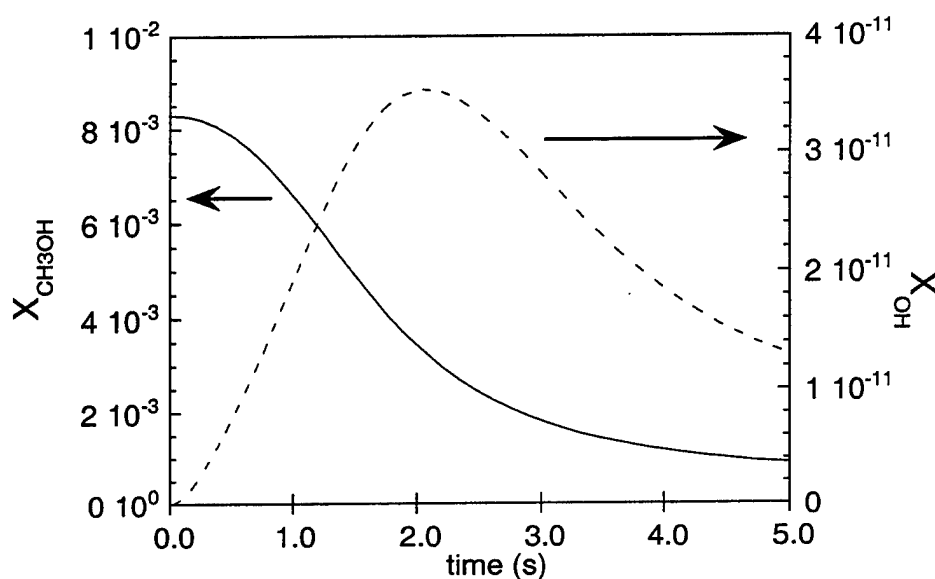


Figure 7.21. Model predictions for the production of a non-equilibrium transient concentration of OH radical during the oxidation of methanol at 450 °C and 25. MPa.

It is interesting to note that the fluorescence background in the co-oxidation case (Figure 7.19) increases. This may be due to the formation of higher hydrocarbons such as polycyclic aromatics. We suggest that some of the benzene is partially oxidized, but as the oxidizer radical pool is depleted, the phenoxy radicals that are formed begin to undergo condensation reactions. This type of behavior was also observed by the MIT group, who report that the formation of a small amount of a wide range of higher aromatics including three rings species that have some absorbance at 514 nm such as anthracene, dibenzofuran, and, xanthone.

### 7.5.3 Summary - cooxidation of benzene and methanol

The combined results and analyses completed at Sandia, Princeton, and MIT, demonstrate of the concept of enhanced oxidation kinetics in benzene in a mixture with methanol. The results correlated well with the transient concentration of hydroxyl radical that is predicted by the methanol oxidation model. The data reproduce the delay in consumption of benzene predicted by the model prior to the accumulation of OH in the system, as well as the approximate timeframe (1.5 s -3.0 s) where we expect to see the greatest consumption of benzene. These experiments show conclusively that the presence of an easily oxidized component of a mixture can enhance the oxidation of a

more kinetically robust component. The data are consistent with the interpretation from the MIT group that the rate-limiting step in benzene conversion is hydrogen abstraction by OH and not by HO<sub>2</sub>. If HO<sub>2</sub> were important in benzene conversion, as it is in methanol at this temperature, there would be some loss of benzene during the first 1.5 seconds. However, the data shows that there is almost no conversion relative to the 40-50% conversion of methanol.

We note that because the more reactive species will always be consumed faster, any mixture will eventually become depleted in the reactive component prior to the robust one and therefore there will always be some of the less reactive material left to be converted at the non-enhanced rate. Given this, high conversion (>99.99 %) of stable species such as aromatics will still be largely determined by their own intrinsic oxidation rate and adding a reactive component may not improve the time needed to obtain complete destruction.

This is not to say, however, that reactive species in the feed cannot be effective in raising the temperature of the system faster when operating under autothermal conditions. By this indirect route, the robust components could be removed faster since the time-temperature history of the mixture reaches an elevated temperature more rapidly than would have occurred in the absence of the reactive component in the feed.

## 7.6 References

1. T. S. Norton, F. L. Dryer. "An Experimental and Modeling Study of Ethanol Oxidation Kinetics in an Atmospheric Pressure Flow Reactor" *Int. J. Chem. Kinet.* **24**, 319-344, 1992.
2. N.M. Marinov "A Detailed Chemical Kinetic Model for High Temperature Ethanol Oxidation" *Int. J. Chem. Kinet.* **32**, 183-220, 1999.
3. E. Croiset, S.F. Rice, R.G. Hanush "Hydrogen Peroxide Decomposition in Supercritical Water", *AIChE Journal* **43**, 2343-2352, 1997.
4. E.E. Brock, P.E. Savage "Detailed Chemical Kinetics Model for Supercritical Water Oxidation of C<sub>1</sub> Compounds and H<sub>2</sub>" *AIChE Journal* , **41**, 1874-1888. 1995.
5. E.E. Brock, Y. Oshima , P.E. Savage, J.R. Barker, "Kinetics and Mechanism of Methanol Oxidation in Supercritical Water." *J. Phys. Chem.* **100**, 15834-15842, 1996.
6. B. Eiteneer, C.L. Yu, M. Goldenberg, M. Frenklach, "Determination of Rate Coefficients for Reactions of Formaldehyde Pyrolysis and Oxidation in the Gas-Phase." *J. Phys. Chem. A*, **102**, 5196-5205. 1998.
7. M. Pecullan, K. Brezinsky K, I. Glassman " Pyrolysis and Oxidation of Anisole near 1000 K" *Journal Of Physical Chemistry A* **101**, 3305-3316, 1997.

8. J.L DiNaro, J.W. Tester, J.B. Howard, K.C. Swallow. "Experimental Measurements of Benzene Oxidation in Supercritical Water" *AIChE J.* **46**, 2274-2284, 2000.
9. R. Li, T.D. Thornton, P.E. Savage "Kinetics of CO<sub>2</sub> Formation from the Oxidation of Phenols in Supercritical Water" *Environ. Sci. Technol.* **26**, 2388-2395, 1992.
10. J.L DiNaro, J.B. Howard, W.H. Green, J.W. Tester, Bozzelli, J.W. "Elementary Reaction Mechanism for Benzene Oxidation in Supercritical Water" *J. Phys Chem A*, **104**, 10576-10586, 2000.
11. S.F. Rice, T.B. Hunter, Å.C. Rydén, R.G. Hanush, "Raman Spectroscopic Measurement of Oxidation in Supercritical Water I. Conversion of Methanol to Formaldehyde" *Industrial and Engineering Chemistry Research* **35**, 2161-2171, 1996.

## Section 8: Heteroatoms

### 8.1 Introduction

#### 8.1.1 Overview

In general, real waste feeds that will be processed by SCWO for DOE and DoD applications are not simply C,H,O organic compounds. In fact, it is the presence of functional groups containing halogens, oxidized nitrogen, and sulfur that cause many substituted organic compounds to be hazardous and challenging to mineralize. The promise of SCWO is to treat real materials that are difficult to incinerate. To be successfully developed to dispose of explosives, unusual munition formulations, mixed wastes, vehicle and aircraft changeout fluids, paints and strippers, and other industrial formulations, SCWO systems will need to process complicated functionalized organics. In this project, we have explored two key types of functionalization: chlorinated and nitro-substituted compounds. These two groups represent the two main classes of chemicals that the DoD and DOE are looking for alternatives to incineration. This work has only been able to make a partial contribution to the understanding of these systems, but does raise some important considerations which future progress in describing these more complicated SCWO kinetics will be able to exploit.

An important application of SCWO is intended to be the environmentally benign destruction of halogenated alkane and aromatics. These chemicals have had heavy use in industrial applications for many years. Examples of these compounds are polychlorinated biphenyls (PCBs), trichloroethylene (TCE), trichloroethane (TCA), and methylene chloride. These compounds have been shown to form chlorinated dioxins when incinerated and therefore have attracted the attention of technology development interests attempting to supplant incineration as a hazardous waste destruction method. Within the context of mechanism development for treating this class of compounds, the research team at MIT has conducted a combined experimental and theoretical approach to explore the oxidation and hydrolysis chemistry of this group of materials. The model system was chosen to be methylene chloride because of its obvious structural simplicity that would make a computational approach to the sub-critical hydrolysis process possible. All of the work reported below on methylene chloride was done at MIT.<sup>1,2</sup>

Another aspect of the early literature (pre-1992) on SCWO, highlighting its potential practical advantages, is the repeated citing that no NO<sub>x</sub> is formed during processing of typical feeds. However, over the past ten years, there are data from several tests showing that incomplete processing of many feeds containing oxidized nitrogen can result in nitrite (NO<sub>2</sub><sup>-</sup>) and nitrate (NO<sub>3</sub><sup>-</sup>) in the liquid effluent.

Within this SERDP project, interest in the nitrogen chemistry has two sources. First, since many potential feedstocks for SCWO destruction of DoD wastes include explosives or other energetic materials, it is expected that organic nitro functionalities (R-NO<sub>2</sub>) will be common. Our experience has shown that these NO<sub>2</sub> groups can be

used as an internal oxidizer in a practical system, provided that the supplemental oxidizer (air,  $O_2$ ) is not introduced as a competing reactant. Thus, a knowledge of the reaction kinetics of nitrogen-containing species will prove to be very valuable for engineering designs of a staged processing system. Second, effluents containing aqueous nitrate ion and vapor phase  $NO_x$  are highly undesirable due to their corrosive nature and toxicity. Practical system designs operating with effluent containing significant amounts of these materials will be unacceptable. As a result, a better understanding of the detailed mechanisms and kinetics of reactions of nitrogen-containing feeds is needed to design away from these conditions.

There is a significant body of work from Buelow, Dell'Orco, Foy, and coworkers at Los Alamos National Lab examining the behavior of feeds containing  $HNO_3$  reacting with organic material and  $NH_3$ .<sup>3,4</sup> They show that, over a wide range of conditions, the gas phase  $N_2/N_2O$  selectivity varies greatly from as high as 25 to as low as 1.4. Therefore, although the formation of  $N_2O$  is not nearly as important as residual  $NO_2$  or  $NO$ , an understanding of  $N_2O$  reactivity under SCWO conditions will be important from a modeling standpoint. In addition, its presence in the purportedly "clean" effluent from waste processing could have unforeseen regulatory ramifications in the future. Our results on  $N_2O$  have not been published as yet in the archival literature and therefore a more in-depth presentation is found in this section than this Final Report contains for many of the other aspects of this project.

#### ***8.1.2 Papers and Reports***

The work on ammonium picrate (Explosive D) at Sandia cited below was supported by the Naval Surface Warfare Center, Crane, IN and not by SERDP. The reports on shipboard waste were supported by DARPA and the Office of Naval Research. The work on organic dye and pyrotechnic oxidation kinetics constituted some of the feasibility testing that has led to the production prototype plant at Pine Bluff Arsenal and was supported by TACOM-ARDEC and Picatinny Arsenal. All of these projects benefited, either directly or indirectly, from the experimental and testing expertise that was developed here at Sandia as a result of this SERDP project.

C.A. LaJeunesse, B.E. Mills, B.G. Brown "Supercritical Water Oxidation of Ammonium Picrate" Sandia Report SAND95-8202, 1994.

S.F. Rice, R.R. Steeper, C.A. LaJeunesse "Destruction of Representative Navy Wastes Using Supercritical Water Oxidation" Sandia Report SAND94-8203, 1993.

S.F. Rice, C.A. LaJeunesse, R.G. Hanush, J.D. Aiken, S.C. Johnston "Supercritical Water Oxidation of Colored Smoke, Dye, and Pyrotechnic Compositions" Sandia Report SAND94-8209, 1994.

S.F. Rice, R.G. Hanush, T.B. Hunter, R.R. Steeper, J.D. Aiken, E. Croiset, C.A. LaJeunesse "Kinetic Investigation of the Oxidation of Naval Excess Hazardous Materials in

Supercritical Water for the Design of a Transpiration-Wall Reactor" Sandia National Laboratories Report SAND97-8219, 1997.

C.A. LaJeunesse, B.E. Mills, S.F. Rice "Case Study on the Destruction of Organic Dyes in Supercritical Water" in *Chemical Oxidation* (W.W. Eckenfelder, A.R. Bowers, J.A. Roth Eds.) Technomic, Lancaster, PA 1997, Volume 5, pp. 13-21.

S.F. Rice, R.R. Steeper "Oxidation Rates of Common Organic Compounds in Supercritical Water" *Journal of Hazardous Materials*, **59**, 261-278, 1998.

J.W. Tester, P.A. Marrone, M.M. DiPippo, K. Sako, M.T. Reagan., T. Arias, W.A. Peters "Chemical Reactions and Phase Equilibria of Model Halocarbons in sub- and Supercritical Water (200 to 250 bar, 100 to 600 °C)" *Proceedings of The Fourth International Symposium on Supercritical Fluids*, May 1997.

P.A. Marrone., P.M. Gschwend, K.C. Swallow, W.A. Peters, J.W. Tester "Product Distribution and Reaction Pathways for Methylene Chloride Hydrolysis and Oxidation Under Hydrothermal Conditions" *J. of Supercritical Fluids* **12**, 239-254, 1998.

J.W. Tester, P.A. Marrone, M.M. DiPippo, K. Sako, M.T. Reagan., T. Arias, W.A. Peters, "Chemical Reactions and Phase Equilibria of Model Halocarbons in sub- and Supercritical Water (200 to 250 bar, 100 to 600 °C)" *J. of Supercritical Fluids* **13**, 225-240, 1998.

## 8.2 Chlorinated species

### 8.2.1 - Experiments of hydrolysis of $\text{CH}_2\text{Cl}_2$ in sub- and supercritical water

An important aspect of the SCWO of halogenated species surrounds the competition between oxidation reactions, that ultimately produce CO and  $\text{CO}_2$ , and hydrolysis which is merely the substitution of the halogen atoms with oxygen. In the case of methylene chloride ( $\text{CH}_2\text{Cl}_2$ ), for example, hydrolysis is represented by the conversion of  $\text{CH}_2\text{Cl}_2$  to formaldehyde ( $\text{CH}_2\text{O}$ ). Although this is technically removal of the organo-halogen species, it is only part of the overall process needed for waste destruction. The MIT group has conducted a in-depth evaluation of the hydrolysis of methylene chloride to lay the backbone of the fundamental understanding of the nature of this process in sub- and supercritical water.

Data from both oxidation and hydrolysis experiments of methylene chloride were to evaluate the competing role of hydrolysis during SCWO of this feed. Specifically, typical SCWO application methods proscribe the preheating of the feed which exposes tubing and piping to both sub- and supercritical conditions. The experiments conducted on methylene chloride used the MIT tubular reactor system at 24.6 MPa and a temperature range from ambient to 600°C. Residence times varied from 7 to 17 s during heatup and 4 to 9 s at final (isothermal) temperature.  $\text{CH}_2\text{Cl}_2$  conversions

ranged from  $26 \pm 9\%$  to  $99.9 \pm 0.1\%$ . Product species were analyzed by gas chromatography.

The experiments revealed that significant conversion occurs in the non-isothermal preheater tubing section under subcritical conditions, as well as in the supercritical isothermal section maintained at a temperature between  $450$ - $600^\circ\text{C}$ . Oxygen ( $\text{O}_2$ ) (added at the beginning of the isothermal section) has a significant effect on  $\text{CH}_2\text{Cl}_2$  conversion only at temperatures above  $525^\circ\text{C}$ . Major products from  $\text{CH}_2\text{Cl}_2$  hydrolysis and oxidation are formaldehyde ( $\text{HCHO}$ ), hydrochloric acid ( $\text{HCl}$ ), carbon monoxide ( $\text{CO}$ ), carbon dioxide ( $\text{CO}_2$ ), methanol ( $\text{CH}_3\text{OH}$ ), and molecular hydrogen ( $\text{H}_2$ ), with small amounts of methane ( $\text{CH}_4$ ) observed at temperatures above  $562^\circ\text{C}$ . For the conditions studied, essentially all the chlorine is converted to  $\text{HCl}$  with only trace quantities of chloromethane ( $\text{CH}_3\text{Cl}$ ), chloroform ( $\text{CHCl}_3$ ), 1,1-dichloroethylene ( $\text{C}_2\text{H}_2\text{Cl}_2$ ), cis-1,2-dichloroethylene, trans-1,2-dichloroethylene, and trichloroethylene ( $\text{C}_2\text{HCl}_3$ ) detected in the gaseous product stream. Under oxidation conditions, essentially all of the carbon is converted to  $\text{CO}_2$  by a final temperature of  $600^\circ\text{C}$  and a total residence time of 23 s.

The occurrence of  $\text{CH}_2\text{Cl}_2$  hydrolysis during heatup at subcritical conditions was evidenced by: 1) similar reaction products, i.e.  $\text{HCHO}$  and  $\text{HCl}$ , to those identified in literature studies of  $\text{CH}_2\text{Cl}_2$  hydrolysis under subcritical conditions; 2) corrosion in the preheater tubing attributed to  $\text{CH}_2\text{Cl}_2$ -derived  $\text{HCl}$ ; and 3) similar  $\text{CH}_2\text{Cl}_2$  conversions with and without heating in the supercritical isothermal section.  $\text{CH}_2\text{Cl}_2$  temperature-time histories in the heatup section were determined from heat transfer calculations.

An extensive literature search was conducted to find heat transfer correlations for water under sub- and supercritical conditions to better quantify the hydrolysis kinetics. These correlations were needed to model the temperature-time history of the feed solution in the preheater tubing. More than one correlation was needed to account for the different physical and geometric conditions that exist at different positions in the preheater tubing. Together these correlations allow calculation of the internal heat transfer coefficient and take into account the following: flow regime (laminar or turbulent); tube orientation (horizontal or vertical); direction of flow (up or down for vertical orientation); the presence of mixed convection (forced and natural); heat transfer effects near the critical point; and the lowering of the transition to turbulence under conditions where natural convection is significant. The constant external heat transfer coefficient was fit to the experimental data so as to match the measured temperature at the end of the preheater tubing. The fitted values were found to be in very good agreement with what would be expected for tubing in a fluidized sandbath under these conditions.

These heat transfer coefficient values were used in a differential heat balance to predict the temperature and time profiles as a function of position in the preheater tubing. These profiles help us to explain some of the unusual trends observed in experimental conversion values, and to correctly predict high, but subcritical, temperatures. This

more detailed analysis confirmed that almost all of the observed hydrolysis reactivity occurred at lower temperatures and that hydrolysis was suppressed at supercritical temperatures and 24.6 MPa.

### 8.2.2 - Hydrolysis model - molecular scale

The fact that hydrolysis conversion of  $\text{CH}_2\text{Cl}_2$  was very low under supercritical conditions is actually not that surprising when considering the effects on this reaction of the changing nature of the water environment as temperature increases. The transition state complex formed from the reaction of  $\text{CH}_2\text{Cl}_2$  and  $\text{H}_2\text{O}$  is more polar (higher charge density) than either of the two reactants. Therefore, a decrease in the water solvent polarity (as occurs with increasing temperature near the critical point and beyond) results in less stabilization of the transition state and consequently a slower reaction rate relative to that in lower temperature liquid water.

To quantify this effect, one needs to incorporate a correction factor into the standard Arrhenius form of the reaction rate constant. This correction factor is based on the change in the Gibbs free energy,  $\Delta G$ , involved in transferring a molecule from a medium of dielectric constant  $\epsilon=1$  (vacuum) to a medium of greater dielectric constant  $\epsilon$ , and can be derived from a combination of electrostatics and transition state theory. The actual form of the correction factor depends on the dielectric constant and temperature of the medium, as well as the dipole moment ( $\mu$ ) and radius ( $r$ ) of both reactants and the transition state complex. This correction factor to the standard Arrhenius rate constant is derived from a combination of Kirkwood and Transition State theories.

*Ab initio* electronic structure calculations were used to model the form and properties of the transition state species of the hydrolysis reaction. The results of these calculations agree very well with both theories regarding the nature of the  $\text{CH}_2\text{Cl}_2$  hydrolysis reaction and our own experimental findings. The transition state position (identified as the local maximum in energy along the reaction coordinate, see Figure 8.1) is calculated to occur between a carbon atom and oxygen atom separation distance of 1.72 - 1.63 Å at 25 - 600°C respectively, compared to a value of 1.8 Å predicted by other theories. The calculated dipole moment of the transition state species varies between 8.2 - 9.9 Debye over the same temperature range, which is much greater than reactant values of 1.6 Debye for  $\text{CH}_2\text{Cl}_2$  and 1.85 Debye for  $\text{H}_2\text{O}$ , as expected. The planar structure of the transition state, followed by a stereochemical inversion of position of all non-leaving substituents on the  $\text{CH}_2\text{Cl}_2$  molecule, resulting from the calculations is consistent with that for an  $\text{S}_{\text{N}}2$  reaction. The calculated activation energy increases from about 125 to 188 kJ/mol (30 to 45 kcal/mol) over the range of 25 - 600°C. This increasing activation energy, along with a decreasing distinction between maximum and minimum points in the energy profile with increasing temperature (Figure 8.1), indicates that the hydrolysis reaction rate should become slower with increasing temperature, as was observed experimentally. This result is quantitatively expressed through the increasingly negative value of the correction factor with increasing temperature. By 550°C, the reaction rate calculated using the correction factor is predicted to decrease by about



3700 compared to that calculated using just the usual Arrhenius form for the rate constant alone.

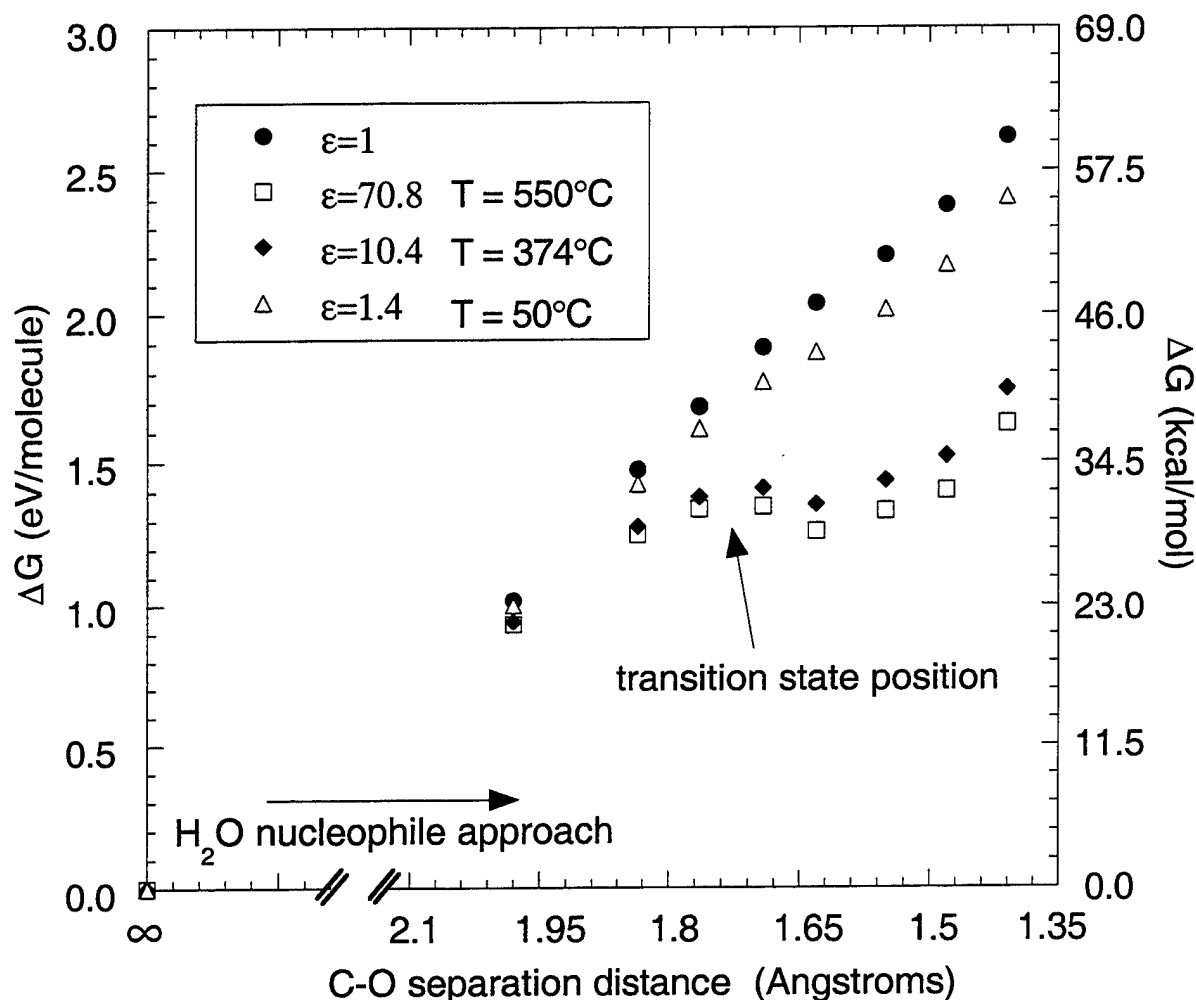


Figure 8.1 Total energy with Kirkwood correction factor vs. relative position of  $\text{CH}_2\text{Cl}_2$  and  $\text{H}_2\text{O}$  at different dielectric constants.

### 8.2.3 - Global model

The original motivation for this  $\text{CH}_2\text{Cl}_2$  hydrolysis modeling was to account for the significant hydrolysis reaction observed experimentally under subcritical conditions and very little reaction observed under supercritical conditions. As described above, such an effect is not unusual for this type of reaction. The loss of polarity of water as it is heated through the critical point should result in a reduced reaction rate because of the decreasing stability of the polar transition state complex in the increasingly less polar water solvent. With the proper value and functional form with temperature for the Kirkwood correction factor now determined, we used the correction factor, along with the heat transfer model previously developed for experimental temperature-time

predictions, to determine a global hydrolysis rate expression by nonlinear regression of the experimental data.

The form of the rate expression used in the nonlinear regression is as follows:

$$d[\text{CH}_2\text{Cl}_2]/dt = -A \exp((E_a + KC(T))/RT) [\text{CH}_2\text{Cl}_2]^a [\text{H}_2\text{O}]^b \quad (8.1)$$

where  $A$  is the pre-exponential factor,  $E_a$  is the activation energy at 25°C,  $KC(T)$  is the Kirkwood correction factor, and  $a$  and  $b$  are the reaction orders of  $\text{CH}_2\text{Cl}_2$  and  $\text{H}_2\text{O}$  respectively. The regression program determines optimized values of  $E_a$ ,  $A$ ,  $a$ , and  $b$  through an iterative scheme while taking account of reaction in both the non-isothermal preheater and the isothermal supercritical main reactor. Determining a meaningful value of  $b$  has been difficult because of the high water concentration ( $\sim 1000$  greater than  $[\text{CH}_2\text{Cl}_2]$ ) in the dilute solutions used and the fact that it is highly correlated with  $E_a$  and  $A$ . Setting  $b = 1$  (its theoretical value for an  $\text{S}_{\text{N}}2$  reaction) leads to values for the remaining kinetic parameters of  $E_a = 209 \pm 48$  kJ/mol,  $A = 10^{16.3 \pm 5.7} \text{ L}^{1.49} / \text{mol}^{1.49} \text{ s}$ , and  $a = 1.49 \pm 0.86$ . With  $a$  also set equal to its theoretical value of 1 (which lies within the uncertainty of its regressed value),  $E_a$  and  $A$  become  $180 \pm 14$  kJ/mol and  $10^{12.9 \pm 1.0} \text{ L/mol s}$  respectively. All uncertainties cited reflect 95% confidence intervals.

Both sets of parameters do a very good job at predicting the data at lower sandbath temperatures and residence times ( $< 550^\circ\text{C}$ , 11 s). Predicted  $\text{CH}_2\text{Cl}_2$  conversions at the end of the main reactor are lower than they were without the correction factor and are almost the same as that predicted at the end of the preheater, exactly as observed experimentally. At higher sandbath temperatures and residence times, the predicted conversion at the end of the main reactor still matches the experimental conversion well, but there is an increasing difference with that predicted at the end of the preheater, which was not observed experimentally. This suggests that values of the correction factor at higher temperatures may not be large enough. Also, both values of  $E_a$  from the two regressions cited above are higher than that of 130 kJ/mol determined from a combination of vacuum *ab initio* calculations and Kirkwood theory.

#### 8.2.4 Oxidation

Because of the significant hydrolysis in the preheater, there was only a relatively small concentration of  $\text{CH}_2\text{Cl}_2$  left (between 0.2 - 0.6 mM) by the time the feed reached the supercritical main reactor where  $\text{O}_2$  was first introduced in the experimental runs. There was also a significant amount of HCHO and other hydrolysis/pyrolysis products present in the feed at the entrance to the main reactor. Thus, the oxidation was not of pure  $\text{CH}_2\text{Cl}_2$  but of a mixture of intermediate hydrolysis products. This fact may therefore have an effect on the values of the optimized oxidation kinetic parameters determined, and their reliability for describing oxidation of more concentrated solutions of  $\text{CH}_2\text{Cl}_2$ .

The experimental data show  $\text{CH}_2\text{Cl}_2$  effluent concentrations from oxidation experiments to be statistically the same as that observed in corresponding hydrolysis experiments up to sandbath temperatures of  $525^\circ\text{C}$  and total residence times of up to

16 s (6 s exposed to O<sub>2</sub>). At higher temperatures and residence times, CH<sub>2</sub>Cl<sub>2</sub> conversion under oxidation conditions increases (relative to that from hydrolysis) until complete conversion is seen by 562°C, 18 s total residence time (6 s exposed to O<sub>2</sub>). This behavior suggests an oxidation reaction with a high activation energy. Our results from the regression program agree with this, predicting an optimal value for the oxidation activation energy of 673 kJ/mol.

Work at MIT has continued since the completion of this part of the project supported by SERDP. With the support of additional sponsors, this picture of oxidation of CH<sub>2</sub>Cl<sub>2</sub> has been confirmed and the direct oxidation of methylene chloride is indeed quite slow. We conclude that a good strategy for processing halogenated wastes will necessarily involve a sub-critical hydrolysis step.

## Section 8.3 Nitrogen and SCWO

### 8.3.1 N<sub>2</sub>O stability in supercritical water

Our initial hypothesis for the formation of N<sub>2</sub> from nitrates in SCWO was that nitrates sequentially were reduced to form N<sub>2</sub>O and that N<sub>2</sub>O was the final intermediate in this process. We also suspected that it was likely that this final step might be rate limiting. As it is common in some examples of SCWO of energetics materials to see N<sub>2</sub>O in the gaseous effluent,<sup>3</sup> it seemed reasonable that quantifying the conversion of N<sub>2</sub>O to N<sub>2</sub> at typical SCWO conditions was the first place to start.

The Sandia team initiated this investigation of the stability of N<sub>2</sub>O decomposition to N<sub>2</sub> and O<sub>2</sub> in supercritical water by comparing our results to low-pressure high-temperature gas phase data reported by Johnsson et al.<sup>5</sup> We made a number of simple measurements that consisted of recording the time evolution of approximately 1-2% N<sub>2</sub>O in supercritical water in to 400 -550 °C temperature range. The experiments were conducted similarly to the previous kinetics experiments we have done when long reaction times are involved such as the water-gas shift experiments. We used the SCVR as the optically accessible reaction vessel and monitored the kinetics of the reaction using Raman spectroscopy. A fixed pressure of N<sub>2</sub>O was placed in the reactor and water was injected to bring the pressure to 3800 psi. The reaction times scale is on the order of hours. However, we conclude that there is an apparent increase, by about a factor of 15, in the reaction rate in supercritical water relative to the rate obtained by extrapolating the Johnsson et al. data to lower temperature, making no adjustment for effects of elevated pressure. A more recent publication by Allen et al.<sup>6</sup> and coworkers revisiting this topic indicates that the high-pressure limit for the thermal decomposition of N<sub>2</sub>O follows the expression:

$$k_{\infty} \text{ (s}^{-1}\text{)} = 7.91 \times 10^{10} \exp \left( -56020 \text{ (cal/mol)} / RT \right). \quad (8.2)$$

They report a 30% error estimate using data determined in the temperature range of 830 °C - 900 °C. They also explored the effect of water vapor on the reaction rate and found no particular enhancement in the rate that could be ascribed to the presence of water in

this temperature range. They suggest that the elementary reaction (Eq. 8.3) that depends on the presence of water that could enhance the decomposition reaction is very likely to be much slower than previously thought.

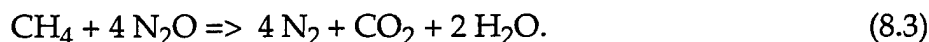


Inserting an experimental temperature of 515 °C into  $k_\infty$  expression above yields a reaction rate constant of  $2.29 \times 10^{-5} \text{ s}^{-1}$ . This compares exceptionally well with our value of  $2.3 \times 10^{-5} \text{ s}^{-1}$  obtained from a 17-hour experiment in supercritical water in which the temperature varied from 513 °C to 517 °C. Clearly, the presence of water does not affect the reaction chemistry of  $\text{N}_2\text{O}$  decomposition at low temperatures, even at very high densities, contradicting the results of Johnsson and in excellent agreement with Allen.

### 8.3.2 $\text{N}_2\text{O}$ and methane experiments

The next step was to determine the reactivity of  $\text{N}_2\text{O}$  as an oxidizer in an SCWO system. Using a method similar to the decomposition experiments above, but with a greater concentration of  $\text{N}_2\text{O}$ , we prepared the SCVR with approximately 725 psi of  $\text{N}_2\text{O}$  at the reaction temperature of interest. Methane, prepressurized to 4500 psi, was then injected into the supercritical mixture to reach the final composition in the pressure range from 4200-4600 psi. The pressure was observed to rise several hundred psi over the course of the reaction. Raman spectroscopic measurements were conducted, as we have done previously, using the same system response calibration methods described in Section 2.

Figure 8.2 shows the concentration of methane as a function of time during oxidation by  $\text{N}_2\text{O}$  at 500 °C and 4330 psi. The figure also shows the concentrations calculated assuming complete conversion to  $\text{CO}_2$  according to the equation



In this particular experiment there is insufficient  $\text{N}_2\text{O}$  to fully convert all of the  $\text{CH}_4$  to  $\text{CO}_2$ . It appears that the final  $\text{CH}_4$  concentration is only roughly approaching the expected limit, but is likely to have a final value less than the simple stoichiometry predicted by Eq. 8.3. Thus, we can speculate that some CO being formed as an intermediate, as evidenced by the fact that the calculated  $\text{N}_2\text{O}$  concentration appears to pass through zero. This can be interpreted as indicating an oxidation process having two steps, comparable in rate. The first step removes methane to form intermediates and a second results in the final products. Figures 8.3 and 8.4 show the  $\text{CH}_4$  concentration at 520 °C as a function of time for lower concentration of initial fuel such that there is an excess of  $\text{N}_2\text{O}$  present. Note that the loss of  $\text{CH}_4$  is almost linear in time. Figures 8.5 and 8.6 were recorded at a slightly higher temperature, 540 °C, for two different initial  $\text{CH}_4$  concentrations, but still at lean conditions. The 540 °C rate is clearly greater than at 520 °C, but is still clearly not first-order in methane. In Fig. 8.5 and 8.6, the initial rates of methane conversion, obtained by fitting the first 300 seconds of reaction time, are approximately  $1.1 \times 10^{-4}$  and  $1.0 \times 10^{-4} \text{ mol/l-s}$  respectively.

Comparison of the data in Figures 8.2-8.6 clearly indicates that the kinetics are not first order in methane. In fact, the oxidation appears to be near zeroth order in  $\text{CH}_4$  and perhaps first order in  $\text{N}_2\text{O}$ .

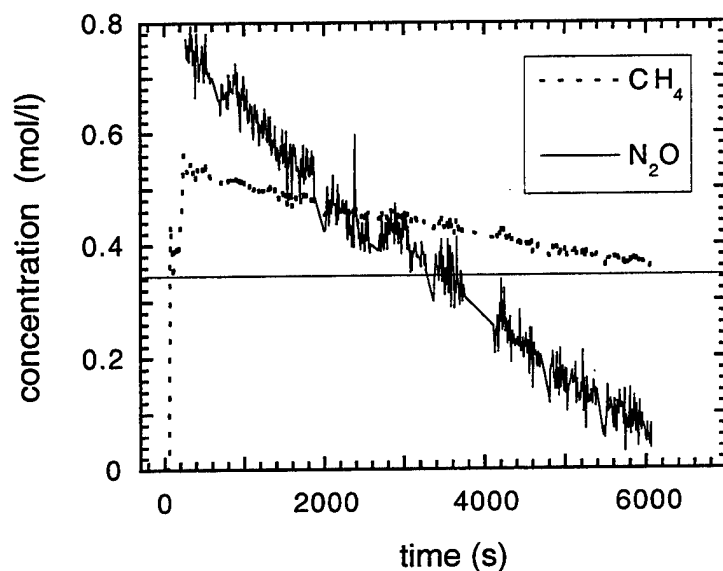


Figure 8.2 Evolution of the concentration of  $\text{CH}_4$  with time at  $500^\circ\text{C}$  and 4330 psi measured in Sandia's SCVR experiments. Also included in the figure is the calculated concentration of  $\text{N}_2\text{O}$  based on the conversion stoichiometry in Eq. 8.3. The line drawn on the figure represents the concentration of  $\text{CH}_4$  expected to remain after all of the  $\text{N}_2\text{O}$  is consumed.

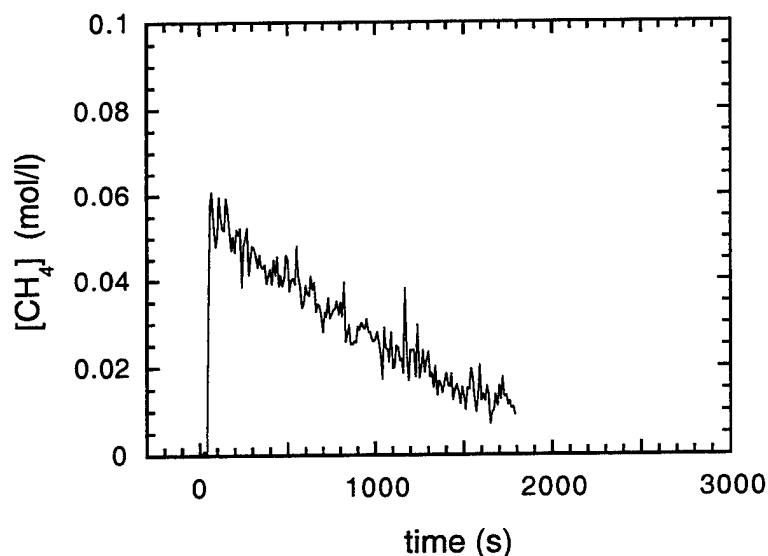


Figure 8.3 Evolution of the concentration of methane with time at  $520^\circ\text{C}$  and approximately 4500 psi, measured in SCVR experiments.

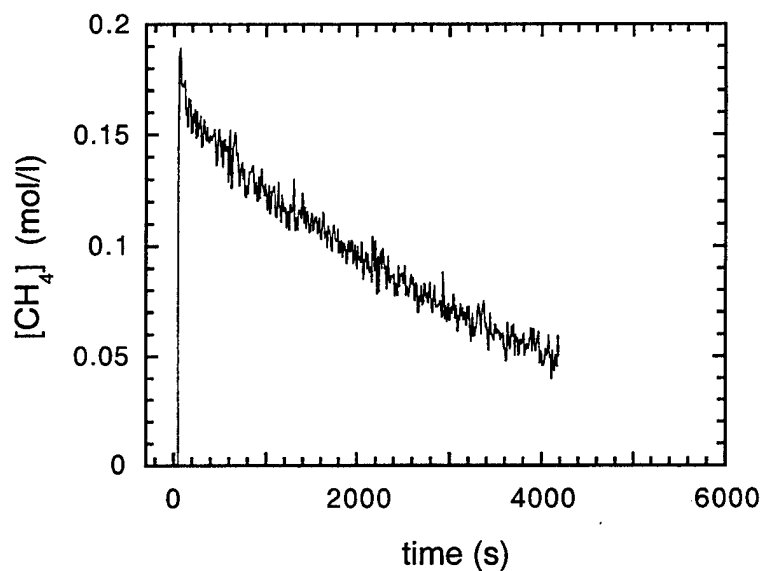


Figure 8.4 Evolution of the concentration of methane with time at 520 °C and approximately 4500 psi, measured in SCVR experiments, with a greater amount of initial  $\text{CH}_4$  than in Fig. 8.3.

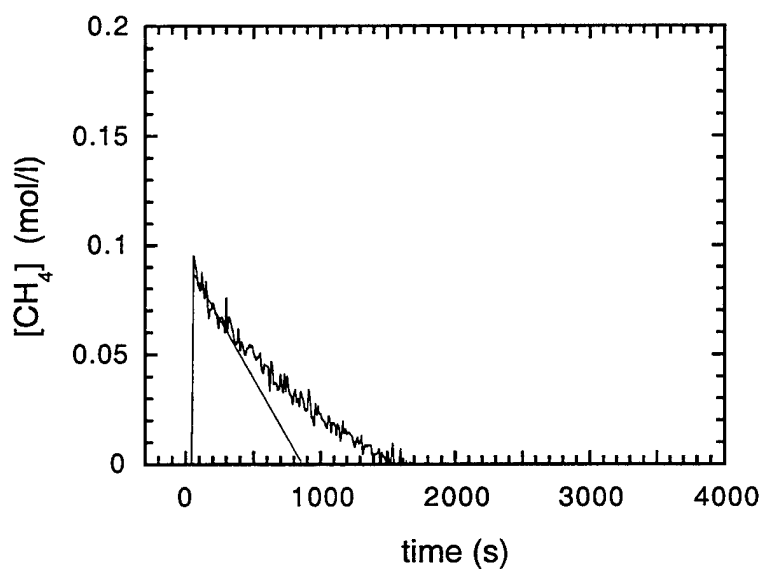


Figure 8.5 Evolution of the concentration of methane with time at 540 °C and 4500 psi, measured in SCVR experiments. The straight line is a fit to the initial 300 s of the reaction.

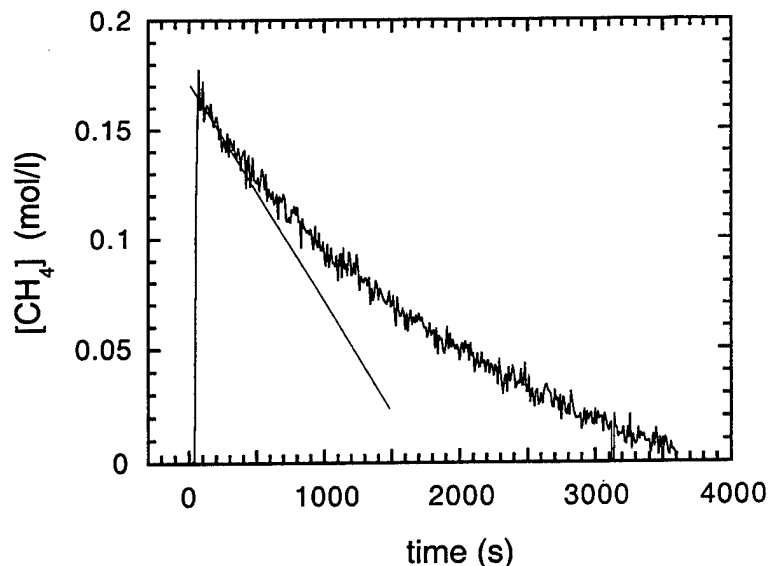
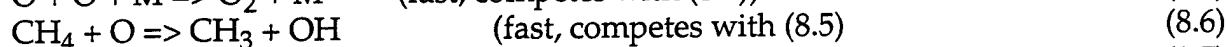
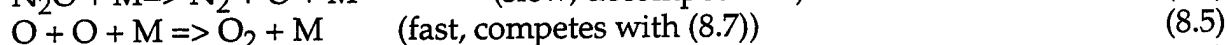
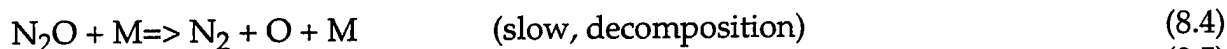


Figure 8.6 Evolution of the concentration of methane with time at 540 ° C and 4500 psi, measured in SCVR experiments. The straight line is a fit to the initial 300 s of the reaction.

A very simple reaction scheme that is consistent with the zeroth order kinetics that we observe can be represented by reactions 8.4-8.8 below.



This scheme can account for the formation of a fairly stable intermediate, such as CO as suggested by Figure 8.2. We know from Section 4 that Reaction 8.8 forms no accumulation of transient CO. That is to say, the rate-limiting step the of the Eq. 8.8 global process is the initial H-atom abstraction from methane to form methyl radical. In order to have accumulation of CO, the overall loss of methane needs to have a comparable rate. The scheme above provides this by permitting rapid abstraction of H from  $\text{CH}_4$  by O atoms that are directly generated from the thermal decomposition of  $\text{N}_2\text{O}$ . Thus producing a very reactive radical, albeit at a slow rate.

### 8.3.3 $\text{N}_2\text{O}$ and methane modeling

In our earlier analysis of the oxidation of methane and methanol by  $\text{O}_2$  in SCWO, we used a slightly modified C1 mechanism developed for combustion: the GRI 1.2. Subsequent to the development of GRI 1.2 the same team issued GRI 2.11, which contains a significant amount of  $\text{N}_2$  and  $\text{NO}_x$  chemistry. This mechanism has been

developed to predict the formation of NO<sub>x</sub> in methane/air combustion. As a result, it contains a fairly complete set of reactions involving N<sub>2</sub>O and methane.

Figure 8.7 shows the calculated evolution of the carbon-containing species during the reaction of methane with N<sub>2</sub>O in supercritical water calculated using the GRI 2.11 mechanism. The model predicts the conversion rate to be about a factor of two slower than is observed at 520 °C, which is in adequate agreement with the data to infer that much of the important chemistry is qualitatively correct.

An examination of the pathways in the GRI mechanism indicate that the process is probably more complicated than our simple picture (Eq. 8.4 -8.8) suggests.

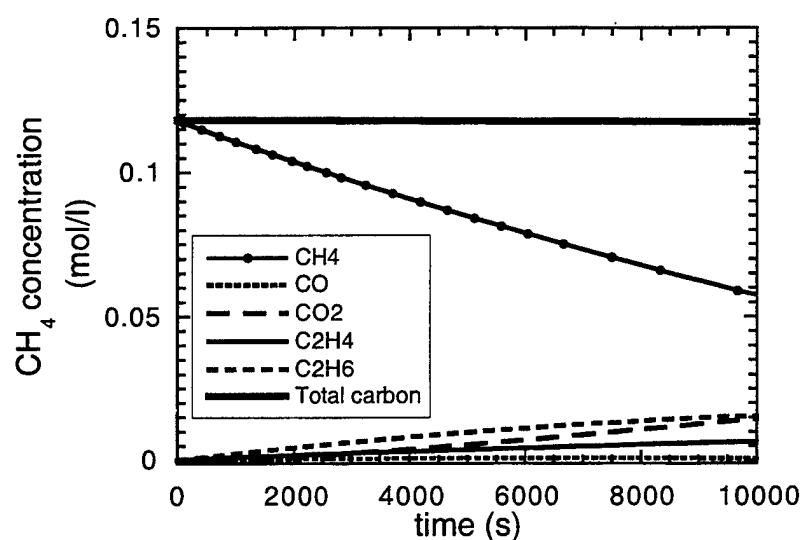
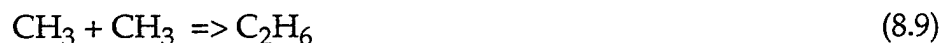


Figure 8.7 Evolution of carbon-containing species as a function of time at 520 °C and 31.0 MPa in the presence of 5.0 MPa partial pressure of N<sub>2</sub>O as calculated using the GRI 2.11 mechanism for the conditions present in Fig 8.4.

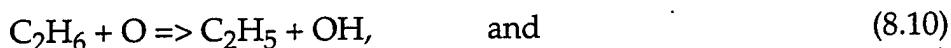
The GRI 2.11 mechanism shows the process to be controlled by the N<sub>2</sub>O thermal decomposition and then followed by reaction 8.6, as is described in the simple scheme, but the subsequent fate of the CH<sub>3</sub> radical is different

Early in the reaction, the conversion rate is still most sensitive to Eq. 8.4 followed by reaction (8.6), but reactions (8.7) and (8.8) are insignificant. The GRI 2.11 mechanism dictates that CH<sub>3</sub> radical chemistry is dominated by recombination

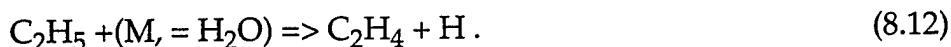


and subsequent oxidative dehydrogenation described in reactions 8.10 – 8.12.





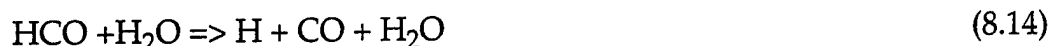
followed by



The small production of  $\text{CO}_2$  is the result of oxidation chemistry from



and subsequent reaction of HCO:



As the reaction progresses from the initial feed conditions, there is a steady increase in the concentration of OH. This is brought about by reactions 8.12, 8.14, and 8.15 forming H followed by



The consumption of  $\text{CH}_4$  then becomes dominated by



Interestingly, this does not add to an increase in the conversion rate or any oxidation since  $\text{CH}_3$  recombination still dominates the carbon pathway.

During the experiment shown in Fig. 8.4, we did not continuously monitor the other species. However, at the end of the reaction we measured no CO, but surprisingly, a  $\text{CO}_2$  concentration that roughly corresponded to 1/10 of the initial  $\text{CH}_4$  concentration. Clearly, there was a lot of carbon missing. We can speculate that the missing carbon may be accounted for as  $\text{C}_2\text{H}_6$  and  $\text{C}_2\text{H}_4$ , but no attempts to measure the presence of higher hydrocarbons were made.

In general, however, it appears the elementary reaction model may capture the behavior most of the methane/ $\text{N}_2\text{O}$  system, predicting very slow oxidation to  $\text{CO}_2$  and mostly methyl radical coupling to ethane and ethylene. The difference in the observed conversion rate at 520 °C and the model prediction of about a factor of two may be directly related to the present accuracy of the parameters used for the  $\text{N}_2\text{O}$  thermal decomposition rate (Eq. 8.4) at these conditions in the mechanism.

We note that the GRI 2.11 mechanism, as used in this calculation, assumes an ideal gas equation of state with P and T as the state variables. This results in a water density of

only about 75% of the actual water density at these nonideal conditions. We have examined the effect of simply repeating the calculation at higher total pressure and corresponding increased water mole fraction and have found no effect on the reaction rate of  $\text{CH}_4$  and only a several percent increase in the production rates of  $\text{C}_2\text{H}_4$  and  $\text{C}_2\text{H}_6$ .

#### 8.3.4 Methanol oxidation by $\text{N}_2\text{O}$

The  $\text{N}_2\text{O}$  oxidation measurements were extended to methanol to explore the comparison of the GRI 2.11 model predictions in this more reactive system. In the work conducted on methanol oxidation by oxygen, we found that the GRI 1.2 model produced good agreement with methanol oxidation rates if a key reaction of methanol with  $\text{HO}_2$  was added. We have compared this elementary reaction mechanism (with nitrogen chemistry added in the 2.11 release) for methanol oxidation by  $\text{N}_2\text{O}$  and found that agreement between the model and the experimental results is poor. However, our experiments show that the conversion rate for methanol in supercritical water in the absence of oxygen appears to be independent of  $\text{N}_2\text{O}$  concentration; the presence of  $\text{N}_2\text{O}$  simply serves to change the product spectrum.

Figure 8.8 shows the integrated Raman intensity of the methanol band at  $2940\text{ cm}^{-1}$  and the intensity of the methane band at approximately  $2915\text{ cm}^{-1}$  as a function of time subsequent to the addition of methanol to a mixture of supercritical water and  $\text{N}_2\text{O}$  at 31.0 MPa and  $500^\circ\text{C}$ . The figure also includes the corresponding Raman band intensities in supercritical water with no  $\text{N}_2\text{O}$ . On the basis of these data, we may infer the rate of reaction of methanol under these conditions and recognize that the overall conversion is much faster than observed for methane.

In the absence of  $\text{N}_2\text{O}$ , methanol is converted to a product mixture of  $\text{CH}_4$ ,  $\text{H}_2$ , and  $\text{CO}$  in supercritical water with little or no  $\text{CO}_2$  being formed at this temperature. In the presence of  $\text{N}_2\text{O}$ , there appears to be little increase in the reaction rate, but the product mix shows significant oxidation. Note that little  $\text{CH}_4$  is formed. The final concentration of  $\text{CO}_2$  was measured and found to be about 50% of the initial methanol concentration with no  $\text{CO}$  or  $\text{H}_2$  detected. We have been unable to account for the missing carbon. However, we did not attempt to measure the presence of formaldehyde which may very likely be present during the partial oxidation of methanol. We also did not look for higher hydrocarbons (e.g. ethane) as we have suggested might be present with methane.

In contrast, the GRI model predicts conversion of methanol only to  $\text{CO}$  and  $\text{H}_2$  with a rate that is significantly enhanced in the presence of  $\text{N}_2\text{O}$  and is much faster than the observed conversion, see Fig. 8.9. The GRI model predicts simple pyrolysis in pure supercritical water to proceed about a factor of 10 slower than is observed, but it is important to remember that the GRI model is designed for methane oxidation and is not designed to accommodate methanol reactivity specifically. Many methanol pyrolysis and oxidation reactions that may be important in this slow, low temperature chemical system are not included. However, it is surprising that it is predicting more rapid chemistry than is observed with  $\text{N}_2\text{O}$  in the mixture.

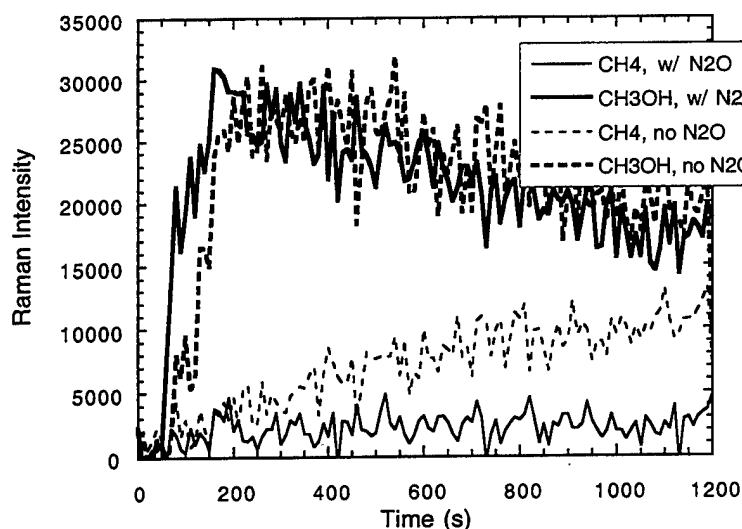


Figure 8.8 Experimental evolution of methane and methanol as a function of time at 500 °C and 31.0 MPa in supercritical water with and without the presence of 5.0 MPa partial pressure of N<sub>2</sub>O.

### 8.3.5 N<sub>2</sub>O Summary

It appears that the GRI 2.11 mechanism represents the methane chemistry fairly well, but it is surprising that the model does not handle the methanol reactivity very well. Regardless of the accuracy of the model, however, it is clear that N<sub>2</sub>O is not an especially reactive species at these conditions, and if formed during the oxidation of nitrogen-containing organics, it will not be converted easily to N<sub>2</sub>. This result has important implications regarding the final gaseous effluent of SCWO equipment designed to process energetic materials and potential DOE wastes containing nitrate ions.

N<sub>2</sub>O is recognized as a "greenhouse gas" and, per molecule, is much more effective at playing a role in global warming models than is CO<sub>2</sub>. There has been a steady increase in atmospheric N<sub>2</sub>O since 1850 and the rate has been about twice as fast as CO<sub>2</sub>. It has been speculated the N<sub>2</sub>O may also contribute to stratospheric ozone depletion. About half of the atmospheric N<sub>2</sub>O originates from soil (fertilizer use is primary in the increase in the last 100 years) and half from combustion sources. In the future, greater regulatory scrutiny of N<sub>2</sub>O sources may occur.

One of the main attractive features of SCWO is the relatively harmless gaseous effluent that is produced and there are a number of reports that show little or no NO<sub>x</sub> vapor effluent is produced. The processing of nitro-containing explosives formulations for DoD applications may, under certain conditions produce a great deal of N<sub>2</sub>O. In all likelihood this is probably a very small amount relative to other N<sub>2</sub>O sources, such as industrial energy use and agriculture which produce 1.3 x10<sup>6</sup> metric tons per year

domestically. It should be made clear, however, that once produced in an SCWO environment,  $N_2O$  does not rapidly convert to  $N_2$  and if low  $N_2O$  effluent is desired, simply increasing typical SCWO reaction times from 10 to 20 seconds will not reduce these emissions substantively.

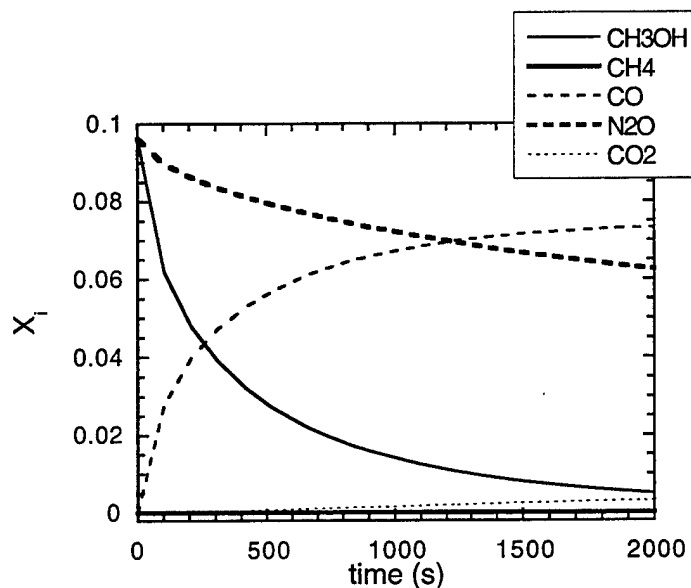


Figure 8.9 Evolution of methane as a function of time at 500 °C and 31.0 MPa in the presence of 5 MPa partial pressure of  $N_2O$ , as calculated using the GRI 2.11 mechanism.  $X_i$  refers to the mole fraction of a particular species. The initial mole fraction of methanol is 0.095 and the  $N_2O$  concentration is near the initial values used in the experimental measurements in Fig. 8.8.

### 8.3.6 Nitromethane oxidation and pyrolysis.

The goal of this work was to gain insight into the reaction kinetics of a model energetic material to develop a picture of the reduction of oxidized nitrogen to  $N_2$  in supercritical water. This is highly desirable because of the interest in using SCWO to dispose of munitions and rocket motors which contain a variety of compounds consisting of  $NO_2$  groups attached to aromatic rings.

The approach was to use nitromethane as a simple energetic compound in the SFR and monitor the formation of intermediates and products as we had successfully done on the previous systems described above. A kinetic scheme would be developed based on the observed disappearance of  $CH_3NO_2$  and the rate of production and partitioning of the feed nitrogen into the various nitrogen oxides and  $N_2$ .

This effort is the only significant disappointment within the scope of the overall project. Feeding nitromethane into the SFR proved to be exceptionally problematic. After many attempts to complete these experiments, the effort was abandoned. Major changes to

the experimental procedure and equipment would be needed to move forward and these changes were beyond the scope and budget of the project.

Although it was determined to be easy to monitor  $\text{CH}_3\text{NO}_2$  in supercritical water using Raman spectroscopy and begin to measure its pyrolysis and oxidation, it was not possible to operate the reactor in a safe manner for any significant length of time. In the updated feed configuration that was used to minimize hydrolysis in the SFR, every attempt to feed high concentration of  $\text{CH}_3\text{NO}_2$  in the HPLC pump injector resulted in an explosion in the injector capillary. All of these small explosions were easily contained by the reactor shield, but were clearly not acceptable operating procedure. Attempts to cool the injector line until immediately prior to the reactor were unsuccessful.

We strongly recommend that any attempts by any researcher in the field of SCWO kinetics carefully plan for these types of events to occur when studying nitrated organics. The entire experiment should be conducted within a certified explosives cell, which would constitute the minimum starting point for the development of a safe experimental procedure.

#### 8.4 References

1. P.A. Marrone, P.M. Gschwend, K.C. Swallow, W.A. Peters, J.W. Tester "Product Distribution and Reaction Pathways for Methylene Chloride Hydrolysis and Oxidation Under Hydrothermal Conditions" *J. of Supercritical Fluids* **12**, 239-254, 1998.
2. J.W. Tester, P.A. Marrone, M.M. DiPippo, K. Sako, M.T. Reagan, T. Arias, W.A. Peters "Chemical Reactions and Phase Equilibria of Model Halocarbons in Sub- and Supercritical Water (200 to 250 bar, 100 to 600 °C)." *J. of Supercritical Fluids* **13**, 225-240, 1998.
3. D.M. Harridine, S.J. Buelow, P.C. Dell'Orco, R.B. Dyer, B.R. Foy, J.M. Robinson, J.A. Sanchez, T. Spontarelli, J.D. Wander "Oxidation Chemistry of Energetic Materials in Supercritical Water" *Hazardous Waste and Hazardous Materials*, **10**, 223-246, 1993.
4. P.C. Dell'Orco, H.K. Eaton, R.T. Reynolds, S.J. Buelow "The Solubility of 1:1 Nitrate Electrolytes in Supercritical Water" Los Alamos National Laboratory Report LA-UR-92-3359, 1992.
5. J. E. Johnsson, P. Glarborg, K. Dam-Johansen "Thermal Dissociation of Nitrous Oxide at Medium Temperatures" Twenty Fourth Symposium (International) on Combustion, 917-923, 1992.
6. M.T. Allen, R.A. Yetter, F.L. Dryer "The Decomposition of Nitrous-Oxide at  $1.5 \leq P \leq 10.5$  atm and  $1103 \leq T \leq 1173\text{K}$ " *Int. J. Chem. Kin.* **27**, 883-909, 1995.

## ***Section 9: Computational Fluid Dynamics Modeling of Transpiration-wall SCWO Reactors***

### **9.1 Introduction**

#### ***9.1.1 Pine Bluff Arsenal background***

With management oversight from the U.S. Army Defense Ammunition Center (DAC), and leveraged support from the Environmental Security Technology Certification Program (ESTCP) Office, the U.S. Army Tank-automotive and Armaments Command, Armament Research, Development and Engineering Center (TACOM-ARDEC), in conjunction with Sandia National Laboratories and its contractors, has been developing supercritical water oxidation technology for use in the demilitarization of a variety of military smoke and dye formulations. This technology development has resulted in the design, construction, and preliminary operation of a prototype supercritical water oxidation system (SCWO) at Pine Bluff Arsenal (PBA) in Arkansas. The role of this SERDP project in this effort has been both direct and indirect. From an indirect standpoint, this SERDP project has provided a source of technical expertise for Sandia engineers and Sandia's contractors (in particular, Foster Wheeler Development Corp., FWDC) in many aspects of the basic reaction chemistry and thermochemical properties of supercritical water oxidation. In addition, experimental results from this project on alcohol reactivity have directly influenced the design of some of the critical components of the reactor itself. Over the past year, the prototype unit at PBA has been brought on line that will be capable of processing complicated feeds slated for demilitarization by the military services.

The design of this system relies on several innovations that permit the reactor to process material with high inorganic content and a wide range of heating values. Specifically, these novel design features are the use of: 1) a transpiration-wall design that can significantly mitigate scaling and corrosion as well as limit over-temperature of the reactor pressure wall; and 2) a multi-port injector that facilitates the initiation of oxidation reactions with minimum feed preheating.

This project is a joint activity of Sandia, TACOM-ARDEC, PBA, and two key private contractors, FWDC and GenCorp Aerojet. Sandia has collaborated with Foster Wheeler Development Corp. (FWDC) and Aerojet GenCorp to use Aerojet's advanced platelet transpiration-wall technology as a foundation for the system design. This section outlines the design development methods of the reactor and presents results on an approach to modeling the flow and chemistry within the reactor as a way to better understand the system operation and to point to improvements in the future.

#### ***9.1.2 Papers and Reports***

S.F. Rice, B.C. Wu, W.S. Winters, C.D. Robinson "Engineering Modeling of the Pine Bluff Arsenal Supercritical Water Oxidation Reactor" *Proceedings of The Fifth International Symposium on Supercritical Fluids* Atlanta, GA April 8-12, 2000.

C.A. LaJeunesse, B.L. Haroldsen, S.F. Rice, B.G. Brown "Hydrothermal Oxidation of Navy Shipboard Excess Hazardous Materials" Sandia Report SAND97-8212, 1997.

## 9.2 Transpiration-wall (TW) SCWO

### 9.2.1 TW concept and small scale testing

The PBA plant is unique in that it is designed for the disposal of a variety of unusual munition materials that are incompatible with more traditional disposal methods such as open burning or incineration. The transpiration-wall approach<sup>3</sup> improves on earlier SCWO pilot-level systems by integrating corrosion mitigation with a better strategy for preventing scaling and fouling due to solids accumulation. In doing so, this unit, and others that have been developed by this team, represent an innovative approach to solving these key issues that have, until now, presented significant impediments to the commercialization and acceptance of SCWO as a generally-applicable waste treatment technology.

This overall design strategy has brought to light an additional very important aspect of the practical use of SCWO. This is the issue of heat management in a high-pressure, high-temperature exothermic process. Earlier small-scale systems were essentially simple tubes that relied on an externally heated feed and oxidizer to provide the reactants with a sufficiently high mixture temperature to produce rapid oxidation and high conversion. However, the energy consumption of such a design becomes prohibitive upon scale-up from a bench system. In addition, excessive preheating of feeds to initiate rapid reaction effectively limits the concentration of the waste. This was realized first by the MODAR group a number of years ago and has been the subject of several modeling investigations. The MODAR solution was to develop an annular injector and a semi-recirculating vessel reactor that required minimal feed preheat once the reactor had reached steady-state. This idea represented a significant improvement on a simple tubular approach, but it relies on internal recirculation patterns to facilitate initiation of rapid oxidation of the incoming waste stream. These recirculation patterns caused problems with clogging of the gas effluent system.

The transpiration-wall reactor design, shown schematically in Figure 9.1, is intended to take advantage of a multiport injector to minimize preheating energy load while simultaneously maintaining turbulent plug flow to assure high conversion and greater simplicity for effluent management. By combining this feed method with a transpiration-lined vessel, low corrosion and minimal scaling can be achieved in a simple flow system with a well-defined residence time. As stated above, the PBA system is based on these two major design ideas. However, new results from fluid dynamical modeling of this system suggest that the flow in this reactor may be more complicated than originally postulated.

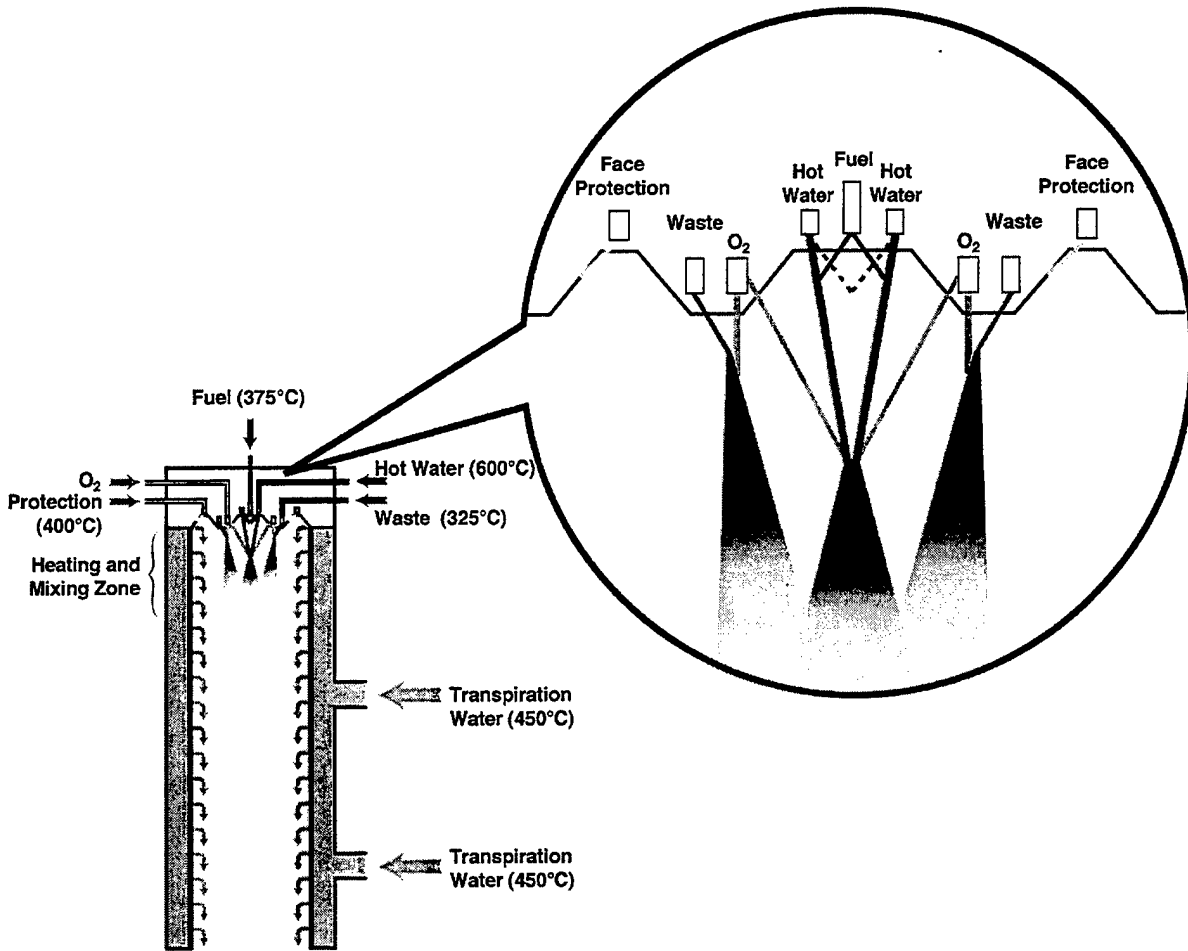


Figure 9.1 Illustration of transpiration wall design concept and the autothermal feed injector used in the PBA SCWO system.

Sandia's Engineering Evaluation Reactor (EER) demonstrated the successful operation of this design concept in 1995-1996. This small-scale system consisted of a 2.79 cm (1.1 inch) internal diameter, 91 cm (3.0 ft) long turbulent flow reactor with a nominal flow capacity of 10 g/s. A number of tests were conducted focusing on two major aspects of the system: mitigation of inorganic deposits and ease of autothermal operation. These tests showed that the transpiration-wall design was effective at reducing deposits of sodium sulfate in the feed, but indicated that transpiration flows greater than those that could be obtained in the laboratory-scale system would be necessary to fully eliminate the problem. Aerojet's experience in this technology combined with these tests led to the final flow rates used in the detailed design of the transpiration-wall platelet for PBA.<sup>4</sup>

Because of the considerable transpiration flow rate required in the full-scale system, every effort was made to reduce the amount of water needed in preheating the feeds. This constraint led to the development of a feed injector that uses a small amount of



auxiliary fuel and a small amount of 600 °C supercritical water to provide the heat needed to sustain the oxidation of the waste. Isopropanol is chosen as the fuel because it is reactive at a low temperature and has a well understood oxidation kinetics at these conditions. Successful testing of the feed injector, illustrated in Figure 9.1, at the 1.1 inch diameter scale, was demonstrated for a number of surrogate waste feeds.<sup>5</sup>

Figure 9.2 shows a typical test sequence in which a thermocouple located below the injector, inside the reactor, was used to detect reaction initiation and extinction for various flow conditions. The figure displays the internal temperature of the reactor five inches below the injector ports and the effluent total organic carbon (TOC). The results from these tests determined the flow and preheating parameters for the full-scale system. A key aspect of the of the bench-scale testing pointed to the possibility that the full-scale system could be operated with no preheating of the waste feed stream while still achieving high conversion. Note that the tests using the EER presented in Figure 9.2 were conducted using air as the oxidizer and n-propanol as the auxiliary fuel. The detailed understanding of i-propanol and n-propanol developed by this SERDP project permitted the simple substitution to i-propanol in the PBA system.

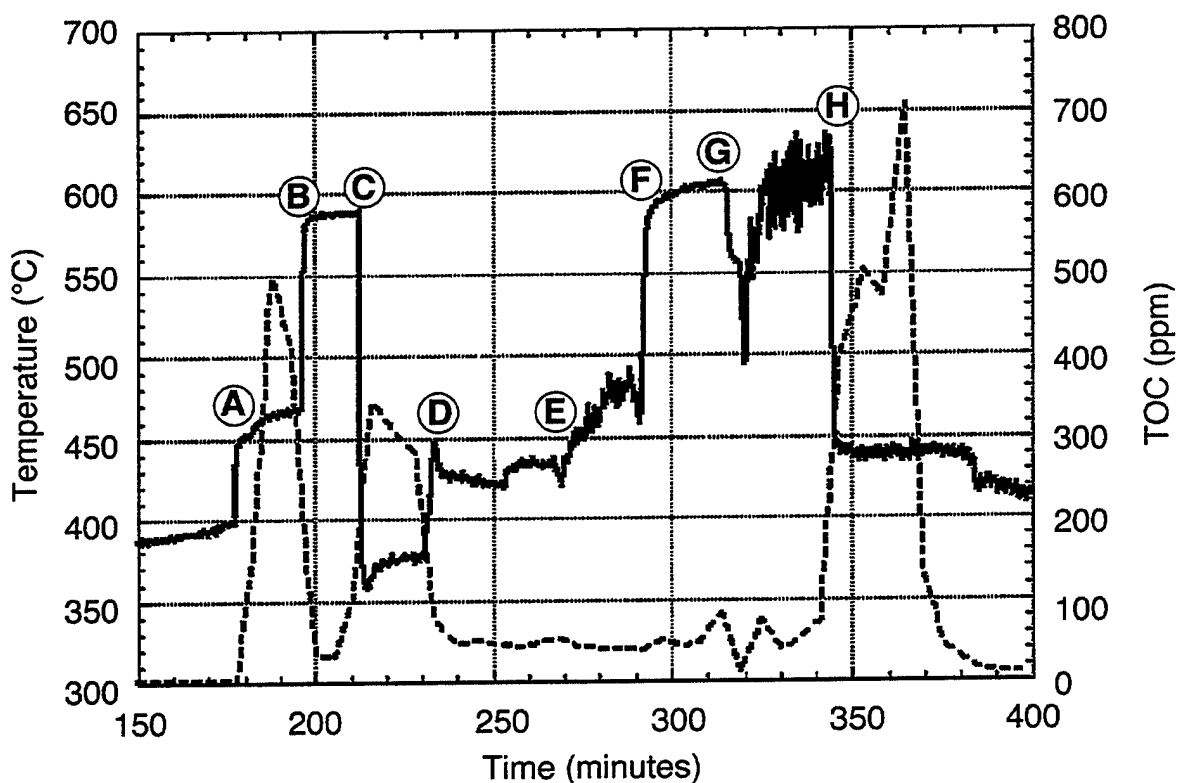


Figure 9.2. Experimental traces of the internal reactor temperature (solid line) and TOC (dashed line) during operation of the EER at a variety of feed conditions. See Table 9.1 for a description of the key operation events.

**Table 9.1 - Events on Figure 9.2 Records**

Index	Action
A	Reactor operating with preheated water and oxidizer (air). At "A" a preheated 10% solution of n-propanol and water was introduced
B	Air was introduced and oxidation of the n-propanol initiation fuel raised the temperature. TOC dropped. <sup>a</sup>
C	Pure water with no organic content was introduced through the waste injector ports. The initiation reaction was quenched. TOC increased.
D	5% methanol was added to the waste feed line. Oxidation restarted. TOC dropped.
E	Methanol concentration was increased to 10%. TOC remained low, temperature increased slowly.
F	Methanol concentration was rapidly increased to 15% TOC remains low, temperature increased abruptly.
G	Waste line was switched from 15% methanol to a 7% mixture of JP-5 jet fuel and water.
H	Air was turned off. Oxidation stopped

a - The TOC instrument was on a 0-1000 scale such that the quantitative accuracy at the lower readings is suspect, however, oxidation was probably not complete and the ~50 ppm values are close to that of the actual effluent. Residence time in this reactor was only several seconds, depending on feed rates.

### **9.2.2 Fluid dynamical modeling - preliminaries**

An important advantage of the transpiration-wall design is that the pressure vessel can be maintained at a significantly lower temperature than the reacting flow. However, this also impairs an important direct diagnostic (temperature) of the overall reactor operation. From this point of view, a large payoff can be obtained if the temperature of the flow through the reactor can be accurately estimated from the external reactor thermocouples. As a result, the final task of this project was to begin to develop a computational fluid dynamics (CFD) model coupled with a heat transport model though the platelet liner, transpiration water plenum, and pressure vessel wall to directly relate the external measurements to the internal conditions.

Several years ago, Oh and coworkers<sup>1,2</sup> generated a CFD model of the MODAR SCWO system using the commercially available code, FLUENT. That work was successful in identifying the existence of recirculation patterns within an annular injection configuration. This project attempts to build on that success and introduce more realistic reaction chemistry and well and represent the more complicated problems associated with the transpiration-wall design.

The model under development in this project includes the effects of multispecies flow, heat transfer and chemistry. The goal is the development of a general two-dimensional transient computer code for treating supercritical water/waste flows and reactor-

specific models representing the Sandia bench-scale supercritical water experiments and the full-scale Pine Bluff supercritical water reactor.

The thermodynamics of supercritical water and reactor operating conditions present the modeler with a unique set of challenges. Flow in the Sandia bench scale reactor (EER) can be characterized by the following dimensionless parameters:

$$Re = \frac{\rho V D}{\mu} \geq 6200 \quad (9.1)$$

$$Gr = g A(T) D^3 \geq 2.2 \times 10^9 \quad (9.2)$$

$$\frac{Gr}{Re^2} \geq 60 \quad (9.3)$$

where

$$A(T) = \frac{\beta \Delta T \rho^2}{\mu^2} \quad (9.4)$$

and  $\rho, \mu, \beta, \Delta T, g, V, D$  are the density, viscosity, volume expansion coefficient, thermal deviation from reference, gravitational acceleration, mean flow velocity, and reactor diameter respectively. The parameters in equations (9.1-9.3) were calculated for a reactor temperature and pressure of 400 °C and 24.1 MPa, assuming the flow stream to be predominantly supercritical water. The characteristic dimension used in the parameters was the reactor diameter. For the Sandia bench-scale experiments, the reactor diameter is only 2.79 cm. A more realistic diameter for the full-size reactor increases the Reynolds and Grashof numbers by more than an order of magnitude.

Equation (9.1) indicates that reactor flows are turbulent, even when the flow velocity is based on the average flow rate over the entire reactor cross-section. Equations (9.2-9.3) indicate that buoyancy plays a key role in reactor fluid dynamics. This high level of buoyancy causes a strong coupling between the energy and momentum equations.

It is well-known that the density and specific heat vary by nearly an order of magnitude over a narrow temperature range near the critical value at a reduced pressure ( $P/P_c$ ) of 1.1. There are similar variations in the transport properties (viscosity and thermal conductivity). The severe spike in the specific heat near the critical point at the reactor operating pressure is most problematic. This spike can cause numerical difficulties when the enthalpy (energy) equation is integrated in space and time. These numerical instabilities are made worse by order-of-magnitude variations in density and to a lesser extent changes in transport properties. Figure 9.3 illustrates how the temperature-dependent part of the Grashof number varies over the reactor temperature range. The same variation for an ideal gas (based on the molecular weight of water) is shown for comparison purposes.

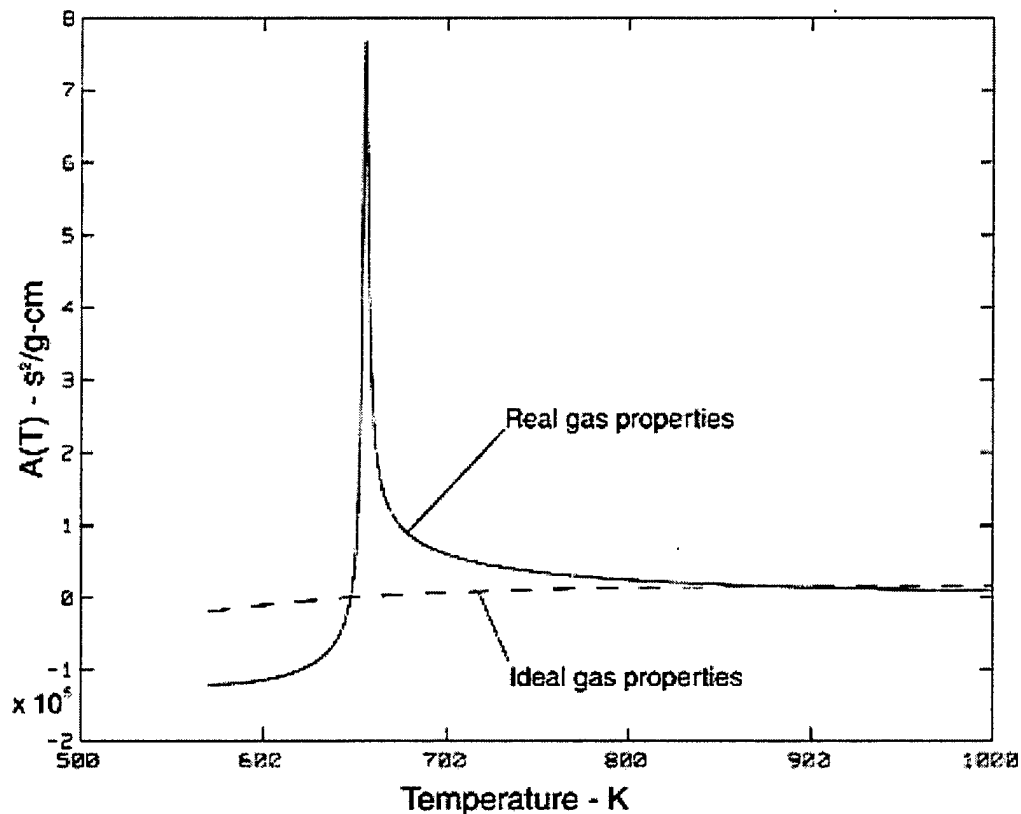


Figure 9.3. Temperature dependent Grashof parameter,  $A(T)$ , variation with temperature for water at 24.1 MPa, just above the critical pressure 22.4 MPa.

The Sandia-developed chemically reacting flow code CURRENT was modified to include the thermodynamic and transport properties of supercritical water based on the NBS steam tables and transport data. An ideal-mixture model has been implemented, in which mixture properties (density, specific heat, viscosity, and thermal conductivity) are determined from the individual component properties and component mole fractions. Ideal-gas equations of state, for the all components other than water, was assumed initially, but present formulation does not preclude the addition of real-gas equations of state for mixture components in future efforts.

In order to account for the expected turbulent flow characteristics, a number of turbulence models have been implemented. These include a simple enhanced viscosity model, the  $k-\epsilon$  model, and Durbin's V2F model.

Calculations were performed using the implemented mixture model, with full buoyancy and turbulent flow. In order to eliminate the numerical difficulties discussed in the previous section, these initial calculations were performed with an ideal-gas

equation of state for water. The calculations were intended to simulate flow through the EER. An example of computed results is shown in Figure 9.4 for a methanol and oxygen reacting system in an idealized geometry representing the top half (40 cm) of the EER. A mixture of high temperature water,  $O_2$ , and,  $CH_3OH$  enters the top of the reactor through a small opening at the reactor centerline. Low speed/low temperature transpiring water enters the reactor through the side walls over the entire reactor length. The distribution of  $CH_3OH$  is shown on the left with high concentrations represented by light gray and low concentrations represented by dark gray. Flow streamlines are shown on the right. A strong recirculation zone is evident near the top of the reactor.

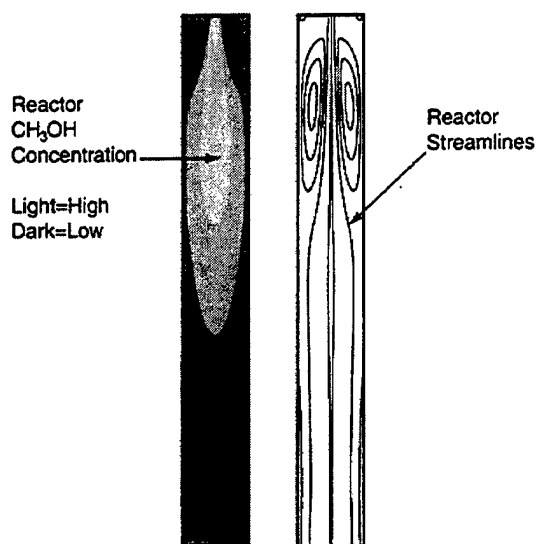


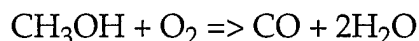
Figure 9.4. Reactor cross-sections showing methanol concentrations and flow streamlines.

### 9.2.3 Fluid dynamical modeling - reaction chemistry and real equation of state

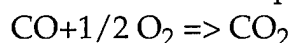
A number of challenges were revealed during the early stages of transitioning the TW CFD calculation to include a real-gas EOS and reacting chemistry. Convergence problems from the non-ideal EOS were overcome after developing a new methodology that is well-suited for this kind of problem and simplified chemistry was incorporated. Within the limitations of the simplified chemistry, we were able to mimic both ignited and non-reactive flow conditions that were dependent on the injection velocity and transpiration water thermal and flow properties.

The first approach was to use simple two-step global kinetics with methanol as the fuel and oxygen as the oxidizer. This mechanism provides for the reaction to be first order in methanol and to be fairly low order in  $O_2$ . The rate parameters are chosen such the methanol conversion is well represented in the 450-550 °C range at 25 MPa. This two step scheme has the advantage of producing CO as an intermediate and requires a higher temperature to oxidize the CO than does methanol. Thus, despite the simplicity, a most of the key aspects of SCWO of methanol can be captured.

**Table 9.2 Two -step methanol mechanism**



$$\text{rate 1} = 1.0\text{E}+08 \exp(-14000/T \text{ (K)}) [\text{CH}_3\text{OH}]^{1.0} [\text{O}_2]^{0.2}$$



$$\text{rate 2} = 3.0\text{E}+08 \exp(-16100/T \text{ (K)}) [\text{CO}]^{1.0} [\text{O}_2]^{0.3}$$

$$d[\text{CH}_3\text{OH}]/dt = -\text{rate 1}$$

$$d[\text{H}_2\text{O}]/dt = + 2(\text{rate 1})$$

$$d[\text{CO}]/dt = +\text{rate 1} - \text{rate 2}$$

$$d[\text{O}_2]/dt = -\text{rate 1} - 1/2 (\text{rate 2})$$

$$d[\text{CO}_2]/dt = + \text{rate 2}$$

The real gas EOS produces difficulties in achieving computational convergence because the density varies so much as a function of temperature. As CURRENT passes through a full iteration, the change in density due to heat release from the oxidation chemistry affects the buoyancy and thus dramatically changes the flow structure. Because of this close coupling, convergence was very slow. This problem was overcome by performing an initial non-reacting calculation at higher temperature that was near the average system temperature after the heat release from the reaction. Once this high temperature flow solution was found it could be used as a starting point for the reacting system.

Figure 9.5 shows the results from a calculation where 90% of the methanol is converted to CO and CO<sub>2</sub>. The presence of a recirculation zone about 13 cm into the reactor is easily observed in the figure on the left showing the streamlines. The flow almost stagnates at the base of this zone. Below this point the flow smooths out, but there is a weaker recirculation zone in the second half of the reactor that rotates in the opposite direction. The lack of streamlines in the center show that the flow in the second section is nearly plug flow.

The second figure from the left shows the temperature profile. The upper recirculation zone creates a quasi-batch reactor in the top section and illustrates that there is a slightly hotter spot in the center. The next two profiles are methanol and oxygen concentration which nearly mirror each other. The last two profiles are CO and CO<sub>2</sub>. The sequential formation of CO followed by the production of CO<sub>2</sub> is evident.

Figure 9.6 shows the streamlines for a calculation that has only one modification from the calculation detailed in Figure 9.5. The injector hole size has twice the area as in Fig. 9.5 such that the injector stream velocity is 208 cm/s and not 416 cm/s. The difference in the result is extreme and can be best interpreted by examining the centerline mole fractions shown in Figures 9.7 and 9.8 comparing the streamlines.

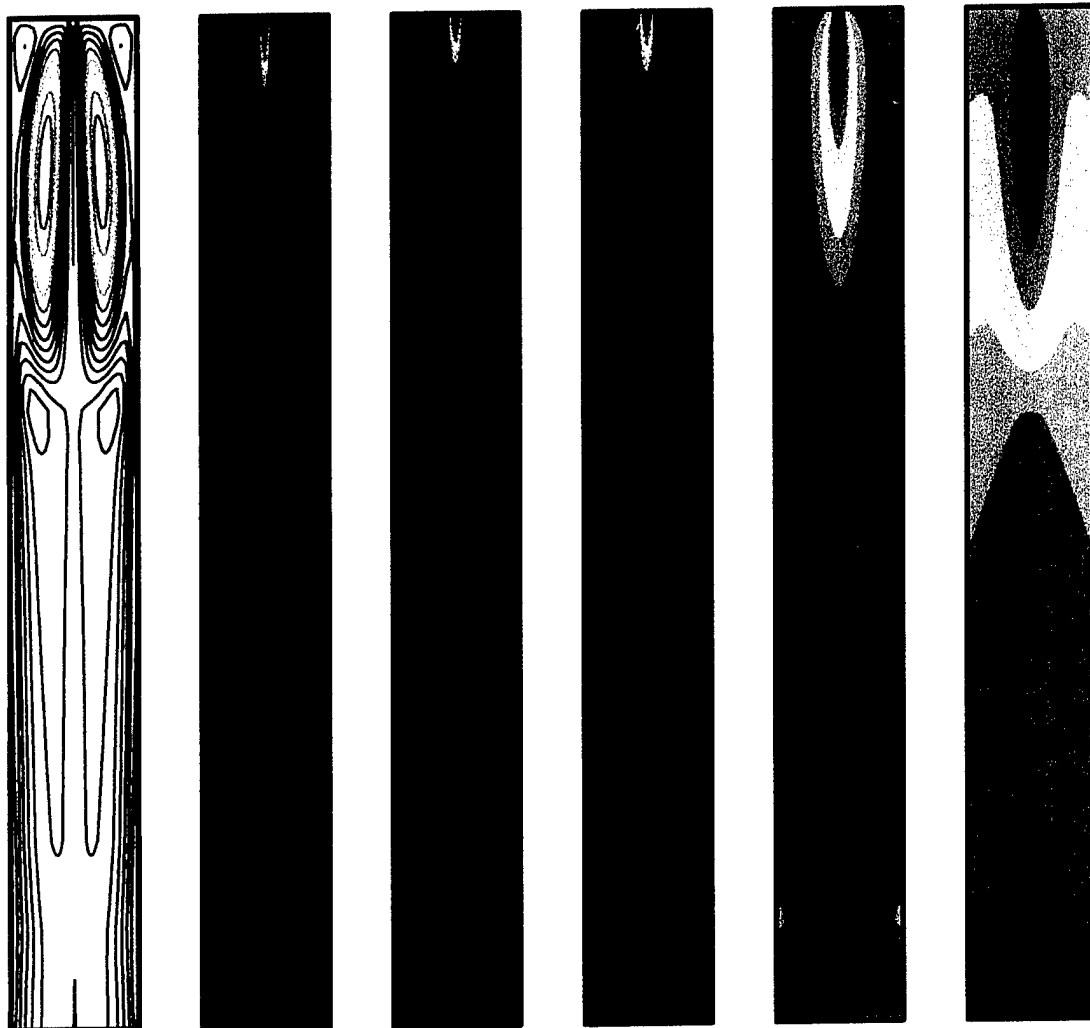


Figure 9.5 Results from calculation with an input temperature of 550 °C and a transpiration temperature of 410 °C. Feed is premixed 8 % methanol and 16% oxygen. From left to right: streamlines, temperature, methanol concentration, O<sub>2</sub> concentration, CO concentration, CO<sub>2</sub> concentration. For the concentration profiles, temperature and stream functions the color scheme is red-high, blue-low.

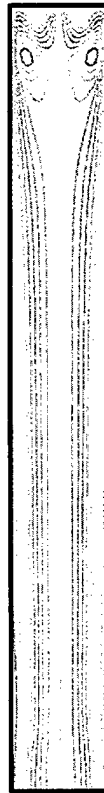


Figure 9.6. Streamlines for the conditions with an injector flow velocity of 208 cm/sec.

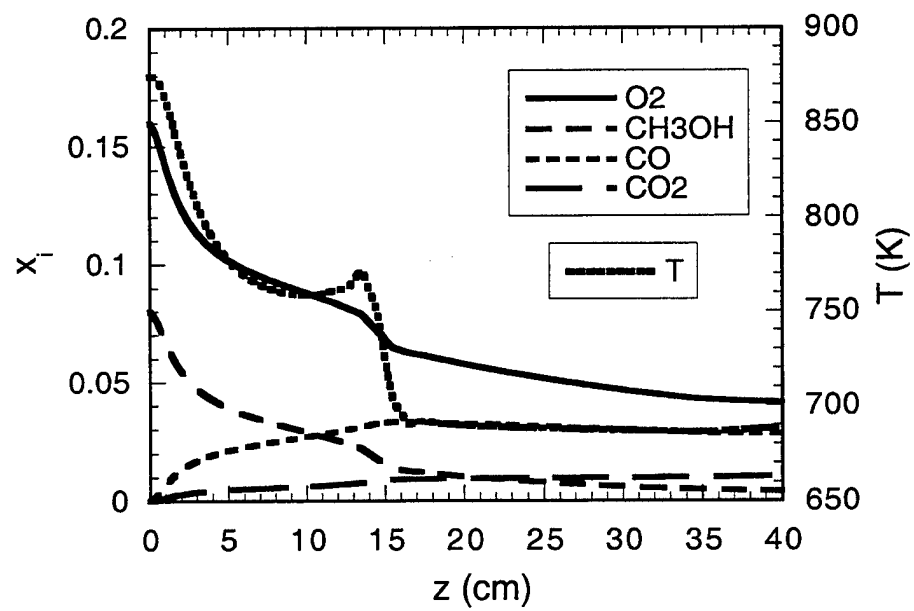




Figure 9.7. Species mole fractions and temperatures on the centerline for injector velocity of 416 cm/s. Same calculation as Fig. 9.5.

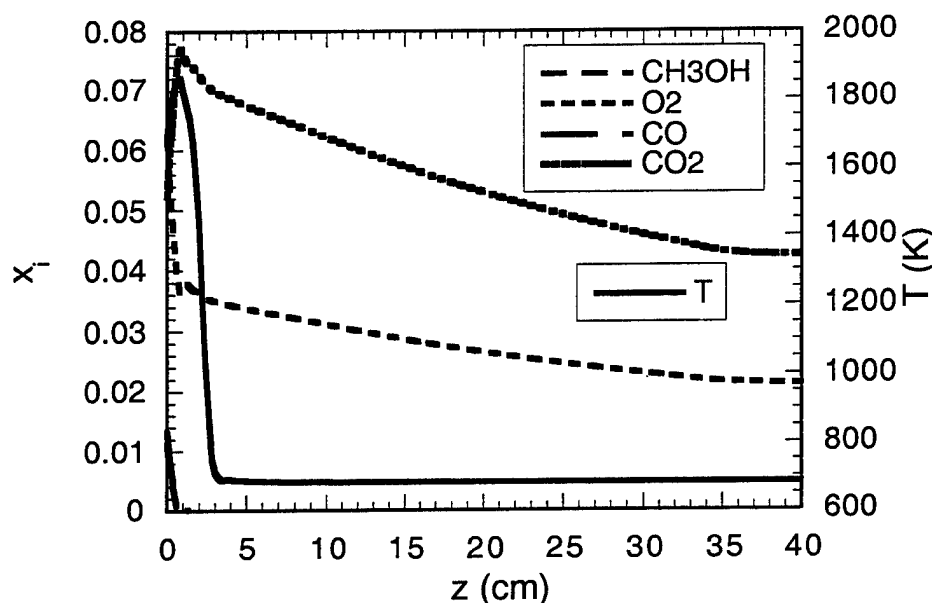


Figure 9.8. Species mole fractions and temperatures on the centerline for injector velocity of 208 cm/s.

The 416 cm/sec injection in Fig. 9.7 causes the reactor to operate as intended, at least to some degree. The oxidation reaction occurs over a large region within the reactor. Sufficient heat is generated from the reaction to offset the cooling from the transpiration water to produce an overall flow that smoothly converts the fuel to  $\text{CO}_2$ , CO and water. In this simulation, the temperature is too low at the outlet to take the reaction to completion. The recirculation zone serves to dilute and cool the injected feed and extends the reaction well into the vessel. The conditions for the simulation in Fig 9.8 differs only by changing the injection flow velocity by a factor of two, however, the operation of the reactor is completely different. In this situation the slower feed does not result in the same recirculation pattern and thus the reaction is not dissipated throughout. In this mode, there is essentially a premixed flame ( $T > 1800\text{K}$ ) coming out of the injector. All of the fuel is fully converted to  $\text{CO}_2$  in a very small and hot volume at the tip of the injector.

Obviously, these calculations only begin to address of the range of operational conditions that can be explored. However, they do point out the significant changes that can occur in this complicated system as flowrates and preheat temperatures are varied. These calculations also illustrate the enormous potential for CFD modeling to aid in the design and operation of such systems.

#### 9.2.4 PBA full-reactor modeling

The motivation for developing this CFD model was ultimately to be able to simulate the operation of the Pine Bluff Arsenal system. Because there are no sensors, even thermocouples, inside the main reactor vessel, operation of the system relies on the external temperature of the reactor pressure vessel as a key system parameter. In order to advance the simple EER model illustrated in the previous section to the full-scale reactor, a number of steps were needed. They were:

- 1) Develop a reduced elementary reaction mechanism for the initiation fuel (isopropanol) and the waste feed that is sufficiently compact to permit convergence of CURRENT. The goal is to move past the simple two step model and have a mechanistic scheme that provides for the initiation chemistry to be based on radical chain propagation and peroxide decomposition. Such a mechanism will properly provide for co-oxidation effects as well as reflect the proper fuel and oxidizer concentration dependence over several decades of conversion.
- 2) Generate a finite element grid for the full-scale PBA system that better approximates the behavior of the multiport injector. The injector in the PBA system has near four-fold symmetry and has over two dozen separate injection holes arranged in eight rings supplying fuel, oxygen, hot supercritical water, and waste slurry as individual streams. These need to be approximated in the 2-D axisymmetric geometry of the calculation as concentric rings.
- 3) Extend the overall simulation to include the transpiration-wall plenum and pressure vessel wall. The heat transfer performance of the transpiration water must be approximated and the outside temperature calculated to be able to compare the results of the overall simulation with the external thermocouples mounted on the reactor.

The approach on mechanism reduction started with an attempt to reduce the modified GRI methanol model of Section 4 to a smaller number of key reactants and reactions. The first goal was to have this model work within the previously established geometry of the EER with the premixed injector illustrated in the subsection 9.2.3 above. The plan was that once the methanol mechanism reduction was established, a similar approach could be used for generating a reduced isopropanol mechanism based on the skeleton of the ethanol model.

Table 9.2 shows the results of this effort. The reduced mechanism accurately reproduced the results of the larger scheme over the temperature range of 450 -550 °C when comparing their performance in an isothermal plug flow geometry. That is, the concentration profiles as a function of time for methanol, CO and CO<sub>2</sub> were very similar in the Senkin calculation.

Although this model significantly reduced that number of species, the set of differential equation is stiff, meaning that there are many reactions in the above scheme that occur

on a sub-microsecond timescale and others that occur on a timescale that is orders of magnitude slower. The mass flux in the reactor is also slow when compared to the elementary chemistry. As a result, we were unable to obtain converged solutions using this simplified mechanism within the single port injector test system in Section 9.2.3.

Still, there was an opportunity to obtain useful information on the Pine Bluff system if we could complete Step 2 with global kinetics expressions for the fuel and oxidizer. These results would enable us to predict conversion and ignition phenomena as a function of feed preheating conditions. If this could be done, extension to the third step was still possible. Again, this proved impossible within the scope of the project. Here, the difficulty arose from the sizing and fluid velocity of the injector ports.

In the real system, the injection of the individual flows is through small (~0.02 in) holes arranged in rings around the centerline of the reactor. See Figure 9.1. However, these holes are not a complete ring covering 360° as in an annular slit. There are simply two or four holes located at 180° or 90° separation along the circumference of a ring. The geometry is truly 3-dimensional. The problem in representing this situation in two dimensions comes from the need to keep both the mass flow and stream velocity the same as in the real system. As an example, consider the four waste feed holes. There are four holes approximately 0.05 in diameter located at a radius of about 1.5 in from the centerline of the injector head. The total area is 0.0078 in<sup>2</sup>. For same area, and therefore the same linear flow velocity and momentum for the stream, an annular slit of 3 in diameter would be only  $8.2 \times 10^{-4}$  in wide. Thus, there is a mismatch between the small computational cell needed to represent the injector and the scale of the overall problem by almost four orders of magnitude. This flow geometry could not be made to converge even without any reaction chemistry.

**Table 9.2 Reduced methanol model**

**Table 9.2a - Reactions**

R1	CH <sub>3</sub> OH+O <sub>2</sub> =>CH <sub>2</sub> OH+HO <sub>2</sub>	2.00E+13	0.00	44910.00
R2	CH <sub>3</sub> OH+HO <sub>2</sub> =>CH <sub>2</sub> OH+H <sub>2</sub> O <sub>2</sub>	3.98E+13	0.00	19400.00
R3	CH <sub>3</sub> OH+OH=>CH <sub>2</sub> OH+H <sub>2</sub> O	2.35E+13	0.00	1775.0
R4	CH <sub>2</sub> OH+O <sub>2</sub> =>CH <sub>2</sub> O+HO <sub>2</sub>	1.80E+13	0.00	900.0
R5	H <sub>2</sub> O <sub>2</sub> =>OH+OH	2.28E+13	0.000	43019.0
R6	OH+H <sub>2</sub> O <sub>2</sub> =>HO <sub>2</sub> +H <sub>2</sub> O	7.83E+12	0.000	1331.00
R7	OH+HO <sub>2</sub> =>H <sub>2</sub> O+O <sub>2</sub>	2.89E+13	0.00	-497.00
R8	HO <sub>2</sub> +HO <sub>2</sub> =>O <sub>2</sub> +H <sub>2</sub> O <sub>2</sub>	4.22E+14	0.00	11983.0
R9	HO <sub>2</sub> +HO <sub>2</sub> =>O <sub>2</sub> +H <sub>2</sub> O <sub>2</sub>	1.32E+11	0.00	-1620.0
R10	CO+HO <sub>2</sub> =>OH+CO <sub>2</sub>	1.51E+14	0.00	23648.0
R11	HO <sub>2</sub> +CH <sub>2</sub> O+O <sub>2</sub> =>H <sub>2</sub> O <sub>2</sub> +HO <sub>2</sub> +CO	3.01E+12	0.000	13076.00
R12	OH+CH <sub>2</sub> O+O <sub>2</sub> =>H <sub>2</sub> O+HO <sub>2</sub> +CO	3.49E+09	1.18	-497.0
R13	OH+CO+O <sub>2</sub> =>CO <sub>2</sub> +HO <sub>2</sub>	1.17E+07	1.354	-725.0

**Table 9.2b - Rate Expression**

Units are cm<sup>3</sup>, mole, cal;  $k = AT^{n} \exp(-E/RT)$  listed as A, n, E

		A	n	E
R1 = k1[O2][CH3OH]	k1 =	2.000E+13	0.00	44910.00
R2 = k2[CH3OH][HO2],	k2 =	3.98E+13	0.00	19400.00
R3 = k3[OH][CH3OH],	k3 =	2.35E+13	0.00	1775.0
R4 = k4[CH2OH][O2],	k4 =	1.8E+13	0.00	900.0
R5 = k5[H2O2],	k5 =	2.28E+13	0.00	43019.0
R6 = k6[OH][H2O2],	k6 =	7.83E+12	0.00	1331.00
R7 = k7[OH][HO2]	k7 =	2.89E+13	0.00	-497.00
R8 = k8[HO2]**2,	k8 =	4.22E+14	0.00	11983.0
R9 = k9[HO2]**2,	k9 =	1.32E+11	0.00	-1620.0
R10 = k10[CO][HO2],	k10 =	1.51E+14	0.00	23648.0
R11 = k11[HO2][CH2O]	k11 =	3.0100+12	0.000	13076.00
R12 = k12[OH][CH2O]	k12 =	3.49E+09	1.18	-497.0
R13 = k13[OH][CO],	k13 =	1.17E+07	1.354	-7 25.0

**Table 9.2c - Individual species production and consumption**

$d[O_2] = -R_1 -R_4 +R_7 +R_8 +R_9 -R_{11}-R_{12} -R_{13}$   
 $d[OH] = -R_3 + 2*R_5 -R_6 -R_7 +R_{10} -R_{12} -R_{13}$   
 $d[H_2O] = +R_3 +R_6 +R_7 +R_{12}$   
 $d[HO_2] = +R_1 -R_2 +R_4 +R_6 -R_7 -R_8 -R_9 -R_{10} +R_{12} +R_{13}$   
 $d[H_2O_2] = +R_2 -R_5 -R_6 +R_8 +R_9 +R_{11}$   
 $d[CO] = -R_{10} +R_{11}+R_{12} -R_{13}$   
 $d[CO_2] = +R_{10} +R_{13}$   
 $d[CH_2O] = +R_4 -R_{11} -R_{12}$   
 $d[CH_2OH] = +R_1 +R_2 +R_3 -R_4$   
 $d[CH_3OH] = -R_1 -R_2 -R_3$

### 9.2.5 CFD modeling summary

At the present time and with the present state-of the-art of CFD and reacting chemistry computational tools, it is not likely that the PBA reactor can be modeled in a way that would be physically meaningful or accurate. This is not to say that without additional effort in reacting CFD code development that this problem could not be addressed, even within a few years. However, before much headway can be made, a directed effort at code improvement will be necessary. External to this project, there is a great deal of work going on worldwide to develop more efficient methods for dealing with these wide timescale variations in CFD modeling for application to the chemical industry. These developments will have a direct impact on modeling SCWO reactors in the near future.

This effort has had some significant success, however. At least two important and formerly underappreciated concepts have been illustrated by this work. The most important is the effect of inlet velocity on total conversion and internal temperature

profiles. The competing effects of dilution of the jet by the cool transpiration water and the heat release from the reaction determine the average time-temperature profile that the fuel-oxygen mixture experiences. The other effect is that of the strong buoyant recirculation that serves to create a reacting lower density bubble some distance below the injector port that sits on a near stagnation plane within the reactor. The consequence of this is to move the highest temperature place in the reactor several diameters below the injector. It is interesting to note that in the Pine Bluff system, the highest external temperatures of the pressure vessel are measured at this point and not at the top of the reactor. It is also valuable to note that in the EER testing, where internal thermocouples were available, the highest temperature was also observed about 4-5 reactor diameters below the injection point.

### 9.3 References

1. C.H. Oh, R.J. Kochan, J.M. Beller "Numerical-Analysis and Data Comparison of a Supercritical Water Oxidation Reactor" *AIChE J.* **43**, 1627-1636, 1997.
2. C.H. Oh,, R.J. Kochan , T.R. Charlton, A.L. Bourhis "Thermal-Hydraulic Modeling of Supercritical Water Oxidation of Ethanol" *EnergyFuels* **10**, 326-332, 1996.
3. M.F. Young,,M.C. Stoddard, B.L. Haroldsen, K.S. Ahluwalia, C.D. Robinson "The Transpiring Wall Platelet Reactor for Supercritical Water Oxidation of Materials with High Inorganic Loading" *Proceedings of The Fourth International Symposium on Supercritical Fluids*, Sendai, Japan May 11-14, 1997. p. 167.
4. H.H. Mueggenburg, J.W. Hidahl, E.L. Kessler., D.C. Rouser "Platelet Actively Cooled Thermal Management Devices" AIAA/SAE/ASME/ASEE 28th Joint Propulsion Conference and Exhibit, 1992, Nashville, TN.
5. C.A. LaJeunesse, B.L. Haroldsen, S.F. Rice, B.G. Brown "Hydrothermal Oxidation of Navy Shipboard Excess Hazardous Materials" Sandia Report SAND97-8212, 1997.

## Appendix A SERDP Publications

### Sandia National Laboratories

- R.R. Steeper, S.F. Rice "Optical Monitoring of the Oxidation of Methane in Supercritical Water"; in *Physical Chemistry of Aqueous Systems*, (H.J. White, J.V. Sengers, D.B. Neumann, J.C. Bellows Eds.) Begell House, New York, 1995, p. 652.
- R.R. Steeper, S.F. Rice "Kinetics Measurements of Methane in Supercritical Water" *Journal of Physical Chemistry* **100**, 184-189, 1996.
- R.R. Steeper, "Methane and Methanol Oxidation in Supercritical Water: Chemical Kinetics and Hydrothermal Flame Studies" Sandia Report SAND96-8208, 1996.
- S.F. Rice, T.B. Hunter, Å.C. Rydén, R.G. Hanush "Raman Spectroscopic Measurement of Oxidation in Supercritical Water I. Conversion of Methanol to Formaldehyde" *Industrial and Engineering Chemistry Research* **35**, 2161-2171, 1996.
- T.B. Hunter, S.F. Rice, R.G. Hanush "Raman Spectroscopic Measurement of Oxidation in Supercritical Water II. Conversion of Isopropanol to Acetone" *Industrial and Engineering Chemistry Research*. **35**, 3984-3990, 1996.
- R.G. Hanush, S.F. Rice, T.B. Hunter, and J.D. Aiken "Operation and Performance of the Supercritical Fluids Reactor (SFR)" Sandia National Laboratories Report SAND96-8203, Livermore, CA, 1996.
- S.F. Rice, T.B. Hunter, and R.G. Hanush "Oxidative Reactivity of Simple Alcohols In Supercritical Water Using *In Situ* Raman Spectroscopy"; Proceedings of the Second International Symposium on Environmental Applications of Advanced Oxidation Technologies February 28 -March 1, 1996 San Francisco CA, pp. 8-76:8-88, 1997.
- C.A. LaJeunesse, B.L. Haroldsen, S.F. Rice, B.G. Brown "Hydrothermal Oxidation of Navy Shipboard Excess Hazardous Materials" Sandia Report SAND97-8212, 1997.
- E. Croiset, S.F. Rice, and R.G. Hanush "Hydrogen Peroxide Decomposition in Supercritical Water" *AIChE Journal* **43**, 2343-2352, 1997.
- R.R. Steeper, S.F. Rice, and J.D. Aiken "Water-Gas Shift Reaction Kinetics in Supercritical Water" *Proceedings of The Fourth International Symposium on Supercritical Fluids*, Sendai, Japan May 11-14, p. 575. 1997
- S.F. Rice, R.R. Steeper, C.A. LaJeunesse, R.G. Hanush, and J.D. Aiken; "Design Strategies for High-Temperature, High-Pressure Optical Cells" *Proceedings of The*

*Fourth International Symposium on Supercritical Fluids Sendai, Japan May 11-14, p. 163, 1997.*

S.F. Rice, "Application of the GRI 1.2 Methane Oxidation Model to Methane and Methanol Oxidation in Supercritical Water"; *Proceedings of The Fourth International Symposium on Supercritical Fluids Sendai, Japan May 11-14, p. 571, 1997.*

S.F. Rice, R.R. Steeper, J.D. Aiken, "Water Density Effects on Homogeneous Water-Gas Shift Reaction Kinetics" *J. Phys. Chem. A* **102**, 2673-2678, 1998.

E. Croiset, S.F. Rice, "Direct Observation of H<sub>2</sub>O<sub>2</sub> During Alcohol Oxidation by O<sub>2</sub> in Supercritical Water" *Ind. Eng. Chem. Res.* **37**, 1755-1760, 1998.

S.F. Rice, R.R. Steeper, "Oxidation Rates of Common Organic Compounds in Supercritical Water"; *Journal of Hazardous Materials* **59**, 261-278, 1998.

S.F. Rice, R.R. Steeper, C.A. LaJeunesse, R.G. Hanush, and J.D. Aiken. "Design Strategies for High-Temperature, High-Pressure Optical Cells" Sandia Report SAND99 -8260, 1999.

S.F. Rice, B.C. Wu, W.S Winters, C.D. Robinson. "Engineering Modeling of the Pine Bluff Arsenal Supercritical Water Oxidation Reactor" 5th International" *Proceedings of The Fifth International Symposium on Supercritical Fluids Atlanta , GA April 8-12, 2000.*

S.F. Rice J. J. Wickham "Hydrogen Raman Linewidths in Supercritical Water and Carbon Dioxide" *J. Raman Spectroscop.* **31**, 619-624 , 2000.

S.F. Rice/ E. Croiset "Oxidation of Simple Alcohols in Supercritical Water III. Formation of Intermediates from Ethanol." Submitted to *Ind. Eng. Chem. Res.* **40**, 86-93, 2001.

## **University Collaborators**

### ***Princeton University***

M. Pecullan, K. Brezinsky K, I. Glassman " Pyrolysis And Oxidation of Anisole near 1000 K" *Journal Of Physical Chemistry A* v. **101** 3305-3316, 1997

M. Pecullan, K. Brezinsky K, I. Glassman. "Pyrolysis and Oxidation of Phenol" *Journal of Physical Chemistry A* **102**, 8614-8619, 1998

Pecullan, M. S.; "Pyrolysis and Oxidation Kinetics of Anisole and Phenol" Princeton University, Ph. D. Thesis (1997).

**Massachusetts Institute of Technology**

J.W. Tester, P.A. Marrone, M.M. DiPippo, K. Sako, K.; M.T. Reagan, T. Arias, T.; W.A. Peters "Chemical Reactions and Phase Equilibria of Model Halocarbons in Sub- And Supercritical Water (200 to 250 Bar, 100 To 600 °C)" *Proceedings of The Fourth International Symposium on Supercritical Fluids*, pp .881-894, 1997.

B.D. Phenix "Hydrothermal Oxidation of Simple Organic Compounds" Massachusetts Institute of Technology, Ph. D. Thesis, 1997.

P.A. Marrone, P.M. Gschwend, K.C. Swallow, W.A. Peters, J.W. Tester "Product Distribution and Reaction Pathways for Methylene Chloride Hydrolysis and Oxidation Under Hydrothermal Conditions" *J. of Supercritical Fluids* **12**, 239-254, 1998.

J.W. Tester, P.A. Marrone, M.M. DiPippo, K. Sako, K.; M.T. Reagan, T. Arias, T.; W.A. Peters "Chemical Reactions and Phase Equilibria of Model Halocarbons in Sub- and Supercritical Water (200 To 250 Bar, 100 To 600 °C)." *J. of Supercritical Fluids* **13**, 225-240, 1998.

B. Phenix, J. DiNaro, M. Tatang, J.W. Tester, J.B. Howard, G. McRae "Incorporation of Parametric Uncertainty into Complex Kinetic Mechanisms: Application to hydrogen oxidation in supercritical water" *Combustion and Flame*, **112**, 132-146, 1998.

J.L DiNaro, "Oxidation of Benzene in Supercritical Water: Experimental Measurements and Development of an Elementary Reaction Mechanism" Massachusetts Institute of Technology, Ph. D. Thesis 1999.

J.L DiNaro, J.B. Howard, W.H. Green, J.W. Tester, Bozzelli, J.W. "Elementary Reaction Mechanism for Benzene Oxidation in Supercritical Water" *J. Phys Chem A*, **104**, 10576-10586, 2000.

J.L DiNaro, J.W. Tester, J.B. Howard, KC Swallow. "Experimental Measurements of Benzene Oxidation in Supercritical Water" *AIChE J.* **46**, 2274-2284, 2000.



This page intentionally left blank

**Initial External Distribution:**

Dr. Paul Maupin  
Office of Science SC-14  
U.S. Dept. of Energy  
19901 Germantown Rd.  
Germantown, MD 20874

Mr. Sam Fuguli (2)  
HydroGeoLogic Inc.  
1155 Herndon Parkway, Suite 900  
Herndon, VA 20170

Dr. Robert W. Holst  
SERDP Program Office  
Program Manager for Compliance and  
Global Environmental Change  
901 North Stuart Street, Suite 303  
Arlington, VA 22203

Dr. Bradley P. Smith  
SERDP Program Office  
901 North Stuart Street, Suite 303  
Arlington, VA 22203

Mr. Crane Robinson  
Armament Research  
Development & Engineering Center  
(ARDEC)  
SMCAR-AES-P  
Building 321  
Picatinny Arsenal, NJ 07806-5000

Mr. James Q. Wheeler (2)  
Director  
Defense Ammunition Center  
ATTN: SMAAC-DO  
1 C Tree Road  
McAlester, OK 74501-9053

Dr. Robert Shaw  
Chemical & Biological Sciences Div.  
U.S. Army Research Office  
Research Triangle Park, NC 27709-2211

Prof. Martin A. Abraham  
Dept of Chem. and Environ. Eng.  
University of Toledo  
Toledo, OH 43606

Prof. Michael Antal  
Dept. of Chemical Engineering  
2540 Dole St.  
Honolulu, HI  
96822

Prof. Joan F. Brennecke  
University of Notre Dame  
Department of Chemical Engineering  
Notre Dame, IN 46556

Dr. Kenneth Brezinsky  
Dept. of Chemical Engineering  
U. of Illinois, Chicago  
810 S. Clinton St. M/C 110  
Chicago, IL 60607

Prof. Keith Johnston  
University of Texas at Austin  
Chemical Engineering Dept.  
26th and Speedway  
Austin, TX 78712-1062

Dr. Yukihiko Matsumura  
Environmental Science Center  
University of Tokyo  
7-3-1 Hongo, Bunkyo-ku  
Tokyo 113  
JAPAN

Dr. Yoshito Oshima  
Dept. of Chemical System Engineering  
University of Tokyo  
7-3-1 Hongo, Bunkyo-ku  
Tokyo 113  
JAPAN

Prof. Jefferson W. Tester  
Massachusetts Institute of Technology  
Room E40-455  
77 Massachusetts Avenue  
Cambridge, MA 02139

Mr K.S. Ahluwalia  
Foster Wheeler Development Corp.  
Engineering Science & Technology  
12 Peach Tree Hill Road  
Livingston, NJ 07039

Dr. William Killilea  
Stone and Webster  
245 Summer St.  
Boston, MA 02210

Dr. David A. Hazelbeck  
General Atomics  
M/S 15-100D  
3550 General Atomics Court  
San Diego, CA 92121-1194

Dr. Steven J. Buelow  
Los Alamos National Laboratory  
MS J567 C-PCS  
Los Alamos, New Mexico 87545

Prof. Eric Croiset  
Dept. of Chemical Engineering  
200 University Ave. W.  
Waterloo, Ontario  
Canada N2L 3G1

Dr. Robert E. Huie  
National Institute of Standards and  
Technology  
Chemistry A261  
Gaithersburg MD 20899

#### **Sandia Internal Distribution:**

MS0710 6245 A.P. Sylwester  
MS1393 G.C. Allen, 09800  
MS9001 M.E. John, 8000  
Attn: 8100 J.C. Vitko  
MS9103 K. Wally, 08120  
MS9105 A. McDonald, 08118  
MS9105 D. Ariizumi, 8119  
MS9105 B. Haroldsen, 08118  
MS9105 M.C. Stoddard, 08119  
MS9105 B.C. Wu, 08119  
MS9042 W.S. Winters, 08742  
MS9054 W.J. McLean, 08300  
MS9055 F.P. Tully, 8350  
MS9051 L.A. Rahn, 08351  
MS9055 J. Goldsmith, 08353  
MS9051 R. Gallagher, 08356  
MS9053 R. Carling, 08360  
MS9052 D. R. Hardesty, 08361 (2)  
MS9053 J.O. Keller. 08362  
MS9052 S.W. Allendorf, 08361  
MS9052 M.D. Allendorf, 08361  
MS9052 T.A. McDaniel, 08361

MS9052 C. Shaddix, 08361

MS 9052 L. Blevins, 08361

MS 9052 R. Behrens, 08361

MS 9052 S. Margolis, 08361

MS 9052 R. Hanush, 08361

MS 9052 S. Rice, 08361 (20)

MS 9052 J. Taylor, 08361

MS 9131 K. D. Overby, 8528 (2)

MS 9018 Central Technical Files, 8945-1  
(3)

MS 0899 Technical Library, 9616

MS 9021 Classification Office,  
8511/Technical Library, MS 0899, 9616

MS 9021 Classification Office, 8511 for  
DOE/OSTI

MS 9021 Technical Library

MS 9053 R. Steeper, 08362

MS 9201 H. H. Hirano, 16000

MS 9403 D. K. Ottesen, 8723

MS 9403 B. Mills, 08723

MS 9671 A. Pontau, 08358

This page intentionally left blank



**Sandia National Laboratories**